Fabricating Functional Luminescent Metal-Organic Framework Nanosheet Materials

Dylan A. Sherman

Trinity College

University of Oxford

A thesis submitted for the degree of

Doctor of Philosophy

Trinity 2024

Preface

This dissertation is submitted for the degree of Doctor of Philosophy in the University of Oxford, United Kingdom. The research presented in this work was carried out by the author between October 2020 and October 2024 in the Department of Engineering Science, under the supervision of Professor Jin-Chong Tan.

To the best of my knowledge, the work described in this dissertation is original, except where due reference has been made, acknowledging the work of others. Nothing has been included that is the outcome of work done in collaboration with others, except where explicitly noted. No part of this dissertation, or any similar to it, has been, or is currently being submitted for any degree at this, or any other university. This integrated thesis is less than 250 pages in length.

The work presented herein has been prepared for submission, or partially published in the following journal papers:

- **D. A. Sherman**, M. Gutiérrez, I. Griffiths, S. Mollick, N. Amin, A. Douhal, J.-C. Tan, "Guest Entrapment in Metal-Organic Nanosheets for Quantifiably Tuneable Luminescence", *Advanced Functional Materials*, 33, 2214307 (2023).

- **D. A. Sherman,** W. Kamal, S. J. Elston, A. A. Castrejón-Pita, S. M. Morris, J.-C. Tan, "Stable photoinduced metal-organic nanosheet blue phosphor for white light emission", *Materials Today Chemistry*, 38, 102089 (2024).

- **D. A. Sherman,** E. Landberg, A. R. Peringath, S. Kar-Narayan, J.-C. Tan, "Fine-scale Aerosol-Jet Printing of Luminescent Metal-Organic Framework Nanosheets", *ACS Applied Materials & Interfaces* (2024).

- **D. A. Sherman**, L. Doná, C. Besnard, L. Mester, B. Slater, J. Fernando-Perez, C. Allen, J. Silvestre-Albero, B. Civalleri, J.-C. Tan, "Elucidating Guest-Host Mechanisms in ZIF-L for Tuneable Highly Luminescent Functional Materials", *prepared for submission*.

Other manuscripts related to the work presented in this thesis:

- Y. Zhang, S. Mollick, M. Tricario, J. Ye, **D. A. Sherman**, J.-C. Tan, "Turn-On Fluorescence Chemical Sensing through Transformation of Self-Trapped Exciton States at Room Temperature", *ACS Sensors*, 7(8), 2338-2344 (2022).

- M. Tricarico, S. Mollick, V. Kachwal, **D. A. Sherman**, J.-C. Tan, "Exploring the Photophysical and Mechanical Behavior of Fluorescent Metal–Organic Framework Monoliths", *Chemistry of Materials*, 36(17), 8247-8254 (2024).

For those I lost along the way,

whose final moments I missed.

Acknowledgments

Four years ago, I farewelled my childhood bedroom and family home and ventured across the globe, in the middle of a global pandemic, to embark on this DPhil. What followed, was the journey of a lifetime, guided and supported by the most incredible and inspiring group of people. Mere words will not suffice to thank everyone, but I aim at least to acknowledge their importance to seeing this thesis precipitate from the murky waters of an idea.

Thank you firstly to my supervisor, Professor Jin-Chong Tan. Without your expertise, encouragement, and vision, I would not be writing on this page today. I cannot be more appreciative of your willingness to respond at any time and undertake reviews at the eleventh hour, and your everlasting enthusiasm to push beyond the possible and achieve more than I could comprehend. I'd also like to acknowledge the many collaborations Jin-Chong helped cultivate, from which grew many branches of new science for this thesis.

To all of our collaborators across the globe (Mario and Prof. Douhal at UCLM, Lorenzo and Prof. Civalleri at UNITO, Judit and Prof. Silvestre-Albero at the University of Alicante, Lars at Attocbue, Erik, Anjana, and Prof. Kar-Narayan at Cambridge, Chris and Mohsen at ePSIC, Gianfelice and Mark at Diamond's B22 line, Waqas and team in Engineering Science, and Harry, Nader, and Coral from

the Oxford Chemistry NMR Facility) thank you for going above and beyond, making me feel welcomed and a part of your labs, sharing your local cultures and cuisines, and offering so much trust, interest, and insight into the projects on which we embarked. Your contributions have added much vibrancy to this work.

Formally, I'd like to thank the many funders who made this thesis, my time at Oxford, and the many trips to conferences and events possible. These include the Australian Sir John Monash Foundation, the Clarendon Fund, Trinity College, Department of Engineering Science, the Royal Society of Chemistry, the American Chemical Society, and Prof. Jin-Chong Tan's PROMOFS ERC Consolidator Grant.

Thank you to all MMC Lab members who I've been fortunate to call colleagues – Yogesh, Vishal, Yang, Tianhuai, Tao, Sujeet, Samraj, Mounir, Michele, Medhi, Mario, Jinke, Jiahao, Cyril, Chuzhan, Ben, Arun and Annika. Your friendship, motivation (especially over weekends of night shifts at the beamline!) and plentiful supply of cakes made our group a wonderful place to be. Thank you especially to our post-docs for always checking in and offering advice, even as I often ran in and out of labs and offices faster than many materials can fluoresce. Thank you also to members before my time, especially Abhijeet, for much of the foundational work that inspired this thesis. To future members, thank you for any work that continues from this thesis. I can't wait to see what science evolves.

I found myself part of so many supportive communities around Oxford, from the 2021 Clarendon Council and broader Clarendon community to the orienteers in OUOC, local Aussie scholars (including my honours desk comrade who found his

way to London), and the mighty percussion section of the OUO. Thank you to the many friends I've found in each for creating so much happiness, many memorable moments, and endless adventures. Thank you also to my home away from home, Trinity College. I can't thank everyone, but to the fellows, junior deans, staff, and dining team (especially Andrei!) who made me feel part of the community, thank you for your support. To my many friends in Trinity's MCR, especially the 2020-21 Nunnery Household, thank you for your enduring company through unpredictable times.

On a personal note, I am beyond fortunate to have had the support of such a loving family. Your visits, deliveries from Aus, and Facetimes were bright moments of each day, and your constant care grounded me and kept me going no matter what I faced. While you're no longer here to express it, Grandma & Pop, your love, joy, and humour are everlasting and helped me through every day. Finally, Karina, thank you for always being there, believing in me, and selflessly sharing your kind and warming love unconditionally. We did it.

Abstract

Luminescent metal-organic frameworks (LMOFs) are promising materials for myriad chromatic based applications, from organic-light emitting diodes (OLEDs) to sensors and optoelectronics. This arises from the rational tunability of MOFs, which imparts control over material properties so they can be tailored to particular use cases. Yet, the 3D nature of LMOFs creates challenges for optical transparency, sensing sensitivity, and device integration. Metal-organic framework nanosheets (MONs) have the potential to overcome these limitations by retaining the benefits of MOFs but in an atomically thin morphology of large planar dimensions.

This integrated thesis establishes luminescent MONs (LMONs) as next-generation MOF materials for lighting, indicators, and sensors (Chapter 1). Chapter 2 introduces the emerging field of MONs, and the techniques employed in this work to study the photophysical properties of materials. In Chapter 3, a robust *in situ* guest incorporation strategy for luminescent dyes in MONs is established. The incorporation of red, green, and blue emitters in various combinations endowed MONs with new luminescent properties, including white light emission (WLE), that could be tuned based on guest content and arrangement. The improved fabricability available with MONs is demonstrated in Chapter 4, by realising aerosol jet printing as a new methodology for creating fine-scale MOF-based luminescent thin film patterns and micro-structures.

Chapter 5 expands the concept of luminescent guest@MONs to thicker (~ 200 nm) 2D ZIF-L materials, allowing the benefits of 2D guest intercalation to be coupled with more regular porosity. The result was increased predictability of structure-property relationships that could be used to better tune luminescent behaviours, along with an ability to grow *in situ* luminescent ZIF-L oriented films.

A critical review of the studies in this thesis is provided in Chapter 6, accompanied with an outlook for the future directions of LMON-based optical devices.

Contents

List of Figures

List of Tables

List of Abbreviations

1D	One-dimensional
2D	Two-dimensional
3D	Three-dimensional
ACQ	Aggregation caused quenching
AEEE	Aggregation enhanced excimer emission
AFM	Atomic force microscopy
AJP	Aerosol-jet printing
ATR-FTIR	Attenuated total reflection Fourier transform infra-red spectroscopy
BET	Brunauer-Emmett-Teller
bIm	Benzimidazolate
CCT	Colour correlated temperatures
CIE	Commission Internationale de l'Éclairage
CP	Coordination polymers
DCl	Deuterium chloride
DF	Density Functional Theory
DG	Dual-guest
DI	Deionised water
DMF	Dimethylformamide

DoD	Drop-on-demand
EtOH	Ethanol
FE-SEM	Field emission scanning electron microscopy
FLIM	Fluorescence lifetime imaging microscopy
FRET	Förster resonance energy transfer
F	Fluorescein
HAADF-STEM	High-angle annular dark-field scanning transmission electron microscopy
HC	7-hydroxycoumarin
H-aggregate	Hypsochromic-aggregate
HQ	8-hydroxyquinoline
HR-TEM	High resolution transmission electron microscopy
Hmim	2-methylimidazole
IPA	Isopropyl alcohol
IR	Infra-red
J-aggregate	Jelley-aggregate
LED	Light emitting diode
LMOF	Luminescent metal-organic framework
LMON	Luminescent metal-organic framework nanosheet
MC	7-methoxycoumarin
MeOH	Methanol
MOF	Metal-organic framework
MON	Metal-organic framework nanosheet

NaCl	Sodium chloride
nano-FTIR	Near-field nanoscale Fourier transform infra-red spectroscopy
NMR	Nuclear magnetic resonance
NTC	Naphthalene tetracarboxylic acid
OLED	Organic light emitting diode
PD	Pyromellitic diimide
PDMS	Polydimethylsiloxane
PET	Polyethylene terephthalate
PLQY	Photoluminescent quantum yield
PsHet	Pseudo-heterodyne
PXRD	Powder x-ray diffraction
QCL	Quantum cascade laser
RB	Rhodamine B
RGB	Red, green, blue
SAED	Selected area electron diffraction
SBU	Secondary building units
SEM	Scanning electron microscopy
s-SNOM	Scattering-type scanning near-field optical microscopy
TCSPC	Time-correlated single-photon counting
TGA	Thermal gravimetric analysis
TEM	Transmission electron microscopy
TG	Triple Guest

TPE	Tetraphenylethylene
UV	Ultraviolet
UV-A	Ultraviolet A
UNESCO	United Nations Education, Scientific, and Cultural Organisation
VIS	Visible
WLE	White light emission
WLED	White light emitting diodes
Z7-NS	ZIF-7-III nanosheets
ZHQ	Zn(II) 8-hydroxyquinoline
ZIF	Zeolitic imidazolate framework

List of Symbols

Å	Angstroms
θ	Angle
τ	Fluorescence lifetime
°C	Degrees Celsius
cm	Centimetres
cm^{-1}	Wave number
g	Grams
J	Joules
K	Kelvin
mL	Millilitres
mg	Milligram
mm	Millimetres
mmol	Millimole
mN/m	Millinewton/metre
mol	Mole
nm	Nanometres
ns	Nanoseconds
Pa s	Pascal second

pH	Potential of hydrogen
s	Seconds
S_0	Ground singlet state
S_1	First excited singlet state
T_1	First excited triplet state
μm	Micrometres
μs	Microseconds
W	Watt
wt	Weight

1

Introduction

1.1 Motivation

Light is a foundational element of life and a guiding force of human history since its genesis. Without light, we would lose the critical sense of sight. Beyond its necessity as an energy source powering photosynthetic processes, and now photovoltaics, light has been harnessed by humans as a critical resource for development. One could trace this back to the first fires and then torches that were used to control light nearly 300,000 years ago, providing sight in the dark for survival and exploration.[1] Later, light directing devices such as glass prisms and lenses led to the advent of microscopy and telescopes. The milestone invention of the lightbulb revolutionised the generation of light and has since rapidly evolved into light emitting diodes (LEDs), organic light emitting diodes (OLEDs) and new quantum technologies, such as quantum dots, that manipulate light at the nanoscale. As a society, we now rely on light ubiquitously across essential services to power communications, information & education, entertainment and more. The United Nations Education, Scientific, and Cultural Organisation (UNESCO) declared 2015

as the International Year of Light and Light-Based technologies in recognition of the importance of light and optical technologies.[2]

Colour is a key phenomenon of light and is determined by the wavelength of light. Our perception of colour relies on how light interacts with objects (i.e. absorption, reflection, and emission) and how our biological processes, especially related to the retina, process this light. In nature, colour acts as an evolutionary device for camouflage, a signal of danger to predators, or communications with individuals of the same species to attract mates. For humanity, colour is a favourable feature of light, from being valued in commerce through dyes and pigments, to the creation of art and fashion.[1] Now, colour is an essential component of screens, and indicators for mechanical systems, to name but a few applications. To manipulate the colour of light, however, requires precise tools and the tuneability of material properties. Of particular interest is achieving white light emission (WLE), which relies on either broadband emission across the visible spectrum, or multicomponent emission from distinct colours that combine to produce white light (e.g. red, blue, and green, or blue and yellow).[3]

Producing light requires energy input and conversion. Luminescence is a highly effective and tuneable mechanism to achieve this, being the emission of light without heat due to energetic excitation. Fluorescence, a type of luminescence, involves the absorbance of typically higher energy light, e.g. ultraviolet (UV) or blue visible, followed by spontaneous emission at lower energies.[4] A range of organic molecules, typically aromatics, are well studied for their ability to fluoresce

with emission colours across the visible spectrum.[5] They are utilised in diverse applications including *in vivo* biological imaging and tagging, as a component in LEDs, making textiles whiter, measuring protein binding, detecting and quantifying certain materials, and sensing more generally (e.g. of chemicals, pressure, or temperature).[5] Organic molecular fluorophores often exhibit short lifetimes, however, due to photoinduced decomposition. They are also difficult to control, typically being non-emissive in the solid state due to aggregation of the fluorophores and a lack of tuneable crystallinity that could be used to control packing arrangements.

To better control fluorophores, and hence their suitability for applications, a range of composite materials have been reported. Metal-organic frameworks (MOFs), porous crystalline hybrid materials, are a common host superstructure that can be used to encapsulate guest organic fluorophores in porous cavities. The resultant "guest@host" MOF materials are a class of luminescent metal-organic frameworks (LMOFs) that have been found to stabilise guests, control the turning on and off of fluorescence, evoke new guest-guest and host-guest interactions, and otherwise tune the luminescent properties of the guest.[6] LMOF guest@host materials, however, still have limitations. For example, the three-dimensional (3D) MOF architecture can cause self-absorption and quenching, leading to guest leaching into the external environmental surrounds over time, and can exhibit delays in sensing due to the organic dyes being buried in the superstructure. Even if these are overcome by careful material design, LMOF powders are difficult to shape and fabricate into thin film optoelectronic devices.

Two-dimensional (2D) nanosheet materials, those with atomically thin height but micron scale lateral dimensions, theoretically offer resolutions to these issues. The morphology increases optical transparency with increased exposed surface areas and active sensing sites, while the layered structure can provide a degree of directional emission control and sensing. The nanoscale thickness and strong interlayer intermolecular forces offer the potential for improved fabricability. While luminescent guests have been intercalated into widely reported 2D materials, such as metal oxides, clays, and MXenes, these materials lack the customisability of MOFs.[7] Metal-organic framework nanosheets (MONs) present a promising alternative by uniting the benefits of 2D materials with the porosity, rational design and tuneability of MOFs.[8]

To date, MONs have been primarily explored for catalysis, sensing, gas and molecular selectivity, and photovoltaics.[8] Few luminescent MONs (LMONs) exist, and those that do incorporate luminescent ligands into the framework, which can limit the degree of tuneability (e.g. guest loading and arrangement of luminescent active components).[9] The guest@host design is a promising mechanism to introduce fluorophores into MONs by intercalating guests between 2D nanosheet layers, but the concept has yet to be fully realised in MON systems. One reason for this is the challenging synthesis of MONs, typically requiring exfoliation of multi-layered 2D systems, which would extract any captured guests within the system.

1.2 Contributions

This thesis aimed to establish the incorporation of solid-state organic molecular dye guests into 2D MONs to access a range of functional luminescent properties for various light-based applications. The key research objectives were to:

1. Design a synthesis methodology for guest@MON systems.
2. Develop a range of guest@MON LMON systems using various organic dye guests with the purpose of understanding the effect of the 2D MON structure on the fluorescent properties of each system.
3. Fabricate fluorescent thin films of LMONs for light-based applications.

Chapter 2 provides background theory on MOF and MON materials, luminescence, and the key methods used in the reported studies. Chapter 3 (associated with Papers I and II), presents a versatile *in situ* guest incorporation strategy for MONs and demonstrates how incorporating a blue, green, and red guest emitter into MONs, individually and in different combinations, allowed new luminescent properties to be created and tuned. Chapter 4 (associated with Paper II and III), illustrates the benefits of the MON morphology for device fabrication, realising aerosol jet printing as a new methodology for creating MOF thin films. Finally, Chapter 5 (associated with Paper IV) offers a contrasting study that applies guest@host design to the thicker (~ 200 nm) 2D ZIF-L (ZIF = zeolitic imidazolate framework) structure, establishing structure-property relationships relating to the morphology and luminescence of ZIF-L.

There were three aspects to the luminescent guest@MON studies: synthesis, functionality, and fabrication.

1. Synthesis (Chapter 3). Typically, MONs are synthesised top-down *via* exfoliation of layered 2D materials.[10-11] Diffusion is then relied upon for guest encapsulation.[12] Not all MOF materials contain open channels, however, and those that do often exhibit guest leaching post-diffusion. To shift from post synthetic modification, a bottom-up *in situ* guest incorporation synthesis is required. This work, using ZIF-7-III as a case study system, established a facile, low energy, salt-templation synthesis using only NaCl, the MON reactants and the guest materials. It was shown to produce few-layer thin (2-4 nm), but laterally wide (4-6 μm) nanosheets of guest encapsulation MON materials. A range of morphological and structural studies were reported to characterise the MONs.

2. Luminescent mechanisms for functional MONs (Chapter 3). Using nanosheets of ZIF-7-III (Z7-NS) as a model system, various fluorescent mechanisms were observed for the first time in MONs by changing guest type and quantity. A triple guest system including a red, blue, and green emitter simultaneously exhibited triple monomeric RGB emission to create WLE fluorescence. The enabling and control of these mechanisms was a direct result of the nanosheet morphology surrounding the guests. Luminescent related material properties such as photoluminescent quantum yield (PLQY), photostability, and emission intensity were investigated and

compared with 3D analogue systems to identify the benefits achieved by using 2D MON systems.

3. Fabrication and shaping (Chapter 4). Combining the mechanistic and morphological benefits of guest@Z7-NS MON systems described above, this work investigated the improved fabricability of Z7-NS LMONs over 3D analogues. An initial study used inkjet printing. This was followed by a systematic study employing a new technique for MOFs and MONs: aerosol-jet printing (AJP). This versatile technique was explored through different printing strategies to create various fine-scale fluorescent patterned thin films and 3D pillared structures.

Chapter 5 shifts from MONs to broader 2D ZIF systems, exploring the 2D layered ZIF-8 analogue, ZIF-L, and the design of luminescent guest@ZIF-L systems. ZIF-L, averaging 150-200 nm in height and 5 × 10 μm wide, contains large cushion shaped cavities of 9.4 × 7 × 5.3 Å, ideal for the entrapment of small dye molecules.[13] A catalogue of dyes suitable for encapsulation in ZIF-L was studied, using fluorescein (F) as a case study. Perylene is also explored, as an example of a single-guest WLE system when encapsulated in ZIF-L. Given the expanded density in the *z*-axis, the work, in contrast to MON studies, more precisely considers guest positioning within the host and the relationship this has on morphology and luminescent properties. Ultimately, as ZIF-L can grow oriented thin films on certain surfaces, the ability to grow luminescent oriented guest@ZIF-L films *in situ* was examined.

2

Background

2.1 Metal-Organic Frameworks

MOFs are a class of porous coordination polymers (CPs) popularised by Yaghi in 1995,[14] following Robson and Hoskins' pioneering work.[15] MOFs are multidimensional structures comprised of metal cation or cluster nodes that are bridged by multidentate and multi-topic organic ligands *via* coordination bonds (Figure 2.1).[16] A rigid and ordered structure results, creating a highly crystalline extended network of varying multidimensionality. The topology of this structure resolves from the geometry of the metal-ligand coordination spheres, as illustrated in Figure 2.1. The diverse range of nodes and linkers that can be incorporated into MOFs provides a handle for design that imparts control over local interactions to tune chemical and physical properties of the bulk material.

Since their inception, over 100,000 MOFs have been synthesised, with many more predicted.[17-19] Systematic approaches to MOF design can lead to isoreticular series and analogue materials that allow for rigorous structure-property relationship studies, providing a guide-rail for MOF synthesis. This has led to a plethora of

tuneable properties including conductivity, luminescence, charge transfer, spin-state bistability, magnetism, and ferroelectricity.[20] These have led to myriad applications, including chemical and molecular sensing,[21] drug release and biomedicine,[22] polymer templating, electronic devices, and platforms for clean energy.[23] Ultimately, synergising these properties (e.g., magnetism and charge transfer), can produce newfound material characteristics, leading to breakthrough multifunctional materials.[24]

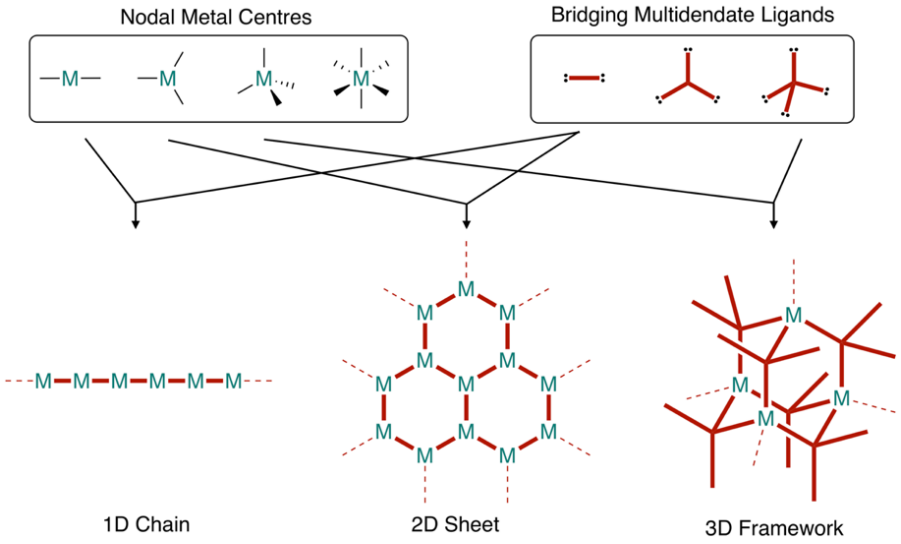

Figure 2.1. Structural representations of multidimensional CPs derived from metal and ligand components.

2.2 Luminescence

Luminescence is a key property sought after in MOF materials.[25] A material is luminescent if it emits photons (light) upon absorption of electromagnetic radiation (typically a photon in the UV to blue region).[26] This can occur *via* fluorescence,

where after an electron is excited, it relaxes from the lowest singlet excited state S_1 to the ground state S_0 by emission of a photon (Figure 2.2). Alternatively, luminescence can occur *via* phosphorescence, where intersystem crossing occurs from the singlet excited S_1 state to the triplet excited state T_1, followed by a photon-emitting transition to the ground state S_0 (Figure 2.2).[27] This thesis focuses on fluorescence. Excited state lifetimes of fluorescence are typically in the range of 1-100 ns, while phosphorescence lifetimes are of at least 1 μs.[25] If a radiative relaxation pathway is not stable, non-radiative relaxation to the ground state will result and the material is non-emissive. Typically, fluorescent molecules are conjugated. This provides π electron clouds that enable more mobile electrons and stabilised energetics compared to non-conjugated systems. Fluorescent molecules also have restricted pathways of non-radiative decay (e.g. vibrational relaxation), achieved, for example, by confining molecules or restricting molecular rotation.

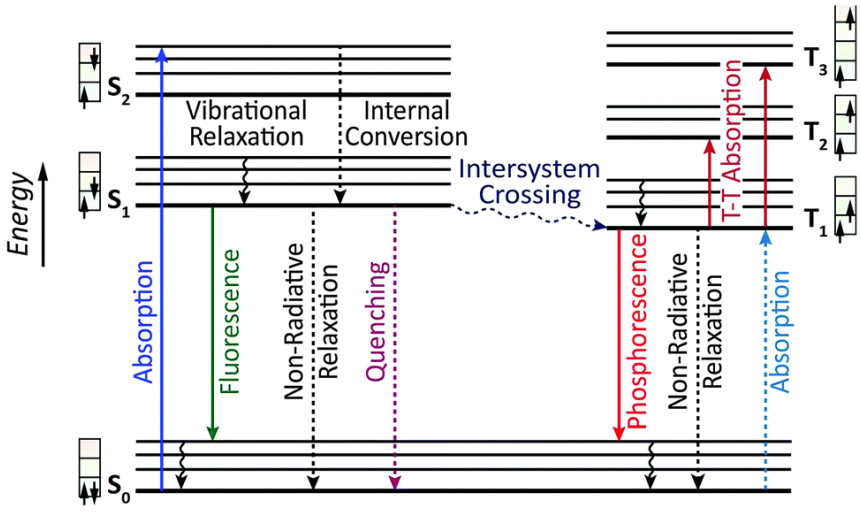

Figure 2.2. Energy diagram of photon emission pathways. Reproduced with permission from Ref. [26]. Copyright Royal Society of Chemistry, 2014.

The intensity of, or entire ability to, luminesce can be varied by various factors including confinement and aggregation.[28] At this point, only the concept of common dimer aggregates will be established. In the following chapters, various dye-dye interactions are expounded, where appropriate, to explain photophysical observations of guest dyes in MOF materials. A dimer can be considered to contain two transition dipole moments. These can interact either in-phase (repulsive) or out of phase (attractive), leading to an increase and decrease in system energy, respectively, compared to the monomer.[29] Geometrically, the first scenario involves molecules aligning side by side ('head to head'), termed H-aggregates (H = hypsochromic), while in the second scenario molecules align in-line ('head to tail'), termed J-aggregates (J = Jelley, one of the researchers who discovered the aggregate) (Figure 2.3).[30] H-aggregates exhibit a blue shift in absorption but quenching of fluorescence as the lowest excited energy level is forbidden (Figure 2.3). J-aggregates, in contrast, exhibit a red shift of absorption and emission compared to the monomer and sharp spectral bands attributable to minimal energy loss between absorption and emission (see Stokes Shift in §2.4.3).

These two scenarios are only the end points of a spectrum of geometric arrangements and depending on the angle between monomers, intermediate electronic states may form. Beyond this, myriad other interactions, such as charge transfer between the two monomeric units, could compete with and alter the isolated concept of a J- and H-aggregate.[31] This is to say that the model presented above is simplistic, but fundamental in interpreting the data presented in the studies that

follow. While the concept will not be expanded upon further in this thesis, it is pertinent to note that significant computational work has more comprehensively studied and defined the operation of dimers.[32] Since 2001, there is also the well-established concept of aggregation-induced emission. This is typically red shifted emission, but with a large stokes shift, which results from aggregation that prevents H-aggregates and suppresses non-radiative deactivation pathways (e.g., molecular rotation).[33-34]

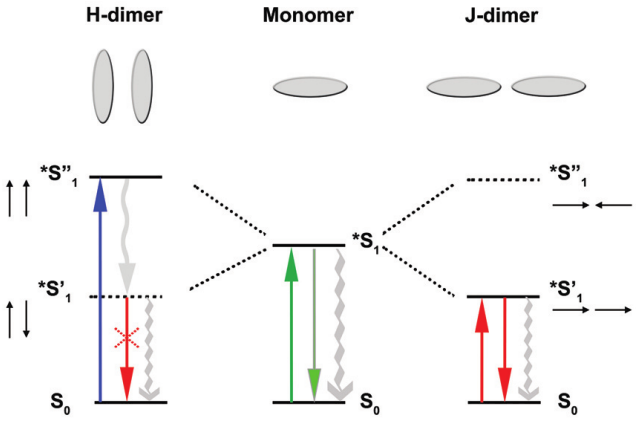

Figure 2.3. The effect of dimer aggregates on the energetics of fluorescence for common organic molecular dyes. Reproduced with permission from Ref. [29]. Copyright Royal Society of Chemistry, 2016.

2.2.1 Luminescent MOFs

LMOFs are a powerful subset of MOFs useful for sensing,[35] energy harvesting,[36] light-emission,[37] catalysis, and more broadly optoelectronic systems.[38] Recent works have also demonstrated the potential of LMOFs to form part of more environmentally friendly WLE OLED alternatives.[3,39] LMOFs

exhibit crystallinity, porosity, and tuneability, which are key advantages over other luminescent materials such as polymers, salts, or organic chromophores. By absorbing excitation energy, typically in the UV or visible (VIS) light regions, LMOFs undergo photon emission.[40] Luminescence can be introduced into MOFs through a variety of ways including ligand-centred emission, ligand-metal interactions (either from the metal-ligand or *vice versa*), metal-centred emission, and *via* encapsulated guest molecules in the LMOF pores (guest@MOF).[25] This work focusses on guest-induced luminescence.

MOFs are ideal superstructures to host luminescent guests, due to the combination of crystalline rigidity, flexibility from organic linkers, and regular channel structures and controllable pore sizes.[40-41] Guests are typically organic dyes, but have also included metal ions, metal complexes, and quantum dots.[6] While a number of luminescent guest@MOF materials have been synthesised using post-synthetic confinement, more robust and functional guest-based LMOF materials have been synthesised using *in situ* confinement.[6] This method enables the entrapment of bulky guests in the porous cavities of MOFs, increases uniformity of guest distribution in the MOF (compared with diffusion processes), and provides more efficient reactions, often under milder conditions.[42]

As a neutral host, MOFs offer luminescent guests a protective structure to improve photo and chemical stability. The framework can be used to tune the luminescent properties of the guest;[6] it is well established that organic dyes are sensitive to surrounding environmental conditions (e.g., polarity or acidity), leading to shifts in

emission. The confinement of guests can also decrease or suppress non-radiative processes, causing an improvement in PLQY and fluorescence lifetimes (see §2.4.3).[6] MOF structures can also influence the organisation of guest molecules, affecting the nature and degree of molecular aggregation and/or interaction. When not a neutral host, MOFs can interact with guests to induce new properties in the material, or can contribute fluorescence independent to the guest, which when combined produces a composite emission profile of the guest and host.[6,43]

LMOFs do experience limitations, however. LMOF sensitivity can be reduced due to interpenetration or labile coordination geometries of metal oxo-clusters.[44] Often, LMOFs are reliant on diffusion processes in the MOF channels, which can lead to slower responses of luminescent signal changes when acting as a sensor.[45] 3D MOF frameworks can also impede emission *via* self-quenching.

2.3 Metal-Organic Nanosheets

2.3.1 Definition

Nanosheets are materials with single or few-atom thickness (1-10 nm typically) but comparatively large micron-scale lateral planar dimensions, creating high surface-to-volume atom ratios.[10] A range of archetypal 2D materials have been reduced to nanosheets to date,[46] including black phosphorus,[47] MXenes,[48] layered metal hydroxides and oxides,[49] hexagonal boron nitride,[50] and graphitic carbon nitrides.[51] In doing so, the nanosheet materials have been reported to achieve unprecedented physical, electronic, chemical, and optical properties unattainable in the 3D layered bulk counterparts.[46] These benefits arise from the properties

accessible in a nanosheet morphology, including high external surface areas, accessible active sites, and nanoscopic dimensions. Challengingly, restricting material size in one or more dimensions can limit long-range effects, functionality, and the structural diversity afforded by stacking 2D sheets into bulk 3D materials.[46]

MONs are an increasingly sought-after form of MOFs that unite the properties of 2D materials with 3D MOF characteristics.[8,52] MONs provide a competitive alternative to the currently reported 2D nanosheet materials by combining the benefits of a nanosheet morphology with the character of metal-organic composition. This character includes benefits such as structural diversity and tuneability by rational modular design, programmable functionality, and highly ordered pore arrays with abundant accessible active sites.[8] The first notable report of MONs was in 2010, with more frequent annual contributions (50-100 papers per year) since 2018.[8] To date, focus has been on a small portfolio of MONs, primarily from square planar Cu, Co or Ni secondary building units (SBUs), ZIFs, or Zr and Hf clusters. In recent years, reviews for the field have extended beyond synthesis and concepts,[52-53] to specific applications including catalysis,[54] gas and liquid separation,[55] and electrocatalysis.[8,56]

2.3.2 Synthesising MONs

The study of MONs is still in its infancy and synthesis is often the greatest impediment to studying nanosheets of MOFs.[10] The synthesis of MONs is still specific to each material type, not yet being fully generalised and rationalised.

Targeting specific morphologies or properties is typically achieved through experimental trials and is considered more 'of an art than a science'.[57] Most studies utilise top-down disassembly of 2D layered MOFs using techniques illustrated in Figure 2.4. These techniques are energy- and time-intensive and can result in MONs of non-uniform nanosheet dimensions with rough fragmented surfaces. The exfoliated sheets are often also unstable, reaggregating over time to the thermodynamically preferred stacked morphology. Direct bottom-up syntheses offer more control and consistency of material morphology but are less reported due to needing tailorable techniques depending on the material, with low yields frequently cited. Reported strategies (see Figure 2.4) for ZIFs have included diffusion,[58] surfactant assistance,[59-60] salt-confinement,[61] and interfacial synthesis.[62]

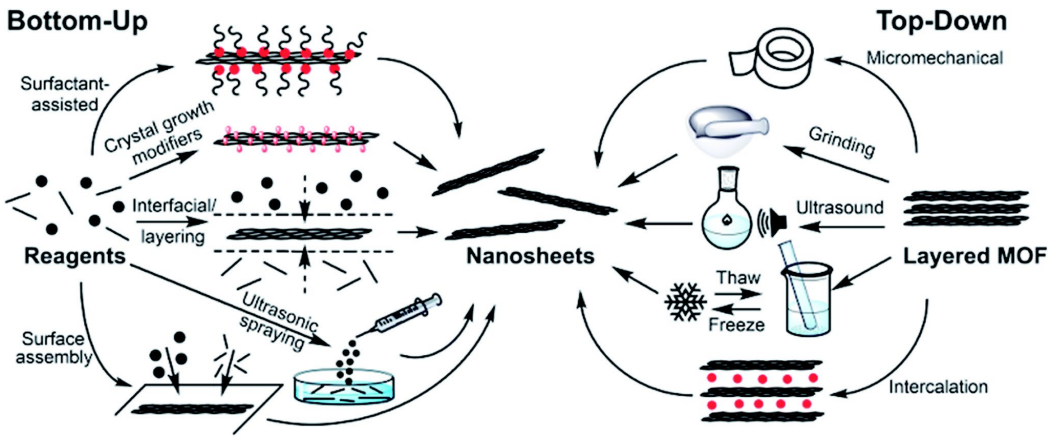

Figure 2.4. Synthesis routes for MONs. Reproduced with permission from Ref. [52]. Copyright Royal Society of Chemistry, 2018.

2.3.3 Properties and Applications of MONs

MONs have been implemented across various applications, including gas separation and water purification,[63-64] energy storage,[65] light harvesting and emission,[8] electronic devices,[66] catalysis,[54,56] and sensing.[67] Catalysis is of particular interest, followed by sensing and separation.[8] For catalysis applications, including photocatalysis and electrocatalysis, studies have found improvements over 3D MOFs due to active sites being more exposed than in 3D frameworks. A Zr based MON, for example, exhibited higher degrees of conversion and faster reaction kinetics than a 3D analogue.[68-69] Exposed active sites in MONs have also been utilised for effective sensing of small organic molecules, ions, and biological molecules.[8] Similarly, greater exposed surface area in MONs has improved separation of gases such as CO_2,[8] and led to uses such as water purification, with removal of heavy metals and ions.[63,70-72] More recent works explore MONs for electronics, including as films on electrodes for lithium-ion batteries,[73-74] or as a hole buffer layer within an OLED system, which showed a nearly twofold improvement in device lifetime compared to conductive polymer-based devices.[75] MONs are also being implemented as the photoactive layer of photovoltaics.[76-77]

2.3.4 Luminescent MONs

One of the less studied areas of MONs is their potential as luminescent materials for light emission, sensing, and optoelectronics. A strand of LMOF research has

focussed on producing nanoscale MOF materials to create higher performing chemical sensors, but the field has not merged into the study of MONs.[78] An effective fluorescent nano-emitter should exhibit negligible dye leaching, structural stability under ambient conditions and repeated use, and high quantum efficiency. The increased specific surface area of MONs theoretically provides the possibility of increased emission intensity, with the thinness improving optical transparency.[79-80] The confinement of electrons in an ultra-thin region also facilitates improved electronic behaviour and the control of excitons. In theory, this should optimise sensitivity and efficiency of LMOF light-emission capabilities.[11] The layered structure of MONs also provides strong in-plane covalent bonding, coupled with inter-layer intermolecular forces. These provide mechanical strength and flexibility, resulting in MONs being typically highly dispersive and stable in water or solvents.[8] These properties make it easier for MONs to be processed in solution *via* deposition as homogenous layers to fabricate films and ultra-thin nano-devices.[66] By controlling nanoscopic dimensions it has been shown that emission chromaticity can be carefully tuned to desired ranges.[8]

2D layered MOFs currently employ inherent luminescence *via* the design of emissive linkers, metal ions, or ligand-metal charge transfer, with a focus on sensing.[81] A 2D copper-based MOF AUBM-6 was exfoliated, for example, to form few-layer thick nanosheets. The nanosheets exhibited up to threefold greater emission intensity when sensing Pd^{2+} ions than bulk AUBM-6.[79] One distinct work used zirconium based MONs with a tetraphenylethylene-based tetracarboxylate ligand (TCBPE) to create white light emitting diodes (WLEDs).

The MONs produced yellow emission centred at 560 nm with high PLQY (50 %). A suspension of the MON was placed in a cavity above a GaN-InN blue emitting LED chip to produce WLE with Commission Internationale de l'Éclairage (CIE) coordinates (0.37. 0.41). A 30 % reduction in output power was observed following 168 h of operation, which was attributed to degradation of the linker upon light-exposure. A novel route to LMONs is employing the guest@MOF approach. To the best of our knowledge, the only work to date that has considered this approach is a system of lanthanide hydrate@MOF nanosheets (HSB-W5-NS) *via* metal ion guest@MOF.[82] No reported studies have attempted to incorporate luminescent organic dyes.

2.4 Methods and Techniques

Each paper presented in this thesis includes a comprehensive methods section outlining the technical aspects of data collection and synthesis. In this section, a summary of the techniques, and associated purposes, are briefly discussed to establish the experimental approach taken across all studies.

2.4.1 Structural characterisation

Diffraction was primarily employed to examine the structure of guest@MOF systems in this thesis. Powder x-ray diffraction (PXRD) was used to confirm sample crystallinity and examine any potential deviations from expected crystal structures

by analysing Bragg diffractions. Guests were not expected to show Bragg diffraction peaks given they are unlikely to exhibit long-range periodicity, and they comprise a low wt % of the guest@MOF material; PXRD typically requires 5-10 wt % for detection.[6] Notably, MON data were not of sufficient resolution to undertake any refinements, even when synchrotron radiation was used to collect PXRD. While electron diffraction was attempted for one guest@MON sample, along with ZIF-L, data were not sufficiently complete enough to solve a crystal structure. For local scale structural analysis, selected area electron diffraction (SAED) was used. Thermal gravimetric analysis (TGA) was used to assess chemical components *via* rate of decomposition, while guest loading in a MOF host was determined by solution ^{1}H nuclear magnetic resonance (NMR) spectroscopy after digesting the guest@MOF material with deuterium chloride (DCl).[83]

Chemical bonding, and complementary structural information, was analysed with vibrational spectroscopy techniques, including attenuated total reflection Fourier transform infra-red spectroscopy (ATR-FTIR) or Raman spectroscopy.[84] Specifically, the techniques offered information about molecular structure, symmetry, and the strength and type of bonds between atoms based on the vibrational bands observed in spectra. The mid-infrared (4000-400 cm^{-1}) was the typical range examined for organic ligands and molecular guests in MOFs by identifying specific functional groups. The far-infrared, including the terahertz region (400-10 cm^{-1}) provided insight into framework bonding between metal nodes and ligands by identifying collective models (simultaneous vibrations of all atoms).[85] In this thesis, terahertz spectroscopy was collected at the Diamond

Synchrotron (B22 beamline). At a bulk level, these techniques were useful to identify any variation in the MOF framework bonding upon guest incorporation, along with identifying the presence of any concentrated guest content.

Typically, however, guest content used for LMOF and LMON materials is too low in concentration for detection by ATR-FTIR, primarily due to signal oversaturation by the organic linkers of the MOF framework. Near-field nanoscale Fourier transform infra-red spectroscopy (nano-FTIR) instead offers a method of probing infra-red (IR)-active vibrational bands at the local surface environment (10 nm scale) of samples by circumventing the diffraction limit of light.[86] The technique has been established as an effective method for identifying the presence of guest species such as Rhodamine B (RB) on the surface of MOFs including ZIF-8.[87] For this thesis, a neaSNOM AFM system by neaspec GmbH was used to undertake nanoFTIR measurements. The instrument was used in tapping mode, with illumination of a platinum-coated cantilever tip probe from a tuneable broadband IR laser. Near-field interactions between the tip and the sample modified the IR light which was detected in the backscattered light from the tip. Detailed discussion of the computational and physical theory underpinning the technique can be found in reference [88].

2.4.2 Morphological characterisation

Atomic force microscopy (AFM) was used to image surface topography, while scanning electron microscopy (SEM) and transmission electron microscopy (TEM)

were used to analyse the morphology of synthesised materials. A Si wafer substrate was used to ensure conductivity of the sample. MON samples for SEM were typically sputter-coated with up to 30 nm of Au (10x the thickness of the nanosheets) so morphological features were prominent. MON and ZIF-L samples were highly beam sensitive when imaged with TEM, so samples could not be analysed at high resolution to determine any extent of porosity or guest ordering.

2.4.3 Luminescence Analysis

LMOF materials were examined in the solid state using an FS-5 spectrofluorometer. Various data were collected, as described below.

Emission spectra. A measure of the emission from a sample at a fixed excitation wavelength. Samples were excited with a xenon lamp, the light from which was directed towards the sample using a system of internal mirrors.

Excitation spectra. A measure of the alteration of emission intensity at a particular wavelength as the excitation wavelength alters. Hence, these data indicated the absorption by a sample, across a region of light, to emit the specified wavelength.

Absorption spectra. A measure of the degree of absorption of light as a function of the wavelength of incident light (measured using a solid-state UV-VIS spectrophotometer).

Stokes' law provides that fluorescence emission occurs at a longer wavelength than the excitation wavelength due to the loss of vibrational energy when electrons relax from the excited to ground state.[89] The extent of wavelength shift is known as the Stokes Shift (Figure 2.5). A larger Stokes Shift avoids spectral overlap between the excitation and emission spectra, which can result in re-absorption of light and a reduction in the effectiveness of emission.

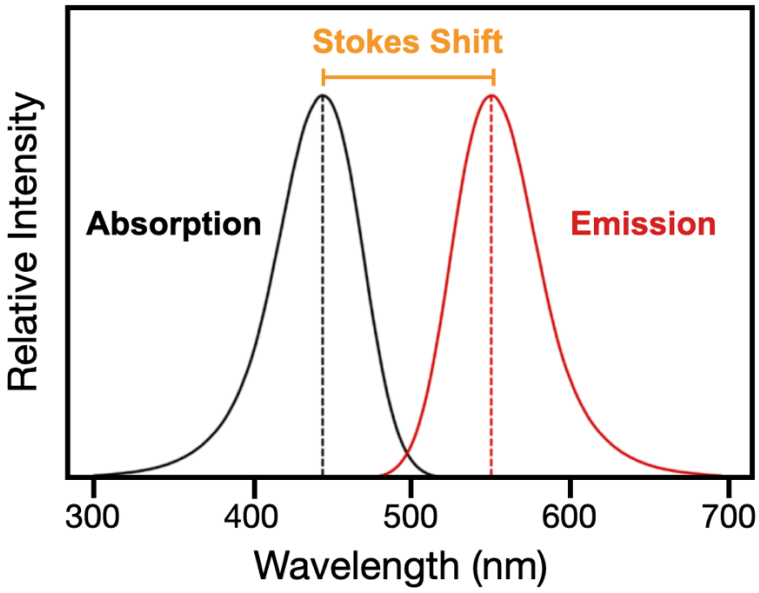

Figure 2.5. Illustration of emission and excitation spectra, according to Stokes' law and Kasha's Rule, exhibiting minimal spectral overlap.

If the emission and excitation spectra of a sample are mirror images, then the sample follows Kasha's Rule.[90] This indicates that photon emission is expected only from the lowest excited state (S_1 in the case of fluorescence), despite the level to which the molecule is initially excited. Where a molecule is excited to a higher electronic state, the molecule first undergoes rapid internal conversion that is faster

than fluorescence, so that the molecule vibrationally relaxes to S_1 before then undergoing fluorescence from $S_1 \rightarrow S_0$ (see Figure 2.6). When Kasha's Rule is followed, excitation spectra can be considered fluorescence detected absorption spectra.[91] For many guest@MOF samples, and materials investigated in this thesis, Kasha's rule does not apply. This is a result of more complex energetic profiles formed by guest-host and guest-guest interactions.

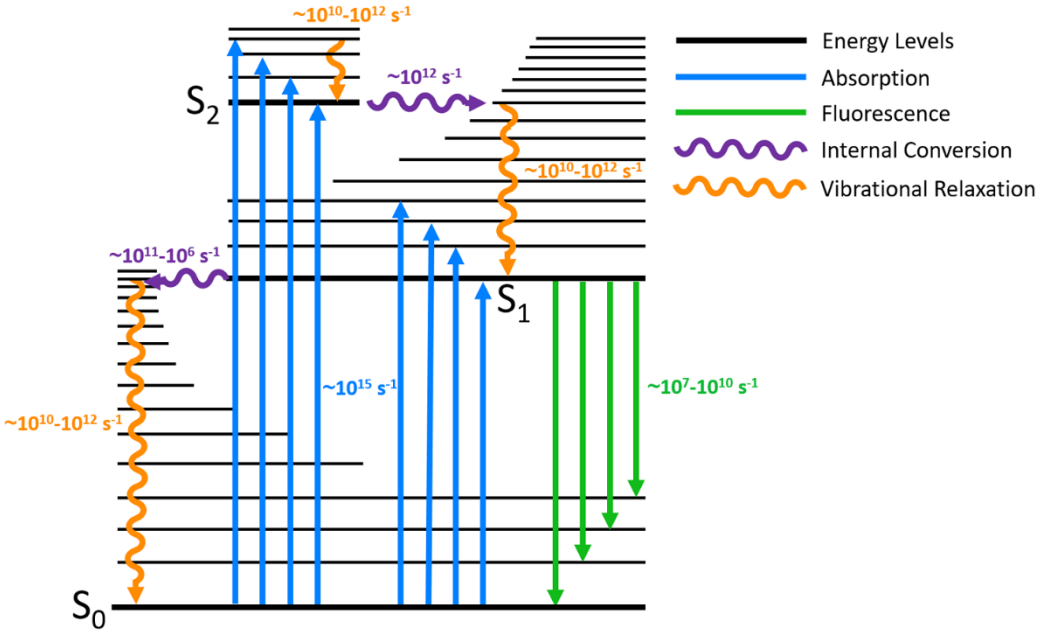

Figure 2.6. Perrin-Jablonski diagram with estimated timescales of excited state processes related to fluorescence for a typical organic dye. Reproduced with permission from Edinburgh Instruments. Copyright Edinburgh Instruments, 2021.

Photoluminescent Quantum Yield (PLQY). PLQY is defined as the number of photons emitted per photon absorbed by a system. PLQY for fluorescence is determined by the radiative and non-radiative (e.g. internal conversion, intersystem crossing, energy transfer) transition rates of the system.[92] Thus, PLQY can be

interpreted as the probability that a system, once in the excited state, will relax to the ground state through a radiative process (i.e., fluorescence). In this work, absolute PLQY was measured, compared to a relative quantum yield measurement that requires a reference sample.[93] This used an integrating sphere to capture all light emitted by a sample followed by comparing the number of emitted photos with the number absorbed by the sample.

According to Vavilov's Rule, the PLQY of fluorescence is independent of the wavelength of excitation.[93] This typically applies for the majority of molecules that obey Kasha's Rule. However, literature has established various exceptions, including materials at the nanoscale, which can exhibit excitation dependent emission typically resulting from trapped excitons and excimer emission.[57]

Fluorescence Lifetime (τ). This measure corresponds to the average time a molecule remains in the excited state before relaxing to the ground state.[4] The value was determined by exciting a sample with short excitation pulses from an LED laser (typically at the sample's absorption maximum) and measuring the fluorescence intensity decay. The studies in this thesis used time-correlated single-photon counting (TCSPC) to measure fluorescence lifetime. The technique measured the time between an excitation pulse and a single emitted photon. The single photon was converted by a detector to an electronic pulse, which could be timed from the excitation pulse. This was repeated with a large population of photons (typically 10,000).

TCSPC data was represented as the rate of decay for an excited state population of a sample [*M**] at time *t*,

$$[M^*](t) = [M^*]_0 e^{-(kt)} \qquad \textit{Equation 2.1}$$

where $[M^*]_0$ is the number of molecules in the excited state at the arrival time of the excitation pulse.[94] Both radiative and non-radiative rate constants are associated with the process, with *k* representing the sum of all rate constants.

The samples measured in this work exhibited multi-exponential decays, due to fluorophores existing in multiple states (e.g. monomers or dimers). The multi-exponential decay model used for data fitting was:

$$I(t) = \sum_{i=1}^{n} B_i \, exp\,(\frac{-t}{\tau_i}) \qquad \textit{Equation 2.2}$$

where $I(t)$ is fluorescence intensity at time *t*, normalised to the intensity at t=0, τ_i is the lifetime of the *i*th decay component and B_i is the component amplitude. The number of components was estimated based on the expected photophysics.

Local Scale Fluorescence. To complement the bulk analyses above, fluorescence microscopy and fluorescence lifetime imaging microscopy (FLIM) were used in various studies. These techniques coupled optical microscopy with the measuring capabilities of a spectrofluorometer to analyse luminescence on isolated single particles of a bulk sample at the local scale. Further detail on each technique is provided, where appropriate, in Chapter 3 (Paper I) and Chapter 4 (Paper III).

3

Synthesising tuneable luminescent metal-organic nanosheets

3.1 Premise

MONs offer inherent benefits for the development of functional luminescent materials, when compared to 3D MOFs. Atomic thickness and increased external surface area can theoretically improve optical transparency, while inter-layer intermolecular interactions provide strong guest binding and chemical stability. To harness these benefits, this chapter establishes a guest@MON design to synthesise LMONs. Various luminescent guests are studied, with each demonstrating a beneficial photo-mechanism accessible due to guest confinement in the MON host structure. The work concludes by demonstrating how multiple guests can be simultaneously intercalated to achieve tuneable WLE, a critical commercially relevant application for emissive MOF materials. With overreliance on rare-earth metals for LEDs, alternate phosphor materials derived from more sustainable processes are in high demand.

3.2 Synthesising guest@MONs

3.2.1 Selecting a Framework Candidate – ZIF-7

ZIFs are a class of MOFs known for large porous cages and relatively high thermal and chemical stability.[95] They are formed analogously to aluminosilicate zeolites, with a framework constructed from tetrahedral building units with metal-linker-metal bond angles of 145° (as for Si-O-Si bonds in silicon-based zeolites).[95] ZIF-7 [$Zn(bIm)_2$, bIm = benzimidazolate]) is one of the earliest reported ZIFs and forms with a typical ZIF sodalite topology. The Zn(II) metal centres are more environmentally friendly compared with more toxic metal centres as Cu, Cd, or Pb. ZIF-7 has also been reported to exhibit stability in humid conditions and aqueous solutions (attributable to being hydrophobic) and at high temperatures (up to 400 °C).[96] ZIF-7 is known to undergo two phase transitions. The first is the conversion of ZIF-7-I to ZIF-7-II by removing dimethylformamide (DMF) solvent molecules from the framework pores (Figure 3.1).[97] ZIF-7-II can then convert to the densest and thermodynamically stable 2D phase, ZIF-7-III, comprising of $Zn_2(bIm)_4$ layers, *via* selective hydrolysis of Zn-N bonds in ZIF-7. This 2D stacked phase is ideal for exfoliation to form nanosheets. Z7-NS have been used as a matrix for the ionization of small molecules,[98] molecular sieving, and membranes.[99]

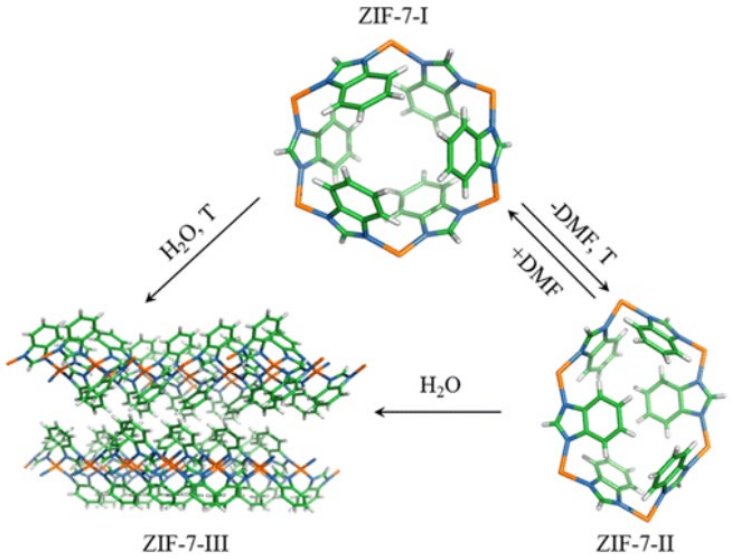

Figure 3.1. Structural phases of ZIF-7. Reproduced with permission from Ref. [97]. Copyright American Chemical Society, 2018.

ZIF-7-III layers comprise a (4,4) square planar grid formed by corner-sharing networks, quadruply linked, of ZnN_4 tetrahedra (Figure 3.2). Each monolayer, ~0.5 nm thick, stacks orthogonally rotated on the *z*-axis *via* C-H/π interactions, producing 2D channels of ~1 nm in height through the (220) plane. The exposed bIm linkers of each Z7-NS layer form a herringbone layout, creating two theoretical inter-layer guest positions (Figure 3.2). One is a horizontal alignment within the bIm V-openings, where a gap of around 0.5 nm exists along with space for any flexible components of guest molecules to reside in the pockets between the bIm ligands. Alternatively, guests can be located vertically between the bIm ligands. The bIm ligands do exhibit a degree of rotational flexibility that could allow for structural relaxation around a guest. The bIm 'claws' could also act as a grip to ensure entrapment of any guests within the cavities to avoid potential leaching.

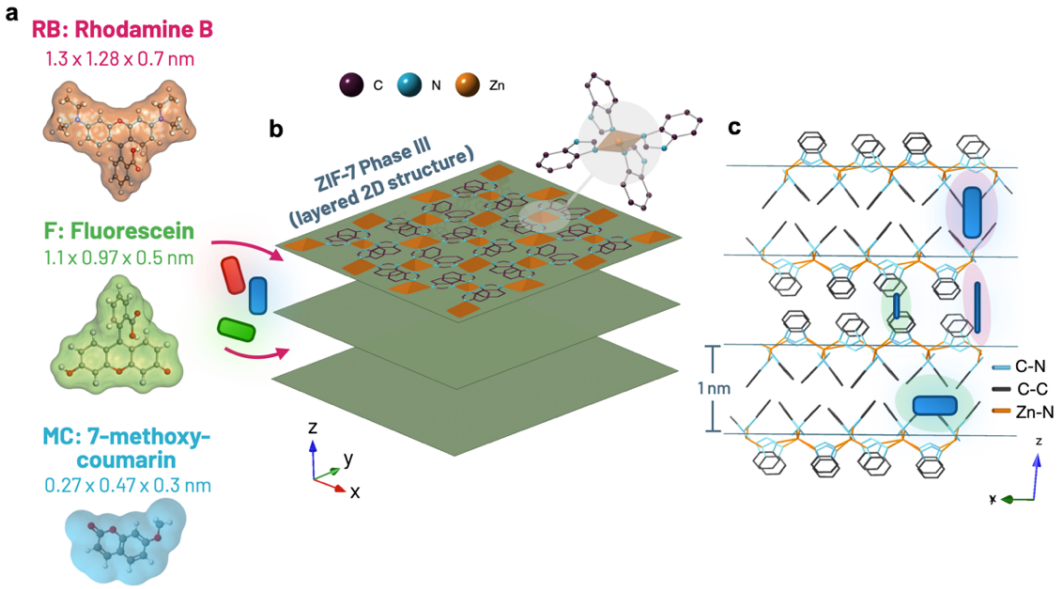

Figure 3.2. (a) Fluorescent guest molecules used in this study, including molecular dimensions. (b) Structure of 2D ZIF-7-III, showing the crystal structure of a single Zn tetrahedra, and a monolayer. (c) Cross section of ZIF-7-III *b*-axis indicating possible guest positions (blue rectangle). Structure determined from published crystallographic data.[97]

3.2.2 Synthesis Routes to Nanosheets

Beyond devising a reliable MON synthesis, a recurring challenge is ensuring the formed nanosheets remain stable, rather than re-aggregate into 2D stacked materials. In this study, potential routes for synthesising ZIF-7-III as nanosheets were first explored, and from these it was determined which could be augmented to include a step of guest encapsulation. To date, only top-down exfoliation strategies of synthesising ZIF-7-III nanosheets have been reported.

3.2.3 Z7-NS Top-Down Synthesis Approaches

The synthesis of ZIF-7-III was first optimised in terms of yield and morphology to achieve the most suitable material for exfoliation. Two techniques were compared: a hydrothermal 'traditional' three-step synthesis from ZIF-7-I, and a direct mechanical synthesis (Figure 3.3). In the mechanical synthesis, an acid-base reaction occurs where $Zn(NO_3)_2 + 2C_7H_6N_2 + 2NaHCO_3 \Rightarrow$ ZIF-7-III + $2NaNO_3 + 2H_2O + 2CO_2$. The mechanical technique produced a yield of 76.7 % (139 mg) while the traditional synthesis resulted in a 1.1 % (197 mg) yield, attributable to multiple washing steps required to isolate the product after each reaction stage. PXRD patterns (Figure 3.3) indicated that while both methods resulted in ZIF-7-III, mechanically synthesised ZIF-7-III were less crystalline, with a lower intensity reflection corresponding to the (002) plane at $2\theta = 9.137°$. AFM and SEM showed that the hydrothermally synthesised particles of ZIF-7-III formed rectangular layers with minimal defects and a single particle height of around 380-400 nm, composed of single 2D sheets each with an average height of 2.2 nm. In contrast, the mechanically synthesised ZIF-7-III presented more uneven edges along each particle, with a range of minor defects producing an uneven surface. The particles had a similar height of 390 nm, although they were laterally smaller by around 25 %. Given the consistency and uniformity of the traditional synthesis ZIF-7-III, it was theorised these samples would produce more ideal exfoliated nanosheets.

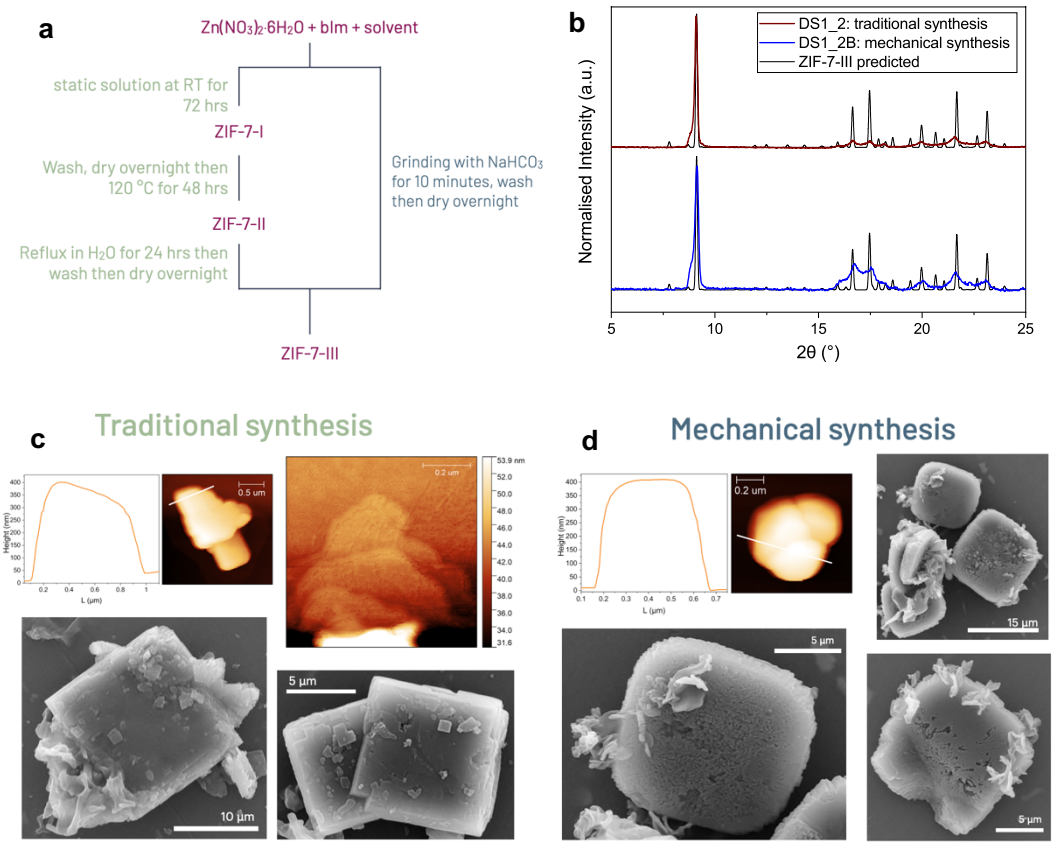

Figure 3.3. (a) Conventional hydrothermal (green) vs mechanochemical (blue) synthesis procedures. (b) PXRD patterns of synthesis products. (c-d) AFM and SEM of the products.

Three previous reports have demonstrated exfoliation of ZIF-7-III using sonication/ball-milling/centrifuging (producing 1.12 nm thick sheets of 2.5 µm width),[100] ultrasonication/centrifuging in propanol (producing less even sheets of around 1 nm height but 0.3 µm width),[98] or microwave rapid exfoliation (producing sheets that were very even and uniform of around 1-2 µm width and few nm height).[101] Sonication was prioritised in this study due to equipment access limitations. Two variables were modifiable to tune the exfoliation technique: sonication energy (distributed ultrasonication bath or concentrated probe), and

solvent. An ideal solvent should move between the layers of ZIF-7-III to then encourage the exfoliation of layers. Steric bulk, polarizability, and surface tension contribute to the effectiveness of solvents in achieving this.[98] A solvent with a surface energy comparable with the material to be exfoliated reduces the enthalpy of mixing, encouraging greater interaction and penetration of the space between layers by the solvent. Greater polarizability is also likely to encourage layer separation. With comparable 2D systems, such as $MoSe_2$ and WS_2, reported to have surface energies of around 25 mN/m,[101] methanol (MeOH) to pentanol were selected for study. Propanol was excluded given previous reports of ineffectiveness.[98]

Initial studies (Figure 3.4) with MeOH showed that the mechanically derived materials exfoliated less successfully, resulting in layer decomposition rather than layer separation to produce single-layer materials. Using a sonication probe (producing 4000 J of energy) also resulted in disintegration of the crystal, rather than 'peeling off' layers, as desired. In contrast, MeOH ultrasonication of the traditional synthesis material resulted in semi-exfoliated particles, producing thin layers of ZIF-7-III (AFM determined height of around 40 nm, 10 % of ZIF-7-III). When increasing the chain length of solvent to butanol and pentanol, the material was partially exfoliated but to larger and thicker particles. In all cases, however, there was no bulk uniformity of the degree of exfoliation, resulting in a mixture of partially exfoliated layered materials and single-few layer sheets of various sizes. It is noted that reducing agitation and sonication during ZIF-7-III synthesis may result in more uniform initial 2D stacks to exfoliate from, thereby improving the

exfoliated sheets. Works also propose an additional wet grinding step before sonication, which improves inter-layer solvent penetration by avoiding agglomeration.

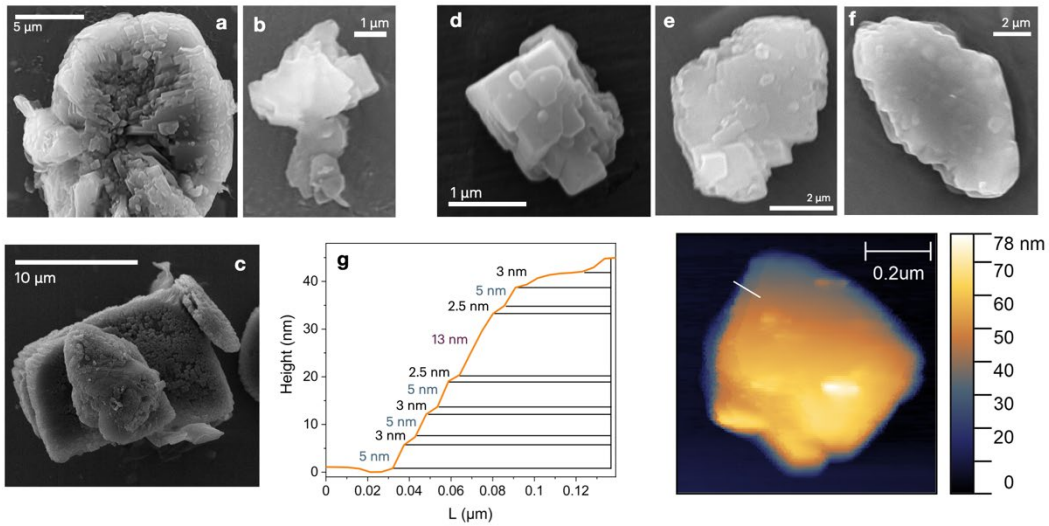

Figure 3.4. (a-f) SEM images of exfoliated ZIF-7-III particles using a sonication probe (a-b), ultrasonication exfoliation of mechanically synthesised ZIF-7-III (c) and traditionally synthesised ZIF-7-III in methanol (d), butanol (e) and pentanol (f). (g) AFM with corresponding height profile of the white line at the particle edge. Particle is from the same sample as in (d).

This brief investigation did not conclude any reliable method of producing nanosheets. Moreover, any guests encapsulated in ZIF-7 were not retained during conversion to ZIF-7-II and -III due to the loss of pore space. Additionally, including guests in the solvent used for exfoliation did not lead to any guest incorporation; an expected result given the energy required to separate layers of ZIF-7-III. The results acted as an important control comparison, however, for the nanosheets that were next synthesised using a novel bottom-up methodology.

3.2.4 Z7-NS Bottom-up Synthesis Approaches

As no bottom-up synthesis has been previously reported for ZIF-7-III nanosheets, a range was selected from related materials in literature (Figure 3.5), with only a few strategies excluded based on being specialised to a particular MOF that was chemically distinct from ZIF-7. One strategy, diffusion, slowed the interaction between metal ions and ligands such that once a layer of ZIF-7-III forms, it drops from the interface between the ions and ceases to react, leaving the material in single-layer sheets.[58] Other strategies involved coating ligands with surfactants during synthesis to create steric hindrance to multiple layer formation.[60,62] None of these techniques were adaptable to ZIF-7-III after multiple attempts, except for salt-templating.

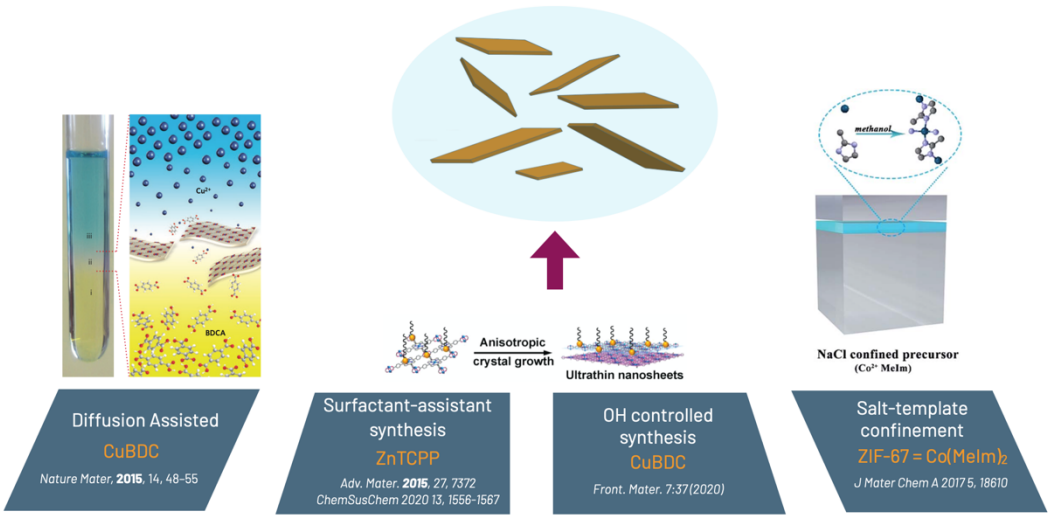

Figure 3.5. Selected bottom-up nanosheet synthesis routes attempted for ZIF-7-III. Images sourced with permission from references indicated within the figure.

3.2.5 Salt Template Nanosheet Synthesis

Paper I reports the successful modification of a bottom-up strategy employed for ZIF-67 nanosheets involving synthesis with an excess of NaCl.[61] In that work, salt crystals of just 1 μm in lateral dimension were used to grow nanosheets in the voids between salt crystals.[61] Salt can act in three primary ways when used as a templating agent during synthesis: 1) as a surface for controlled material growth, 2) as a self-assembly directing agent, or 3) as a porogen (Figure 3.6).[102-103] In Paper I, salt crystal faces were intended to act as a surface for ZIF-7-III growth that limits growth in the third dimension ('hard template'). Due to the strong electrostatic attractions between NaCl surfaces and reagents, previous studies using metal nitrides and oxides (e.g., MoO_3) have demonstrated that single layered growth of nanosheets typically formed on smooth salt surfaces of large dimensions (e.g., 20 μm side length) that could then be removed by dissolving NaCl.[102-104]

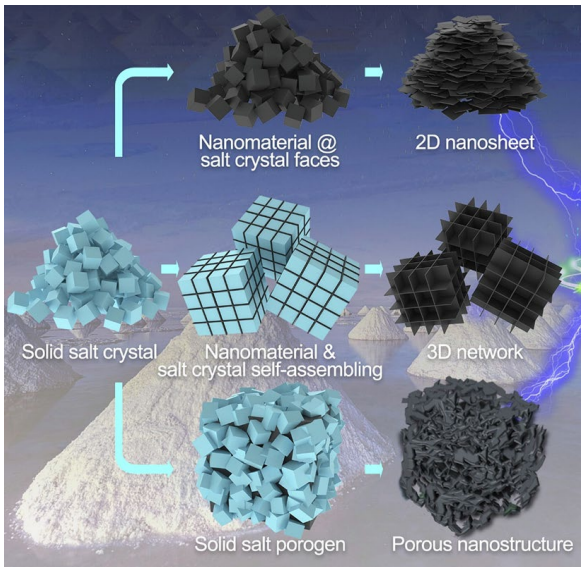

Figure 3.6. Primary synthesis procedures involving salt templates to direct growth. Reproduced with permission from Ref. [103]. Copyright Elsevier, 2020.

Coating salt crystals in $Zn(NO_3)_2$ (by stirring) followed by addition of the ligand (bIm) with minimal solvent led to reagents forming MONs on salt crystal surfaces. Optical microscopy and SEM imaging of a NaCl crystal before synthesis, compared to the reaction mixtures after stirring (Figure 3.7), revealed such growth. After removing NaCl *via* heating and washing, it was possible to isolate large lateral size single layer nanosheets of homogenous morphology (see §3.2.5.1). Valuably, the developed salt-technique was scalable (tested up to 10 times initial quantities, producing yields from 93 mg to 1.22 g (7-80 %)) and used environmentally friendly and low-cost materials (NaCl). Once removed by dissolution, the NaCl could also be isolated *via* recrystallisation and re-used in future syntheses.

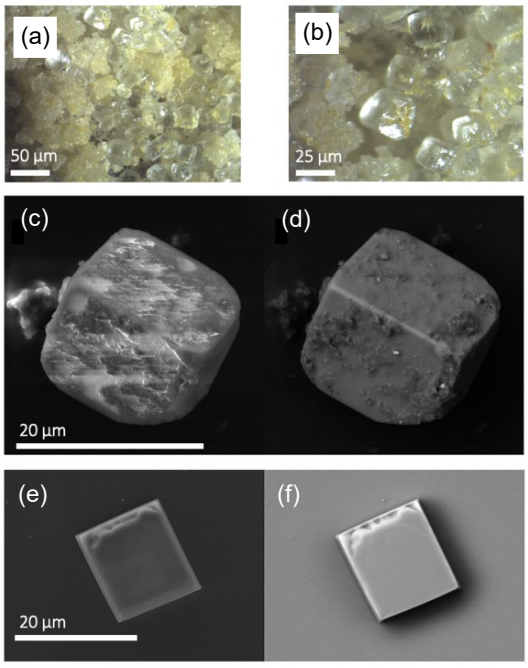

Figure 3.7. (a-b) Stereoscopic optical microscope images (x50) of NaCl crystals coated with F@Z7-NS growth prior to washing. (c) secondary electron (SE) and (d) backscattered electron (BSE) FE-SEM images of a single NaCl crystal coated in Z7-NS prior to washing. (e) SE and (f) BSE FE-SEM images of a single NaCl crystal before synthesis.

3.2.5.1 Nanosheet structure and morphology

PXRD and SAED analyses (Paper I, Figure 3) confirmed the nanosheets retained the ZIF-7-III crystal structure, but with limited intensity in the *z*-axis (e.g. the intensity ratio of X-ray reflections *I*(002)/*I*(220) varied from 14.814 in ZIF-7-III to 3.941 in ZIF-7-NS), indicating reduced diffraction in the *z*-axis. SAED also showed no z-axis planes, only (220), (110) and (440). AFM, field emission scanning electron microscopy (FE-SEM), and TEM imaging (Paper I, Figure 2-3) revealed Z7-NS consistently formed as isolatable few-layer thin nanosheet particles (Figure 3.8). The height of over 80 particles was determined *via* individual AFM topography imaging, with a calculated mean height of 1.9 nm for Z7-NS (*vs* 300-400 nm for ZIF-7-III). Particles were a mixture of flat surfaces, with some edge curling. Similar curling has been observed by silica nanosheets from mechanical strain while mixing during synthesis.[105] Particles ranged in size with the smallest lateral dimensions of ~5×2 μm^2, average of ~10×5 μm^2, and largest of ~20×10 μm^2. Conveniently, the smaller and larger nanosheets were found to be separable by gravitational sedimentation. The morphology remained comparable after 6 months of immersion in water or MeOH, with only slightly increased curling at the nanosheet edges.

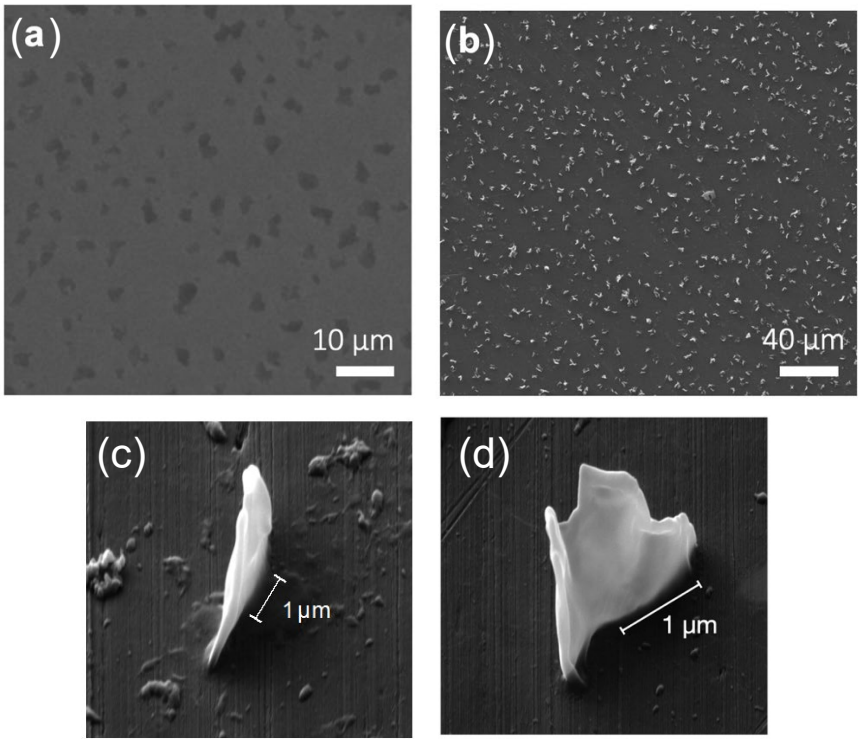

Figure 3.8. (a-b) FE-SEM of Z7-NS particles distributed on silicon substrate (left) and aluminium stub with 25 nm gold coating (right). (c-d) FE-SEM imaging of Z7-NS (with 25 nm gold coating) at a 45° tilt. Due to tilt, scale is not accurate to measure thickness.

The effect of salt quantity was briefly studied to confirm the essential role it plays during synthesis. Room temperature ZIF-7-III synthesis was undertaken with no salt followed by sequential additions of NaCl. While PXRD confirmed the ZIF-7-III structure of the products from each experimental condition, SEM showed varying morphology. This ranged from stacked layers with no salt, to layered globules at 5 mg NaCl (comparable to the sheets reported for ZIF-67, which grew between salt crystals).[61] At 10 mg NaCl particles formed independently, but with multiple sheets of ZIF-7-III per particle. Employing an excess of NaCl ensured void space between the dense NaCl was minimised, directing growth preferentially on the NaCl surfaces to produce few layer nanosheet particles.

Future work could further examine the salt-templating method to achieve controllability of the process. For example, the lateral size of the formed nanosheets is known to be controllable by salt crystal size, while the smoothness and sample morphology may be adjustable using different mixed salts (e.g. potassium chloride).

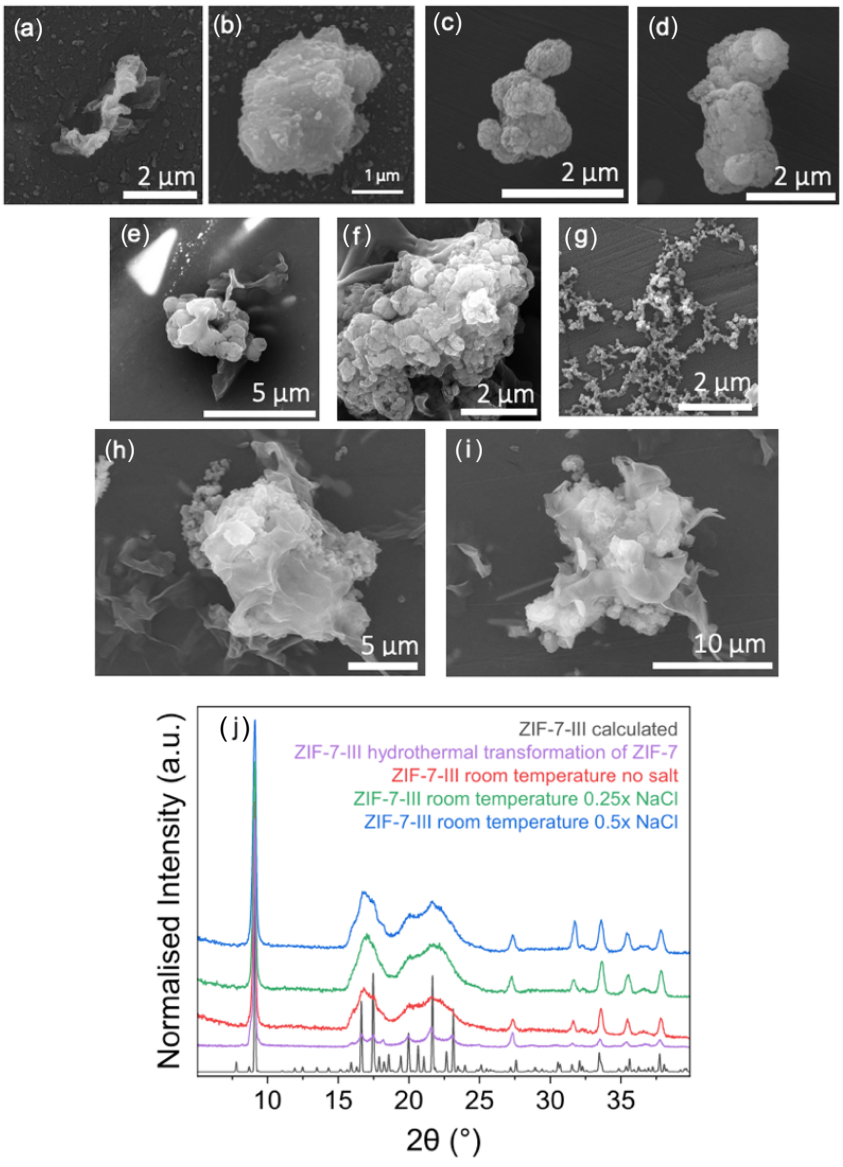

Figure 3.9. (a-i) SEM images of various ZIF-7-III particles from samples synthesised by hydrothermal transformation of ZIF-7 (a-b), room temperature synthesis no salt (c-d), room temperature with 0.25x NaCl (e-g), and room temperature with 0.5x NaCl (h-i). (j) PXRD of ZIF-7-III samples.

3.2.6 Guest incorporation by salt templating

Developing a direct salt assisted strategy for synthesising Z7-NS allowed for the incorporation of guests *in situ* into Z7-NS by dissolving guest material into the methanol synthesis solution (Figure 3.10). Three luminescent dyes were selected as guests for incorporation in the study across Papers I and II: green emitter fluorescein (F), red emitter rhodamine B (RB), and blue emitter 7-methoxycoumarin (MC) (see rationale in §3.3). Data presented in Papers I and II confirmed the presence of guests given the luminescent properties of the materials (see §3.3), while the morphology and structure of the guest@Z7-NS particles remained consistent with the host Z7-NS.

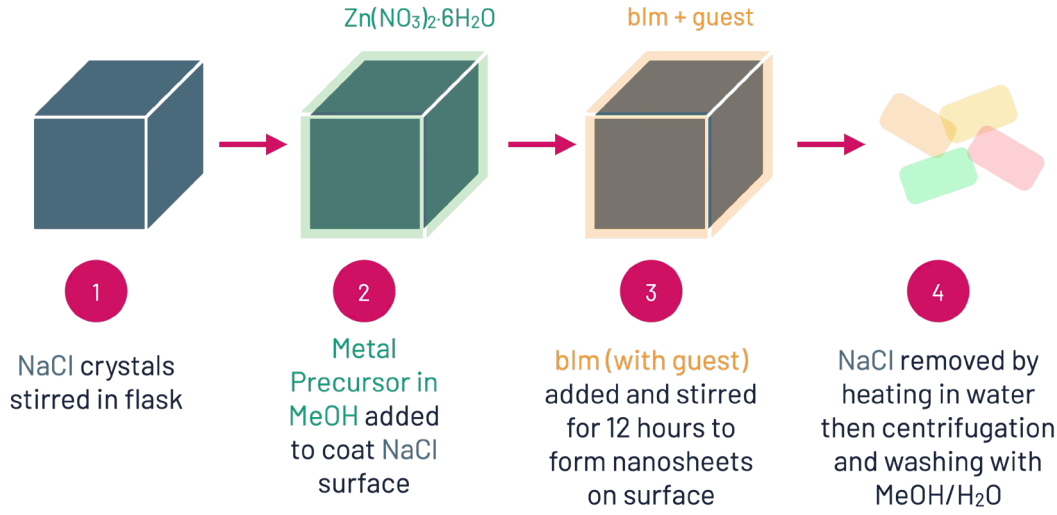

Figure 3.10. Salt-templated synthesis mechanism for guest@MONs.

Confinement, rather than surface adhesion, of guest particles is desirable to increase guest stability (by the protective host framework), increase host-guest interactions, and reduce guest leaching into external environments. Attempts to diffuse or coat

Z7-NS with guests by placing Z7-NS into a solution of guest molecules were unsuccessful. Given the *in situ* nature of synthesis, this implied some degree of incorporation into the Z7-NS particles. As outlined in §3.2.1, the structure of Z7-NS does offer sites for guest incorporation. Even if the guests settled on the surface of one nanosheet layer during synthesis, it is possible for an additional layer to stack above this to intercalate the guest between Z7-NS layers.

The nanoconfinement of guests, compared with less desirable surface adhesion, was confirmed by a range of data presented in Papers I and II. Of note, the guest@Z7-NS materials were thoroughly washed post-synthesis in a solvent in which the guest is soluble, to extract any surface adhered guest molecules, or particles agglomerated with Z7-NS particle aggregates. The nanosheets were too small to undertake more precise diffraction studies for guest positioning.

Firstly, nanoFTIR was used to probe the chemical composition of the local nanostructure of guest@Z7-NS materials. Vibrational spectra indicated consistency with Z7-NS, with no additional bands present. As a surface technique (to a probing depth of ~10 nm), nanoFTIR indicated the absence of any substantial dye on the surface of the nanosheets. FLIM was used to confirm single-particle fluorescence emission from guest@Z7-NS particles, confirming the incorporation of guests into the particles. PXRD indicated that the *d*-spacing between nanosheet layers increased following guest intercalation, from 9.44 Å in Z7-NS to 9.57 Å in F@Z7-NS and RB@Z7-NS, and to 9.66 Å for F+RB@Z7-NS. Similarly, AFM average heights indicated growth in the *z*-axis and thickness of particles, to 2.6 nm for

F@Z7-NS, 2.8 nm for RB@Z7-NS, 2.9 nm for MC@Z7-NS, and 3.9 nm for F+RB@Z7-NS. This height average increase is complementary to the introduction of more bulky guests into the Z7-NS layers, suggesting successful guest incorporation. After suspending the guest@Z7-NS particles in MeOH for 6 months, no noticeable guest leaching had occurred, further indicating the successful binding of the guest molecules into the Z7-NS particles. Finally, as explained in §3.3, a range of luminescent properties were observed in guest@Z7-NS materials which are atypical for mere surface absorption, but instead nanoconfinement.

3.3 Fluorescent Guest@MON Properties

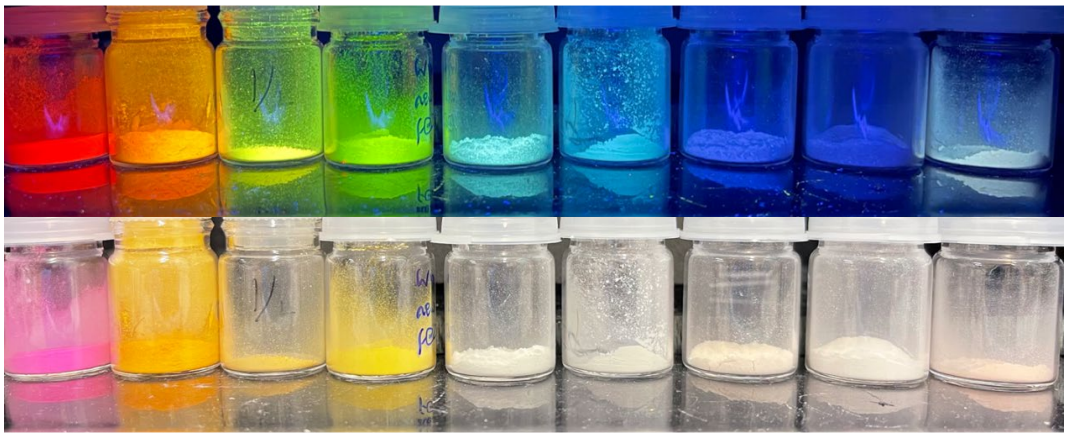

Figure 3.11. Various guest@Z7-NS samples under UV (above) and ambient conditions (below), illustrating the diverse range of emission colours achieved.

3.3.1 Experimental design

The purpose of synthesising guest@MON materials in this study was to introduce, then tune, luminescent properties in MON materials that are desirable for lighting applications.

Guests were selected with the intention of forming a white light emissive system, so included a red, green, and blue emitter. F is a common and well-studied green emitter, already reported in a number of guest@MOF materials including ZIF-8.[83] RB, as a red emitter, has been similarly encapsulated in MOF materials, including ZIF-71,[106] and is a dye frequently used for biological staining. Both are strongly emissive.

Selecting a blue guest was more challenging, with a range of options including MC, pyrene, perylene, 8-hydroxyquinoline (HQ), Zn(II) 8-hydroxyquinoline (ZHQ), coronene, and tetraphenylethylene (TPE) (Figure 3.12). All materials were synthesised as guest@Z7-NS systems, along with guest@ZIF-7 systems for preliminary screening. Characterising the emission properties of these materials, along with analysis of molecular structures, led to MC as the best candidate. Coumarins are common blue phosphor components.[107] MC is a small molecule with a planar structure. It is a neutral, stable species with limited electron density. It is also naturally occurring in flora and biologically compatible.[108]

Across Paper I and II, after guest emitters were nanoconfined in Z7-NS, the photophysical properties of the resulting materials were systematically evaluated.

The sections that follow in §3.3 outline the various fluorescence photo-mechanisms that were accessed by guest@MON design. In many cases, comparisons to guest@ZIF-7 materials (the analogous 3D material) were made, so the effects of 2D MON confinement could be deduced.

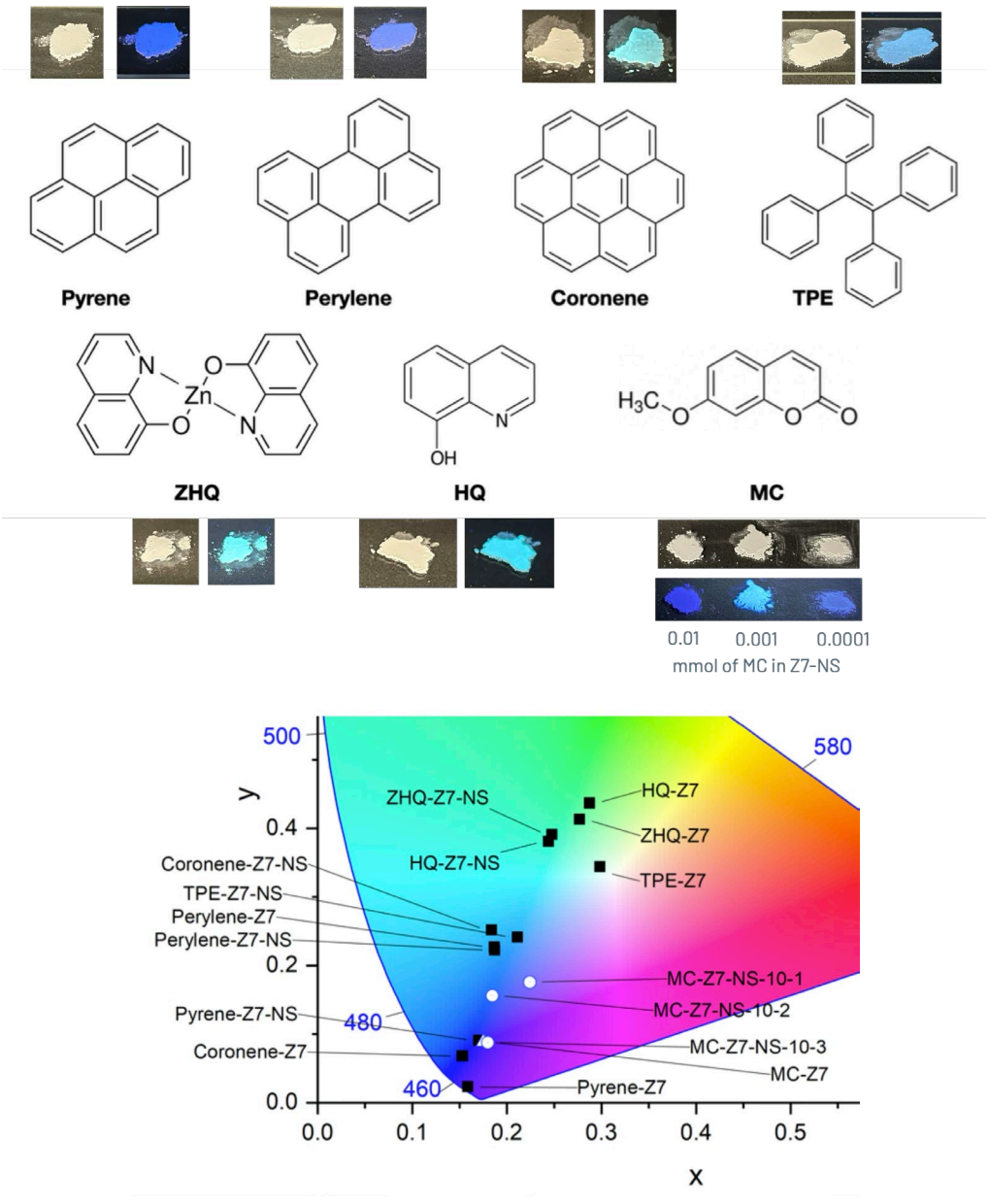

Figure 3.12. Various blue chromophores confined in Z7-NS, showing each guest@Z7-NS under ambient (left) and UV (right) conditions. Below: emission chromaticity of each guest@Z7-NS sample, compared with synthesis of the same guests in 3D ZIF-7.

3.3.2 'Turn on' fluorescence

RB and F in powder form are non-emissive due to aggregation-caused quenching. Previous encapsulation of RB or F in MOFs has demonstrated that confinement in MOF pores turned on fluorescence by preventing dye aggregation (Figure 3.13).[83,106,109] The same result was achieved when RB and F were entrapped in Z7-NS MONs. Paper I, Figure 5 provides detailed photophysical analysis of F@Z7-NS and RB@Z7-NS, including emission and excitation spectra along with TCSPC fluorescence lifetime data for three different guest loadings of each sample.

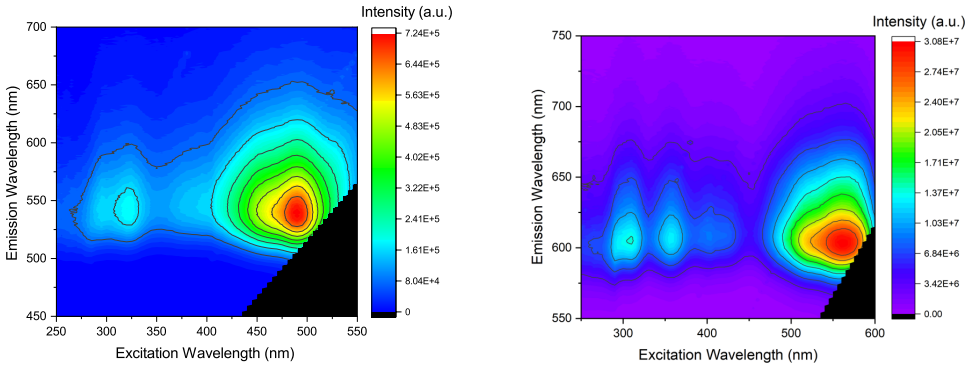

Figure 3.13. Emission of F@Z7-NS (left) and RB@Z7-NS (right).

These data show that even at the lowest guest loadings, RB and F formed in an even quantity of monomeric species and J-aggregates in RB@Z7-NS and F@Z7-NS, respectively. In contrast, RB@ZIF-8 was reported to have a 70:30 ratio of monomers:J-aggregates, and 80:20 for F@ZIF-8.[110] The increase in aggregates may result from the open inter-layer space allowing for greater guest overlap, compared with isolation in discrete cages in ZIF-8. Of note, ZIF-7 was not a suitable

comparator as the guest molecules were not of appropriate sizes to be encapsulated in the cages of ZIF-7 (diameter of 5.58 Å *vs* 11.70 Å for ZIF-8). The J-aggregate dimers could be head-to-tail or overlapped at an angle through a slipped cofacial arrangement. Given the close proximity of guests within the interlayer spacing of Z7-NS, this is geometrically feasible. As J-aggregates result in more intense but lower energy emission than monomers, the proportion achieved in Z7-NS is favourable: overall intense emission was observed within the expected green chromaticity for F and orange-red chromaticity for RB. An additional benefit of the nanosheet morphology was photostability: after 24-hour exposure with a 150 W xenon lamp irradiation at each material's absorption maximum, RB@Z7-NS lost 10.5 % intensity, while F@Z7-NS lost 11.6 %. Both retained emission colour, and emission reduction stabilised after 14 hours. This is a noticeable improvement over the reported 35 % intensity loss for F@ZIF-8 and 13 % loss for RB@ZIF-8 after 24 hours.[83,110]

When loading increased significantly, the quantity of H-aggregates increased from 5-6 % to 10-20 %. This resulted in decreased emission intensity and lower PLQY. Of note, H-aggregates (stacked dimer arrangement) are more likely to reside on particle surfaces where there is less steric confinement. This is typical for dye@MOF materials, and often indicates when the porous space for guest incorporation has been oversaturated and remnant guest particles reside instead on the exterior of the framework.

3.3.3 Preventing photodimerisation

Many coumarins, including MC, undergo photodimerization when exposed to ultraviolet A light (UV-A, around 365 nm).[111] The process involves a [2+2] photocyclisation reaction that breaks the C=C bond adjacent to the carbonyl in two MC molecules, followed by bonding these together by forming a cyclobutene ring.[112] The dimer is non emissive, having lost aromaticity and therefore a stable pathway for fluorescence. Paper II analyses the photodimerization of MC using ATR-FTIR coupled with emission and excitation spectra to correlate observed chemical changes with photophysical alterations (Paper II, Figure 3). Photodimerization in MC has also been shown to cause large crystallographic distortions due to an increase in the *a*-axis by 6.8 Å to 14.6 Å, inducing strain in crystallites and a loss of crystallinity.[111] The lifetime for MC and similar coumarins, therefore, is not sufficient for use in LED related applications unless the photodimerisation can be prevented.

In Paper II it is reported that by entrapping MC in Z7-NS, it was possible to prevent photodimerisation. Certain photophysical features indicated MC had been incorporated in the framework. Firstly, a blue-shift of 20 nm was observed in emission, typical of confined guests in a host structure. The Stokes shift also reduced from 53 nm to 45 nm, implying less energy is lost during the emission process. Finally, no aggregation band was observed in emission spectra, as seen in molecular MC, indicating a degree of physical molecular separation once positioned in the inter-layer cavities of Z7-NS. It is theorised that the positioning of

MC in Z7-NS primarily prevented photocyclisation from occurring. [2+2] photocyclisation of MC has been found to require double bonds within 3.83 Å.[113] Unlike typical photocyclisation reactions, the bonds do not need to also be parallel, instead undergoing a rotation of 65° with respect to each other after UV absorption.[114] Hence, not only physical proximity but also orientational flexibility is required, two qualities hindered by confinement in the host Z7-NS framework. Paper II also reports on MC@ZIF-7, the 3D analogue to MC@Z7-NS, which was found to similarly prevent photodimerisation, but inherently exhibit lower fluorescence performance in terms of quantum yield and emission intensity (see further in §3.3.4.1).

3.3.4 Enabling inter-guest interactions

As provided in §3.3.2, F and RB exhibited aggregation in Z7-NS, a form of guest interaction within dimer units, that resulted in improved or diminished fluorescence emission depending on the dimer arrangement. This section concentrates on wider-scale interactions across all guest species incorporated in Z7-NS.

3.3.4.1 Homogeneous guest interactions

Not only did MC@Z7-NS prevent photodimerisation, but it also created new MC inter-guest interactions that improved emission chromaticity, PLQY, and intensity. MC has previously been encapsulated in micellar systems, p-sulfonatocalix[4]arene,[115] and cyclodextrin,[116] but these have caused

fluorescence suppression due to non-polar cavities or hydrogen bonding.[117] No work has reported on methods to enhance the fluorescence of MC.

Upon UV-A exposure for 2 hours, MC@Z7-NS exhibited an irreversible red-shift from purple to vibrant blue emission, corresponding to a 5-fold intensity increase of emission, increase in PLQY from 20.7 % to 26.6 %, and an increase in Stokes shift to 80 nm (Paper II, Figure 5). A large Stokes shift effectively prevents self-absorption, improving overall emission efficiency and intensity. The brighter blue emission is more desirable for blue LEDs and a component for WLE systems. Due to the lack of detectable MC bands using PXRD or vibrational spectroscopy, photophysical data were used to elucidate potential mechanisms.

Emission and excitation data measured across 24 hours revealed that while excitation bands remained consistent, an additional emission band formed at longer energy than the typical MC monomer emission band (Figure 3.14). This implied that the same monomeric species absorb energy to reach an excited state, but emission is occurring through both the monomer pathway ($S_1 \rightarrow S_0$) and an additional pathway. This additional pathway is often a result of charge transfer. As a polar molecule, MC comprises a weak methoxy electron donor and a carbonyl electron acceptor. A full resonance pathway exists for electron delocalisation between the donor and acceptor, permitting intra-molecular charge transfer. Alternatively, two closely aligned MC molecules, arranged to have one donor component and one acceptor component in close proximity, could enable the overlap of delocalised π systems sufficient for inter-molecular charge transfer.

Similar behaviour was observed by encapsulating a MC based coumarin in a crown ether, where both local excitation and an internal charge transfer band occurred, with charge transfer resulting from the close alignment of fluorophores (within 8-10 Å) provided by the diaza-crown.[118] Notably, MC@ZIF-7 did not exhibit the photoinduced band formation, suggesting the increased molecular overlap achieved in interlayer spaces may be a factor in enabling a charge transfer driven interaction.

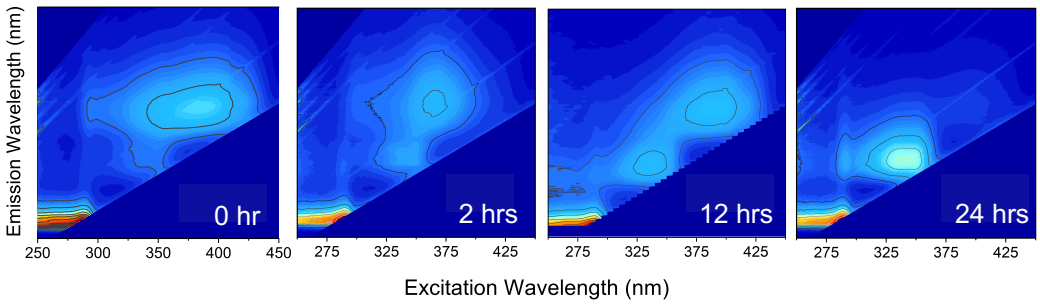

Figure 3.14. Emission-excitation maps of MC@Z7-NS after various lengths of UV exposure (0, 2, 12, 24 hrs from left to right).

Less clear is the reason for the interaction to occur post-UV exposure. One hypothesis posited in Paper II relates to molecular movement: MC is known to undergo molecular rotation and movement upon excitation, a feature that enables dimerisation. Chromophores such as RB have previously been shown to exhibit movement under UV exposure over time, leading to, for example, self-aggregation in confined domains on silica nanoparticles.[119] Here movement of MC may enable greater electron cloud overlap for CT.

3.3.4.2 Heterogeneous guest interactions

The combination of F and RB in Z7-NS resulted in a dual-guest system, which was studied to develop a yellow emitter DG@Z7-NS. The system exhibited tuneable emission chromaticity that varied across red to green by adjusting the ratio of F:RB confined in the framework (see Paper I, Figure 7). It was established, by analysing the properties of 20 unique DG@Z7-NS samples of varying F:RB ratio, that the emission colour was quantifiable. This was derived from a linear relationship between red and green values (from RGB values) of emission chromaticity, along with a logarithmic relationship between the green RGB value and F:RB synthesis ratio. From the developed equations, emission colour could be predicted given a set F:RB synthesis ratio. Conversely, if a particular emission colour was required, the F:RB synthesis ratio needed to achieve this could be determined. A notable result from this finding is that such a relationship implies there is a discrete subset of colours (an 'emission chromaticity fingerprint') that is attainable by this particular dual-guest system. While a number of luminescent MOF systems have proven tuneability by a subset of examples, this is the first study known to the authors that quantified tuneability.

Importantly, Paper I deduced the emission mechanism behind the tuneable emission observed in DG@Z7-NS was a result of inter-guest interactions in the form of Förster resonance energy transfer (FRET) (see Paper I, Figure 6). FRET (Figure 3.15) is a physical process whereby energy is transferred non-radiatively from an excited donor dye to an acceptor dye by way of long-range dipole-dipole

intermolecular interactions. The phenomenon is distance dependent, with the efficiency of FRET dependent on the inverse sixth power of the intermolecular separation distance and is typically observed between 1-10 nm. As the emission band of F overlaps with the absorption band of RB, it is theoretically possible for F molecules, in the excited state, to exhibit energy transfer to RB. Not all excited energy, however, is often transferred and F will still exhibit a degree of fluorescence, allowing for yellow emission colour. Unlike trapping guests in the pores of frameworks such as ZIF-8, the tight space within the MON layers creates a favourably short distance between guest dyes. Evidence for FRET is established in Paper I. This included additional fluorescence lifetime decay components, attributable to short lasting FRET interactions. A shift in emission energies of F and RB compared to physical mixing of F@Z7-NS and RB@Z7-NS also indicated more complex intra-molecular interactions were occurring in DG@Z7-NS. Finally, the emission bands of RB were observed beyond the typical excitation ranges of RB, indicating an alternate energy source other than direct excitation (i.e., FRET).

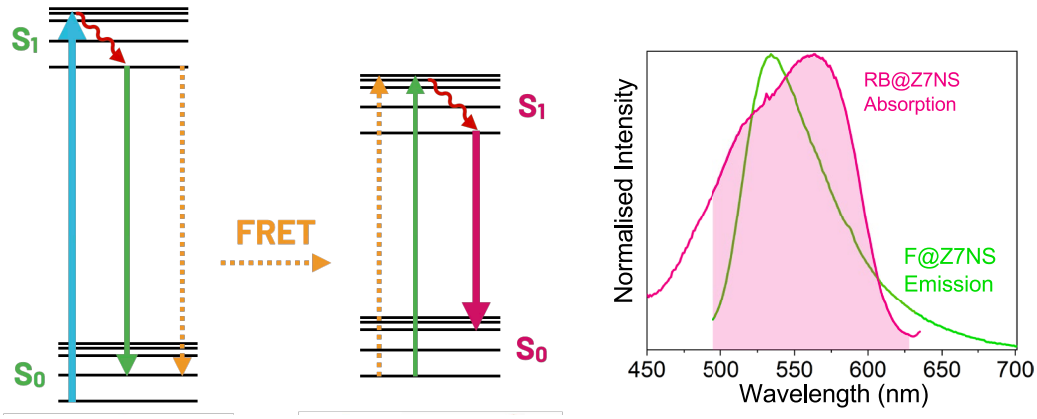

Figure 3.15. Left: FRET mechanism with F on the left and RB on the right. Right: Energy transfer through the overlap of F emission with RB absorption bands.

3.4 White light emission

The third component in this first study was combining the red, green, and blue emitters studied to produce a WLE emitting system. Standard WLE is characterised by the CIE coordinates of (0.33, 0.33) and colour correlated temperatures (CCTs) between 2500-6500 K. While ideal WLE has been achieved for the few reported dye@MOF WLE materials, there is still a challenge in balancing high PLQY (often only attainable up to 20-30 %), with ideal CCT and CIE coordinates, long-term physico-chemical and photo-chemical stability, and fabricability for workable OLED devices.[120]

Several studies report WLE nanosheet materials based on metal-oxides or boron nanosheets that increase pathways for charge transfer and increase efficiency, while also creating easier-to-fabricate thin film devices.[121-125] Only two works known to the authors have reported WLE MONs. One yellow-emitting Zr MON with TPE-based ligands was combined with a blue LED to produce WLE with CIE coordinates of (0.37, 0.41).[126] The second study reported a composite of lanthanide hydrates@2D MOF. While this system achieved CIE coordinates of (0.31, 0.33) at 6370 K, PLQY was relatively low (3.3-8 %) and the guest incorporation and long-term stability were unclear.[82]

Paper II, Figures 7-8 detail 30 samples of Z7-NS that were prepared with different MC:F:RB ratios in order to obtain a 3 phosphor WLE system (TG@Z7-NS). Emission colour temperature ranged between 4000-8000 K on the Planckian locus, corresponding to incandescent lightbulbs typically rated at 4200 K, daylight at

5500 K, and an overcast day at 6500 K. An ideal WLE sample with chromaticity coordinates (0.33, 0.34) was achieved, with a remarkably high PLQY of 65.08 % (see Figure 3.16). Emission, excitation, and lifetime data showed the contribution from the three phosphors, with no evidence of aggregation or inter-guest interactions. This is expected given the mix of dyes now within the Z7-NS framework, inhibiting any favourable alignment of molecules for guest-guest interactions. The material did exhibit limitations, however. Firstly, 75 % intensity was lost during 24 hours of exposure to 150 W xenon lamp at 350 nm, although emission chromaticity remained consistent when observed by eye. Secondly, the ratio of MC:F:RB determined by NMR digest in the ideal WLE Z7-NS material was 148:14:1, disproportionately weighted towards MC due to the dye being a weaker emitter. Furthermore, the synthesis ratio was 34058000:2650:1 (see Figure 3.17), indicating limited MC was intercalated during synthesis. Hence, while an effective proof of MON WLE, further study should optimise the suite of guests selected to balance emission intensities and ranges.

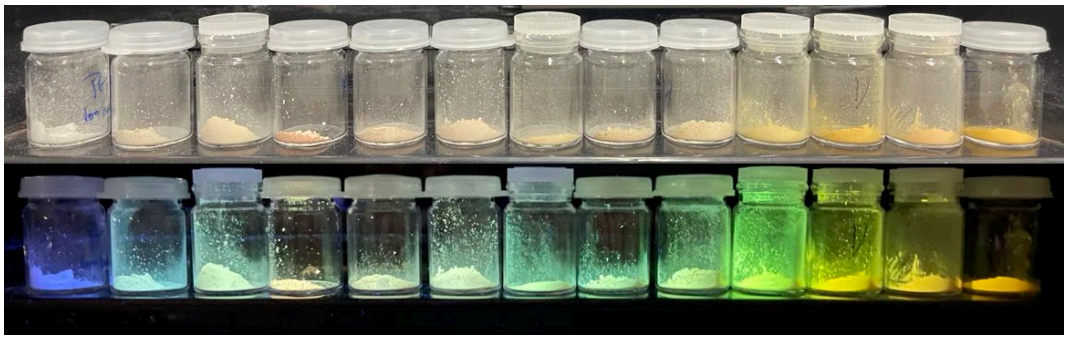

Figure 3.16. Selection of TG@Z7-NS samples exhibiting a range of WLE.

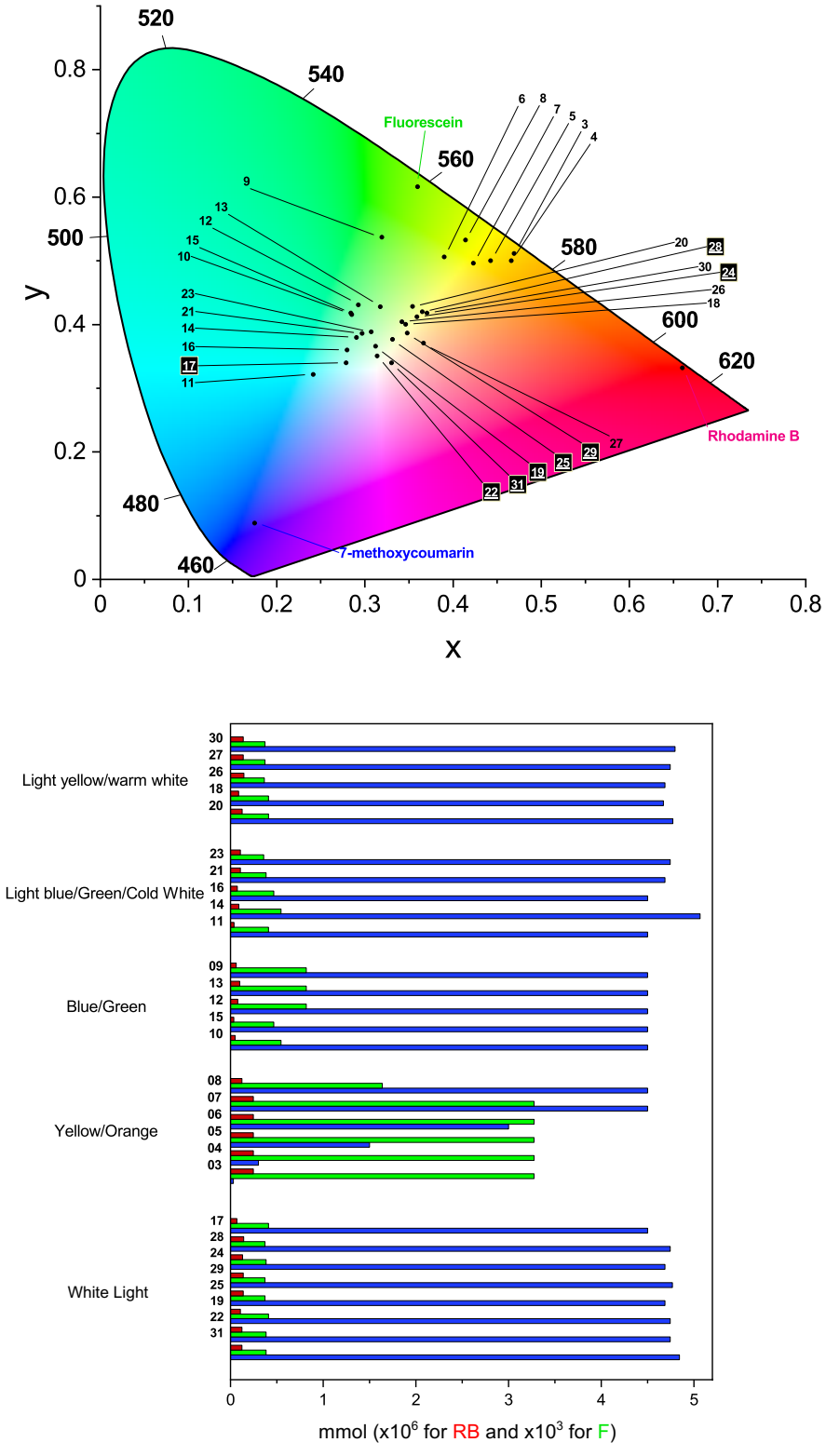

Figure 3.17. TG@7-NS emission (above), corresponding to MC: RB: F ratios (below).

3.5 Implications and Applications

The studies reported in this chapter across Papers I and II established the first bottom-up synthesis of ZIF-7-III nanosheets. In doing so, it also presented a new methodology for guest@MON synthesis. While the applications targeted in this study were luminescence, this method could be applied to any guest, including conductive or redox active guest molecules.

In the case of luminescence, this study has established how various emission mechanisms can be accessed through confinement of light-emissive guests in the Z7-NS structure. These ranged from turning on guest fluorescence, to preventing photodimerisation, tuning emission chromaticity, controlling guest-guest interactions, and mixing guests in multi-guest confinement to achieve WLE. Further mechanisms such as turn off and switching fluorescence, along with more diverse guest-guest interactions, or even phosphorescence, are still highly relevant to explore for MONs. Ultimately, myriad molecules are available to endow MONs with new properties ideal for applications, from pressure sensors that could take advantage of the large surface area in 2D MONs, to environmental sensors, expected to be more responsive than bulk materials given MON exposed active sites.

A third key fundamental realised in this study is the quantifiability of emission chromaticity tuning. Devising tuneability that is predictable and precise is significant for guest@MOF and guest@MON materials, or luminescent guest@host materials more generally. The implication that emission chromaticity is limited to a discrete subset of RGB values presents a strong theoretical foundation

for rationally designing future guest@host systems. By modelling predicted energetics of the dyes, followed by mapping a sample synthesis, it is possible to design systems of discrete colour ranges, with *a priori* 'emission chromaticity fingerprints', ideal for a range of nanophotonic applications from unique identifiers for product quality assurance and covert security tags, to sensing and lighting, or layered semi-conductors. While beyond the scope of this work, it would be of interest to examine whether such quantifiability can extend to other guest@MON systems, and if so, whether there is an underpinning fundamental principle of fluorescence emission from which the relationship is derived.

3.6 Paper I

Guest entrapment in metal-organic nanosheets for quantifiably tuneable luminescence

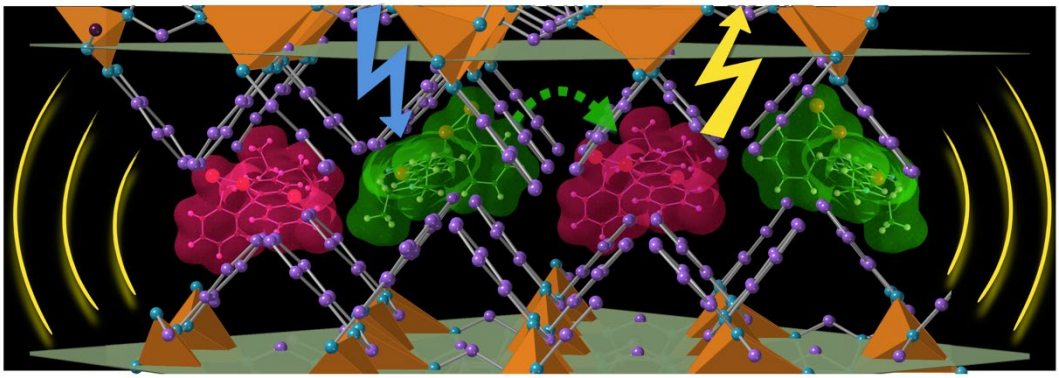

Figure 3.18. Illustration of RB (red) and F (green) entrapped in Z7-NS, undergoing FRET to produce yellow fluorescence emission.

Supporting information for this manuscript can be found here:

https://onlinelibrary.wiley.com/action/downloadSupplement?doi=10.1002%2Fadfm.202214307&file=adfm202214307-sup-0001-SuppMat.pdf

ADVANCED FUNCTIONAL MATERIALS
www.afm-journal.de

Guest Entrapment in Metal-Organic Nanosheets for Quantifiably Tuneable Luminescence

*Dylan A. Sherman, Mario Gutiérrez, Ian Griffiths, Samraj Mollick, Nader Amin, Abderrazzak Douhal, and Jin-Chong Tan**

Luminescent metal-organic frameworks (LMOFs) are promising materials for nanophotonic applications due to their tuneable structure and programmability. Yet, the 3D nature of LMOFs creates challenges for stability, optical transparency, and device integration. Metal-organic nanosheets (MONs) potentially overcome these limitations by combining the benefits of metal-organic frameworks (MOFs) with an atomically thin morphology of large planar dimensions. Herein, the bottom-up synthesis of few-layer thin ZIF-7-III MONs via facile low-energy salt-templating is reported. Employing guest@MOF design, the fluorophores Rhodamine B and Fluorescein are intercalated into ZIF-7 nanosheets (Z7-NS) to form light emissive systems exhibiting intense and highly photostable fluorescence. Aggregation and Förster resonance energy transfer, enabled by the MON framework, are revealed as the mechanisms behind fluorescence. By varying guest concentration, these mechanisms provide predictable quantified control over emission chromaticity of a dual-guest Z7-NS material and the definition of an "emission chromaticity fingerprint" – a unique subset of the visible spectrum that a material can emit by fluorescence.

1. Introduction

Metal-Organic Framework (MOF) nanosheets, recently termed Metal-Organic Nanosheets (MONs), are an increasingly sought-after form of MOFs that unite the properties of 2D materials with 3D MOF characteristics.[1,2] Nanosheets are high surface-to-volume atom ratio materials with single or few-atom thickness (1–10 nm typically) and comparatively large micron-scale lateral planar dimensions.[3] Archetypal 2D materials, such as MXenes,[4] layered double hydroxides (LDH) and oxides,[5] and graphitic carbon nitrides,[6] have been reduced to nanosheets in multiple studies.[7] These nanosheets have unprecedented physical, electronic, chemical, and optical properties unattainable in their 3D layered bulk counterparts.[7] MONs provide a competitive alternative to these nanosheet materials by adding key MOF characteristics derived from the metal-organic composition. These include structural diversity and tuneability, programmable functionality, mechanical anisotropy,[8,9] and highly ordered pore arrays with abundant accessible active sites.[1] To date, MONs have shown great promise in gas separation and water purification applications,[10,11] energy storage,[12] light harvesting and emission,[1] electronic devices,[13] catalysis,[14,15] and sensing.[16] ZIF nanosheets are particularly intriguing, given that 3D ZIFs exhibit high stability, hydrophobicity, and large pore size.[17] ZIF-7 [$Zn(bIm)_2$, bIm = benzimidazolate] is isolatable in a dense thermodynamically stable 2D-layered phase ZIF-7-III ($Zn_2(bIm)_4$),[18] making it viable for the formation of nanosheets (**Figure 1**).[19] ZIF-7 nanosheets have been used as a matrix for the ionization of small molecules,[20] molecular sieving,[21] and membranes.[21]

D. A. Sherman, S. Mollick, J.-C. Tan
Multifunctional Materials & Composites (MMC) Laboratory
Department of Engineering Science
University of Oxford
Parks Road, Oxford OX1 3PJ, UK
E-mail: jin-chong.tan@eng.ox.ac.uk

M. Gutiérrez, A. Douhal
Departamento de Química Física
Facultad de Ciencias Ambientales y Bioquímica
INAMOL
Universidad de Castilla-La Mancha
Toledo 45071, Spain
E-mail: mario.gutierrez@uclm.es; abderrazzak.douhal@uclm.es

I. Griffiths
Department of Materials
University of Oxford
16 Parks Road, Oxford OX1 3PH, UK

N. Amin
Department of Chemistry
University of Oxford
Mansfield Road, Oxford OX1 3TA, UK

The ORCID identification number(s) for the author(s) of this article can be found under https://doi.org/10.1002/adfm.202214307

DOI: 10.1002/adfm.202214307

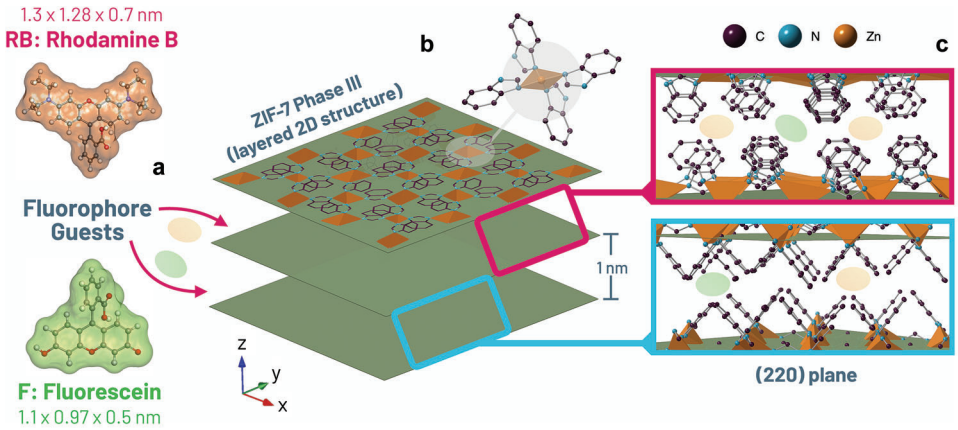

Figure 1. Schematic of material design with structures from single crystal ZIF-7-III data.[33] a) Chemical structures of Rhodamine B and Fluorescein. b) Single secondary building unit with ZnN_4 tetrahedra highlighted on a single sheet (monolayer) of $Zn_2(bIm)_4$ in the *xy*-plane of a segment of ZIF-7-III layered structure with green planes indicating the (002) *d*-spacing. c) Cross section of the (220) plane, illustrating the perpendicular arrangement of layers and interlayer spacing. For all representations: carbon (purple), nitrogen (blue), Zn(II) (orange), oxygen (red), hydrogen (omitted for clarity).

The study of MONs is still in its infancy, with synthesis and stability often the greatest challenges.[3,22] Most studies rely on top-down disassembly of 2D layered MOFs,[23,24] which is energy and time consuming, and typically result in MONs of non-uniform nanosheet dimensions with rough surfaces that commonly reaggregate.[23] Bottom-up synthesis provides greater morphological control and stable isolated sheets, but with few reports in high yield.[14] Examples of bottom-up techniques tailored to specific MOFs, such as ZIF-8 and ZIF-67, include modulation,[25,26] diffusion,[27] surfactant assistance,[28,29] salt-confinement,[30] and interfacial synthesis.[31] To our knowledge, though, there are no reports of ZIF-7-III nanosheet bottom-up synthesis, only top-down delamination.[20,31,32,33] While rarely used for MONs, salt-templating is a frequently cited method of synthesizing nanosheets of 2D materials.[34,35] Acting as a hard-templating agent, salt crystal faces provide an energetically favorable surface for the growth of consistently thin nanosheet materials. Given the ubiquity of NaCl, and ease of its removal via dissolution in H_2O, this method has significant benefits environmentally and for scalability.

One of the lesser explored areas of MONs is luminescent optoelectronics. A fluorescent nano-emitter should have negligible dye leaching, structural stability under ambient conditions and repeated use, and high photoluminescence quantum yield (PLQY). Key to making nano-emitters application-ready is the ability to tune luminescence energetics and chromaticity. Studies have demonstrated that the emission chromaticity of luminescent MOFs (LMOFs) with chromophore guests can be tuned qualitatively by varying the guest loading concentration within the framework pores.[36,37] To our knowledge, however, there is no numerical study of the precise relationship between guest concentration and resulting material luminescence chromaticity. Finding such a correlation would provide unprecedented precision tuneability of luminescence energetics for nano-emitters, a function critical to advancing the field of MON optoelectronics from layered semiconductors to sensors and organic light-emitting diode (OLED) materials.

The majority of LMOF literature targets 3D bulk materials,[38] but these are often unstable in solution due to guest leaching. The host framework can also impede emission via self-quenching, either through energy interconversion and absorption or physical shielding.[39] In contrast, the atomic thickness and increased specific surface area of MONs improve optical transparency, while still allowing strong in-plane covalent bonding for stronger guest binding and chemical stability.[40,41,9] The confinement of electrons in an ultra-thin region also facilitates the control and directionality of excitons emission, which theoretically allows for the optimization of guest luminescence.[42] Exfoliated materials such as AUBM-6-NS, for example, have reported up to threefold greater emission intensity than the bulk AUBM-6.[40]

At present, the overwhelming majority of luminescent MONs (LMONs) utilize inherent luminescence via the design of emissive linkers, metal ions, or via ligand-metal charge transfer.[43] A novel route to LMONs is employing the guest@MOF approach and, to the best of our knowledge, the only work to date considering this approach is the system lanthanide hydrate@MOF nanosheets (HSB-W5-NS).[44] Dyes, alternatively, are ideal for use in guest@MOF systems.[45] Rhodamine B (RB) and Fluorescein (F) (Figure 1a) are two of the most employed guests due to their high PLQY and stability.[46] While F and RB do not fluoresce in solid-state due to aggregation-caused quenching (ACQ),[47,48] isolating monomers via encapsulation in pores of 3D MOFs,[49–52] can induce fluorescence in solid state while also improving long-term guest stability.[53,54] In 3D MOF materials, in situ guest encapsulation strategies are typically employed to overcome small pore apertures prohibiting dye diffusion.[52] In a 2D MON system, we theorize this encapsulation is analogous to intercalation, which has been achieved for RB and F in LDH systems and clays,[55,56] yet the resulting systems are frequently reported as being unstable or lack tuneability.[57,58] The intercalation of organic fluorophores is yet to be explored in MONs, despite the apparent advantages of a more flexible and customizable parent matrix to control loading and tune interlayer spacing.

Herein, we report the first in situ bottom-up synthesis of ultrathin $Zn_2(bIm)_4$ MONs (Z7-NS) via a low-energy and

scalable salt-template synthesis. We show that the fluorescent dyes RB and F can be incorporated into individual Z7-NS using this synthesis to yield highly stable fluorescent guest@MON systems with tuneable emission of visible light. Utilizing nanoscale analysis techniques, we reveal the underpinning mechanisms of guest intercalation. When the dyes are intercalated simultaneously, a dual-guest yellow emitting nano-system results, whose emission chromaticity is precisely tuneable via numerical modelling.

2. Results and Discussion

2.1. Synthesis and Structure of Z7-NS Guest@MON Materials

Z7-NS were synthesized in situ using an environmentally benign salt-templating technique during a one-pot reaction (see Experimental Section). In brief, after coating a large excess of NaCl crystals in $Zn(NO_3)_2$ solution, benzimidazole (bIm) was added with minimal solvent (MeOH) and mixed rapidly to grow Z7-NS. The nanosheets were isolatable by dissolving NaCl in H_2O. Optical microscopy and SEM imaging of a NaCl crystal before synthesis, compared to the reaction mixtures after stirring (Figure S1, Supporting Information), revealed preferential growth of the nanosheets on the surfaces of NaCl crystals, thereby limiting growth along the z-axis. It is well reported that salt particles with large dimensions (such as 20 μm used in this synthesis) and smooth surfaces (see NaCl in Figure S1, Supporting Information) act as this hard template for synthesizing 2D sheets of materials such as metal nitrides and oxides (e.g., MoO_3).[34,35,59] This contrasts with the only reported ZIF nanosheets (ZIF-67) synthesized with salt, which used salt crystals of just 1 μm to grow nanosheets in the voids between salt crystals.[30]

To examine the essential role of the dense NaCl matrix in forming nanosheets, the Z7-NS synthesis was repeated with varied NaCl quantities and compared with ZIF-7-III synthesized using hydrothermal transformation of ZIF-7.[33] All syntheses produced materials with a ZIF-7-III crystal structure, confirmed by PXRD (Figure S2, Supporting Information). The morphology, however, varied progressively with the addition of NaCl. As seen in SEM imaging (Figure S2, Supporting Information), hydrothermal synthesized ZIF-7-III formed layered stacks, while the direct room temperature synthesis without salt produced aggregated layered globules. Synthesis with 0.25x NaCl quantity results in the layered globules beginning to aggregate via interconnected nanosheet layers, similar to the nanosheet networks seen in the reported ZIF-67 salt temptation. At 0.5x NaCl quantity, particles form independently and are predominantly composed of intertwined nanosheets with some remaining globules. This suggests that isolated nanosheets are forming on NaCl surfaces, but the voids in the less dense NaCl crystal confinement likely allow for precursor solution to still concentrate and form stacked materials around the nanosheets. When a large excess of NaCl is used in standard reaction conditions, the void space is filled by the dense NaCl matrix, directing growth preferentially on NaCl surfaces without 3D protrusions.

Fascinatingly, by adding F or RB dissolved in methanol into the synthesis solution, facile in situ guest incorporation into the framework was achieved. Two single-guest systems (F@Z7-NS and RB@Z7-NS) at various guest loadings (guest@Z7-NS-10^{-1}, -10^{-2} and -10^{-3} M using synthesis guest quantities of 0.03, 0.003 and 0.0003 mmol respectively) were formed, along with a dual-guest system (entrapping F and RB simultaneously, DG@Z7-NS). Guest loading was quantified using ^{1}H NMR (see Figure S3 and Table S1, Supporting Information) with data confirming guest loading increases with an increase in guest concentration during synthesis. Synthesis was scalable, tested up to 10 times the initial quantities, producing solid material yields from 93 mg to 1.22 g (70%–80%). Z7-NS remained as stable dispersions in H_2O or MeOH, confirmed by Tyndall scattering (Figure S4, Supporting Information), and are thermally stable up to 550 °C (Figure S5, Supporting Information).

AFM and FE-SEM imaging (**Figure 2**) revealed Z7-NS consistently formed as isolatable few-layer thin nanosheet particles, with this morphology being maintained after the incorporation of guest molecules. The height of over 80 particles per material was determined via individual AFM tomography imaging (Figure 2a,b), with calculated mean heights of 1.9 nm for Z7-NS, 2.6 nm for F@Z7-NS, 2.8 nm for RB@Z7-NS and 3.9 nm for DG@Z7-NS. This height average increase is complementary to the introduction of more bulky guests into the Z7-NS layers, suggesting successful guest incorporation. Height distributions (Figure 2b) and height profiles (Figure 2w) for each material indicate a monolayer of Z7-NS being ≈1.2 nm, with samples preferentially forming in 1–4 layers aggregates dependent on guest (*c.f.* ZIF-7-III 2D layer stacks of 200 nm average height) (Figure S2, Supporting Information).

AFM height profiles (Figure 2w) along with AFM imaging and FE-SEM (Figure 2c–g for Z7-NS, Figure 2h–l F@Z7-NS, Figure 2m–q for RB@Z7-NS and Figure 2r–v for DG@Z7-NS) indicate nanosheets form mostly as flat plate-like sheets, with occasional curling observed (e.g., Figure 2k–n) that cause concentrated protrusions in AFM surface imaging and 3D particles from thin flat surface-layers of nanosheets observable in SEM (Figure S6, Supporting Information). Similar curling has been observed by silica nanosheets from mechanical strain while mixing during synthesis.[60] AFM phase images (corresponding to the first harmonic of the probe tip's tapping frequency) of select samples imaged in Figure 2 (Figure S7, Supporting Information) highlight the phase homogeneity of imaged nanosheets even with height anomalies on the surface of base nanosheet layers that correspond to potential curling in the z-axis (e.g., Figure 2d). This is in contrast with the distinct phases for Figure 2d and the right particle in Figure 2s, which show contamination on the sample slide. Particles range in size with the smallest lateral dimensions of ≈5×2 μm^2, average of ≈10×5 μm^2, and largest of ≈20×10 μm^2. Fragmentation via the formation of micro-holes was observed in nanosheets ultrasonicated for over 5 min (Figure S8, Supporting Information), suggesting the particle size variations derive from the mixing, purification, and isolation of synthesized materials. Conveniently, the smaller and larger nanosheets were found to be separable by gravitational sedimentation. SEM micrographs of Z7-NS imaged at a 45° tilt highlighted the thinness, curvature, and isolated nature of the nanosheets (Figure S9, Supporting Information). Large-area FE-SEM imaging was collected to confirm consistency with these morphological parameters and homogenous particle dispersion across sample slides, on which they were drop casted for microscopic examinations (Figure S10, Supporting Information). The

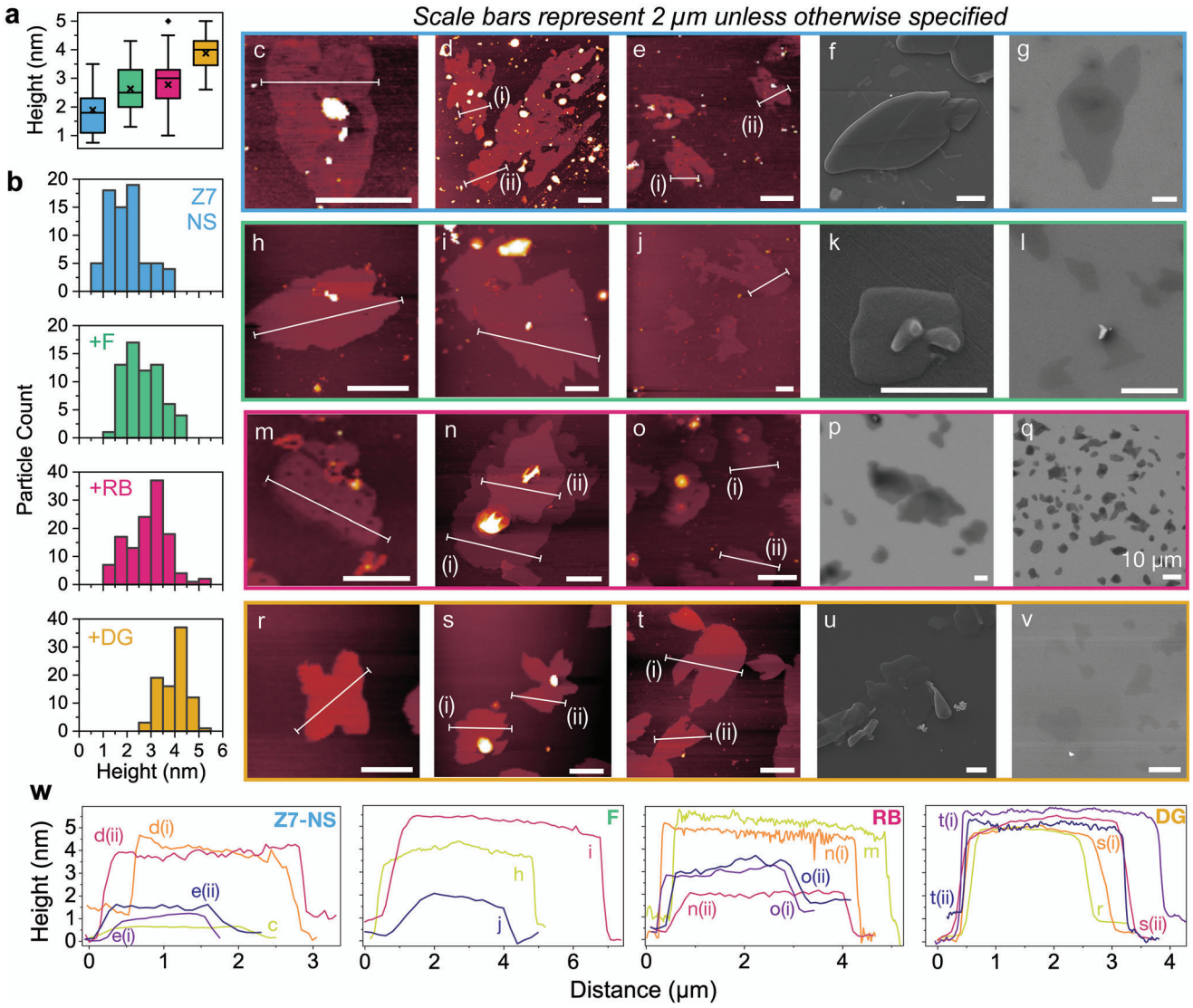

Figure 2. a,b) Heights of over 80 particles of each material (Z7-NS – blue, F@Z7-NS [+F] – green, RB@Z7-NS [+RB] – pink, DG@Z7-NS [+DG] – orange) measured individually using AFM imaging. a) Box plot indicating quartile ranges, median (line), outliers (diamond) and the average height (cross) of each material. b) histogram (0.5 nm bins) height distributions for each material. c–v) AFM surface imaging of material particles on silicon wafer and FE-SEM secondary electron micrographs collected at 10 keV and working distance of 9 mm (samples were either drop-cast onto an aluminium specimen stub and coated with 25 nm of gold [f, k and u], or drop-cast on a silicon wafer [g, l, p-q, v]). Each row is a different material: Z7-NS (c-g), F@Z7-NS (h-l), RB@Z7-NS (m-q) and DG@Z7-NS (r-v). w) Height profiles across select positions in AFM imaging for each material.

morphology remains comparable after 6 months of immersion in water or MeOH, with only slightly increased curling at the nanosheet edges (Figure S11, Supporting Information).

The nanosheet morphology and guest incorporation do not affect the long-range periodicity growth of the host framework, with ZIF-7-III like crystal structure confirmed by direct alignment of PXRD pattern reflections (**Figure 3**a), IR and Raman spectroscopic bands (Figures S12 and S13, Supporting Information). There is no indication of structural transformation or other phase impurities such as NaCl (Figure S14, Supporting Information). Diffraction data further indicate the ultrathin 2D nature of the Z7-NS and the retention of crystallinity across the thin 2D plane. In PXRD patterns (Figure 3a), peak broadening compared to ZIF-7-III and significant reduction in the relative peak intensity ratio of $I(002)/I(220)$ reflections from 14.814 in ZIF-7-III to 3.941 in ZIF-7-NS indicate reduced diffraction in the *z*-axis (out-of-plane orientation, see Figure 1b) of the Z7-NS. HR-TEM (Figure 3b,c; Figure S15, Supporting Information) shows large domains of consistent *d*-spacing across a single nanosheet with an interlayer spacing of 0.56 nm, corresponding to the (220) planes, and 0.25 nm within each of the (220) layers, corresponding to the (260) planes. In the SAED pattern (Figure 3d), three distinctive planes are identifiable upon indexing: the (220) (lowest angle (*hkl*) reflection with no symmetry about the *z*-axis), (110) and (440). All three planes have no *z*-component of symmetry. Thus, we posit the nanosheet has minimal atomic density in the *z*-axis, while the *xy*-plane is significantly atomically dense to produce intense diffraction.

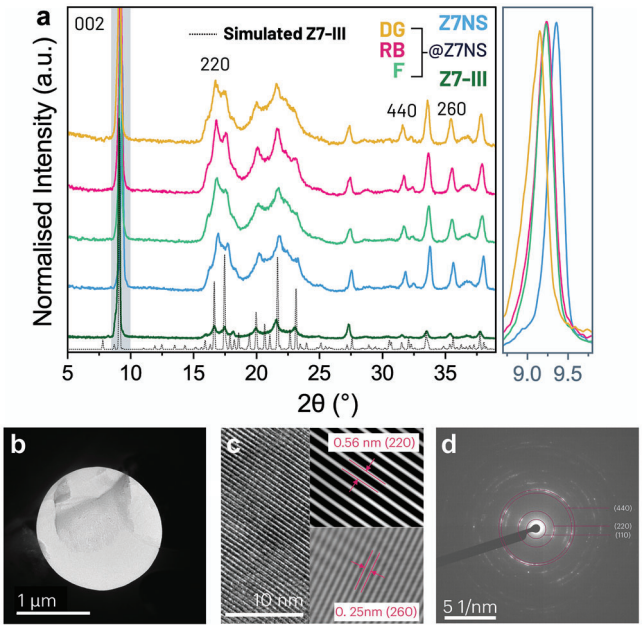

Figure 3. a) PXRD patterns of Z7-NS with various dye@Z7-NS. b) TEM image of a single Z7-NS particle studied in (c)-(d). c) Fourier-transform analysed HR-TEM of Z7-NS revealing inter-plane (220) spacing and intra-plane spacing in the (260) plane. d) Selected area electron diffraction (SAED) image of Z7-NS showing indexed planes.

With the ZIF-7 host framework clearly defined, we next considered the location of the guest molecules within the structure. It was not possible to convert the guest@ZIF-7 systems to ZIF-7-III, nor was post-synthesis guest diffusion successful in incorporating guests into ZIF-7-III stacked materials or Z7-NS. Given the molecular dimensions of F and RB (10.191×9.669×6.43 Å for F and 13.683×13.233×6.97 Å for RB),[51] this was expected due to the dense layer packing in ZIF-7-III and limited openings into interlayer spaces. Instead, guests were only incorporable via in situ syntheses, suggesting the guests are in some way being nanoconfined or intercalated within the layered nanosheet system during its formation, rather than merely attached to the external surfaces. Sterically, each guest comprises a xanthene ring with appended phenyl group, known to rotate to a planar conformation in confined spaces (Figure 1a).[61] This, along with their molecular dimensions make the guests feasible to incorporate into the Z7-NS host framework. A single layer of ZIF-7-III comprises of a (4,4) square planar grid formed by corner-sharing networks, quadruply linked, of ZnN_4 tetrahedra (Figure 1b). Each monolayer, of ≈0.5 nm thick, stacks orthogonally rotated on the *z*-axis via C-H/π interactions, producing 2D channels of ≈1 nm in height through the material's (220) plane (Figure 1c). These channels could accommodate F or RB guests, oriented either perpendicularly or at least inclined at an angle to the layers of Z7-NS. Alternatively, a gap of 0.5 nm between layers provides opportunity for parallel dye encapsulation, with guest phenyl rings able to rest within the pockets between the sterically bulky bIm ligands (these protrude from the Zn centers of each layer but have a degree of rotational flexibility to accommodate guests).

PXRD shows that the (002) *d*-spacing between nanosheet layers increased following guest intercalation, from 9.44 Å in Z7-NS to 9.57 Å in F@Z7-NS and RB@Z7-NS, and to 9.66 Å for DG@Z7-NS (Figure 3a). As described earlier, layer height also increased in AFM surface profiles. Vibrational spectroscopy (Raman, MIR and FTIR) revealed no new bands, suggesting no new covalent bonds have formed between the guests and the framework via surface absorption or within the framework (Figures S12 and S13, Supporting Information). Nor are changes observable for the Z7-NS bands, indicating guests are incorporated in a way that does not affect the surrounding host framework. Nano-FTIR (**Figure 4**; Figure S16, Supporting Information) was used to probe the local nanoscale chemical composition of the guest@Z7-NS systems at single points and across 2D fields, with a spatial resolution of ≈20 nm. Near-field vibrational data show the presence of several IR bands, in particular the strong band at 760 cm^{-1} (corresponding to bIm aromatic ring in-plane and out-of-plane deformations),[61] that align with the Z7-NS nano-FTIR spectra and the corresponding materials' ATR-FTIR spectra. There are, however, no strong bands present that correlate to the spectra of F and RB (Figure 4b,c; Figure S16, Supporting Information). Since nano-FTIR is a surface-based technique, the lack of vibrational modes corresponding to F and RB, indicates the absence of any substantial dye on the surface of the nanosheets, as previous studies in our group have demonstrated.[62] Hence, as the presence of dyes are still observable at a single crystal level by a confocal microscopy (vide infra), this would indicate that the dyes are mainly located within the MOF nanosheets rather than distributed on its surface.

Notably, guest@Z7-NS samples showed negligible dye leaching when suspended in MeOH for 6 months, evincing protected encapsulation in the Z7-NS framework. Moreover, to ensure the presence of the dyes within the nanosheets, we have conducted fluorescence lifetime imaging microscopy (FLIM) experiments for the single guest@Z7-NS samples (Figures S17 and S18, Supporting Information). The FLIM images show a good distribution of the fluorescent dyes over the whole nanosheets, with the emission spectra and decay lifetimes (τ) comparable to that obtained for the bulk samples (vide infra). This local scale characterization unequivocally proves the presence of the dyes in the nanosheet.

2.2. Photophysical Properties

The incorporation of dyes into the Z7-NS host enabled turn-on fluorescence of the guest in the solid state, with no indication of emission from the Z7-NS framework (Figure S19, Supporting Information) or energy transfer between the LMON and guest (**Figure 5**a,b). The emission spectral maps of F@Z7-NS and RB@Z7-NS (Figure S20, Supporting Information) systems exhibit a single emission band characteristic of F and RB. A red shift of the emission is seen with increasing guest loading, resulting in tuneable chromaticity as a function of guest loading (Figure S21, Supporting Information). This is an indication of guest aggregation as shown in other LG@MOFs systems.[46,50]

Excitation spectra and time-resolved photobehaviour obtained through picosecond time-correlated single photon counting (TCSPC) corroborate that guest molecule aggregation is a driver of these luminescent properties (Figure 5c,d; Figure S22 and Tables S2 and S3, Supporting Information). The fluorescence decays (observed at three wavelengths, upon excitation at

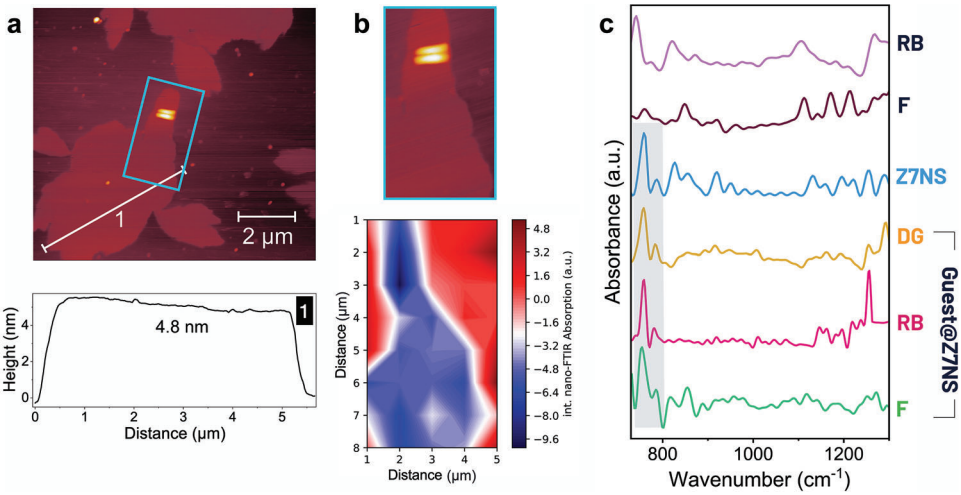

Figure 4. a) AFM topography image (above) of DG@Z7-NS with height profile showing 4.9 nm average height (below) marked by the white line labelled 1 on the image. b) Hyperspectral nano-FTIR imaging across a 2D region of DG@Z7-NS (see in AFM image above) between 725–1271 cm^{-1}. c) Nano-FTIR spectra of various Z7-NS samples.

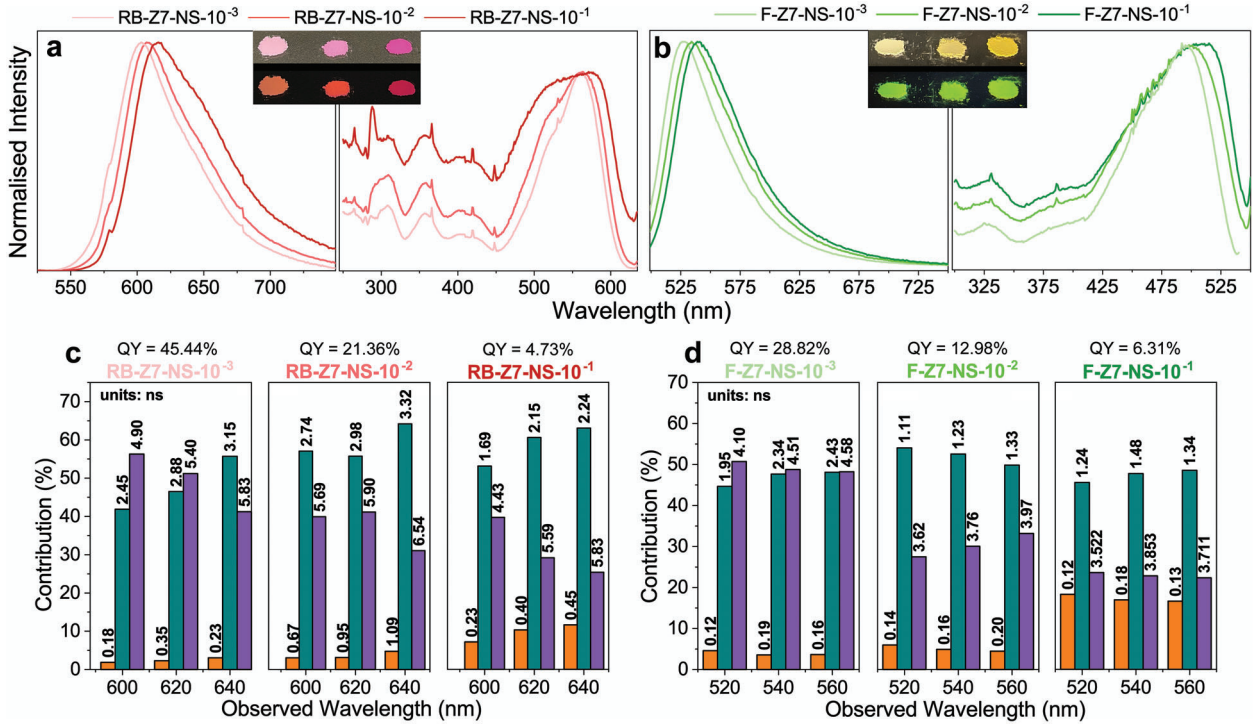

Figure 5. a,b) Emission (left) spectra of guest@Z7 materials excited at 550 nm (RB) and 485 nm (F), and excitation spectra (right) of guest@Z7-NS materials with emission of 650 nm (RB) and 550 nm (F). Inset: powders of guest@Z7-NS-10–3, guest@Z7-NS-10–2 and guest@Z7-NS-10–1 (left-right) under ambient lighting (top) and UV light (bottom). c,d) TCSPC fluorescence lifetime data and photoluminescence quantum yield (QY) of guest@Z7-NS materials across 3 observed wavelengths showing the percentage contribution c on vertical axis and τ values above columns. Orange (τ_1) = H-aggregates, green (τ_2) = J-aggregates, and purple (τ_3) = monomer species.

the maximum of the absorption intensity) of F@Z7-NS and RB@Z7-NS were fitted using a three-component exponential function giving three time constants (τ_1 = 0.16, τ_2 = 1.23, and τ_3 = 3.76 ns for F@Z7-NS at 540 nm; and τ_1 = 0.95, τ_2 = 2.98, and τ_3 = 5.90 ns for RB@Z7-NS at 620 nm) that we assign to H-aggregates (τ_1) (face-to-face), J-aggregates (τ_2) (head-to-tail), and monomers (τ_3) of F and RB, respectively. Our assignment is based on previous findings for guest@MOF systems and agrees with excitons theory.[49,50,63] Upon increasing concentration of the guest molecules, there is a reduction in contribution of the τ_3-component (monomers), while the τ_2-component (J-aggregates) exhibits minor increase proportional to guest loading. This

observation suggests an increment in J-aggregates population, which is causing a red-shift in the absorption and emission spectra as explained above. On the other hand, τ_1-component (H-aggregates) increases its contribution significantly with the guest loading, reflecting a major formation of H-aggregates. This is further supported by the growth of a shoulder band in the excitation spectrum at higher energies (470 nm for F and 515 nm for RB), and the reduction of PLQY, given emission from H-aggregates is theoretically forbidden.[49,64–66]

These data suggest a mix of monomers and J-aggregates are preferred in dilute guest@Z7-NS samples, likely packing horizontally between the sheets given our structural analysis. With increased guest concentration, more efficient packing between layers leads to aggregation, with H-aggregates being more densely packed. Moreover, our structural analysis revealed the possibility of angular guest stacking and slipped cofacial forms of the J- and H-aggregates are well reported.[65] However, a saturation point appears with RB@Z7-NS-10^{-1} evincing a large increase of H-aggregation. The emission spectra of RB@Z7-NS also present a shoulder ≈650 nm that increases in intensity with higher guest loading, most notably from the 10^{-2} to 10^{-1} samples.

Importantly, we theorize this aggregation occurs in chains, producing long-range order resulting in larger orbitals overlap, as seen in the reduced band gap caused by increasing guest loading (Figure S23, Supporting Information) and reported for other guest@MOF materials.[50] This phenomenon is more pronounced in the RB samples where emission decays are dependent on the gated spectral region, indicative of extended aggregate interactions, likely due to the molecular size of RB. Interestingly, while both RB@Z7-NS and F@Z7-NS exhibit solvatochromism in a range of common organic solvents (Figure S24, Supporting Information), solvatochromic shifts are more pronounced in F@Z7-NS (Figures S25 and S26, Supporting Information). The tighter aggregate packing and molecular size of RB may sterically hinder solvent interactions with RB guests, while in F the looser packing provides interaction sites for sensing, showing selectivity for aprotic solvents (via red-shift of emission) and polar protic solvents (higher emission intensity).

The photostability of these materials was also tested, both exhibiting good performance (Figure S27, Supporting Information). After 24 h of intense exposure to the spectrofluorometer's 150 W xenon bulb irradiating at a wavelength corresponding to each materials absorption maximum, RB@Z7-NS lost 10.5% intensity and F@Z7-NS lost 11.6% but retained chromaticity. 90% of this decrease occurred in the first 10 h, with the following 14 h plateauing to a stable intensity. This loss is comparable to F encapsulated in ZIF-8 reported materials, while F@ZIF-8 materials that exhibited surface aggregation saw over 35% intensity loss after 15 h.[49] This shows a great promise for long-term light-emitting device use of the materials.

2.3. Dual-Guest Emission Mechanism

By intercalating F and RB together in Z7-NS, at a total guest concentration below the determined saturation level for both guests, an optimized warm-yellow emitting material (DG@Z7-NS; DG = F+RB) was synthesized. Luminescence was achieved by exciting the material at the absorption intensity maximum of F (495 nm), producing an emission spectrum of two distinct but overlapping bands attributable to F (band at 525 nm) and RB (band at 580 nm, **Figure 6**a). The excitation spectra of DG@Z7-NS present two bands with intensity maxima at 495 nm (comparable to the absorption of F) and 560 nm (due to the absorption of RB dye) (Figure 6b; Figure S28, Supporting Information). Remarkably, when the excitation spectrum is recorded at 725 nm (the emission of F dye is barely existent at this wavelength) the band at 495 nm is still observable. Although RB has some absorption cross section at this wavelength, the excitation spectrum of RB@Z7-NS shows that at 495 nm, the signal is decreasing in intensity (Figure 5a; Figure S29, Supporting Information), rather than being a band maximum as for DG@Z7-NS, meaning that this is a new band not detected for RB@Z7-NS. The absorption of F has its maximum intensity at ≈495 nm (Figure 5b; Figure S29, Supporting Information), so it is logical to attribute this new band observed for DG@Z7-NS to the F dye. Additionally, at 725 nm, the excitation spectrum is recorded in a region where RB emits but F does not (Figure 5a,b). This means the excitation spectrum should be similar to the absorption spectrum of RB. However, the spectrum presents as a combination of F and RB. This indicates F is transferring the energy absorbed through photoexcitation to RB for emission in the 725 nm region. This is strong evidence that a Förster resonance energy transfer (FRET) (Figure 6c) exists from the F to RB molecules within the Z7-NS sheets.[67]

Similar behavior has been reported for FRET phenomenon occurring from MOF materials to different guests.[68] Theoretically, energy transfer is possible between F and RB guests due to the spectral overlap of the emission and absorption bands of F and RB, respectively (in the 520−540 nm region) (Figure 6e).[69] FRET is rarely observed between guest dyes in MOF systems, however, due to the lack of proximity between dye molecules, which are typically entrapped within individual pores. The tight space within the MON layers, contrastingly, favors a short distance between guest dyes, triggering the FRET mechanism.[70] Resultingly, the energy absorbed by F upon excitation is partially interconverted to the RB system, from where it is then emitted simultaneously, to produce a yellow emission; the combination of the emission from F monomers not undergoing FRET and RB (Figure 6). To confirm the energy-transfer mechanism, we physically combined F@Z7-NS with RB@Z7-NS in a 1:1 and 10:1 ratio (Figure 6a). The 1:1 ratio powder mixture shows near-yellow emission and, fascinatingly, the emission spectrum aligns with the mathematical superposition of the individual emission spectra of F@Z7-NS and RB@Z7-NS (Figure 6a). In contrast, the emission spectrum for the dual-guest system shows far greater peak overlap, with a shift of the F emission band to longer wavelengths, while the RB emission shifts to shorter ones.

FLIM experiments were also conducted to shed light on the photophysical mechanism of the DG@Z7-NS at a single crystal level. The images of several isolated MONs were collected using two band pass filters (BPF) at 520 ± 20 nm and 623 ± 25 nm to selectively record the emission of F and RB within the MONs, respectively (Figure 6d; Figure S30, Supporting Information). Remarkably, the fluorescence of both dyes is homogenous across the entire Z7-NS, illustrating the homogenous distribution (within the spatial resolution of the microscope, ≈250 nm) of the two guests throughout the ultra-thin nanosheet system. The emission spectra collected at different individual points of these

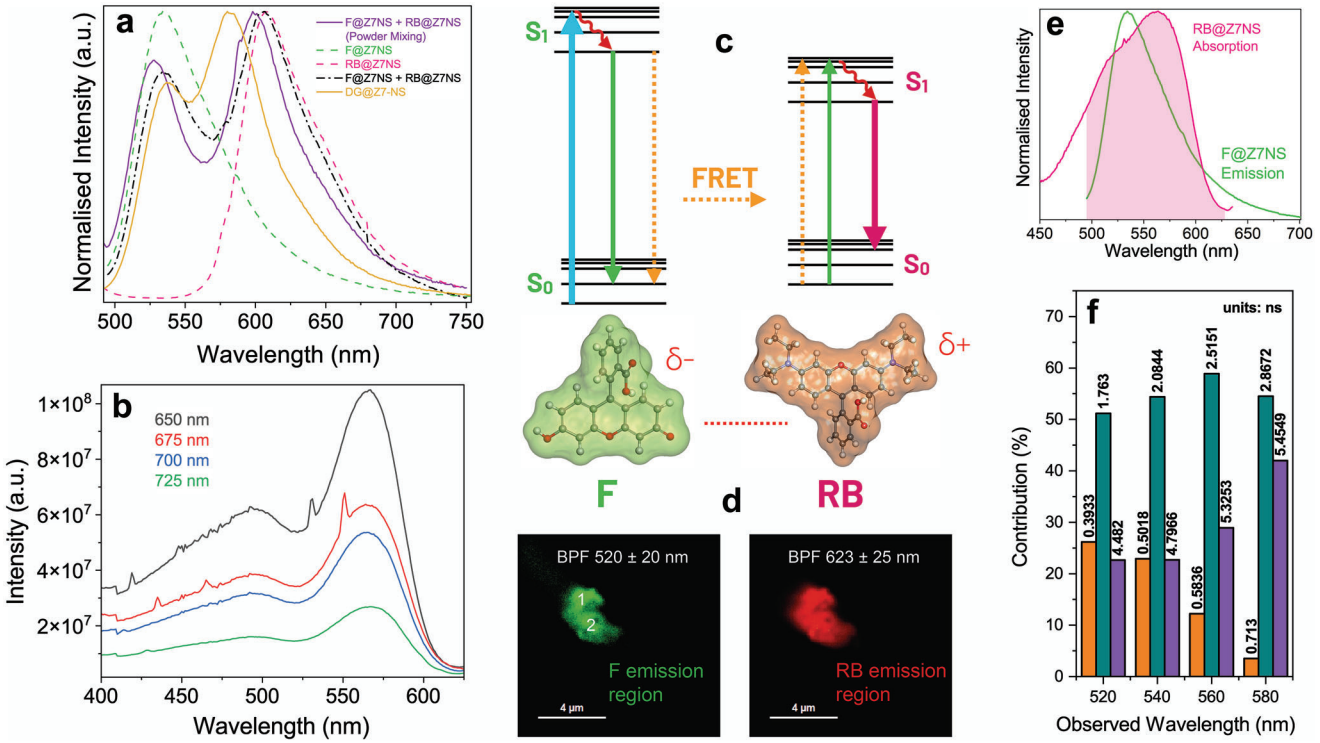

Figure 6. a) Emission spectra of DG@ZIF-7-NS (DG = F+RB) compared to various spectra related to the single-guest F or RB@Z7-NS systems. Black curve indicates mathematical superposition of F@Z7-NS + RB@Z7-NS emission spectra. b) Various excitation spectra of DG@Z7-NS recorded at indicated emission wavelengths. c) Schematic of FRET between F and RB dipole-dipole bound dimers in DG@Z7-NS. d) FLIM of DG@Z7-NS with two band pass filters (BPF) applied (left: 520 ± 20 nm and right 623 ± 25 nm). e) Absorption spectra of RB@Z7-NS overlapped with emission spectra of F@Z7-NS. f) Emission decay lifetimes. Orange (τ_1) = FRET mechanism, green (τ_2) = F, and purple (τ_3) = RB.

nanosheets closely match with the bulk observation, with two emission bands corresponding to F and RB fluorescence, confirming the phenomena identified in spectrofluorometer measurements, and which are originating from the Z7-NS samples rather than other impurities or crystallized fluorophore mixed phases.

Additionally, the fluorescence decays of bulk DG@Z7-NS were analyzed by a sum of 3-components, assigned as follows: RB (τ_3), F (τ_2) and F-RB coupled FRET mechanism (τ_1) (Figure 6f; Figures S31 and S32, Table S4, Supporting Information). τ_3 and τ_2 are assigned as such for two reasons. This first corresponds with the single-guest system monomer component lifetimes (RB@Z7-NS > F@Z7-NS). The emission lifetime of F in the dual guest system (τ_2) is largely quenched compared to F@Z7-NS, while τ_3 is comparable to RB@Z7-NS, strong evidence of a FRET mechanism. Second, as the observed wavelength varies from the E_{max} of F (≈520 nm) to RB (≈580 nm), the τ_3-component contribution increases significantly, indicating that τ_3 is the lifetime of RB. While at 520 nm RB@Z7-NS shows minimal emission (Figure 6a), the DG@Z7-NS emission spectra (Figure S33, Supporting Information) reveals a hypsochromic shift of the RB band by 30 nm, meaning the RB emission band will exist at 520 nm, allowing τ_3 to still be observable at 520–540 nm. τ_1 is greater than the typical 0.1 ns observed for the H-aggregates of the single-guest Z7-NS systems.[50] Furthermore, the contribution of τ_1 rapidly decreases as the observed wavelength increases, and therefore, it is sensible to attribute this contribution to the FRET mechanism, as it is demonstrated below for the DG@Z7-NS single particles.

The time-resolved photobehavior of the isolated thin films in FLIM also aligns with that of the bulk samples, being the emission decays analyses as a sum of three exponentials (τ_1 = 480–520 ps, τ_2 = 1.8–2.0 ns, and τ_3 = 4.6–5.0 ns when recording at 520 ± 20 nm, and τ_1 = 70–90 ps, τ_2 = 1.9–2.2 ns, and τ_3 = 4.4–5.1 ns when gating at 623 ± 25 nm, Figure S30, Supporting Information). Like our previous attribution, the longest τ_3-component, whose contribution is higher at longer wavelengths (623 ± 25 nm BPF), is assigned to the emission lifetime of the trapped RB dye. On the other hand, the τ_2-component, contributing more at the bluest region, is the emission lifetime of trapped F molecules. Finally, the shortest component is decaying in the highest energetic regions (520 ± 20 nm) but rising (negative amplitude) in the lowest ones (623 ± 25 nm), reflects a FRET from trapped F to RB dyes within the nanosheets. These types of short components decaying in the donor emission region, which become rising components in the acceptor emission region, are typical of photoinduced processes. Since at these wavelengths (623 ± 25 nm) the contribution of F to the signal is much weaker than that of RB, the rise must have its origin from the emission of RB. Hence, we attribute this rising component to the FRET from F to RB, as the photoexcitation of F is populating the excited state of RB. A comparison of the decays obtained from DG@Z7-NS and R@Z7-NS in the RB emission region (BPF of 623 ± 25 nm) (Figure S33, Supporting Information), reinforces this

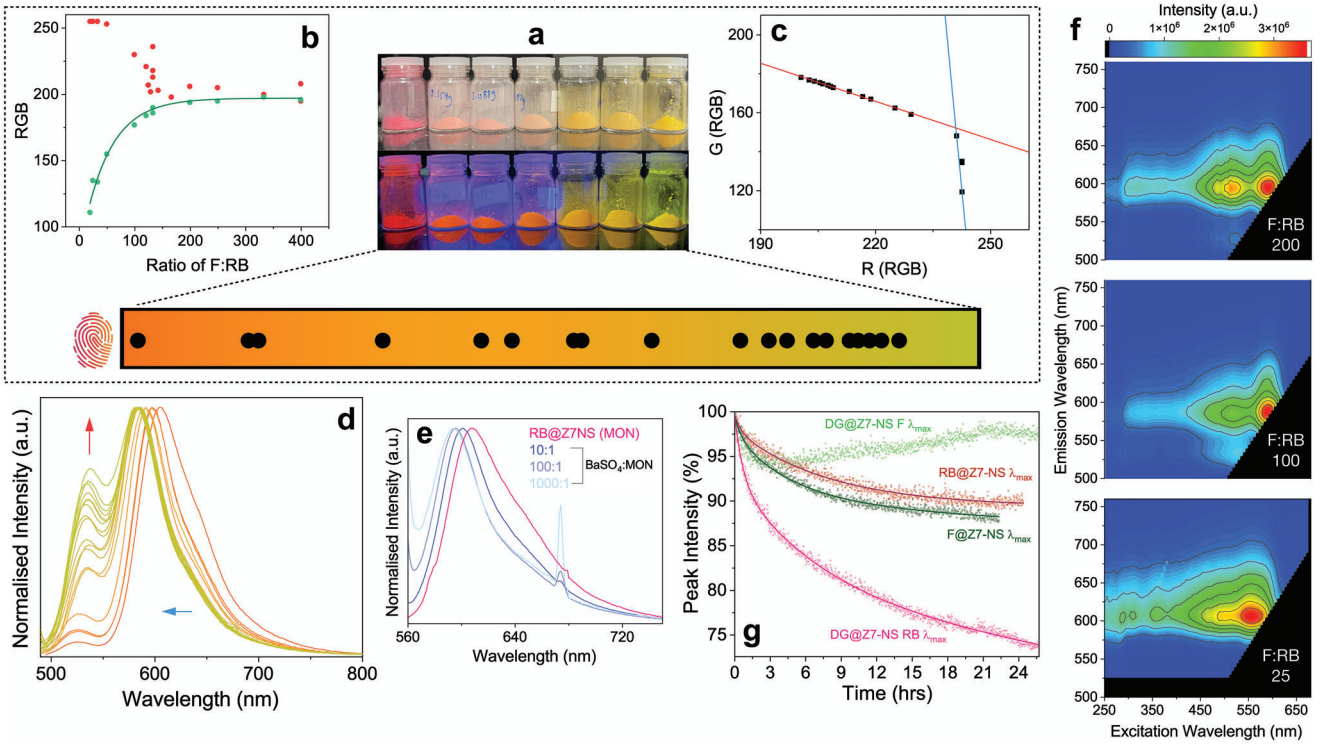

Figure 7. a) Above: selection of synthesised samples in ambient conditions (top) and under UV (bottom), below: predicted finite spectrum of emission chromaticity for DG@Z7-NS derived from correlations, the "emission chromaticity fingerprint", with emission chromaticity of synthesised samples indicated along the spectrum as black dots. b) Correlation between synthesis ratio of F:RB and RGB of emission chromaticity. c) R value of DG@Z7-NS materials correlated with G value (of RGB coordinates, derived from the emission spectra). d) Emission spectra of various DG@Z7-NS samples excited at 470 nm; colours of each spectrum line indicate that sample's emission chromaticity RGB value. e) Emission spectra of RB@Z7-NS when mixed with various ratios of $BaSO_4$. f) Emission-excitation maps of three DG@Z7-NS samples at an F:RB ratio of 25, 100, and 200 (bottom to top). g) Photostability of various guest@Z7-NS samples as a percentage of maximum absorption peak intensity over 24 h with continuous exposure to respective sample Abs_{max}.

finding by presenting a clear rise only in the decay obtained for DG@Z7-NS.

2.4. Tuning the Dual-Guest System

By varying the concentration of F during synthesis of the samples (Table S4 and Figure S28, Supporting Information), a subset of twenty samples of DG@Z7-NS were obtained with distinct emission chromaticity coordinates (**Figure 7**a; Figures S34 and S35, Table S5, Supporting Information). Significantly, the chromaticity of the system can be accurately quantified – allowing for precise fine-tuning of the emission color of DG@Z7-NS. Upon plotting the synthesis ratio of F:RB against the RGB (red-green-blue) values of each sample (Figure 7b), a good logarithmic correlation ($R^2 = 0.997$) was obtained between the F:RB concentration and the G value. Then, when comparing the G value to R value (Figure 7c), we see two clear linear correlations with distinct domains ($R^2 = 0.996$). Together, these data can be used to identify the final emission color of a dual-guest Z7-NS sample based simply on the ratio of F:RB used in the synthetic procedure. If a particular color from green to red is desired, the ratio can be computed using Equations (1) and (2). It is remarkable and of greatest significance is that this relationship confirms that there is only a discrete subset of colors (a "emission chromaticity fingerprint") attainable by this dual-guest system: those that lie on the two G:R correlations (Figure 7c), seen in the spectrum bar of Figure 7a.

$$\textit{Green value}\,(G) = \frac{80.69604}{\left(1 + 1.29\mathrm{E}^{-4} \times \textit{Synthesis Ratio of } F:RB\right)^{155.76324}} \quad (1)$$

$$\textit{Red value}\,(R) = \begin{cases} \dfrac{G - 5721}{-22}, & G < 170 \\ \dfrac{G - 338.15548}{-0.70008}, & G \geq 170 \end{cases} \quad (2)$$

Equations 1 and 2. Quantitative determination of DG@Z7-NS chromaticity based on ratio of F:RB used in the material's synthesis. The empirical coefficients were derived from Figure 7(b) and 7(f) (inset).

The photophysical properties of the dual-guest materials were explored to determine the causes driving these chromaticity findings (Figure 7; Figures S36 and S37, Supporting Information). The spectral changes across the emission spectra of all 20 samples (Figure 7d) also exhibit two clear processes occurring when the concentration of F increases in the system, with high-energy

bands in the excitation spectra vary in similar stages. In the initial phase of 25 to 125 F:RB ratios, there is a blue shift of the RB system along with suppression of a shoulder band identifiable at ≈650 nm. This corresponds to the first steep linear correlation in the R:G chromaticity relationship, with a dramatic increase of F emission with minimal RB value increase. By systematic mixing of the single-guest RB@Z7-NS sample with $BaSO_4$ in increasing ratios as shown in Figure 7e, we suggest that these changes to be a cause of steric hindrance in the system. As the ratio increased from 10:1 to 1000:1, we saw a blueshift of emission peak, and the suppression of a shoulder at ≈650 nm. As more salt crystals were added to RB@Z7-NS, we reasoned that a greater disturbance develops between Z7-NS crystals or even within the layers of sheets in single crystals. This will interfere with long-range interactions that we commented on before and that exists in the RB-Z7 system, particularly the J-aggregates responsible for the shoulder at 650 nm. The result is a general destabilization of the system, and therefore a blue-shifted emission. The same measurement done with F resulted in very minimal shift and spectral shape variance comparably (Figure S38, Supporting Information).

The first process ceases once a ratio of ≈125 is reached, after that the second process dominates: the growth and narrowing of an emission band from F. The change in spectral patterns is most visible when comparing three emission maps (Figure 7f), measured at samples with F:RB ratios of 25, 100 and 200, where a sharpening of emission bands is seen and the growth of a second local maxima at the absorption intensity maxima of fluorescein. Indeed, after the isosbestic point at the R value of 242 in the G:R correlation (Figure 7c) a more subtle linear process also controls this relationship. As shown by the minimal shift from 1000:1 to 100:1 of $BaSO_4$:RB@Z7-NS (Figure 7e), there reaches an equilibrium where steric hindrance no longer affects the energetics. From here, the second process dominates, being the increased emission from fluorescein and the interaction between F and RB molecules as observed in the optimized warm yellow-emitting sample (DG@Z7-NS).

Together, these data reveal that the competitive emission pathways within DG@Z7-NS dictate emission chromaticity. In further support of this are photostability measurements of DG@Z7-NS over 24 h (Figure 7g; Figure S39, Supporting Information). Both guests' decay at rates akin to the single-guest NS systems for the first 3 h, but after the F band begins to intensify as RB continues to diminish. We attribute this to the photodegradation of RB monomers resulting in the reduction of F-RB energy transfer systems. This allows for increased emission from F monomers alone without absorption by RB. This continues until 21.5 h, after that both guests appear to decay at a consistent rate evinced by proportional peak intensity loss in emission spectra. Importantly, always, yellow emission chromaticity is maintained (Figure S39, Supporting Information).

3. Conclusions

This work has demonstrated a new versatile concept for functionalizing 2D MON systems via intercalation of guests. The concept is achieved by the first in situ bottom-up synthesis of Z7-NS using a facile salt-templating methodology. This bottom-up approach produces highly stable, homogenous nanosheets that dispersed without aggregation in solution, and maintain dimensions of a few-layer thickness (*ca.* 2–3 nm) while extended 5×15 μm^2 in plane. The selection and trapping of two fluorophores resulted in two single-guest LMONs, both exhibiting strong fluorescence controllable by guest loading concentration that affects guest packing and aggregation. Importantly, the systems show long-term physicochemical stability with a high resistance to leaching. Ultimately, we showed that combining two guests can result in a warm yellow emitting dual-guest intercalated MON that maintains the structural stability and nanosheet morphology of the single-guest systems. The system allows for an enhanced dual-guest energy-transfer interaction and, most remarkably, emission chromaticity that could be quantified so that tuneability became a precisely predictable process. This realization that emission chromaticity is limited to a discrete subset of RGB values presents a strong theoretical foundation for rationally designing future LMON systems. By modelling predicted energetics of the dyes, followed by mapping a sample synthesis, it is possible to design systems of discrete color ranges, with a priori "emission chromaticity fingerprints", ideal for a range of nanophotonic applications from sensing to lighting, layered semi-conductors, product quality assurance and covert security tags.

4. Experimental Section

Synthesis of ZIF-7-III Nanosheets (Z7-NS): $Zn(NO_3)_2$ (59.5 mg, 0.2 mmol) was dissolved in methanol (MeOH) (2 mL). The solution was then added to a conical flask containing NaCl powder (20 g) under vigorous magnetic stirring. After 20 min, benzimidazole (bIm) (283.5 mg, 2.4 mmol) was then dissolved in MeOH (2 mL). The solution was added dropwise to the conical flask followed by vigorous mixing for 12 h. Deionised H_2O (250 mL) was then added to the flask and heated to 100 °C while stirring. The mixture was then siphoned into 50 mL centrifuge tubes and centrifuged at 10000 rpm for 25 min. The collected powder at the bottom of each tube was combined into one tube, followed by further washing and centrifuging cycles (3 × 45 mL H_2O and 5 × 40 mL MeOH). The final product was dried in the tube for 1 h at 90 °C in an oven (≈70%–80% yield).

Samples characterized by AFM, nano-FTIR, FE-SEM and TEM were prepared by adding 5 mg of Z7-NS in a vial with 10 mL of MeOH. The vial was sonicated for 1 min to disperse the Z7-NS before drop casting the solution onto the sample substrate. To obtain particle size separation, after 24 h, the solution was pipetted from the centre or base of the vial depending on preferred particle morphology.

Synthesis of Guests@Z7-NS Materials: The synthesis above was repeated except that initially Fluorescein (F) or Rhodamine B (RB) (0.003 mmol, 0.0003 mmol or 0.03 mmol) were solubilized with MeOH (2 mL) via sonication. This solution was mixed with the bIm solution before then adding to the $Zn(NO_3)_2$@NaCl vial.

Synthesis of ZIF-7-III: ZIF-7-III was synthesized via an adapted protocol by Peng et al.[33] Synthesis of ZIF-7 (I): DMF (100 mL) was added to a mixture of $Zn(NO_3)_2 \bullet 6H_2O$ (303 mg) and bIm (770 mg). After stirring for 1 h, the solution was kept at room temperature for 96 h. The formed ZIF-7 crystals were collected by centrifugation and washed with MeOH (5×50 mL). The wet product was dried at 50 °C for 8 h and then at 120 °C for 48 h in a vacuum oven.

ZIF-7-III: the obtained ZIF-7 crystals were dispersed in distilled water at a concentration of 0.5 wt.% and then refluxed at 100 °C for 24 h. The resulting turbid dispersion was filtered and washed with distilled water (3×50 mL) and MeOH (4×50 mL). The product was dried at 50 °C for 12 h to form the layered product $Zn_2(bim)_4$.

Powder X-Ray Diffraction: Powder x-ray diffraction (PXRD) patterns were collected using a Rigaku MiniFlex diffractometer equipped with a Cu Kα source and step size of 0.0025° at a scan rate of 0.04° min^{-1}. Sam-

ples were prepared using a 0.1 mm shallow well sample holder. High-resolution XRD patterns were collected at the Diamond Light Source I11 beamline using the MAC detection system. Calibrations were performed using Si powder standard (NIST SRM640c), with an X-ray beam energy of 15 keV (0.826834(10) Å) and scan time of 3600 s. Samples were prepared in borosilicate glass capillaries of 0.5 mm diameter. *d*-spacing was calculated using Bragg's Law.

Attenuated Total Reflectance Fourier Transform Infrared Spectroscopy: Attenuated Total Reflectance Fourier Transform Infrared Spectroscopy (ATR-FTIR) measurements of bulk Z7 and Z7-NS materials were performed using a Nicolet iS10 FTIR spectrometer. High-resolution synchrotron radiation infrared (SR-IR) measurements of the mid-IR and far-IR (FIR) spectra were performed at the Diamond Light Source B22 MIRIAM beamline. FIR and MIR spectra were collected under vacuum, using the ATR module installed on the Bruker Vertex 80 V FTIR bench equipped with the DLaTGS detector. For improved signal-to-noise ratio, liquid helium-cooled bolometer was used in FIR measurements.

Nano-FTIR: Near-field optical measurements were collected using the neaSNOM instrument (neaspec GmbH) based on a tapping-mode AFM. The platinum-coated tip (NanoAndMore GmbH, cantilever resonance frequency 250 kHz and nominal tip radius ≈20 nm) was illuminated by a Toptica broadband mid-infrared (MIR) femtosecond laser. Individual crystals of Z7 and Z7-NS type materials were analyzed by averaging 4 measurements with 18 individual point spectra each. For each sample, at least 10 unique crystals or regions were probed. Each spectrum was acquired from an average of 20 Fourier-processed interferograms with 10 cm^{-1} spectral resolution, 2048 points per interferogram, and an 18-ms integration time. The sample spectrum was normalized to a reference spectrum measured on a silicon surface to reconstruct the final nano-FTIR amplitude and phase. The continuous broadband MIR spectra were attained by combining two illumination sources, then the obtained spectra were combined at 1500 cm^{-1}. All measurements were carried out under ambient conditions (≈40% RH).

Raman Spectroscopy: Raman spectra were collected using the Bruker MultiRAM Raman spectrometer with sample compartment D418, equipped with a Nd-YAGlaser (1064 nm) and a LN-Ge diode as a detector. The laser power used for sample excitation was 50 mW, and 64 scans were accumulated at a resolution of 1 cm^{-1}.

Thermogravimetric Analysis: Thermogravimetric analysis (TGA) was performed using a TA Instruments Q50 TGA machine equipped with a platinum sample holder under an N_2 inert atmosphere at a heating rate of 10°C min^{-1} from 30 to 800 °C.

Atomic Force Microscopy: Atomic force microscopy (AFM) imaging was performed with a neaSNOM instrument (neaspec GmbH) operating in tapping mode. Height topography images were collected using the Scout350 probe (NuNano), which has a nominal tip radius of 5 nm, a spring constant of 42 N m^{-1} and resonant frequency of 350 kHz.

Scanning Electron Microscopy: Backscattered electron and secondary electron scanning electron microscopy (SEM) images were obtained at 10 keV under high vacuum using a SEM Tescan Lyra 3 (Tescan, Czech Republic) with secondary and backscattered electron imaging (SEI and BSE respectively) using a voltage from 10 to 15 keV. Samples were drop cast onto silicon wafer or a polished aluminium specimen stub that was coated with gold (Au) with a thickness of 25 nm using SC7620 sputter coater (Quorum Technologies) at 20 mA plasma current for 3 min.

Spectrofluorimetric Measurements: Steady–state fluorescence spectra, steady–state diffuse reflectance spectra, photoluminescence quantum yield (PLQY), and TCSPC emission decay data were recorded using the FS-5 spectrofluorometer (Edinburgh Instruments) equipped with the appropriate modules for each specific experiment. For TCSPC measurements, the samples were pumped with a 365 nm EPLED picosecond pulsed laser source. Lifetime fitting of the time constants from decay data was performed using the Fluoracle software. Excitation spectra exhibit artefacts (sharp peaks) from equipment operation that were not removed in presented data.

Fluorescence Lifetime Imaging: Fluorescence lifetime images (FLIM) were recorded using an inverted-type scanning confocal fluorescence microscope (MicroTime-200, Picoquant, Berlin) with a 60× NA1.2 Olympus water immersion objective, and a 2D piezo scanner (Physik Instrumente). A 470-nm pulsed diode laser (pulse width ≈40 ps) was employed as the excitation source. A dichroic mirror (AHF, Z375RDC), a 500-nm long-pass filter (AHF, HQ500lp), a 100-µm pinhole, and an avalanche photodiode detector (MPD, PDM series) were used to collect the emission. Moreover, the FLIM and emission decays of the DG@Z7-NS sample were collected using two band pass filters (520 ± 20 and 623 ± 25 nm) to selectively record the emission region of F and RB, respectively. The emission spectrum was recorded using a spectrograph (Andor SR 303i-B) equipped with a 1600×200 pixels EMCCD detector (Andor Newton DU-970N-BV) coupled to the Micro-Time-200 system.

Transmission Electron Microscopy: Transmission electron microscopy (TEM) characterization was performed at 200 keV accelerating voltage using a LaB_6 electron source using a JEM-2100 electron microscope. The images were recorded on a Gatan Orius camera through Digital Micrograph.

Nuclear Magnetic Resonance Guest Loading Analysis: Samples for nuclear magnetic resonance (NMR) were dissolved in a solution composed of 500 µL methanol-d4 and 50 µL DCl/D_2O (35 wt.%). All NMR spectroscopy was done at 298 K using a Bruker AvanceIII spectrometer operating at 600 MHz, equipped with a BBO cryoprobe. Data were collected using a relaxation delay of 20 s, with 128 k points and a sweep width of 19.8 ppm, giving a digital resolution of 0.18 Hz. Data was processed using Bruker Topspin with a line broadening of 1 Hz and 2 rounds of zero-filling. The loading amount was calculated from the molar ratio of compound to bIm. To calculate the molar ratio, peaks corresponding to each compound were integrated and normalized according to the number of protons giving rise to the signal. For fluorescein (F), the doublet at ≈8.30 ppm was used, which corresponds to a single proton (that in the ortho position relative to the carboxyl group). For Rhodamine B (RB) the broad multiplet at ≈8.22 ppm was used, which corresponds to the equivalent single proton in the ortho position relative to the carboxyl group. For benzimidazole the singlet at ≈9.33 ppm was used, which corresponds to the single proton of the imidazole group, adjacent to the two nitrogens. Global spectral deconvolution (in the MestReNova software package) was used to pick and integrate the peaks.

Supporting Information

Supporting Information is available from the Wiley Online Library or from the author.

Acknowledgements

D.A.S. acknowledges the scholarships from the General Sir John Monash Foundation and the Clarendon Fund. J.C.T. and S.M. thank the ERC Consolidator Grant (PROMOFS 771575) and EPSRC (EP/R511742/1) for funding the research. M.G. and A.D. were supported by grants PID2020-116519RB-I00 and TED2021–131650B–I00 funded by MCIN/AEI/10.13039/501100011033 and by the EU; SBPLY/19/180501/000212 and SBPLY/21/180501/000108 funded by JCCM and by the EU through "Fondo Europeo de Desarollo Regional" (FEDER). The authors acknowledge the Diamond Light Source for the provision of beamtime SM27504 at B22 MIRIAM via Drs. Mark Frogley and Gianfelice Cinque, and rapid access beamtime CY29415 at I11 via Dr. Sarah Day. The authors would like to acknowledge Dr. Cyril Besnard and Professor Alexander Korsunsky for the acquisition of the FESEM images. The authors thank the Research Complex at Harwell (RCaH) for access to materials characterization facilities.

Conflict of Interest

The authors declare no conflict of interest.

Author Contributions

Conceptualization was done by D.S and J.-C.T. Methodology was developed by D.S. Synthesis was performed by D.S. AFM, PXRD, nano-FTIR, FIR, MIR and FS-5 spectrofluorimetric measurements were performed by D.A.S. SEM characterization was performed by C.B. and D.S. TEM characterization was performed by I.G. with analysis of the data by D.A.S. FLIM experiments were performed and analyzed by M.G. and A.D. NMR was performed by N.A. TGA, band gap and Raman data was collected by S.M, analysis performed by D.A.S. Manuscript was drafted by D.A.S, with review and editing by D.A.S., M.G., A.D. and J.-C.T. Supervision by J.-C.T.

Data Availability Statement

The data that support the findings of this study are available in the supplementary material of this article.

Keywords

Förster resonance energy transfer, light-emitting materials, metal-organic frameworks, metal-organic nanosheets, optics, fluorescence

Received: December 7, 2022
Revised: June 6, 2023
Published online:

[1] J. Nicks, K. Sasitharan, R. R. R. Prasad, D. J. Ashworth, J. A. Foster, *Adv. Funct. Mater.* **2021**, *31*, 2103723.
[2] D. J. Ashworth, J. A. Foster, *J. Mater. Chem. A* **2018**, *6*, 16292.
[3] M. Zhao, Y. Huang, Y. Peng, Z. Huang, Q. Ma, H. Zhang, *Chem. Soc. Rev.* **2018**, *47*, 6267.
[4] N. K. Chaudhari, H. Jin, B. Kim, D. San Baek, S. H. Joo, K. Lee, *J. Mater. Chem. A* **2017**, *5*, 24564.
[5] H. Yin, Z. Tang, *Chem. Soc. Rev.* **2016**, *45*, 4873.
[6] W.-J. Ong, L.-L. Tan, Y. H. Ng, S.-T. Yong, S.-P. Chai, *Chem. Rev.* **2016**, *116*, 7159.
[7] C. Tan, X. Cao, X. J. Wu, Q. He, J. Yang, X. Zhang, J. Chen, W. Zhao, S. Han, G. H. Nam, M. Sindoro, H. Zhang, *Chem. Rev.* **2017**, *117*, 6225.
[8] J. C. Tan, P. J. Saines, E. G. Bithell, A. K. Cheetham, *ACS Nano* **2012**, *6*, 615.
[9] Z. Zeng, I. S. Flyagina, J.-C. Tan, *Nanoscale Adv* **2020**, *2*, 5181.
[10] Y. Peng, W. Yang, *Adv. Mater. Interfaces* **2019**, *7*, 1901514.
[11] X. Chen, T. Zhang, S. Liu, H. Wen, L. Chen, *IOP Conf. Ser.: Earth Environ. Sci.* **2018**, *170*, 052040.
[12] J. Liu, X. Song, T. Zhang, S. Liu, H. Wen, L. Chen, *Angew Chem Int Ed Engl* **2020**, *60*, 5612.
[13] H. L. Zhu, D. X. Liu, *J. Mater. Chem. A* **2019**, *7*, 21004.
[14] D. Zhu, M. Qiao, J. Liu, T. Tao, C. Guo, *J. Mater. Chem. A* **2020**, *8*, 8143.
[15] C. Tan, G. Liu, H. Li, Y. Cui, Y. Liu, *Dalton Trans.* **2020**, *49*, 11073.
[16] Y. Peng, W. Yang, *Sci China Chem* **2019**, *62*, 1561.
[17] R. Banerjee, A. Phan, B. Wang, C. Knobler, H. Furukawa, M. O'Keeffe, O. M. Yaghi, *Science* **2008**, *319*, 939.
[18] Q.-F. Yang, X.-B. Cui, J.-H. Yu, J. Lu, X.-Y. Yu, X. Zhang, J.-Q. Xu, Q. Hou, T.-G. Wang, *CrystEngComm* **2008**, *10*, 1534.
[19] P. Zhao, G. I. Lampronti, G. O. Lloyd, M. T. Wharmby, S. Facq, A. K. Cheetham, S. A. Redfern, *Chem. Mater.* **2014**, *26*, 1767.
[20] H. L. Liu, Y. J. Chang, T. Fan, Z. Y. Gu, *Chem. Commun.* **2016**, *52*, 12984.
[21] Y. Peng, Y. Li, Y. Ban, W. Yang, *Angew. Chem. Int. Ed. Engl.* **2017**, *56*, 9757.
[22] W. M. Liao, J. H. Zhang, S. Y. Yin, H. Lin, X. Zhang, J. Wang, H. P. Wang, K. Wu, Z. Wang, Y. N. Fan, M. Pan, C. Y. Su, *Nat. Commun.* **2018**, *9*, 2401.
[23] N. Contreras-Pereda, P. Hayati, S. Suarez-Garcia, L. Esrafili, P. Retailleau, S. Benmansour, F. Novio, A. Morsali, D. Ruiz-Molina, *Ultrason. Sonochem.* **2019**, *55*, 186.
[24] Y. Fan, J. Zhang, Y. Shen, B. Zheng, W. Zhang, F. Huo, *Nano Res.* **2021**, *14*, 1.
[25] Y. Zhao, L. Jiang, L. Shangguan, L. Mi, A. Liu, S. Liu, *J. Mater. Chem. A* **2018**, *6*, 2828.
[26] Z. Hu, E. M. Mahdi, Y. Peng, Y. Qian, B. Zhang, N. Yan, D. Yuan, J.-C. Tan, D. Zhao, *J. Mater. Chem. A* **2017**, *5*, 8954.
[27] T. Rodenas, I. Luz, G. Prieto, B. Seoane, H. Miro, A. Corma, F. Kapteijn, I. X. F. X. Llabres, J. Gascon, *Nat. Mater.* **2015**, *14*, 48.
[28] S. C. Junggeburth, L. Diehl, S. Werner, V. Duppel, W. Sigle, B. V. Lotsch, *J. Am. Chem. Soc.* **2013**, *135*, 6157.
[29] M. Zhao, Y. Wang, Q. Ma, Y. Huang, X. Zhang, J. Ping, Z. Zhang, Q. Lu, Y. Yu, H. Xu, Y. Zhao, H. Zhang, *Adv. Mater.* **2015**, *27*, 7372.
[30] L. Huang, X. Zhang, Y. Han, Q. Wang, Y. Fang, S. Dong, *J. Mater. Chem. A* **2017**, *5*, 18610.
[31] K. Zhao, S. Liu, G. Ye, X. Wei, Y. Su, W. Zhu, Z. Zhou, Z. He, *Chem. Sus. Chem.* **2020**, *13*, 1556.
[32] D. Liu, B. Liu, C. Wang, W. Jin, Q. Zha, G. Shi, D. Wang, X. Sang, C. Ni, *ACS Sustainable Chem. Eng.* **2020**, *8*, 2167.
[33] Y. Peng, Y. S. Li, Y. J. Ban, H. Jin, W. M. Jiao, X. L. Liu, W. S. Yang, *Science* **2014**, *346*, 1356.
[34] L. Huang, Z. Hu, H. Jin, J. Wu, K. Liu, Z. Xu, J. Wan, H. Zhou, J. Duan, B. Hu, J. Zhou, *Adv. Funct. Mater.* **2020**, *30*, 1908486.
[35] B. Yan, W. Zhang, X. Qin, Y. Choi, G. Diao, X. Jin, Y. Piao, *Chem. Eng. J.* **2020**, *400*, 125895.
[36] Q. Q. Xia, X. H. Wang, J. L. Yu, Z. Y. Xue, J. Chai, M.-X. Wu, X. Liu, *Dalton Trans.* **2022**, *51*, 9397.
[37] Z. J. Li, X. Y. Li, Y. T. Yan, L. Hou, W. Y. Zhang, Y. Y. Wang, *Cryst. Growth Des.* **2018**, *18*, 2031.
[38] M. D. Allendorf, C. A. Bauer, R. K. Bhakta, R. J. T. Houk, *Chem. Soc. Rev.* **2009**, *38*, 1330.
[39] H. Xu, J. Gao, X. Qian, J. Wang, H. He, Y. Cui, Y. Yang, Z. Wang, G. Qian, *J. Mater. Chem. A* **2016**, *4*, 10900.
[40] R. A. Natour, Z. K. Ali, A. Assoud, M. Hmadeh, *Inorg. Chem.* **2019**, *58*, 10912.
[41] W. W. Zhao, J. L. Peng, W. K. Wang, S. J. Liu, Q. Zhao, W. Huang, *Coord. Chem. Rev.* **2018**, *377*, 44.
[42] Q. Jiang, C. Zhou, H. Meng, Y. Han, X. Shi, C. Zhan, R. Zhang, *J. Mater. Chem. A* **2020**, *8*, 15271.
[43] Y. Zhu, X. Sun, Y. Tang, L. Fu, Y. Lu, *Nano Res.* **2020**, *14*, 1912.
[44] J. Tang, Z. Liang, M. Huang, S. Su, Y. Wen, Q.-L. Zhu, X. Wu, *J. Mater. Chem. C* **2021**, *9*, 14628.
[45] B. B. Guo, J. C. Yin, N. Li, Z. X. Fu, X. Han, J. Xu, X. H. Bu, *Adv. Opt. Mater.* **2021**, *9*, 2100283.
[46] M. Gutierrez, Y. Zhang, J. C. Tan, *Chem. Rev.* **2022**, *122*, 10438.
[47] M. J. T. Snare, F. E. Treloar, K. P. Ghiggino, P. J. Thistlethwaite, *J. Photochem.* **1982**, *18*, 335.
[48] R. N. Sjöback, J. Nygren, M. Kunista, *Spectrochim. Acta* **1995**, *51*, L7.
[49] T. Xiong, Y. Zhang, L. Donà, M. Gutiérrez, A. F. Möslein, A. S. Babal, N. Amin, B. Civalleri, J.-C. Tan, *ACS Appl. Nano Mater.* **2021**, *4*, 10321.
[50] Y. Zhang, M. Gutierrez, A. K. Chaudhari, J. C. Tan, *ACS Appl. Mater. Interfaces* **2020**, *12*, 37477.
[51] A. K. Chaudhari, J. C. Tan, *Adv. Opt. Mater.* **2020**, *8*, 1901912.
[52] A. K. Chaudhari, H. J. Kim, I. Han, J. C. Tan, *Adv. Mater.* **2017**, *29*, 1701463.
[53] R. Xu, Y. Wang, X. Duan, K. Lu, D. Micheroni, A. Hu, W. Lin, *J. Am. Chem. Soc.* **2016**, *138*, 2158.
[54] C. He, K. Lu, W. Lin, *J. Am. Chem. Soc.* **2014**, *136*, 12253.

[55] D. Saliba, M. Al-Ghoul, *Philos. Trans. A Math Phys. Eng. Sci.* **2016**, *374*, 20160138.
[56] U. Riaz, S. M. Ashraf, S. Kumar Saroj, M. Zeeshan, S. Jadoun, *RSC Adv.* **2016**, *6*, 34534.
[57] R. Gao, D. Yan, X. Duan, *Cell Rep. Phys. Sci.* **2021**, *2*, 100536.
[58] M. Hirose, F. Ito, T. Shimada, S. Takagi, R. Sasai, T. Okada, *Langmuir* **2017**, *33*, 13515.
[59] X. Xiao, H. Song, S. Lin, Y. Zhou, X. Zhan, Z. Hu, Q. Zhang, J. Sun, B. Yang, T. Li, L. Jiao, J. Zhou, J. Tang, Y. Gogotsi, *Nat. Commun.* **2016**, *7*, 11296.
[60] Y. Zhang, Z. Teng, Q. Ni, J. Tao, X. Cao, Y. Wen, L. Wu, C. Fang, B. Wan, X. Zhang, G. Lu, *ACS Appl. Mater. Interfaces* **2020**, *12*, 57810.
[61] M. R. Ryder, B. Civalleri, T. D. Bennett, S. Henke, S. Rudic, G. Cinque, F. Fernandez-Alonso, J. C. Tan, *Phys. Rev. Lett.* **2014**, *113*, 215502.
[62] A. F. Möslein, M. Gutierrez, B. Cohen, J. C. Tan, *Nano Lett.* **2020**, *20*, 7446.
[63] M. Kasha, *Discuss. Faraday Soc.* **1950**, *9*, 14.
[64] B. Heyne, *Photochem. Photobiol. Sci.* **2016**, *15*, 1103.
[65] N. J. Hestand, F. C. Spano, *Chem. Rev.* **2018**, *118*, 7069.
[66] D. Setiawan, A. Kazaryan, M. A. Martoprawiro, M. Filtaov, *Phys. Chem. Chem. Phys.* **2010**, *12*, 11238.
[67] T. Förster, *Ann. Phys.* **1948**, *437*, 55.
[68] M. Gutiérrez, F. Sáncheze, A. Douhal, *J. Mater. Chem. C* **2015**, *3*, 11300.
[69] J.-X. Wang, J. Yin, O. Shekhah, O. M. Bakr, M. Eddaoudi, O. F. Mohammed, *ACS Appl. Mater. Interfaces* **2022**, *14*, 9970.
[70] H. Sahoo, *J Photochem Photobiol* **2011**, *12*, 20.

Statement of Authorship for joint/multi-authored papers for PGR thesis

To appear at the end of each thesis chapter submitted as an article/paper

The statement shall describe the candidate's and co-authors' independent research contributions in the thesis publications. For each publication there should exist a complete statement that is to be filled out and signed by the candidate and supervisor **(only required where there isn't already a statement of contribution within the paper itself).**

Title of Paper	Guest Entrapment in Metal-Organic Nanosheets for Quantifiably Tuneable Luminescence
Publication Status	☑ **Published** ☐ Accepted for Publication ☐ Submitted for Publication ☐ Unpublished and unsubmitted work written in a manuscript style
Publication Details	**D. A. Sherman**, M. Gutiérrez, I. Griffiths, S. Mollick, N. Amin, A. Douhal, J.-C. Tan, "Guest Entrapment in Metal-Organic Nanosheets for Quantifiably Tuneable Luminescence", *Advanced Functional Materials*, 33, 2214307 (2023).

Student Confirmation

Student Name:	Dylan A. Sherman		
Contribution to the Paper	D.A.S: conceptualization, methodology, synthesis, data collection (unless stated otherwise below), all data analysis, first draft manuscript, review and editing. D.A.S and C.B: FE-SEM data collection by collaboration (equipment operated by C.B.). I.G.: TEM data collection. M.G. and A.D.: FLIM data collection and contributions to data analysis. N.A.: NMR digest data collection. S.M.: TGA, Raman, and UV-Vis absorption data collection. M.G., A.D., and J.-C.T.: manuscript review and editing. J.-C.T.: supervision. Note: 'by collaboration' indicates D.A.S was present and participating in data collection.		
Signature		Date	1/10/2024

Supervisor Confirmation

By signing the Statement of Authorship, you are certifying that the candidate made a substantial contribution to the publication, and that the description described above is accurate.

Supervisor name and title:	Prof. J. C. Tan		
Supervisor comments	I support this application.		
Signature		Date	1 Oct 2024

This completed form should be included in the thesis, at the end of the relevant chapter.

3.7 Paper II

Stable photoinduced metal-organic nanosheet blue phosphor for white light emission

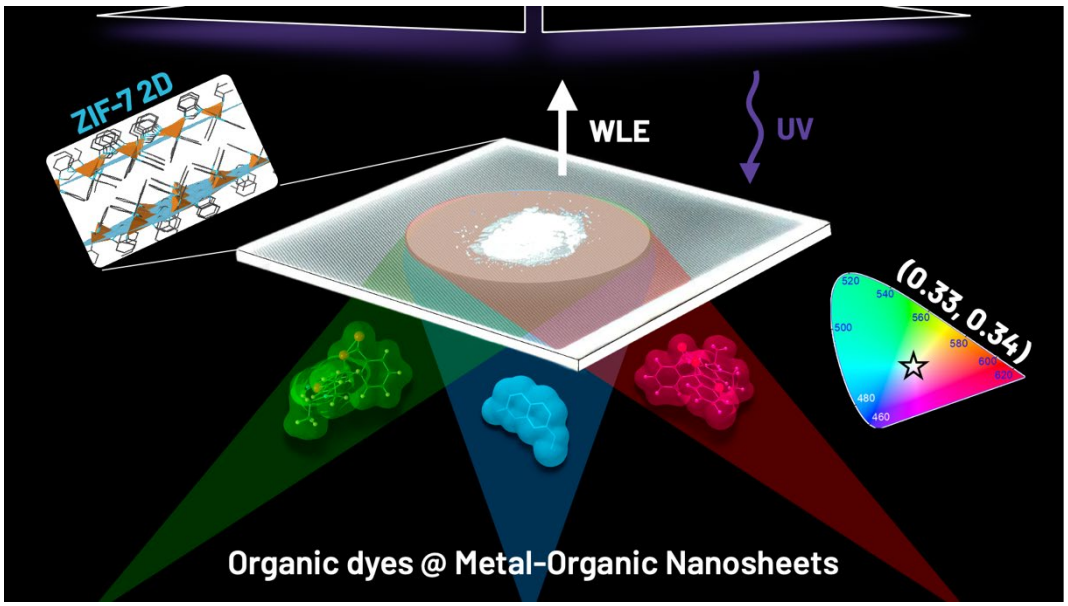

Figure 3.19. Illustration of RB (red), F (green), and MC (blue) producing WLE (0.33, 0.34) in Z7-NS.

Supporting information for this manuscript can be found here:

https://ars.els-cdn.com/content/image/1-s2.0-S2468519424001952-mmc1.pdf

Materials Today Chemistry 38 (2024) 102089

Contents lists available at ScienceDirect

Materials Today Chemistry

journal homepage: www.journals.elsevier.com/materials-today-chemistry/

Stable photoinduced metal-organic nanosheet blue phosphor for white light emission

Dylan A. Sherman [a], Waqas Kamal [b,c], Steve J. Elston [b], Alfonso A. Castrejón-Pita [c], Stephen M. Morris [b], Jin-Chong Tan [a,*]

[a] Multifunctional Materials & Composites (MMC) Laboratory, Department of Engineering Science, University of Oxford, Parks Road, Oxford, OX1 3PJ, United Kingdom
[b] Soft Matter Photonics Research Group, Department of Engineering Science, University of Oxford, Parks Road, Oxford, OX1 3PJ, United Kingdom
[c] Fluid Dynamics Laboratory, Department of Engineering Science, University of Oxford, Parks Road, Oxford, OX1 3PJ, United Kingdom

ARTICLE INFO

Keywords:
Metal–organic framework nanosheets
Inkjet printed nanosheets
Organic light-emitting diodes
Coumarins
Host-guest engineering
Zeolitic-imidazolate frameworks
White-light luminescence

ABSTRACT

Organic-based phosphors are promising alternatives to rare-earth metal based white light-emitting diodes (LEDs). Integrating phosphors into organic LED systems, however, is constrained by limited long-term chemical- and photo-stability, particularly for blue emitters, along with fabricability. Coumarins are common blue emitters for red-green-blue (RGB) or blue-yellow white light emission (WLE) systems but are susceptible to photo-dimerization and decay, both supressing fluorescence. This work employs a guest@host architecture to entrap 7-methoxycoumarin (MC) in metal-organic framework nanosheets (MONs) of the 2D phase of ZIF-7 (Z7-NS). This prevented photodimerization due to the arrangement of dye molecules within the nanosheet spacings. Favourably, upon ultraviolet exposure (365 nm), a new intense broader emission band forms irreversibly, derived from charge-transfer behaviour of the MC chromophores. This resulted in intense blue emission with 4.2 × improved photoluminescence quantum yield (PLQY) (Φ = 26.6 %) compared to molecular MC. Contrastingly, encapsulation of MC in 3D ZIF-7 (MC@Z7) also prevented photodimerization, but only exhibited purple-blue low-intensity, low PLQY MC monomeric fluorescence. The fabricability of MC@Z7-NS was demonstrated by inkjet printing blue emitting thin-films that showed improved homogeneity and quantum yield over MC@Z7. Finally, an RGB triple guest@Z7-NS was synthesised and optimised over 30 samples to produce WLE with ideal CIE coordinates of (0.33, 0.34), high PLQY of 65.08 %, and tuneable cool-warm temperatures. Combined, the work demonstrates the remarkable potential of guest@MON systems for improved WLE OLEDs.

1. Introduction

Rare-earth metal free white light-emitting diodes (WLEDs), such as organic based systems, are a promising alternative to current light-emitting diode (LED) devices (see e.g Refs. [1,2]). The present reliance on rare-earth metal phosphors (e.g., Eu, Y, Ga and In) for LEDs [3] has resulted in costly and energy intensive production and recycling [4,5]. Standard white-light emission (WLE) is characterised by the Commission International de l'Eclairage (CIE) coordinates of (0.33, 0.33) and colour correlated temperatures (CCTs) between 2500 and 6500 K; properties not easily achieved and maintained in operative conditions for extended periods of time. The success of phosphors in doing so requires high quantum efficiency, strong absorption, and high stability.

Advantages of organic phosphors over LED phosphors include large absorption coefficients, wide excitation bands, short fluorescent lifetimes, and low energy materials synthesis and refinement [6]. WLE OLEDs typically comprise a combination of blue and yellow phosphors, or red, green, and blue phosphors (RGB), relying heavily on a fluorescent blue emitter. Blue emitters pose the greatest impediment to integrated OLED lighting, however, due to the high-energy transition required for blue fluorescence that often results in fast degradation and low efficiency [7,8].

Coumarins are common blue phosphor components in WLE systems owing to their extended spectra ranges, stability in less hazardous solvents, and high emission yields [9–11]. 7-hydroxycoumarin is common in triple-phosphor systems. 7-methoxycoumarin (MC), known as Herniarin, is also a strong candidate, being a stable neutral species with limited electron density. Naturally occurring in flora (e.g., chamomilla), MC is readily sourced and biologically compatible, used often for biological labelling, and known to have antimicrobial and

* Corresponding author.
E-mail address: jin-chong.tan@eng.ox.ac.uk (J.-C. Tan).

https://doi.org/10.1016/j.mtchem.2024.102089
Received 14 February 2024; Received in revised form 18 April 2024; Accepted 7 May 2024
Available online 16 May 2024

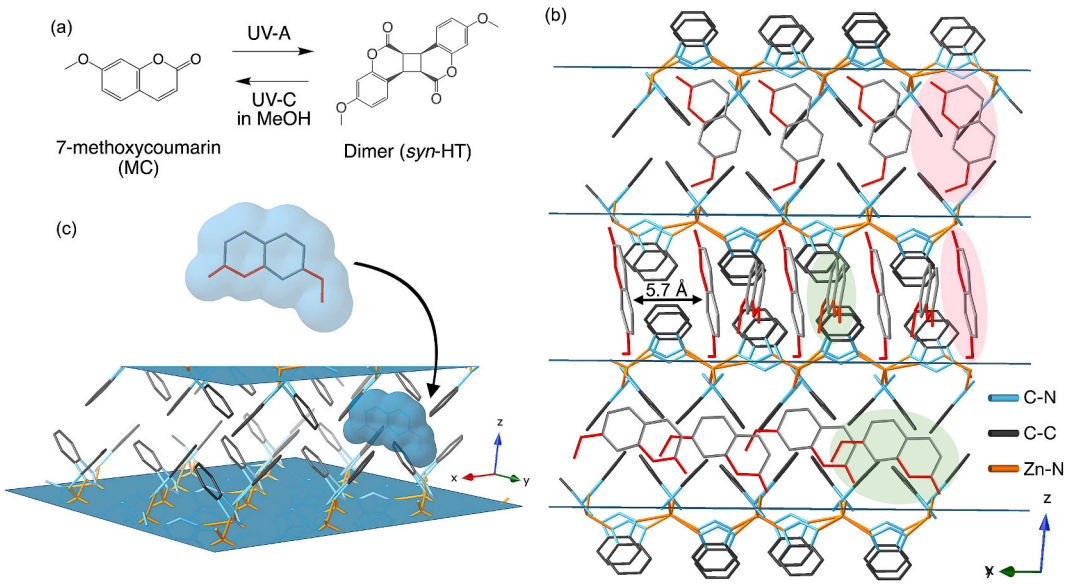

Fig. 1. The structure of MC@Z7-NS. (a) Photodimerization of MC and photoinduced cleavage of the dimer for retroconversion to the monomer. (b) Crystal structure of Z7-NS superimposed with MC to illustrate both horizontal (green) and vertical (red) potential arrangements, with C (black), N (blue) and Zn (orange) atoms represented. (c) 3D interlayer spacing between nanosheets of Z7-NS with the incorporation of a MC molecule. (For interpretation of the references to colour in this figure legend, the reader is referred to the Web version of this article.)

anti-inflammatory properties [10,12–14]. However, like many coumarins, MC photodimerizes via [2 + 2] photocyclization when exposed to ultraviolet A light (UV-A around 365 nm) (Fig. 1a) [15–17]. The photodimer does not fluoresce, impeding the use of MC as a phosphor (although the optical characteristics of MC have not been closely studied in relation to photodimerization and long-term UV exposure) [11]. Coumarin dimerization has been controlled by confinement in superstructures such as cyclodextrins and Pd-nanocages (stereo-, regio- or enantioselective), but little work has attempted to prevent dimerization [18].

Aside from the blue-light emission challenge, multicomponent LEDs exhibit phase separation problems, unequal decay rates of individual phosphors that leads to chromatic aberration, and difficulties in fabrication to obtain homogeneity and device integration [19,20]. The useability of these chromophores has been improved via confinement, which improves long-term stability and control of fluorescence [21]. By controlling the arrangement and therefore interaction of dyes, host frameworks play a critical role in preventing aggregation, and thus quenching, as well as reducing non-radiative deactivation pathways that limit luminescence [22].

Common metal (e.g., Zn and Cu) based Metal-organic frameworks (MOFs) are ideal hosts for encapsulating organic luminescent guest molecules due to their high specific surface area, pore sizes, and unique tuneability and rational designability [6,21]. Guest-based luminescent MOFs (LMOFs) are emerging as next-generation WLE materials for hybrid OLEDs [23]. One LMOF design uses a trio of RGB guests to achieve WLE, with frameworks incorporating the red emitter Rhodamine B (RB), green emitter Fluorescein (F) and a coumarin blue emitter (7-amino-4-(trifluoromethyl)-coumarin or 7-hydroxycoumarin) [12,13]. With a small molecular planar structure, limited rotation, and a similar lifetime to RB and F, MC is a strong blue-emitting guest candidate for MOFs. Indeed, MC has been encapsulated in micellar systems, *p*-sulfonatocalix [4]arene [24], and cyclodextrin [25], but these have caused fluorescence suppression due to non-polar cavities or hydrogen bonding between MC and guanine [26]. There is still a need to explore ways of enhancing the fluorescence of MC.

While quality WLE has been achieved for the few reported dye@MOF WLE materials, there is still a challenge in balancing high photoluminescent quantum yield (PLQY) (often only attainable up to 20–30 %), with ideal CCT and CIE coordinates, long-term physico-chemical and photo-chemical stability, and fabricability for workable OLED devices [27]. Metal-organic nanosheets (MONs) present a potential way to overcome these limitations. At a few nanometres thin, combined with wide micron scale lateral dimensions, nanosheet morphologies and 2D materials offer improved control over thin-film deposition and composite surfaces. Layered inorganic nanoparticles have successfully been utilised to control molecular aggregation and dye structures to tune luminescent properties [28,29]. Our group recently applied the guest@MOF approach to MONs by *in situ* encapsulation of RB and F in nanosheets of 2D ZIF-7-III (Z7-NS), producing a dual-guest yellow emitting MON with quantifiable control over emission chromaticity [30]. Several studies report WLE nanosheet materials based on metal-oxides or boron nanosheets that increase pathways for charge transfer and increase efficiency, while also creating easier to fabricate thin film devices [31–35]. Very limited work, however, has explored the potential offered by WLE MONs. One study synthesised a few-layer Zr MON with a yellow-emitting tetraphenylethylene-based tetracarboxylate ligand that was combined with a blue LED to produce a WLED with CIE coordinates of (0.37, 0.41) [36]. Separately, another study produced a WLE MON via a composite of lanthanide hydrates@2D MOF. While achieving (0.31, 0.33) CIE at 6370 K, the quantum yield (QY) was found to be low (3.3–8%) and the guest incorporation and long-term stability were unclear [37].

This work establishes a new approach to improving coumarin blue phosphors and multi-phosphor WLE systems by integrating organic fluorophores into MONs via a guest@host strategy [21]. MC was entrapped in a Z7-NS host via our established *in situ* guest@MON encapsulation strategy [30]. This not only prohibited MC photodimerization to improve photostability, but also enabled new photoinduced pathways for fluorescence that improved quantum yield and emission chromaticity and intensity. The nanosheet morphology also allowed for inkjet printing to be used to fabricate blue phosphor thin films. The same benefits, in contrast, were not observable in a MC@Z7 system that was also synthesised. Critically, by combining MC with F and RB luminescent dyes in Z7-NS it was possible to accomplish a single RGB WLE MON system, exhibiting CIE coordinates of (0.33, 0.34), competitive high PLQY of 65 % and a controllable range of colour temperature.

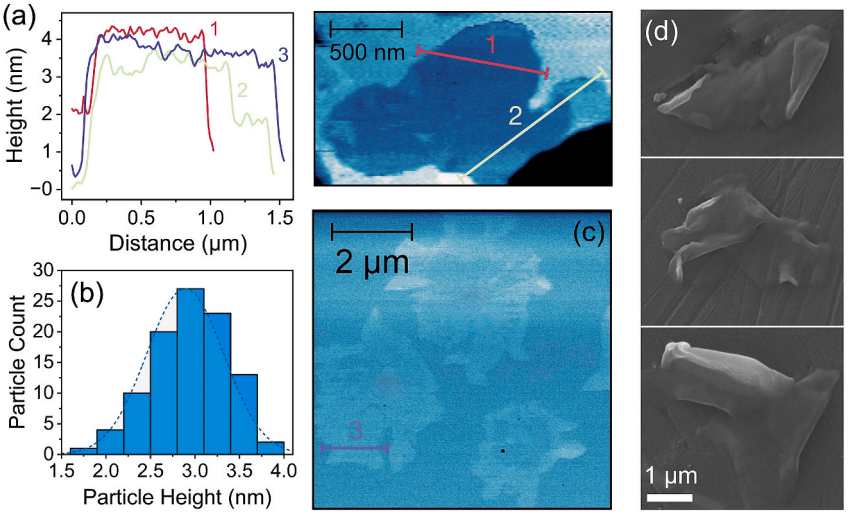

Fig. 2. Morphology of MC@Z7-NS. (a) AFM surface imaging a MC@Z7-NS particle measured on Si wafer (right) with height profiles across indicated lines (left), (b) histogram (0.5 nm bins) of height distribution measured by AFM of 100 MC@Z7-NS particles, (c) AFM scan of multiple MC@Z7-NS particles. (d) FE-SEM images of MC@Z7-NS measured at 10 keV and working distance of 9 mm samples were drop-cast onto an Al specimen stub and coated with 25 nm of Au.

2. Results and discussion

2.1. MC@Z7-NS morphology and structure

In situ entrapment of MC in Z7-NS was achieved using the previously reported salt-templating method employed for the intercalation of F and RB in Z7-NS [30]. 100 isolated MC@Z7-NS nanosheets were measured using atomic force microscopy (AFM) to determine an average particle height of 2.90 nm (± 0.43 nm) and lateral dimensions of ~2 × 3 μm (Fig. 2a–c, Fig. S1). The height profile of a single nanosheet (Fig. 2a) showed a 1.2 nm step at the particle edge, indicating the layered nature of the nanosheets (each sheet being ~ 1 nm based on reported crystal structures of ZIF-7-III) [38]. Field Emission Scanning Electron Microscopy (FE-SEM) images showed similar curled nanosheet flakes (the sample being coated with 25 nm of Au to highlight morphology) (Fig. 2d). Notably, while the nanosheet morphology remained when exposed to air or when stored in solution (MeOH or H_2O) over 3 months [28], the thin sheets were susceptible to fragmentation upon sonication for more than 2 min (Fig. S2). Thermogravimetric analysis showed stability of MC@Z7-NS up to 500 °C (Fig. S3), consistent with Z7-NS.

Powder X-ray diffraction (PXRD) of MC@Z7-NS confirmed retention of the ZIF-7-III crystal structure with no phase impurities (e.g., ZnO, NaCl) despite the introduction of guests into the framework (Fig. S4) [38]. The MC@Z7-NS diffraction pattern also exhibits nanosheet effects, i.e., minimal electron density in the *z*-axis and small crystallite size, observable from peak broadening and the peak intensity ratio of the I *(002)/I(200)* reflections decreasing from 14.8 in ZIF-7-III to 3.7 in MC@Z7-NS.

The previously reported F@Z7-NS, RB@Z7-NS, and F + RB@Z7-NS established that the synthesis method used here resulted in a degree of encapsulation, rather than surface attached guest-host positioning [30]. MC is planar and smaller than RB and F, with the ring structure only 2.7 × 4.7 Å and the remaining methoxy and carbonyl substituents extending in the furthest positions to 7 × 3.5 Å (Fig. 1b and c). Z7-NS contains adequate cavities between the nanosheet layers (Fig. 1c), produced by a herringbone layout of the exposed benzimidazole (bIm) linkers. By superimposing the ZIF-7-III crystal structure [38] with a molecular unit from the MC reported structure [39], potential packing arrangements can be deduced (Fig. 1b). While there is no evidence of uniform packing, two possible positions are accessible simultaneously: a horizontal alignment within the bIm V-openings (green, Fig. 1b) and a vertical alignment between the bIm ligands (red, Fig. 1b). Interestingly, the bIm 'claws' could act as a grip to ensure entrapment of any guests within the cavities to avoid potential leaching.

Vibrational spectroscopy was used to verify a degree of incorporation of MC into Z7-NS. Samples were thoroughly washed with MeOH and H_2O to remove excess MC. Fourier Transform Infrared (FTIR) and Raman spectra were consistent with Z7-NS across a range of MC guest concentrations (Figs. S5–6), with no new vibrational bands or energy shifts occurring. While the minimum concentration of guest species relative to the framework may limit observable MC signal, we also employed nano-FTIR to measure near-field IR spectra of MC@Z7-NS at various points on the surface of the single particle in Fig. 2a. The averaged nano-FTIR spectra (Fig. S7) show a prominent band at 760 cm^{-1} corresponding to the bIm aromatic ring in-plane and out-of-plane deformations of the host framework. No peaks that correspond to the vibrational bands in MC are present contra previous guest@MOF works that show guest signal in nano-FTIR spectra when surface species are present [40]. Terahertz synchrotron radiation (SR)-IR spectra (Fig. S8) also revealed the alignment of vibrational modes of MC@Z7-NS with Z7-NS, except for the band at 214 cm^{-1} being blue shifted by 3 cm^{-1}. This band is assignable to the bending at the bridge of the aromatic rings in bIm [41]. If guests reside within Z7-NS layers, then exposed bIm linkers in the interlayer space (Fig. 1b) may adjust their orientation to a less energetically favourable position to accommodate MC molecules, causing this observed blue shift.

2.2. Photophysical properties of 7-methoxycoumarin

Before examining the effect incorporating MC into Z7-NS has on fluorescence, we first established the emission behaviour of unconstrained MC. For this study, MC (as a thin layer of fine crystalline powder) was exposed to a UV lamp at 365 nm (4 W, 5 cm from sample) for 32 h while measuring two sets of excitation (λ_{obs} = 400, 500 nm) and emission spectra (λ_{ex} = 320, 375 nm) (Fig. 3a–d, f-h). FTIR of the UV-exposed MC sample was used to track the formation of the photodimer (Fig. 3e–i and Fig. S9 for vibrational model visualisations). Most prominently, in the first 2 h of UV exposure, the monomer band at 1706 cm^{-1} corresponding to the C═C pyronic bond lowers in intensity, while a new band at 1758 cm^{-1} assigned to the C═O carbonyl stretching in the MC dimer increases in intensity. This peak is present, but weak, in the initial MC, suggesting a trace of photodimerized species already present.

Tracking the peak intensity of these characteristic bands reveals a logarithmic reaction rate of dimer formation (Fig. S10), suggesting 90 %

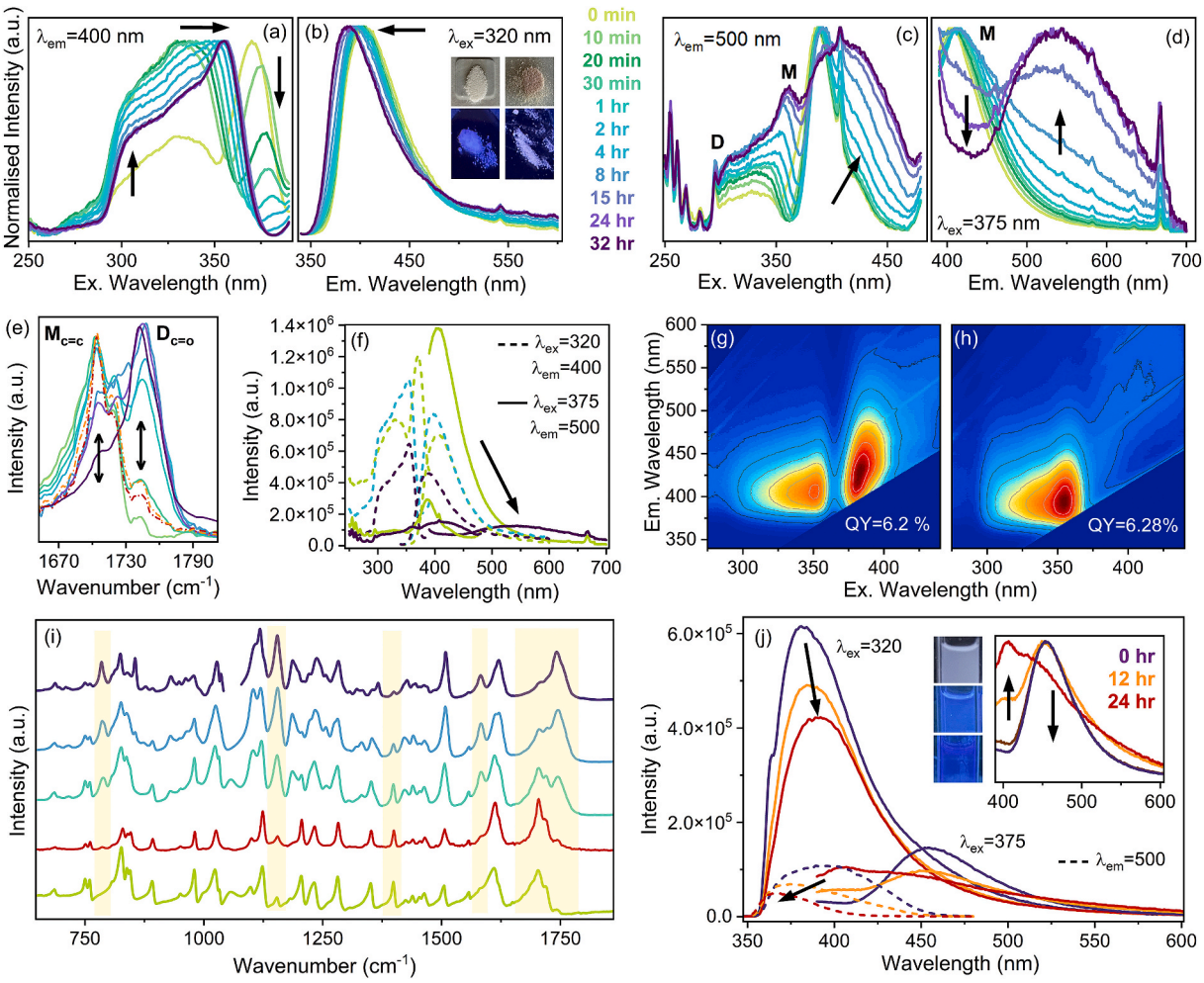

Fig. 3. Fluorescence properties of MC under UV exposure. (a)–(d) Excitation and emission spectra of solid MC observed over 32 h exposure to 365 nm UV (4 W, 5 cm from sample). Excitation spectra measured at λ_{obs} = 400 nm (a) and 500 nm (b), emission spectra measured at λ_{ex} = 320 nm (b) and 375 nm (d). Inset (b) shows MC before irradiation under UV light (left) and after (right). (e) FTIR spectra of MC monomer and dimer species characteristic bands measured over 32 h of exposure to 365 nm UV. (f) Comparison of intensity of emission and excitation spectra presented in (a)–(d). (g)–(h) Emission-excitation maps of MC before (g) and after (h) 365 nm UV exposure. (i) FTIR spectra of MC when exposed to UV (365 nm) and then 254 nm to retroconvert dimers to monomeric species (red spectra). (j) Emission (at λ_{ex} = 320 and 375 nm) and excitation spectra (λ_{obs} = 400 nm) of solid MC post-UV exposure under 254 nm light in MeOH for retroconversion of dimer species to monomers. Inset: normalised emission spectra and sample vial under ambient (top) and UV illumination before (middle) and after (lower) 254 nm irradiation. (For interpretation of the references to colour in this figure legend, the reader is referred to the Web version of this article.)

of dimer formation is completed within the first 2 h. Further spectral changes indicate the formation of the dimer. At 1581 cm^{-1} a band forms, corresponding to the dimer in-plane aromatic ring stretch modes (now connected to the cyclobutene ring), while the band at 1621 cm^{-1} reduces, being the monomer in-plane aromatic stretch. At 1190 cm^{-1} a new peak forms, corresponding to the C–H rocking around the cyclobutene dimer ring. At 1356 cm^{-1} the C=C, C–H rocking band of the monomer reduces while at higher energies a new out of plane C–H, C=C (aromatic) bending band forms at 783 cm^{-1} and the monomeric out-of-plane aromatic bending band at 813 cm^{-1} reduces.

With an awareness of the chemical composition of MC over time with UV exposure, we turn back to examining photophysical properties. Initially, a single emission band at λ_{max} = 400 nm is observed (Fig. 3b), corresponding to MC deep-purple fluorescence via conversion from $S_1 \rightarrow S_0$ [26]. The corresponding excitation region (Fig. 3a) comprised, unexpectedly, two bands: a broad band with λ_{max} = 325 nm corresponding to monomeric emission [26], and an intense, narrowband shoulder at 375 nm. The bands are most prominent in the excitation-emission map of the initial MC sample (Fig. 3g). The secondary band is sharp, at lower energy, and exhibits a minimal Stokes shift (15–20 nm): three characteristics of J-aggregation (head-to-tail arrangement of MC monomer molecules) [42,43]. MC crystallises in the triclinic $P\bar{1}$ system, with molecules packed asymmetrically so that the ethylenic bond of the pyrone cycle form at an angle of 65° [44]. This creates desirable conditions for J-aggregation, where a 'head-to-tail' or 'slipped co-facial' arrangement of neighbouring monomers could result in a negative coupling and lower energy excited singlet state.

After 2 h of UV exposure, the emission from MC is blue-shifted by 10 nm with a 50 % or 86 % reduction in intensity at λ_{ex} = 400 nm and λ_{ex} = 500 nm, respectively (Fig. 3f and visually evident in Fig. 3b, inset). This loss is mostly attributable to the photodimer forming, which possesses no π-orbitals and no mechanism for fluorescence. The excitation spectra (Fig. 3a and c) indicates that J-aggregation has ceased (partially contributing to emission intensity loss), while a new excitation band forms at 300 nm (most prominent at λ_{obs} = 500 nm), assigned to the higher energy absorption of the dimer [45,46]. Notably, physically mixing MC with $BaSO_4$ and Z7-NS also extinguished the aggregate absorption peak (Fig. S11), along with a 5–10 nm blue shift and 30 % reduction in intensity of emission. This suggests the process of photodimerization disrupts the ordered arrangement of molecules by the formation of dimer molecules and corresponding strain that propagates through the crystallites.

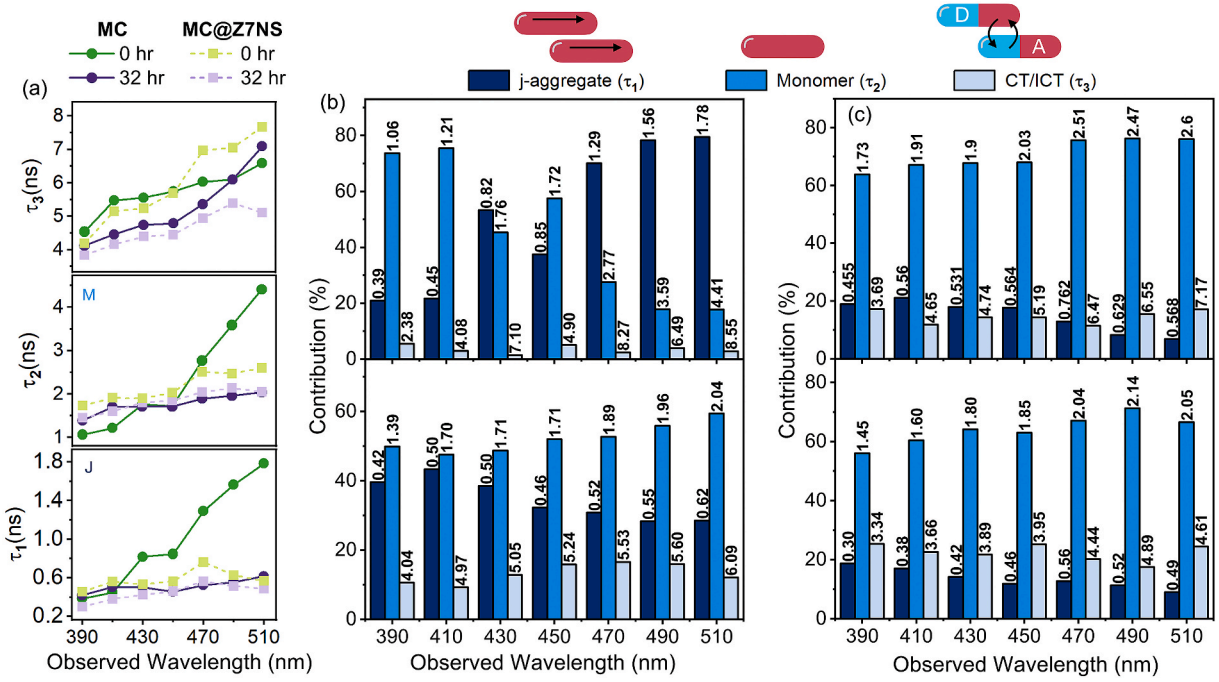

Fig. 4. Lifetime analysis of MC and MC@Z7-NS. (a) Lifetime components (in ns) of τ_1, τ_2 and τ_3 for MC and MC@Z7-NS compared to before (green) and after (purple) UV exposure across a range of observed wavelengths. (b)–(c) Lifetime components of MC (b) and MC@Z7-NS (c) before (top) and after (below) UV exposure. (For interpretation of the references to colour in this figure legend, the reader is referred to the Web version of this article.)

Spectral changes and shifts reduce significantly from 2 h until the 32-h endpoint. Monomer emission continues to reduce in intensity, but now more attributable to photo decay (Fig. 3f). The only notable change is after 4 h, when a broad excitation band with $\lambda_{max} = 411$ nm is observed (Fig. 3c), corresponding to a broad emission band from 500 to 700 nm ($\lambda_{max} = 540$ nm). Relative to monomeric emission, the intensity is negligible (Fig. 3f). The photodimer is photosensitive and is known to form radicals and unexpected decay fragments. Notably, the band is excitation dependent, observable at $\lambda_{ex} = 375$ nm not 325 nm (and emission band are generally observed to vary with excitation wavelength in all spectra of MC over the time analysed). These behaviours resemble a "red-edge" type effect, where a fluorophore's emission energy is dependent on the energy input due to a competing energetic process that occurs after excitation of the fluorophore on a timescale comparable to fluorescence mechanism [47]. Here, the broadband low-energy excitation dependent emission has been observed previously, being attributed to photodegradation of the dimer due to the photochemically active carbonyl group that can cause a biradical character to form that can create free radicals [14,46,48,49].

Together, the data highlight the instability of MC when exposed to UV, driven primarily by photodimerization. Indeed, a recent work confirmed the conversion of monomers to dimers results in the *a*-axis increasing by 6.8 Å to 14.614 Å, with a unit cell volume expansion from 206 Å^3 to 411 Å^3 resulting with transition to *Pbcn*. This large distortion induces strain in crystallites and a loss of crystallinity [17]. This is observed in the PXRD of our UV exposed MC samples too (Fig. S12), and we note the sample colour change from white to brown along with the low emissive nature of UV exposed samples (Fig. 1b).

Picosecond time-correlated single photon counting (TCSPC) data of MC corroborate the spectral observations above (Fig. 4a–b, S13 and Table S1). Fluorescence decays were fitted with a three-component (τ's) exponential function. Monomer emission was tentatively assigned τ_2 in accordance with previous reports [50]. The τ_3 component, exhibiting a longer lifetime, is tentatively assigned to a form of charge-transfer relaxation pathway, while τ_1 is likely related to aggregates. The initial MC sample (Fig. 4b, top) shows wavelength dependent τ_1 and τ_2 with negligible contribution from τ_3; at 390 nm τ_2 dominates while by 510 nm the τ_1 is the major contributor. In contrast, after UV exposure, the contribution of τ_2 remains consistent across observed wavelengths, while τ_1 is initially greater then reduces. Notably, at 390–430 nm, the contribution of τ_1 and τ_2 are close to equal in the converted sample. τ_3 increases across all wavelengths, indicative of the new photo decay activated broadband emission. The lifetime of τ_1 and τ_2 reduce after UV exposure significantly with increased observed wavelength.

After 32 h of UV exposure, MC exhibited predominantly dimer composition (but a lack of crystallinity). The dimer can be symmetrically cleaved back to monomeric MC by UV-C exposure (less than 300 nm) in MeOH, regenerating fluorescence, but the process typically leads to material degradation [15–17]. The UV converted solid sample was first submerged in MeOH for 2 h to confirm no change in emission results from solvent interactions alone (Fig. S14). After exposure to 254 nm UV light over 24 h (4 W lamp) emission reverted to the original monomeric band but was low in intensity (Fig. 3j). FTIR spectra confirms the regeneration of the monomer species bands (Fig. 3i), albeit less intense and with still some presence of the dimer. PXRD indicated amorphization still of the sample (Fig. S12). We conclude, therefore, that while UV exposure does return the sample chemically to monomeric form, the loss of crystallinity and order of the dipole moments interferes with the desirable geometric conditions for effective fluorescence.

2.3. Photophysical properties of MC@Z7-NS

To analyse the effect of entrapping MC in Z7-NS, a system of 12 MC@Z7-NS samples with different guest loadings were prepared. From NMR (Fig. S15), the bIm:MC final loading ratio was determined to be 3.4×10^{-4}, 5×10^{-4}, and 7.2×10^{-4} from synthesis quantities of 1.3, 2.6 and 4.5 mg MC, respectively (and bIm:MC synthesis ratios of 5×10^{-3}, 1×10^{-2} and 1.6×10^{-2}). Fluorescence of MC@Z7-NS (assigned as the 2.6 mg sample) initially appears dark purple (Fig. 5a and h), with a PLQY of 20.7 % (3.3× increase from molecular MC). MC@Z7-NS exhibits a single emission band ($\lambda_{max} = 385$ nm) comparable to the monomeric state of MC (Fig. 5a), with the corresponding excitation band

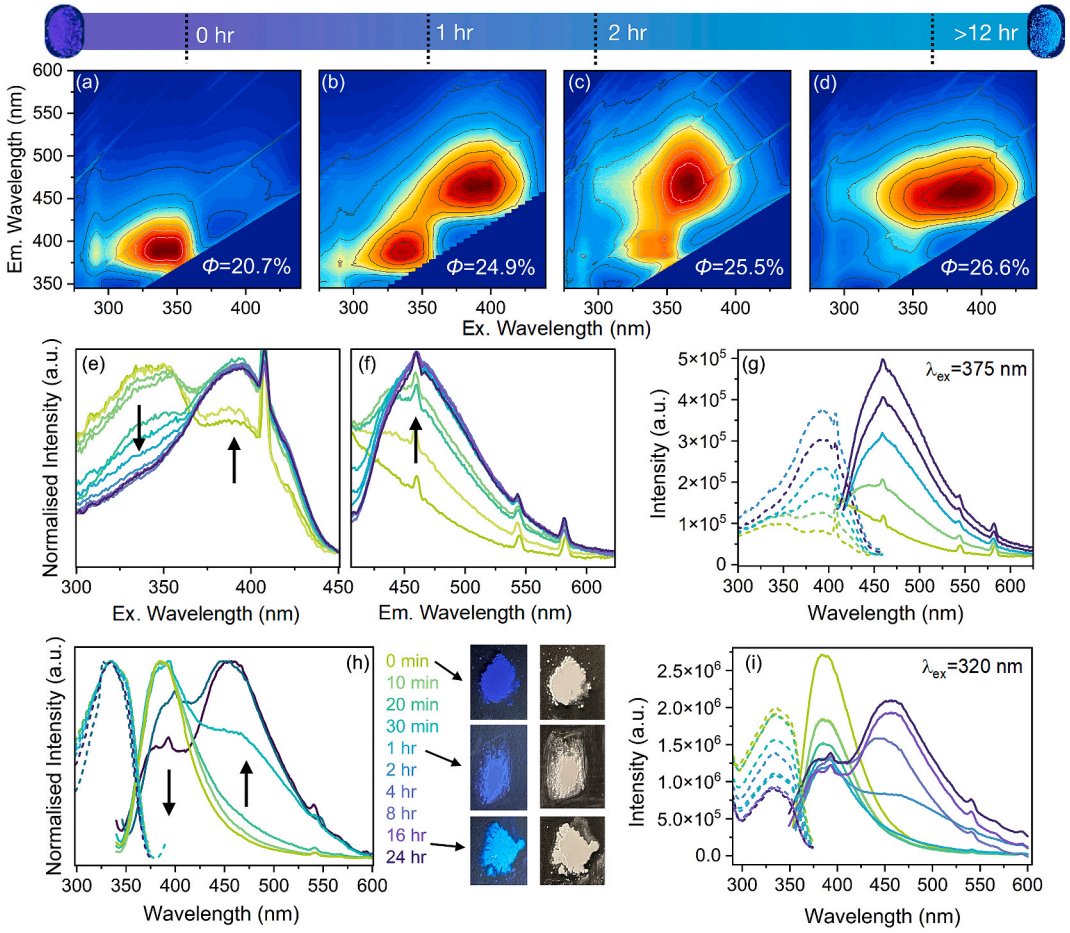

Fig. 5. Photophysical properties of MC@Z7-NS. (a)–(d) Emission-excitation maps of MC@Z7-NS exposed to UV light (365 nm, 4 W) for 0, 1, 2 and 12 h (left to right). Signal intensity indicated by colour (dark blue = weakest, red = strongest). Above: MC@Z7-NS powder under UV irradiation before (left) and after (right) UV exposure. Colour bar represents emission chromaticity as a function of UV exposure time. (e)–(i) Emission and excitation spectra of MC@Z7-NS over 24 h of UV exposure with excitation at 375 nm (e, g), 320 nm (h–i) and excitation observed at 500 nm (f–g) and 400 nm (h–i). Inset: MC@Z7-NS powder under ambient (right) and UV illumination (left) after 0, 1 and 15 h of UV exposure. Spectrum designation indicated by colours of times in (h). Artefact peaks from equipment (410, 545, 580 nm) present across spectra.

Table 1
Emission and excitation maxima, with the corresponding Stokes shifts of MC and MC@Z7-NS under UV exposure.

Sample	MC		MC@Z7-NS			
UV Exposure	0 h	12 h	0 h	1 h	2 h	12 h
Ex1 λ_{max} (nm)	352	355	340	338	340	336
Em1 λ_{max} (nm)	405	395	385	382	379	378
Stokes Shift 1	53	40	45	44	39	42
Ex2 λ_{max} (nm)	384	411		384	375	384
Em2 λ_{max} (nm)	405	540		463	460	458
Stokes Shift 2	21	129		79	85	74

between 300 and 350 nm (λ_{max} = 340 nm). As MC loading increases, the emission band intensity increases (Fig. S16) while the band position remains constant. Solid-state UV–Vis absorption spectra (Fig. S17) also confirms the presence of MC in MC@Z7-NS samples, with a slight increase in intensity of the absorption band at 325 nm upon increased guest loading. While Z7-NS absorbs and emits in the UV (λ_{ex} = 250–280 nm, causing UV-B λ_{em} = 295–320 nm) (Fig. S18), when excited at 325 nm, the framework absorption does not interfere with MC fluorescence (Fig. S19).

The photo behaviour of MC@Z7-NS further supports that MC was incorporated into the nanosheets, rather than simply being a composite mixture. Emission from MC@Z7-NS is blue-shifted 20 nm cf. molecular MC, the higher energy being typical of molecules confined within a host structure. Entrapment is further indicated by a reduction in the Stokes Shift from 53 nm to 45 nm, implying less energy is lost. Unlike molecular MC, no aggregation band is observed in excitation/emission spectra (Fig. 5) or absorption spectra (Fig. S17), suggesting the positioning of MC in inter-layer cavities limits the necessary physical overlap. In contrast, for Z7-NS physically mixed with molecular MC (equivalent to synthesis quantity for MC@Z7-NS), a distinct absorption band was measured, comprised of a larger band at 325 nm and a secondary shoulder at 360 nm (attributable to aggregates) (Fig. S17).

When MC@Z7-NS is exposed to 365 nm UV light, distinct and favourable behaviour is observed in contrast to molecular MC (Fig. 5). Remarkably, there is no evidence of dimerization in the emission spectra or solid-state absorption (Fig. S20). This is likely due to the lack of double bond overlap and alignment between MC molecules, as is needed for dimerization, when entrapped between Z7-NS. Photodimerization via [2 + 2] photocyclization typically requires the favourable topological condition posited by Schmidt, being reactive double bonds parallel in the crystal lattice within 4.2 Å of separation [51]. MC is an exception to this rule, initially, however. While MC has double bonds within 3.83 Å of each other, they are not parallel as is also required. Instead, they are rotated 65° with respect to each other [44]. Studies have revealed that orientational flexibility is key and the absorbance of UV allows for the rotation to generate the syn-head-tail dimer [52,53]. The dimerization of coumarins is known to be highly sensitive to packaging arrangements

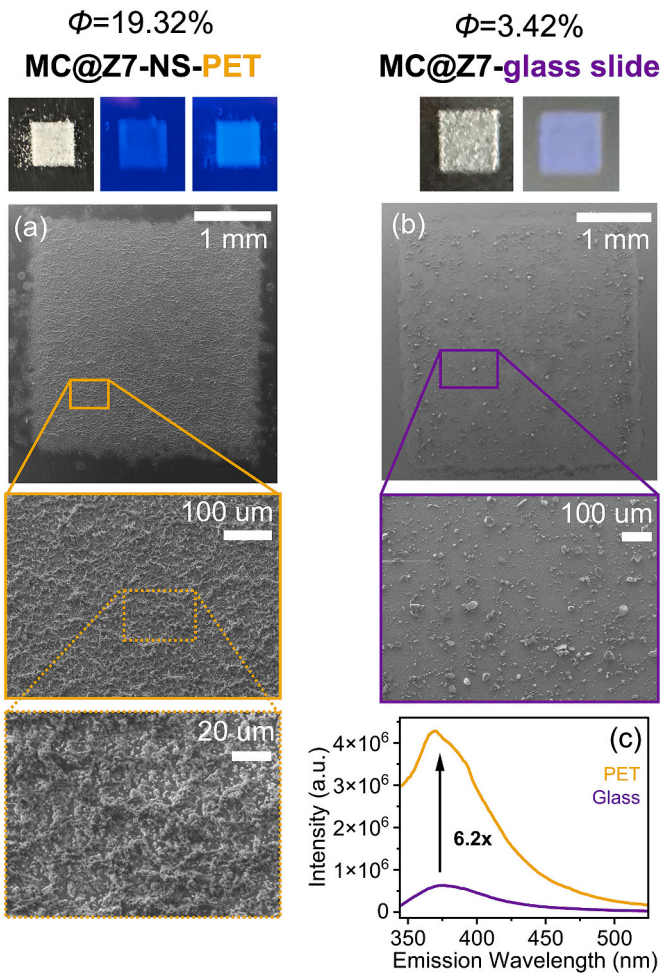

Fig. 6. Inkjet Printed Films of MC@Z7-NS. (a) SEM images of MC@Z7-NS inkjet printed onto PET substrate, viewed at various magnifications. Above: thin film under ambient lighting (left), UV illumination (middle) and post-UV exposure under UV illumination (right). (b) SEM images of MC@Z7 at various magnifications. Above: thin film under ambient lighting (left) and UV illumination (right). (c) Emission spectra of MC@Z7-NS printed films on PET (orange) and glass (purple) before UV irradiation. (For interpretation of the references to colour in this figure legend, the reader is referred to the Web version of this article.)

[44], and increasing pressure has been shown to also limit dimerization of MC [54]. UV exposure over a 2-h period, however, does result in a red-shift of emission to a vibrant blue (Fig. 5a–d) with a 5× intensity increase (λ_{ex} = 375 nm) (Fig. 5g and i). This is associated with an increase in quantum yield from 20.7 % to 26.6 % (4.2× increase cf. molecular MC). A larger Stokes shift of ≈80 nm is observable (Table 1), a notable improvement over molecular MC by effectively preventing self-absorption. These properties are a significant improvement in desirability for a blue emitting LED system over molecular MC.

To reveal the origin of the new band, MC@Z7-NS was exposed over a period of 24 h to a UV lamp (365 nm, 4 W) with excitation and emission spectra measured intermittently. Due to the lack of detectable MC bands using XRD or vibrational spectroscopy (Figs. S21–S22), only photophysical data was useful for elucidating potential mechanisms. Emission maps at select times (Fig. 5b–d) present a clear progression of a second emission band forming at around 475 nm after 1 h (Fig. 5b). At this point, the second band and higher-energy monomeric band appear equal in intensity. The emission spectra comprising the map have an isosbestic point between the two bands, suggesting a relationship between the two emission processes (Fig. S23). After 2 h (Fig. 5c), the second lower-energy band dominates, while after 12 h (Fig. 5d) the monomeric band is entirely extinguished, leaving the second lower-energy band.

At all times, excitation spectra measured at 400 nm results in a single absorption band characteristic of molecular MC with λ_{max} = 325 nm. Intriguingly, however, the corresponding emission spectra observed at 320 nm, while initially exhibiting the monomeric MC emission band, begins to form a second emission band at 475 nm as the initial monomeric band decreases. This implies that the same monomeric species are absorbing energy to reach an excited state, while the emission is occurring through both the initial monomer $S_1 \rightarrow S_0$ pathway and a new pathway.

In contrast, when the sample is excited at 375 nm, no emission band is initially observable but after 1 h a broadband between 400 and 600 nm forms, increasing in intensity by a factor of 5 over 24 h. Correspondingly, excitation observed at 500 nm sees a secondary absorption band at 384 nm, corresponding to the new blue emission observed. This is coupled with the suppression of any traces of the monomeric band observable in initial spectra before UV exposure. A final key observation is that while the Stokes shift of the first emission band is around 42 nm, remaining mostly consistent upon UV exposure, the second broadband has a Stokes shift of, on average, 80 nm (Table 1). Critically, the new band is distinct, both in terms of energy and Stokes shift, from the low-intense broadband observed in molecular MC after UV exposure that was attributed to photo decay. PXRD and FTIR of the sample post-UV exposure reveal no change in crystallinity or chemical bonding, at least of the framework (Figs. S21 and S22). Suspending MC@Z7-NS in MeOH for 6 h did not alter the emission spectra (Fig. S24). Nor did irradiation of MC@Z7-NS in MeOH with 254 nm UV, confirming the process is not reversible like photodimers in MC (Fig. S25).

These data combined suggest the new emission band may arise from a form of intramolecular or inter-molecular charge transfer (CT), a common indicator in spectra induced by CT effects [55]. MC is known to undergo molecular rotation and movement upon excitation, a feature that enables dimerization. Chromophores such as RB have been previously shown that movement under UV exposure can occur over time irreversibly, leading to, for example, self-aggregation in confined domains on silica nanoparticles and as nanosized domains in THF [56]. Here MC may move to enable greater overlap for CT.

MC is a polar molecule comprising a methoxy weak electron donor and carbonyl electron acceptor. This permits intramolecular charge transfer (ICT) which is increased in the excited state. A full resonance pathway exists for electron delocalisation between the donor and acceptor due to the 7-position substituent, allowing the donor group to participate more effectively in the delocalised π system of the coumarin. This creates a "push-pull" effect in coumarins which shifts absorption and emission spectra [57]. Alternatively, the charge transfer may take place between two closely aligned molecules. Di (7-methoxycoumarin-4-methyl)-1,10-diaza-18-crown-6 exhibits both a local excitation and an internal charge transfer band, with charge transfer resulting from the close alignment of fluorophores (within 8–10 Å) provided by the diaza-crown [58]. For MC@Z7-NS, the bIm horizontal claw inter-layer spacing overlaps the methoxy and carbonyl groups of neighbouring MC, potentially enabling CT interactions. The CT process creates a more stable excited state, *i.e.,* the red shifted band compared to the monomeric position. The diaza-crown system, like MC@Z7-NS, also exhibited an isosbestic point, referencing the reciprocal relationship between the locally excited (LE) and CT band.

While MC is capable of π electron overlap and delocalisation, excimer emission has been discounted due to the large spacing (5.7 Å) between MC guests limiting aromatic ring overlap (Fig. 1b). Park et al. demonstrated that for coumarins with substituents in 7- and 4- positions, the fluorescence behaviour of the material is highly sensitive to packing arrangements [10]. Isolated monomer type coumarins exhibited some intermolecular interactions and yielded stronger fluorescence while only isolated-dimer systems (not evinced for MC@Z7-NS) led to emission from excimers.

Lifetime data further provides understanding (Fig. 4c, S26 and

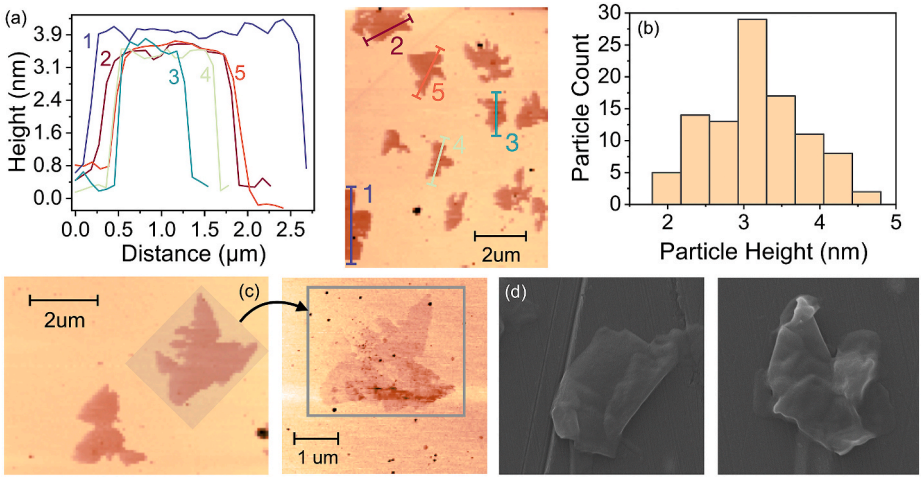

Fig. 7. Morphology of TG@Z7-NS. (a) AFM surface imaging of TG@Z7-NS (right) with height profiles (left); (b) histogram (0.5 nm bins) of TG@Z7-NS particle height of 100 sample size; (c) TG@Z7-NS particles imaged by AFM; (d) SEM Imaging of single TG@Z7-NS particles (material on an aluminium stub with 25 nm gold coating). (For interpretation of the references to colour in this figure legend, the reader is referred to the Web version of this article.)

Table S2). Lifetime data of MC mixed with Z7-NS aligns closely with the MC lifetime data (Fig. S27, Fig. 4b). In MC@Z7-NS, however, the monomer component is a major contributor to lifetime. Lifetime data with varying concentrations of MC is consistent with that obtained for MC@Z7-NS (Fig. S28). Upon UV-exposure lifetimes change less drastically than seen for molecular MC, although τ_3 notably increases in contribution, while the monomeric component reduces. This aligns with the suggestion that a degree of charge transfer is involved in the fluorescence mechanisms after photoirradiation of MC@Z7-NS, as the ICT state lifetime is longer for coumarin entities [59]. Unlike MC, the framework appears mostly independent of observed wavelength, with only a minor reduction of τ_1 percentage contribution as observed wavelength increases.

To examine long term stability, MC@Z7-NS, was exposed to a 150 W concentrated UV irradiation from a Xenon lamp at the sample's absorption maximum (325 nm) over 24 h. Compared with a typical 4 W LED cell, these results reflect a simulation of long-term working-time use. The data (Fig. S29) reveal exponential decay with similar intensity loss to MC (40–50 %), although the less concentrated MC@Z7-NS sample appeared to retain more emission intensity. Importantly, limited chromatic aberration was observed for the MC@Z7-NS samples, compared with the significant blue-shift towards deep purple emission for MC (resulting from photodimerization and decay).

2.4. Comparison to MC@Z7

To confirm the features described are attributable to the 2D architecture of MC@Z7-NS, we prepared MC@Z7, the analogous 3D sodalite ZIF framework. The room temperature *in situ* encapsulation synthesis of MC in Z7 was adapted from a guest@ZIF-8 synthesis protocol with equal MC synthesis quantity to MC@Z7-NS (see Methods). Analysis of the reported ZIF-7 crystal structure confirmed a cavity size of 17.34 × 11.47 $Å^2$, large enough for a MC molecule. The opening of the cavity is 3.7 $Å^2$, discouraging any encapsulated guests from leaching. PXRD and FTIR confirmed the retention of the ZIF-7 framework crystallinity (Fig. S30) with no new bands indicating impurities or surface MC. The material fluoresced deep-blue under UV (Fig. S31) with the emission map of MC@Z7 resembling the monomeric pre-UV exposed MC sample (Fig. S31). After 24 h of UV-exposure, the sample did not alter in emission colour, suggesting the framework encapsulation prevented dimerization in a similar fashion to MC@Z7-NS. No secondary lower-energy band formed, however, and the quantum yield remained low (4.5 %). This reaffirms the importance of an open interlayer spacing arrangement for dye-dye interactions in enabling the more intense blue emission observed in MC@Z7-NS.

2.5. Inkjet printing of MC@Z7-NS thin films

To showcase the potential photoluminescent capabilities of nanosheet blue emitters, thin films of MC@Z7-NS were fabricated using a research-grade inkjet printer (Jetlab II, MicroFab Technologies®). Microscope glass slides and Polyethylene terephthalate (PET) films were used as the two different substrates considered in this demonstration. To determine the optimal film thickness, several layers of MC@Z7-NS were deposited onto a glass substrate, and subsequently tested. The outcomes of these printing trials are presented in Fig. S32, while the final printed film, covering an area of 763.6 μm × 1039 μm with a thickness of 26.15 μm, comprising 12 layers of MC@Z7-NS, is illustrated in Fig. S33 of the supplementary information section. Fig. 6a shows a film of MC@Z7-NS (12 layers) finely printed onto a PET substrate. The SEM images reveal a consistent coating of the sample across the entire printed area. Alicona surface imaging revealed micron-sized surface roughness, resulting in an increase surface area, which in turn improved emission intensity (Fig. S33). In contrast, a printed film of MC-Z7 exhibited aggregation and inconsistent layering (Fig. 6b and S34) with low quantum efficiency (3.42 %). While initially deep-blue/purple emitters (Fig. S32), after UV exposure, printed MC@Z7-NS films exhibited homogenous stable bright-blue emission, similar to that of the powdered sample (Fig. 6a, S35). Samples printed onto PET exhibited an increase of more than 6 × in emission intensity over glass slides after UV exposure (Fig. 6c). PLQY (19.3 %) was closely retained to values observed for powder MC@Z7-NS. While only preliminary, given the complexity of fully realised OLED devices [23,60], these printing results show the potential of luminescent MON thin films via printing for incorporation into opto-electronics such as OLEDs.

2.6. White-light emitter via triple-guest system

With a blue emitter established, we developed a single system triple-guest (TG) WLE material, eliminating the need to combine single guest materials. *In situ* incorporation of MC, F and RB was achieved by mixing the three chromophores in a specific ratio with bIm, $Zn(NO_3)_2$ and NaCl. The resultant material, TG@Z7-NS produced WLE (Fig. 8a–f). The crystal structure and morphology of Z7-NS was maintained in TG@Z7-NS, with no new bands observable in vibrational spectroscopy to indicate surface species of any guest (Figs. S36 and S8). Nano-FTIR also resembled Z7-NS nanoFTIR spectra, with no bands from any guest (Fig. S8). Particle morphology was consistent with MC@Z7-NS (Fig. 7a),

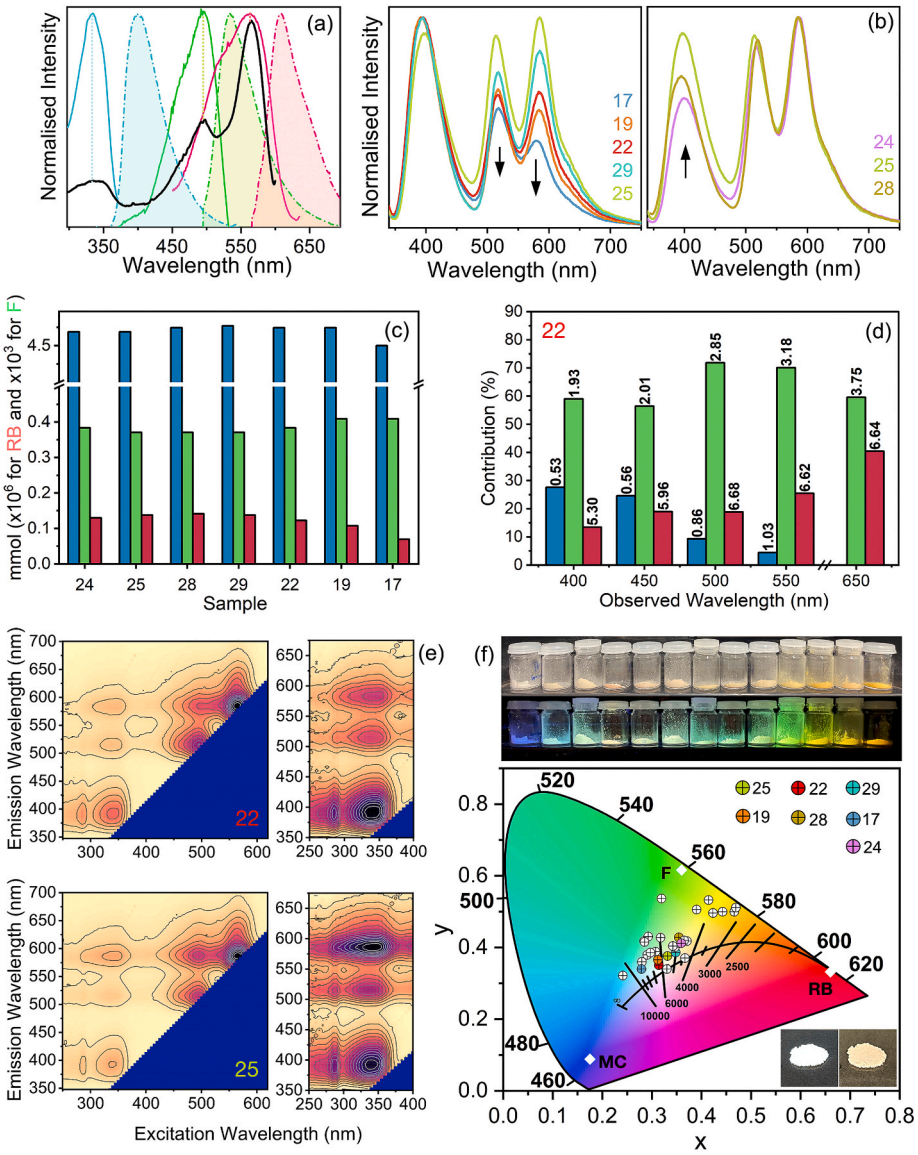

Fig. 8. TG@Z7-NS photophysical properties. (a) Emission (filled and broken lines) and excitation (solid line) spectra of MC@Z7-NS (blue), F@Z7-NS (green) and RB@Z7-NS (red) with excitation spectra of TG@Z7-NS overlayed (observed at 400 nm). (b) Emission spectra of WLE TG@Z7-NS samples. (c) Concentrations of F, RB and M in TG@Z7-NS samples shown in (b). (d) Lifetime data of TG@Z7-NS sample 22. (e) Emission-excitation maps for TG@Z7NS samples 22 (top) and 25 (bottom). (f) TG@Z7-NS samples synthesised and emission chromaticity. Inset: TG@Z7-NS ideal WLE sample under ambient (right) and UV (left) light. Above: select TG@Z7-NS samples under ambient (top) and UV (bottom) light compared with MC@Z7-NS (far left vial) and F@Z7-NS (far right vial). (For interpretation of the references to colour in this figure legend, the reader is referred to the Web version of this article.)

with 100 particles exhibiting an average height of 3.5 nm (± 0.37 nm) and lateral dimensions of *ca.* 2 × 3 μm (Fig. 7b–c, Fig. S37).

30 unique cold-warm white light fluorescence emission colours were achieved depending on the concentrations of MC, F and RB during synthesis (Fig. 8f and S38). Emission colour temperature is mostly within 4000–6000 K and 6000–8000K on the Planckian locus. These ranges correspond to bright white light and colder white light, respectively, with incandescent lightbulbs typically rated at 4200 K, daylight at 5500 K, and an overcast day at 6500 K. An ideal white-light emitting TG@Z7-NS sample with chromaticity coordinates (0.33, 0.34) was achieved by tuning guest synthesis ratios over 30 samples (Fig. 8f, sample 22). The PLQY of TG@Z7-NS was impressively high, 65.08 %, attributable to the thin 2D nature of Z7-NS. Four further clusters of colours were achieved: yellow/green, blue-green, cold white, and warm white (Fig. S39). Emission chromaticity adjusted as expected with the increase/decrease of a contributing chromophore (e.g., maintaining MC and F while reducing RB produces a colder white towards blue emission).

TG@Z7-NS (ideal sample) excited at 330 nm exhibited three distinct emission bands, assignable to MC at 390 nm, F at 515 nm and RB at 585 nm (Fig. 8b). The ideal sample shows equivalent intensity bands from F and RB, while the MC band is more intense with a ratio of 5:3 of MC:F/RB (Fig. 8b). An emission map exhibits the excitation range of 320–360 nm where all three guests emit (Fig. 8e). At longer wavelengths, the dual emission of F + RB (~500 nm), then only single emission of RB (~560 nm), is observable. The excitation spectra (observed at 610 nm emission wavelength) correspond to the emission spectra, with three distinct absorption bands assignable to MC at 300–375 nm, F at 425–520 nm, and RB at 540–600 nm (Fig. 8a). The excitation spectra remain similar over varied F:RB:MC concentrations (Fig. S40).

Simple physical mixing of the F/RB/MC dyes did not produce the same spectral bands, nor did mixing the three single-guest F/RB/MC@Z7-NS systems, highlighting the importance of simultaneous entrapment in Z7-NS for ideal WLE (Fig. S41). UV–Vis solid state

absorption spectra show TG@Z7-NS exhibits 4 bands assigned to Z7, MC, F and RB (Fig. S42). There is no evidence of MC photodimers. The absorption band intensity proportion between MC:F:RB is 10:2:1. While the concentration of MC was significantly greater than F and RB during synthesis (34058000:2650:1 respectively) (Fig. 8c), the final product intensity ratios are less disproportionate. From NMR digest, a MC:F:RB ratio in TG@Z7-NS was calculated to be 148:14:1 (with a bIm:guest ratio of 0.0037, 0.00034 and 0.000025 for MC, F and RB), indicating only a 10 × increase in loading of MC from MC@Z7-NS (Fig. S43). Indeed, TGA was conducted with TG@Z7-NS and compared with a mix of Z7-NS and the powders of MC, F and RB used in synthesis quantities. While the powder mix showed an 8 % weight loss around 150 °C, where the dyes would have decomposed, TG@Z7-NS did not (Fig. S44).

Fig. 8a overlays the emission and excitation spectra of MC@Z7-NS, F@Z7-NS and RB@Z7-NS, showing that the emission of MC overlaps with the absorption of F, and the same for F and RB. Given the spectral overlap, emission by MC may be absorbed by F and the same for F and RB, hence the need for a greater proportion of MC guest in the triple-guest system. While F + RB@Z7-NS was previously reported to exhibit Förster resonance energy transfer (FRET) between F and RB, the incorporation of MC appears to disrupt the process and instead increases the monomeric emission from the F molecules. This is further supported by the blue-shift of the F band as MC is added; while during FRET the F band is red-shifted, a monomeric F emission is relatively blue-shifted.

Lifetime data indicates four lifetime components that do not vary significantly by altering the F:RB:MC synthesis ratios (Fig. 8d, S45-46 and Table S3). These are assignable to MC, F and RB, with the second and third components increasing in contribution as observed wavelength increases and approaches the emission of F and RB. Exposure of the sample to a Xenon lamp (150 W) at 350 nm emission revealed similar long-term exposure exponential decay rates of each fluorophore in the material and the retention of white-light emission after testing despite a 75 % reduction in emission intensity (Fig. S47).

3. Conclusions

This work demonstrates the realistic potential for metal-organic nanosheets as viable host frameworks for WLE diodes. Using room temperature, salt-template based bottom-up syntheses of guest@ZIF-7-NS samples, it was possible to entrap MC to form 3 nm thin blue-emitting nanosheets. The material prevented photo decay and dimerization (which suppresses emission in molecular MC), while simultaneously enabling a more intense, higher quantum yield, bright blue emission band from dye-dye charge transfer interactions. This behaviour was "turned on" irreversibly by UV exposure, enabling MC@Z7-NS to act as a UV exposure sensor in the process. These results surpassed the luminescence and stability properties attainable when MC was encapsulated in the confined pores of the parent 3D ZIF-7 framework. Inkjet printing of the MC@Z7-NS samples also confirmed the benefits of employing nanosheets to obtain more homogenous, less aggregated, thin films of blue emitters over 3D framework hosts.

Finally, by *in situ* entrapment of MC with F and RB it was possible to manufacture a single WLE nanosheet material, TG@Z7-NS, with near ideal emission chromaticity coordinates (0.33, 0.34), high quantum yield (65 %) that outperforms 3D guest@MOF single-phase WLE systems and other MON WLE systems, stability over extended harsh working conditions, and a range of tuneable colours from cold to warm white light depending on guest concentration ratios, all while maintaining a nanosheet morphology of 3.5 nm thinness with 2–4 μm lateral dimensions. Collectively, these findings establish an adaptable blueprint for furthering the design of host@guest metal-organic based OLED nanosheet systems towards manufacturing sustainable, rare-earth metal free materials for efficient and reliable white-light emission.

Materials and methods

Supplied in Supplementary Information.

CRediT authorship contribution statement

Dylan A. Sherman: Writing – review & editing, Writing – original draft, Visualization, Validation, Methodology, Investigation, Funding acquisition, Formal analysis, Data curation, Conceptualization. **Waqas Kamal:** Writing – review & editing, Methodology, Investigation. **Steve J. Elston:** Writing – review & editing, Supervision, Resources. **Alfonso A. Castrejón-Pita:** Writing – review & editing, Supervision, Funding acquisition. **Stephen M. Morris:** Writing – review & editing, Supervision, Funding acquisition. **Jin-Chong Tan:** Writing – review & editing, Supervision, Resources, Project administration, Funding acquisition, Conceptualization.

Declaration of competing interest

The authors declare that they have no known competing financial interests or personal relationships that could have appeared to influence the work reported in this paper.

Data availability

Data will be made available on request.

Acknowledgements

D.A.S. acknowledges the scholarships from the General Sir John Monash Foundation and Clarendon Fund. J.C.T. thank the ERC Consolidator Grant (PROMOFS 771575) and EPSRC (EP/R511742/1) for funding the research. W.K., S.J.E., and S.M.M acknowledge financial support from the EPSRC (UK) through project EP/W022567/1. A.A.C-P acknowledges funding from the John Fell Fund, Oxford University Press, via a Pump-Priming grant (0005176). The authors acknowledge the Diamond Light Source for the provision of beamtime SM27504 at B22 MIRIAM via Drs. Mark Frogley and Gianfelice Cinque, and rapid access beamtime CY29415 at I11 via Dr. Sarah Day. The authors would like to acknowledge Dr. Cyril Besnard and Professor Alexander Korsunsky for the acquisition of the FESEM images along with the Laboratory for In-Situ Microscopy and Analysis. The authors thank the Research Complex at Harwell (RCaH) for access to materials characterization facilities.

Appendix A. Supplementary data

Supplementary data to this article can be found online at https://doi.org/10.1016/j.mtchem.2024.102089.

References

[1] Q. Lin, et al., J. Rare Earths 41 (2023) 1127, https://doi.org/10.1016/j.jre.2022.05.008.
[2] Y.-H. Ma, et al., J. Rare Metals 43 (2023) 736, https://doi.org/10.1007/s12598-023-02334-9.
[3] H. Zhang, H. Zhang, Light, Sci. Appl. 11 (2022) 260, https://doi.org/10.1038/s41377-022-00956-9.
[4] C.C. Pavel, et al., Phys. Status Solidi A 213 (2016) 2937, https://doi.org/10.1002/pssa.201600594.
[5] A. Rollat, et al., Waste Management 49 (2016) 427, https://doi.org/10.1016/j.wasman.2016.01.011.
[6] Z. Sun, et al., Nanomater (2021) 11, https://doi.org/10.3390/nano11102761.
[7] A. Monkman, ACS Appl. Mater. Interfaces 14 (2022) 20463, https://doi.org/10.1021/acsami.1c09189.
[8] Y. Im, et al., Adv. Funct. Mater. 27 (2017) 1603007, https://doi.org/10.1002/adfm.201603007.
[9] R. Dondon, et al., New J. Chem. 23 (1999) 923, https://doi.org/10.1039/a902285f.
[10] S.-Y. Park, et al., Des Pigm 82 (2009) 258, https://doi.org/10.1016/j.dyepig.2009.01.014.

[11] I. Cazin, et al., Polym. J. 13 (2020) 56, https://doi.org/10.3390/polym13010056.
[12] X.Y. Liu, et al., J. Am. Chem. Soc. 141 (2019) 14807, https://doi.org/10.1021/jacs.9b07236.
[13] Y. Chen, et al., Chem. Mater. 31 (2019) 1289, https://doi.org/10.1021/acs.chemmater.8b04126.
[14] N. Nizomov, et al., J. Appl. Spectrosc. 74 (2008) 626, https://doi.org/10.1007/s10812-007-0102-z.
[15] M. Jiang, et al., Phys. Chem. Chem. Phys. 19 (2017) 4597, https://doi.org/10.1039/c6cp08076f.
[16] C.H. Krauch, et al., Chem. Ber. 99 (1966) 625, https://doi.org/10.1002/cber.19660990237.
[17] K. Yano, et al., CrystEngComm 23 (2021) 5780, https://doi.org/10.1039/d1ce00444a.
[18] S.-L. Chen, et al., CCS Chem. 5 (2023) 1225, https://doi.org/10.31635/ccschem.022.202202115.
[19] G. Haider, et al., ACS Nano 10 (2016) 8366, https://doi.org/10.1021/acsnano.6b03030.
[20] Y. Cui, et al., Adv. Funct. Mater. 25 (2015) 4796, https://doi.org/10.1002/adfm.201501756.
[21] M. Gutierrez, et al., Chem. Rev. 122 (2022) 10438, https://doi.org/10.1021/acs.chemrev.1c00980.
[22] S.H. Xing, C. Janiak, Chem. Comm. 56 (2020) 12290, https://doi.org/10.1039/d0cc04733c.
[23] A. Karmakar, J. Li, Chem. Comm. 58 (2022) 10768, https://doi.org/10.1039/d2cc03330e.
[24] B.C.M.A. Ashwin, et al., J. Phys. Org. Chem. 31 (2018) 3788, https://doi.org/10.1002/poc.3788.
[25] B.D. Wagner, et al., J. Incl. Phenom. Macrocycl. Chem. 47 (2003) 187, https://doi.org/10.1023/B:Jiph.0000011779.65838.44.
[26] W. Thongyod, et al., Phys. Chem. Chem. Phys. 21 (2019) 16258, https://doi.org/10.1039/c9cp02037c.
[27] Q. Liu, et al., Langmuir (2023) 3656, https://doi.org/10.1021/acs.langmuir.2c03299.
[28] J. Bujdák, J. Photochem. Photobiol. C. Rev. 35 (2018) 108, https://doi.org/10.1016/j.jphotochemrev.2018.03.001.
[29] K. Fujii, et al., J. Photochem. Photobiol., C 225 (2011) 125, https://doi.org/10.1016/j.jphotochem.2011.10.009.
[30] D.A. Sherman, et al., Adv. Funct. Mater. (2023) 2214307, https://doi.org/10.1002/adfm.202214307.
[31] S. Pal, et al., ACS Appl. Nano Mater. 4 (2021) 8572, https://doi.org/10.1021/acsanm.1c02133.
[32] S. Vempati, et al., Nanoscale Res. Lett. 7 (2012) 470, https://doi.org/10.1186/1556-276X-7-470.
[33] S. Turkdogan, et al., Adv. Funct. Mater. 26 (2016) 8521, https://doi.org/10.1002/adfm.201603620.
[34] N. Sharma, et al., Sens. Actuators B Chem. 348 (2021) 130617, https://doi.org/10.1016/j.snb.2021.130617.
[35] J. Xie, et al., Chem. Sci. 5 (2014) 1328, https://doi.org/10.1039/c3sc53127a.
[36] X. Hu, et al., Chemistry 23 (2017) 8390, https://doi.org/10.1002/chem.201702037.
[37] J. Tang, et al., J. Mater. Chem. C 9 (2021) 14628, https://doi.org/10.1039/d1tc04239d.
[38] P. Zhao, et al., Chem. Mater. 26 (2014) 1767, https://doi.org/10.1021/cm500407f.
[39] N. Ramasubbu, et al., Chem. Comm. (1982) 178, https://doi.org/10.1039/C39820000178.
[40] A.F. Möslein, et al., Nano Lett. 20 (2020) 7446, https://doi.org/10.1021/acs.nanolett.0c02839.
[41] M.R. Ryder, et al., Phys. Rev. Lett. 113 (2014) 215502, https://doi.org/10.1103/PhysRevLett.113.215502.
[42] B. Heyne, Photochem. Photobiol. Sci. 15 (2016) 1103, https://doi.org/10.1039/c6pp00221h.
[43] J.H. Kim, et al., Adv. Mater. 34 (2022) 2104678, https://doi.org/10.1002/adma.202104678.
[44] K. Gnanaguru, et al., J. Org. Chem. 50 (1985) 2337, https://doi.org/10.1021/jo00213a027.
[45] A. Concellón, et al., J. Mater. Chem. C 6 (2018) 1000, https://doi.org/10.1039/c7tc05009g.
[46] K.D. Belfield, et al., J. Phys. Org. Chem. 16 (2003) 69, https://doi.org/10.1002/poc.576.
[47] A.P. Demchenko, Luminescence 17 (2002) 19, https://doi.org/10.1002/bio.671.
[48] L. Zhao, M V, D.A. Loy, K.J. Shea, Chem. Mater. 20 (2008) 1870.
[49] P.D. Wood, L J J, J. Phys. Chem. A 102 (1998) 5585.
[50] G. Wenska, S. Paszyc, Can. J. Chem. 66 (1988) 513, https://doi.org/10.1139/v88-087.
[51] G.M.J. Schmidt, J. Chem. Soc. (1964) (2014), https://doi.org/10.1039/JR9640002014.
[52] L.H. Leenders, E. Schouteden, F.C. De Schryver, J. Org. Chem. 38 (1973) 957, https://doi.org/10.1021/jo00945a025.
[53] R. Fischer, Arch. Pharmazie 279 (1941) 306, https://doi.org/10.1002/ardp.19412790904.
[54] A. Brillante, et al., Chem. Phys. Lett. 218 (1994) 568, https://doi.org/10.1016/0009-2614(94)00017-4.
[55] S. Phukan, et al., J. Photochem. Photobio. A: Chem 303 (2015) 67, https://doi.org/10.1016/j.jphotochem.2015.02.007.
[56] C.Y. Hsu, Y.L. Liu, Chemistry 17 (2011) 5522, https://doi.org/10.1002/chem.201003692.
[57] X. Liu, et al., J. Phys. Chem. C 121 (2017) 13274, https://doi.org/10.1021/acs.jpcc.7b04176.
[58] J. Orbulescu, et al., J. Mater. Chem. 15 (2005) 3084, https://doi.org/10.1039/b501510c.
[59] T. Debnath, H.N. Ghosh, ChemistrySelect 5 (2020) 9461, https://doi.org/10.1002/slct.202001751.
[60] M. Gutiérrez, et al., Adv. Opt. Mater. 8 (2020) 2000670, https://doi.org/10.1002/adom.202000670.

Statement of Authorship for joint/multi-authored papers for PGR thesis

To appear at the end of each thesis chapter submitted as an article/paper

The statement shall describe the candidate's and co-authors' independent research contributions in the thesis publications. For each publication there should exist a complete statement that is to be filled out and signed by the candidate and supervisor **(only required where there isn't already a statement of contribution within the paper itself).**

Title of Paper	Stable photoinduced metal-organic nanosheet blue phosphor for white light emission
Publication Status	☑ **Published** ☐ Accepted for Publication ☐ Submitted for Publication ☐ Unpublished and unsubmitted work written in a manuscript style
Publication Details	**D. A. Sherman,** W. Kamal, S. J. Elston, A. A. Castrejón-Pita, S. M. Moris, J.-C. Tan, "Stable photoinduced metal-organic nanosheet blue phosphor for white light emission", *Materials Today Chemistry*, 38, 102089 (2024).

Student Confirmation

Student Name:	Dylan A. Sherman		
Contribution to the Paper	D.A.S: conceptualization, methodology, synthesis, data collection (unless stated otherwise below), all data analysis, first draft manuscript, review and editing. D.A.S. and W.K.: inkjet printing by collaboration (equipment operated by W.K.). Chemistry NMR Facility: NMR digest data collection. D.A.S and C.B: FE-SEM data collection by collaboration (equipment operated by C.B.). W.K., S.J.E., A.A.C.P, S.M.M, and J.-C.T.: manuscript review and editing. J.-C.T.: supervision. Note: 'by collaboration' indicates D.A.S was present and participating in data collection.		
Signature		Date	1/10/2024

Supervisor Confirmation

By signing the Statement of Authorship, you are certifying that the candidate made a substantial contribution to the publication, and that the description described above is accurate.

Supervisor name and title:	Prof. J. C - Tan.		
Supervisor comments	I support this application.		
Signature		Date	1 Oct 2024

This completed form should be included in the thesis, at the end of the relevant chapter.

4

Printing techniques for fabricating LMON-based devices

4.1 Premise

Fabrication of MOF surfaces and films is a well-recognised challenge in the field, and one that limits the use of MOFs in luminescent-based applications such as micro sensors for pressure and environmental conditions, along with lighting and tagging. Printing techniques, such as direct writing or inkjet printing, have offered the most customisability and precision in constructing LMOF surfaces, but still have limitations. These range from time and cost, the small scope of applicable MOFs due to needing small particle size, and limited ability to control homogeneity of the depositions. This chapter establishes LMONs as a means to overcome these limitations. The morphology and particle size results in improved precision and quality of prints, establishing a new technique for MOF material patterning and coating: aerosol-jet printing (AJP).

4.2 Patterned MOF Films

Synthesised typically as powders, MOFs need to be shaped into desired forms through fabrication techniques to be usable in manufacturing for potential applications. MOF powder is often brittle and insoluble, making this conversion process difficult.[127] Frequently, post synthesis fabrication can compromise the porous structure of MOFs either through a loss of crystallinity (e.g., pelletising or etching) or blocking of pores (e.g., MOF-polymer matrix). Dye@MOF materials have the additional challenge of needing to avoid guest leaching and dilution due to solvent infiltration during material processing.[128]

The integration of MOFs into devices such as sensors and optoelectronics is still often hindered by the lack of versatile and controllable deposition and surface patterning techniques.[38] Most WLE MOF systems rely on rough and uneven deposits of powder for proof-of concept UV-chip based OLED composites.[83,129-133] Very few studies extend investigations into fabrication. Even less considered is fabrication at smaller scales to produce films and patterned surfaces at the micron scale rather than bulk coatings.[3] Thus, processing MOFs into specifically patterned micro- and nano-films that are structurally robust and exhibit operational flexibility is a highly desired area of exploration.[3,134]

Liquid-phase epitaxy, chemical vapour deposition, or electrochemical deposition can effectively grow even surface depositions, but only if the chemistry of the MOF permits such growth.[135] Even then, precise patterning is not viable unless a mould or directing agent for masking is used. Alternatively, techniques such as

lithography (UV, X-ray, electron beam or chemical etching) and lift-off patterning provide subtractive approaches.[136] These techniques risk damaging the framework at the interface and edges of the areas subtracted, and given the interconnected nature of MOF structures, this can have broader repercussions due to extended strain effects in the framework.[137]

4.3 Printing MOF films

A more recent method for WLE guest@MOF fabrication that offers wider applicability, along with improved control and precision, is patterning by printing.[138-139] Printing can also directly enhance functional properties. Our lab, for example, has demonstrated the effectiveness of 3D printing as a tool for light emission control: by combining yellow-emitting ZIF-8 with blue-emitting photopolymer resin, WLE was attained.[109] Adjusting the thickness of the printed pellets altered emission chromaticity. Of note, however, 3D printing for shaping entire objects and structures is beyond the scope of this chapter. MOF framework film printing is dominated by direct ink-writing,[139-141] and some fused deposition modelling (reshaping thermoplastic filaments) (Figure 4.1). A small selection of LMOF materials have been successfully inkjet printed for functions including anti-counterfeiting, watermarks, and sensors.[142]

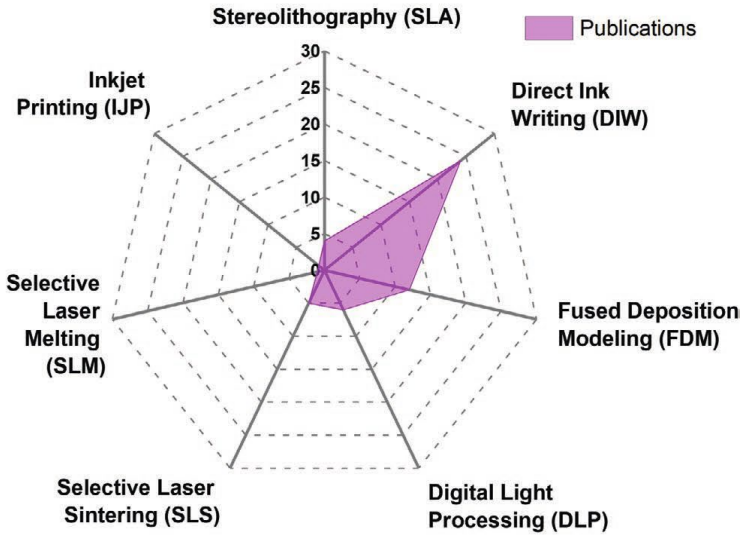

Figure 4.1. Publications of printed MOF materials as of 2022 based on technique used. Reproduced with permission from Ref. [139]. Copyright Wiley, 2022.

Inkjet printing, while not frequently used, offers notable benefits including digital control and scalability, along with being a non-contact and mask-free approach.[142] The process is additive so layers can be added sequentially, albeit often a timely process that requires recalibration between runs.[143] Inkjet printing has been used for applications such as security or climate indicators on packaging, sensor bio arrays, and OLED display pixels.[139] Considerations such as the ink viscosity, surface tension, and interaction between ink and target substrate are critical variables for successful printing.[144] The formulation of inks is a major limitation and a small range of viscosities and surface tensions are required to avoid highly defective and unpredictable prints. Success is often impeded by particle size of the crystalline powders and material instability, which can lead to agglomeration during printing in solvents. [136,145-146]

4.4 Aerosol Jet Printing

AJP is a digitally controlled advanced modern deposition technique. Early uses of AJP, after the first commercial system in 2004, focussed on printing electronic components such as silver conductive patterns, graphene interconnects or perovskite-based photodetectors.[147] Now, applications have expanded to actuators and a gamut of sensors, from biosensors to mechanical sensors for strain, motion sensors, hazardous gas sensors, photosensors, and more.[148] These are useful for human activity monitoring and antibody detection, touch sensors for robotics, construction of prostheses and implants, and integrated microheaters.[148] AJP aligns with a drive to produce smaller, lighter, and higher performing electronic devices while remaining cost effective. By 2032, the market for integrated electronics on and within materials is forecasted to reach $3.5 billion. [148]

AJP utilises a focussed aerosol stream to precisely print materials without contact, with high-spatial-resolution features up to ~ 10 nm. [147,149-150] In brief, the technique involves atomisation of the ink, followed by a stream of inert gas to deposit the ink (see Figure 4.2). The ink travels through tubing (~ 10 s) before being accelerated through a nozzle typically of 20 mm length and 50-300 μm internal diameter. Our studies employed ultrasonic atomisation, producing print droplets of 1-5 μm in diameter. A range of factors can be tuned in the system to optimise prints, including aerosol gas flow rate, sheath flow rate (printed line width), and atomisation strength.

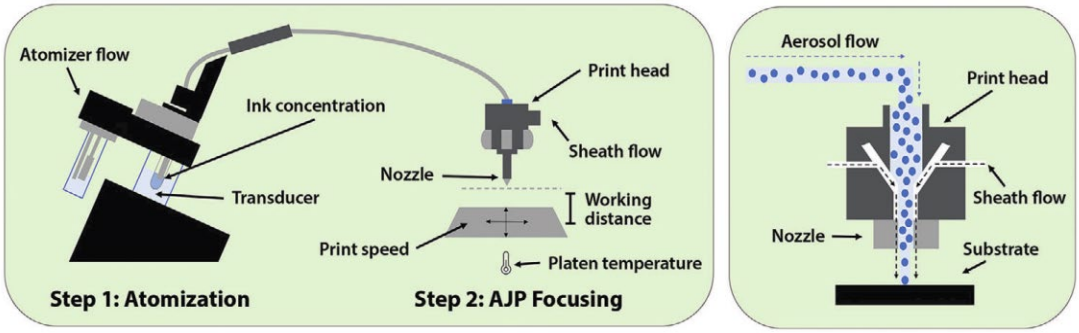

Figure 4.2. Diagram of key components within aerosol jet printing equipment. Right panel represented a zoomed version of the printing head. Reproduced with permission from Ref. [148]. Copyright Wiley, 2023.

AJP offers improved resolution, flexibility, printing speed, precision, and complexity of patterns printable over traditional techniques such as inkjet printing (see Table 4.1).[149] The technique allows for increasing variability in viscosity (0.001-1 Pa s) compared to inkjet printing,[148] reducing the need for careful ink formulation. The distance between the nozzle and substrate can extend up to ~ 10 mm, allowing for printing on stepped or curved surfaces to produce complex geometrical designs. AJP also offers better control to print 3D structures without the need for moulds or support structures, with works creating various porous lattices and micropillar arrays.[151]

Table 4.1. Properties of prints by various techniques.[148]

Printing type	**Viscosity (Pa s)**	**Line width (µm)**	**Thickness per layer (µm)**
Inkjet	0.01-0.02	30-50	0.01-1.0
Aerosol-jet	0.001-1.0	10-120	0.01-3.0
Direct Writing	0.5-5.0	30-50	0.1-100

Substrates for printing have varied from traditional materials such as silicon, glass, and flexible polymers, to more advanced textiles and cellulose. Ink types are typically divided into metallics (silver, gold, platinum), common polymers (e.g., polyaniline and polydimethylsiloxane (PDMS)) and carbon graphene. Materials such as ionic liquids and perovskites are newly established inks currently being explored.

While metals were initially used as inks, research is actively exploring new functional dyes so that manufactured surfaces can achieve more useful functions, such as sensing or lighting.[148,152] Only a few works have reported AJP of luminescent materials. One work has printed UV luminescent quantum dots (5, 32, 23 % PLQY for blue, green and red, respectively).[153-154] Another has used europium-doped yttrium oxide nanospheres for red luminescent patterning.[155] Paper III outlines further examples.

MOFs are, theoretically, an ideal candidate for functional AJP dyes given the rational design and tuneability of MOF materials, coupled with diverse multifunctionality. LMOFs, in particular, provide luminescent functionalities that could be maintained and enhanced through AJP. However, no MOF materials have been directly printed with AJP. This is primarily due to system clogging that can result from using materials that exceed 2 Pa s or a diameter more than 300 nm, given the nozzle for printing typically has a diameter of 50-300 μm. Even where smaller particle sizes can be achieved, MOF particles are often charged and aggregate due to high surface area, resulting in particle clumps too large to print.

The porosity of MOFs also limits robustness when exposed to the process of atomisation and printing. Kravchenko *et al*. reported the only AJP of MOF related materials in 2022.[156] In that work, the metal and ligand precursor solutions were printed such that the crystallites of the MOF (UTSA-280) grew after printing on the Si substrates. A resolution of 100 μm was achieved. Coatings of different colours were achieved by increasing layering, which increased thickness and the scattering of light. The technique did result in limitations: stripes in the printing were observed due to defects caused by partial clogging of the atomiser, and limited control of topography was achieved due to crystalline growth post-synthesis.

4.5 Printing with MONs

4.5.1 Experimental Design

This study established MONs as ideal MOF material alternatives for printing, due to their more compatible 2D morphology and physical properties compared with bulk MOF materials. Two techniques were used to explore this: inkjet printing and AJP.

4.5.2 Inkjet Printing

The first approach employed, included in Paper II (specifically, Figure 6), used a Jetlab II, MicroFab Technologies inkjet printer to print films of MC@Z7-NS. The printer used a drop-on-demand (DoD) technique with a piezoelectric actuator,

which on deformation of the actuator, induced by an electric field, resulted in the formation and release of ink droplets (Figure 4.3). That is, applying a specified electric potential to the piezoelectric transducer created a pressure wave due to a small change in volume, which propagated towards the nozzle and released the ink droplet.

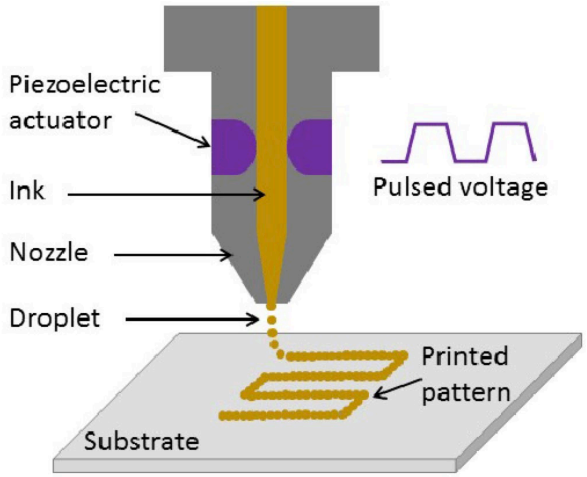

Figure 4.3. Drop-on-demand inkjet printing technique. Reproduced with permission from Ref. [157]. Copyright IOP Publishing, 2019.

30 mg of the LMON was mixed with 5 mL of isopropyl alcohol (IPA) to form an ink. While MeOH and ethanol (EtOH) were also tested as possible ink carriers, they were found to be too volatile, leading to LMON particles not being sufficiently controlled before deposition on a polyethylene terephthalate (PET) surface. Tests were also carried out with 2× and 5× dilution of LMON in the ink, but this was found to produce inconsistent particle deposition, increased aggregation of LMONs, and uneven surface cover. After optimising instrument parameters, a 12-layer square print of 763.6 µm × 1039 µm with a thickness of 26.15 µm was produced

(Figure 4.4). SEM and surface roughness imaging confirmed consistency of surface covering. A degree of roughness resulted from the additive process, which would increase surface area and thereby increase emission.

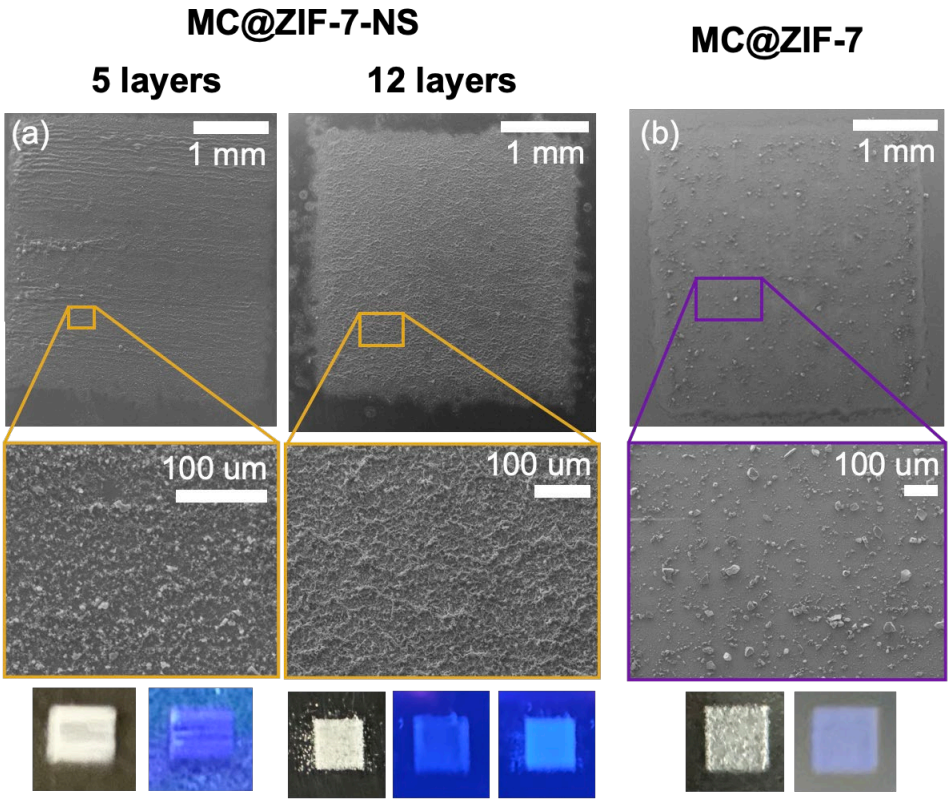

Figure 4.4. (a) SEM of 5 layers (left) and 12 layers (right) of MC@Z7-NS printed on PET. Bottom: photographs of the DoD prints under ambient (left) and 285-nm UV light (middle) with print under UV after 2 hours also shown for the 12-layer sample (right). (b) SEM of MC@ZIF-7 printed on PET, showing photographs of the print under ambient (bottom left) and 285-nm UV (bottom right) light.

The print exhibited luminescence consistent with that reported for MC@Z7-NS, including the transition under UV to lighter blue emission (see Paper II, Figure 6). MC@ZIF-7 was also printed to offer a comparison. In contrast to the LMON printing, 3D MC@ZIF-7 produced non-uniform surfaces with large, aggregated

particles. The printing methodology was also compromised, with large MC@ZIF-7 particles frequently blocking the printing nozzle, limiting controllable flow rate.

As a proof of concept, printing LMONs with inkjet printing was promising, but the method had limitations. Printing pattern options were limited, and the process was often timely due to particles blocking the nozzle of the system. Dyes also required frequent readjustment, and parameters needed retuning for different LMON samples that were attempted. We therefore turned to a more advanced printing system with which a more standard protocol could be developed: AJP.

4.5.3 Aerosol Jet Printing

An Optomec AJ200 was used to print LMON-based inks (Figure 4.5). A UA Max ultrasonic atomiser was fitted to the printer to atomise the ink for deposition. Sheath flow rate and atomiser flow rate were adjusted to optimise the focus ratio (sheath flow rate: atomiser flow rate) of deposition. A start-up focus ratio of approximately 1 was typically used to start material deposition. The focus ratio was increased from 5 to 9 to achieve a more focused deposition for printing. The adjustment ensured a consistent particle flow could form first before then narrowing the focus to produce more precise deposition. The printing speed was 0.5 mm/s on glass and 0.2 mm/s on PET. The nozzle used was a 150 μm tip set at a working distance of 1 mm. Printing was completed at a rate of 0.2 mm/s to ensure precision and efficiency could be balanced.

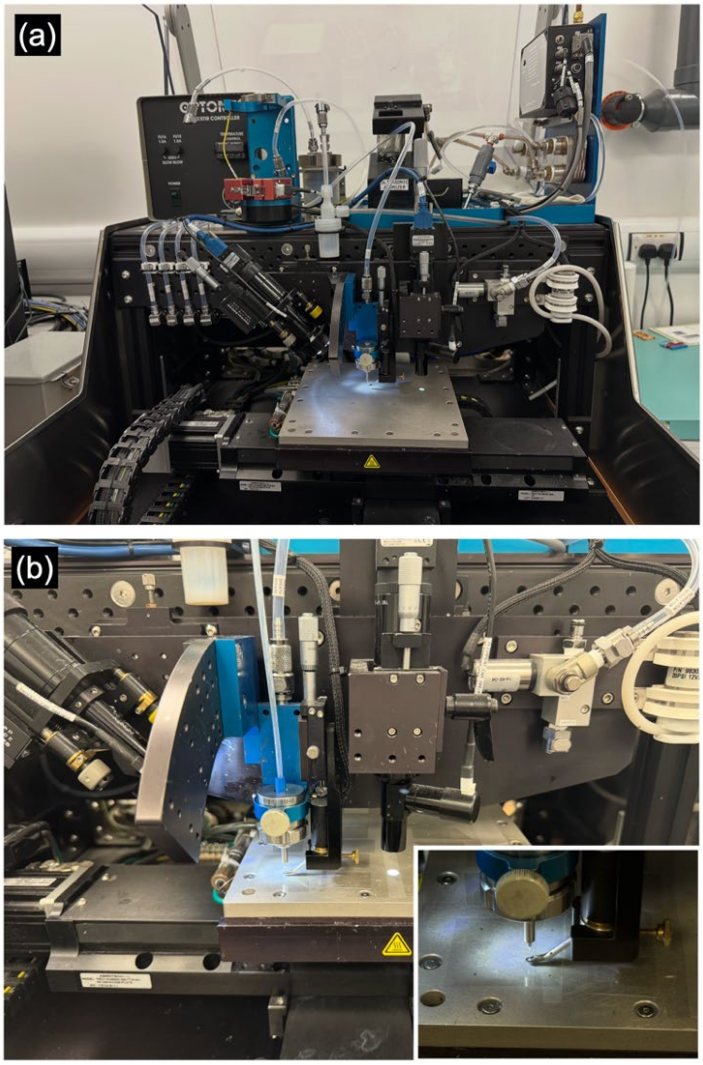

Figure 4.5. Images of Optomec AJ200 showing printing with LMON ink. (a) Complete system including atomiser, nozzle, and printing stage. (b) Printing stage and printing nozzle components (inset – zoom of printing nozzle).

Inks were developed using LMONs in toluene. As with DoD inkjet printing, using a less volatile and aprotic non-polar solvent reduced interactions with LMON particles that could cause aggregation, along with maintaining ink stability during the printing process. LMON concentration was sequentially tested from 10-40 mg/mL. While lower concentrations produced narrower lines (20 μm), overspray

increased. In contrast, the wider lines (45 µm) produced at 40 mg/mL reduced overspray and resulted in more distinct luminescent prints. Beyond 40 mg/mL the ink density was too high to print. 40 mg/mL was therefore selected for the printing study. Prints were characterised using SEM and an optical profilometer (Alicona Infinite) in terms of print thickness, width, cross sectional shape, and surface roughness (Paper III, Figure 1, Figure 4.6). A linear increase in print height was observed with increased layering across all LMON inks, along with consistent heights across different LMONs. Line width was found to decrease with increasing layers, while overspray width increased (a typical profile of AJP).

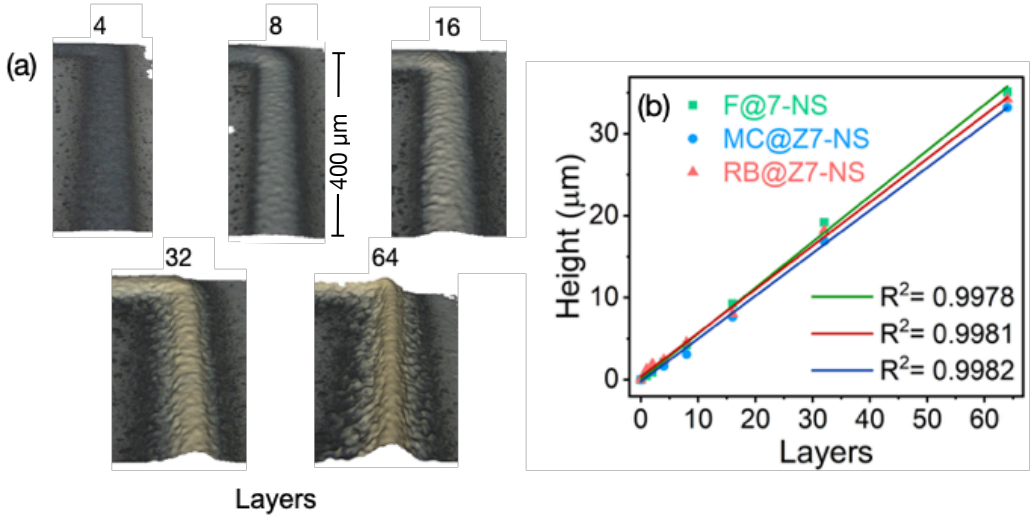

Figure 4.6. (a) Example characterisation of AJP prints with F@Z7-NS of varying layers using optical profilometry. Line width provided in Paper III, Figure 1. (b) Thickness of LMON prints relative to layers printed.

Four strategies were employed to demonstrate the versatility of printing to not only form luminescent films, but also control and enhance the luminescent properties of LMONs. Systematic studies of prints were microscopically analysed using fluorescence lambda scanning and *z*-stack confocal microscopy, a technique rarely employed to examine AJP or films of LMOF materials. These analyses allowed for data on homogeneity of emission and the collection of emission spectra (with a resolution of up to 3 nm) to identify spectral shifts.

Strategy 1 altered emission intensity and shade by printing homogenous LMON inks of different layers (Paper III, Figure 2, Figure 4.7). For three inks, F@Z7-NS, MC@Z7-NS, and RB@Z7-NS, prints of various layers were prepared to observe systematic adjustments in emission intensity. Emission spectra were normalised to the intensity of the 64-layered sample of each ink so inter-ink comparisons were possible. Noticeably, a point of self-quenching was observed at around 32 layers for F@ZIF-L and RB@ZIF-L, after which adding further layers no longer resulted in an increase in emission. In contrast, the weaker MC@Z7-NS blue emitter increased in intensity up to 64 layers. Importantly, printing quality and consistency was observed across all prints. Despite increasing overspray and varied cross-sectional height profiles across the line prints, cross sectional luminescent emission profiles appeared more consistent in emission intensity, showing defined emission patterns with limited diffuse light observed at the edges (Figure 4.7).

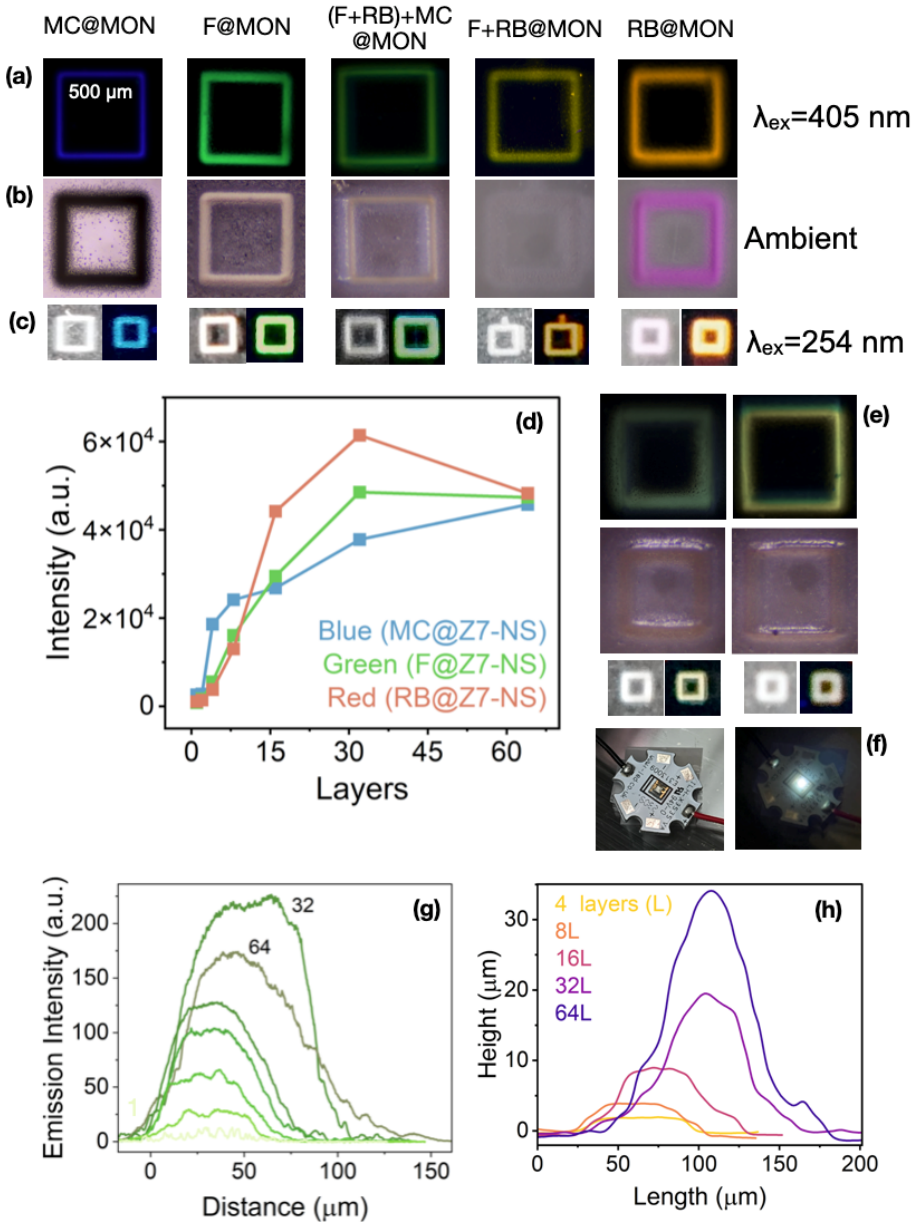

Figure 4.7. Examples of AJP printed LMON square perimeters of 500 × 500 µm. (a) Prints under fluorescence microscopy (405 nm excitation laser). (b) Prints under ambient light microscope. (c) Prints photographed under ambient (left) and 254 nm UV (right). (d) Emission intensity variations of LMON prints with increasing printed layers. (e) White-light emitting prints comprised of blue, green, and red emitting LMON layered prints under 405 nm excitation (above) and ambient light (below). Bottom images are the prints photographed under ambient (left) and 254 nm UV light (right). (f) WLE LMON printed on a UV diode to emit WLE. (g-h) Emission intensity profiles (g) and height profiles (h) perpendicular to line prints of F@Z7-NS prints with varying printed layers.

Strategy 2 involved the printing of different LMONs as layers on top of each other, to adjust chromaticity. Combining MC@Z7-NS and RB@Z7-NS, for example, resulted in a yellow emission, while printing MC@Z7-NS followed by layers of the yellow emitter DG@Z7-NS resulted in a green emitting print (Paper III, Figure 3, Figure 4.7). A systematic study of printing RB@Z7-NS layers on 32 layers of F@Z7-NS, however, exposed the limitation of layer control being dependent on the relative emission strength of the inks printed. Given RB@Z7-NS is a stronger emitter than F@Z7-NS, 1 layer caused an immediate shift from green to yellow. By 8 layers, emission chromaticity had shifted entirely to RB@Z7-NS only. For improved fine control of chromaticity, inks with more comparable emission intensity should be used.

A powerful application of additive layer colour control, however, is the ability to attain white light emission with varying degrees of warmth (Paper III, Figure 7, Figure 4.7). While a triple-guest Z7-NS effectively produced WLE, it required extensive synthesis to attain a sample with ideal emission coordinates. Here, printing combinations of red, green, and blue emitting inks (RB@Z7-NS, F@Z7-NS, and MC@Z7-NS respectively), achieved WLE directly and reliably. To reduce the emission intensity variation effect, layers were printed sequentially from the strongest to weakest emitter, so the most surface area exposed for a print was that of the weakest emitter. The layers were printed directly onto a UV-LED, producing a WLED. A handheld Ocean Insight FLAME-T-UV-VIS-ES miniature spectrometer was used to confirm the WLE broad band emission from the diode

(the diode was placed in a 3D printed cylindrical enclosure to prevent ambient light interfering with measured signal.)

Strategy 3 involved multi-patterning printing at 100-200 μm scales using different LMON inks to produce multi-emitting prints. For analysis and studies, concentric square perimeter prints were employed with the smallest dimension at 120 × 120 μm^2, followed by 300 and 500 μm. Given the average human eye resolution is 200 μm,[158] this meant patterns were mostly indistinguishable by eye, instead producing a single emission colour that combined the printed inks. For example, a 120 μm square perimeter of MC@Z7-NS combined with a 300 μm square perimeter of DG@Z7-NS produced a green emitter by eye, but clear distinguishable emission under microscopy from both inks. This method also allowed for near WLE to be achieved, by printing red, green, and blue emitting concentric squares. Indeed, more optimisation of layering and printing size could have achieved WLE. The fine scale printing achieved with this strategy also creates the possibility for precise micro-security tags that remain covert until illuminated with UV and observed under microscopy.

In contrast, scaling up the technique produced visible, bright visual indicators. For example, 0.5 cm mixed-emission colour rectangles were printed (Figure 4.9), and a detailed intricate lab logo was printed at 2 cm × 2 cm with 4 emission colours (Figure 4.9). No colour bleeding was observed in the emission. Here, printing on an emissive PET substrate (0.35 mm thickness) also allowed for colour of the print

to be hidden when the substrate emission dominated by exciting the sample under a 365 nm UV light.

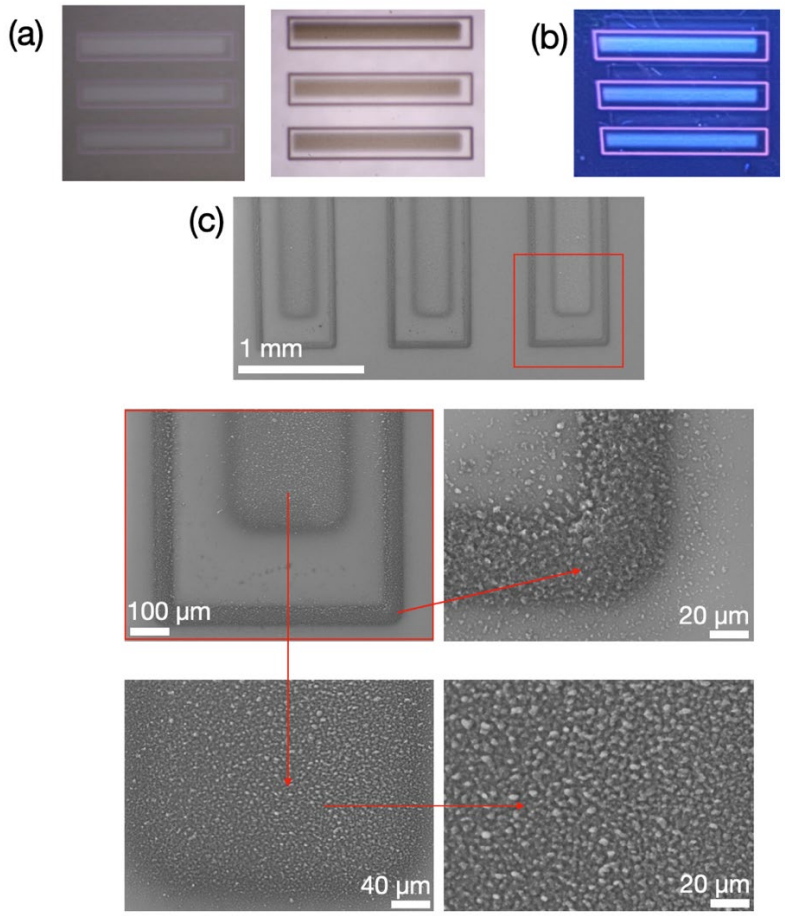

Figure 4.8. Large-scale RB@Z7-NS borders (5 mm × 0.5 mm) filled with F@Z7-NS. (a) Microscope images of prints under ambient conditions. (b) Prints under UV. (c) SEM of a single print edge, highlighting the border and central regions.

MOF 3D structures have been shown to improve application performance by increasing accessible surface area and creating more defined transportation routes. A final strategy, therefore, was to examine how pillars of LMON materials could be constructed. Pillars of 0.43 mm high, with a diameter of 60-80 µm were printed

by dynamically reducing the focus ratio so that less material was printed as the pillar extended in the *z*-axis. Z-stack microscopy revealed fluorescence emission was concentrated at the top of the pillar more than the sides, a potential example of the waveguide effect as seen in coumarin-based microfibres.[159]

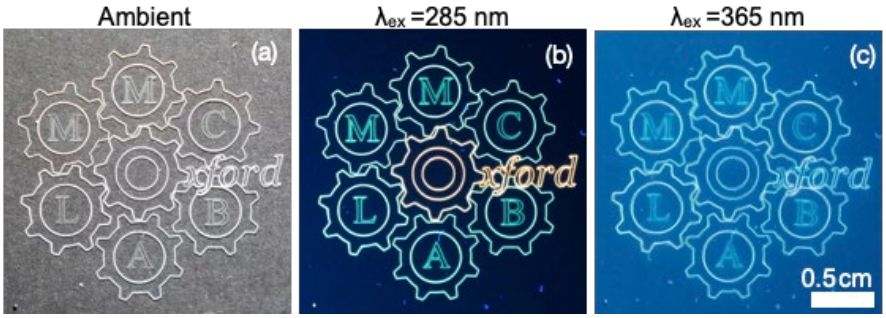

Figure 4.9. 2x2 cm multi-coloured print of the MMC lab logo using various LMON inks, observed under (a) ambient light, (b) 285 nm UV light, and (c) 365 nm UV light, where the PET emission supresses any observable colour variation.

4.6 Implications and Applications

Together, these findings established the significant potential of MONs to overcome the limitations of bulky 3D MOF materials to enable, for the first time, the use of MOF-based inks for aerosol-jet printing of micron-scale patterns. A portfolio of strategies was employed to show the wide range of fabricable patterns, ranging from single-dye printing to multi-dye additive printing and patterning, along with 3D pillar prints. The multi-dye patterning allowed for control of emission chromaticity at a finer level than control by initial synthesis conditions for the MONs, while 3D printing offered a degree of emission directional control. It was demonstrated that

the MON dyes could be printed to form intricate patterns for applications including covert security tags or printed on UV LEDs to create WLE OLEDs.

While this work exemplifies the possible patterns and consequent devices achievable using luminescent functionalised MONs, there are wider-ranging implications of these findings. Specifically, this work offers a new micron-level technique for fabricating MOF-based materials, providing a pathway towards device manufacturing. By altering the functionality of MOF dyes, such as by introducing conductivity, piezoelectric response, sensing capabilities, or electroluminescence, it is feasible to construct myriad new functional MOF surface devices with AJP. These could be for circuitry or micro-sensors for temperature, pressure, or chemical environments (either for biological or mechanical applications). In time, these could be integrated into nano-surfaces, or the development of nano-capacitors, and more.

4.7 Paper III

Fine-Scale Aerosol-Jet Printing of Luminescent Metal−Organic Framework Nanosheets

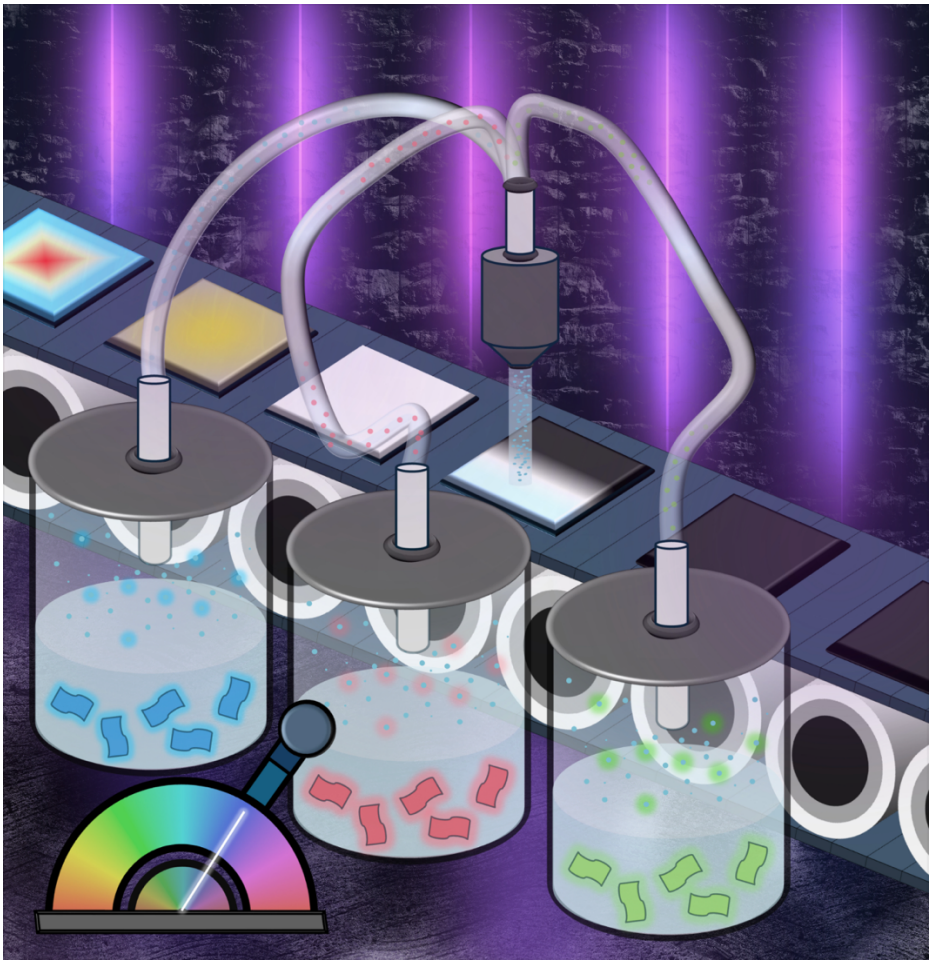

Figure 4.10. Artistic illustration of MON AJP.

Supporting information for this manuscript can be found here:

https://pubs.acs.org/doi/suppl/10.1021/acsami.4c10713/suppl_file/am4c10713_si_001.pdf

ACS APPLIED MATERIALS & INTERFACES

www.acsami.org
Research Article

Fine-Scale Aerosol-Jet Printing of Luminescent Metal−Organic Framework Nanosheets

Dylan A. Sherman, Erik Landberg, Anjana Ramesh Peringath, Sohini Kar-Narayan, and Jin-Chong Tan*

Cite This: https://doi.org/10.1021/acsami.4c10713
Read Online

ABSTRACT: Fabrication of metal−organic framework (MOF) thin films is an ongoing challenge to achieve effective device integration. Inkjet printing has been employed to print various luminescent metal−organic framework (MOF) films. Luminescent metal−organic nanosheets (LMONs), nanometer-thin particles of MOF materials with comparatively large micrometer lateral dimensions, provide an ideal morphology that offers enhancements over analogous MOFs in luminescent properties such as intensity and photoluminescent quantum yield. The morphology is also better suited to the formation of thin films. This work harnesses the preferential features of LMONs to access the advanced technique of aerosol-jet printing (AJP) to print luminescent films with precise geometries and patterns across the micrometer and centimeter length scales. AJP of LMONs exhibiting red (R), green (G), and blue (B) emission were studied systematically to reveal the increase of luminescence upon additive layering printing until a threshold was reached limited by self-quenching. By combining different LMON emitters, emission chromaticity and intensity were shown to be tunable, including the combination of RGB emitters to fabricate white-light-emitting films. A white-light LMON film was printed onto a UV light emitting diode (LED), producing a working white-light-emitting diode. Printing with multiple distinct photoluminescent inks produced intricate multicolor patterns that dynamically responded to excitation wavelength, acting either as micrometer-scale LED-type cells or larger visual tags. Collectively, the work offers an advancement for MOF thin films by printing MON materials using AJP, offering a precise method for manufacturing a wide range of critical functional devices, from luminescent sensors to optoelectronics, and more broadly even the opportunity for printed circuitry with conductive MONs.

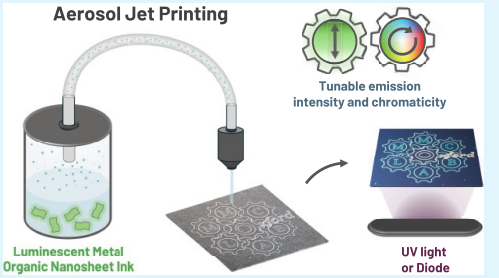

KEYWORDS: *metal−organic framework nanosheets, aerosol-jet printing, luminescent thin films, white-light-emitting diodes, micropatterning*

INTRODUCTION

Metal−organic framework (MOF) materials are evolving with enhanced properties ideal for microscale sensors, electronics, and organic light-emitting diodes (OLEDs).[1−3] A lack of fabrication techniques with control at the microscale and smaller, however, is a significant drawback to integrating MOFs into devices for these applications.[4] White-light-emitting (WLE) MOFs for organic LEDs (OLEDs), for example, are typically fine powders with intrinsic nonthermoplastic properties, brittleness, and insolubility. A common type of luminescent MOF design involves trapping luminescent guest molecules in the cavities of the MOF framework (guest@MOF).[5] The frameworks typically enhance guest stability and offer tunability for the luminescent properties of the guest. These particular WLE materials have the added difficulty of avoiding guest leaching and dilution due to solvent infiltration during material processing.[6] Thus, processing MOF nanocrystals into specific films that are structurally robust and exhibit operational flexibility is a highly desired area of exploration.[4,7]

Most WLE MOF diode-based devices utilize downward conversion from electric power to a blue LED or UV chip, which is absorbed by the MOF composite (yellow- or white-emitting, respectively) to generate WLE.[4] A few also integrate WLE MOF materials into electroluminescent devices.[8] Both methods typically require thin films of MOF composites, and their performance depends on film thickness and surface roughness, which influences charge transport.[8] Most successful WLE MOF works produce a rough and uneven deposit of powder for proof-of-concept MOF emission on UV chips.[9−14] Gong et al. instead dip-coated a 5 mm blue LED blub with a thin film of $[Zn_6(btc)_4(tppe)_2(DMA)_2]$, a WLE LMOF prepared via suspension in ethyl acetate followed by sonication.[15] Our lab has developed methods to circum-

Received: June 28, 2024
Revised: September 24, 2024
Accepted: September 25, 2024

navigate these challenges by preparing a guest@MOF yellow emitter three-dimensional (3D)-printed in a blue-emitting polymer resin and electrospinning high photoluminescence quantum yield (PLQY) MOF@fiber composites.[16−18]

A more recent method for WLE guest@MOF fabrication that offers improved control and precision is patterning by printing. MOF framework printing is dominated by direct ink-writing,[19−21] with a small selection of luminescent MOF materials successfully inkjet printed for functions including anticounterfeiting, watermarks, and sensors.[22] The process is additive so layers can be added sequentially, useful for applications such as security and climate or counterfeit tags on packaging, sensor bioarrays, or OLED display pixels. Considerations such as the ink viscosity, surface tension, and interaction between ink and target substrate are critical variables for successful printing.[23] Success is often impeded by the particle size of the crystalline powders and material instability, which can lead to agglomeration, during printing in solvent.[24−26]

Aerosol-jet-printing (AJP) is a fast-growing alternative manufacturing system that offers increased resolution, flexibility, and printing speed at the micron to nanoscale.[27] The noncontact technique involves the aerosolization of a functional ink that is deposited onto a substrate with resolutions up to 10 μm (typically between 30 and 50 μm).[27−29] Controlled digitally, fine microscale patterns can be achieved in 3D using additive manufacturing, with works achieving lattices and micropillar arrays.[30] While initially used for printing circuitry, the advent of new functional inks has led to printing more complex electronics, displays, and sensors for health and environmental applications.[31,32] Only a few works have reported the printing of luminescent materials. These include printed lanthanide-doped upconversion nanoparticles inks luminescent under NIR excitation;[33] electroluminescent inorganic OLED lines of red, green, and blue with 30 μm width for 140 ppi resolution screens;[34] europium-doped yttrium oxide nanospheres for red luminescent patterning;[35] one work on printing LED modules;[36] and printing of UV luminescent quantum dots (5, 32, and 23% QY for blue, green, and red, respectively).[37,38] Studies have yet to systematically examine how luminescence as a property can be modified as a function of printing parameters.

MOFs are ideal candidates for tunable functional inks, but AJP is limited by particle size being 50 nm or less to allow for ultrasonic atomization.[39] Particle aggregation also impacts the uniformity of particle size distribution, inhibiting effective atomization or further on printing itself. Only one report, to our knowledge, uses AJP related to a MOF. The work by Kravchenko et al. relies on reagent inks to overcome particle printing limitations so that an ultraporous calcium squarate framework forms in situ after printing.[40] Metal−organic nanosheets (MONs), MOF particles with a few nanometer-thin thickness but micrometer-wide planar dimensions, offer a morphology more suited to micro fabrication. Recent works also show how MONs such as ZIF-7-III (two-dimensional (2D) sheets) can be functionalized with guest incorporation to achieve luminescent MON (LMON) materials with particles of 2−5 nm thickness.[41] Emission colors ranged across the visible spectrum and included optimal WLE.[42] The zinc-based ZIF-7-III 2D nanosheets offer enhancements such as increased intensity and quantum yield over analogous guest@ZIF-7 3D materials due to increased surface area, optical transparency, and improved interguest cooperative behaviors due to interlayer packing configurations.[41,42] The fabrication of LMONs into thin films is a yet-to-be-explored opportunity.

This work utilizes organic dyes@ZIF-7-III LMON materials (dyes@Z7-NS) to demonstrate the first direct aerosol-jet printing of a MOF material to produce micrometer-scale control of thin film luminescent patterning. The potential for 3D LMON pillaring for directing emission is also illustrated. By systematically studying the emission properties of micro-patterns with fluorescence microscopy, we sought to establish property relationships that examined the effect of printing strategies on the emission properties of printed LMONs.

METHODS

All of the reagents, solvents, and chromophore guests were commercially acquired from Sigma-Aldrich, Fisher Scientific, and Alfa Aesar, and used as received.

Material Synthesis (Dye@Z7-NS). Material synthesis (dye@Z7-NS) as adapted from Sherman et al.[41] $Zn(NO_3)_2$ (59.5 mg, 0.2 mmol) was dissolved in methanol (MeOH) (2 mL). The solution was added to NaCl powder (20 g) under vigorous magnetic stirring. Benzimidazole (bIm) (283.5 mg, 2.4 mmol) was dissolved in MeOH (2 mL). The chromophore guests (7-methoxycoumarin (MC), fluorescein (F), and/or rhodamine B (RB)) were solubilized with MeOH (2 mL) via sonication and mixed with the bIm solution. After 20 min, the solution was added dropwise to $Zn(NO_3)_2$@NaCl followed by vigorous stirring for 12 h. Deionized H_2O (250 mL) was added to the flask and heated to 50 °C while stirring. The mixture was siphoned into 50 mL centrifuge tubes and centrifuged at 10,000 rpm for 20 min, followed by further washing and centrifuging cycles (3 × 45 mL of H_2O and 5 × 40 mL of MeOH). The final product was dried for 1 h at 90 °C (≈60−70% yield).

Ink. Ink suited for aerosol-jet printing was created by dispersing guest@Z7-NS in toluene to a concentration of 40 mg/mL followed by ultrasonication and vortexing. Optimal ultrasonication and vortexing times were found to be 10 min and 30 s, respectively.

Aerosol-Jet Printing. Aerosol-jet printing was performed using an Optomec AJ200 fitted with a UA Max ultrasonic atomizer to atomize the ink and deposit it on various substrates, primarily poly(ethylene terephthalate) (PET) film and glass slides. Sheath flow rate (sccm)/atomizer flow rate (sccm) determines the focus ratio for the deposition. The following AJ200 settings were generally used for deposition; A start-up focus ratio of approximately 1 until material deposition was achieved followed by a printing focus ratio of 5:9 to achieve a more focused deposition. Printing speed was 0.5 mm/s on glass and 0.2 mm/s on PET (0.35 mm thickness). A 150 μm tip nozzle was used with a working distance of 1 mm. The ultrasonic atomizer current was set between 0.5 and 0.6 A with the ultrasonic atomizer cooling water temperature at 14 °C. The substrate area (platen) was set to 70 °C. For pillar formation, a focus ratio of 0.375:1 was used to increase material deposition and reduce the risk of pillar breakage due to high gas flow.

Fluorescence Microscopy. Fluorescence microscopy images were collected using a Zeiss LSM780 with a 10× confocal lens. Lambda scanning (at a resolution of either 9 or 3 nm) was used to image fluorescence with laser lines of either 405 nm (diode source), 488 nm (argon multiline 25 mW), or 543 nm (HeNe 1 mW). Data was analyzed using Zeiss ZEN 3.9.

Scanning Electron Microscopy (SEM). Scanning electron microscopy was performed using a Hitachi SEM (TM3030 Plus 0865). Field-emission SEM (FE-SEM) was obtained at 10 keV under high vacuum using a Tescan Lyra 3 (Tescan, Czech Republic) with secondary and backscattered electron imaging (SEI and BSE, respectively) under 10−15 keV.

White-Light Emission Spectra. White-light emission spectra were collected using an Ocean Insight spectrometer. The output signal was carried by optical fiber, with one exposed end of the fiber 3 cm above the emitting diode, to the Ocean Insight FLAME-T-UV−vis-ES miniature spectrometer (200−850 nm). The spectrometer was

https://doi.org/10.1021/acsami.4c10713
ACS Appl. Mater. Interfaces XXXX, XXX, XXX−XXX

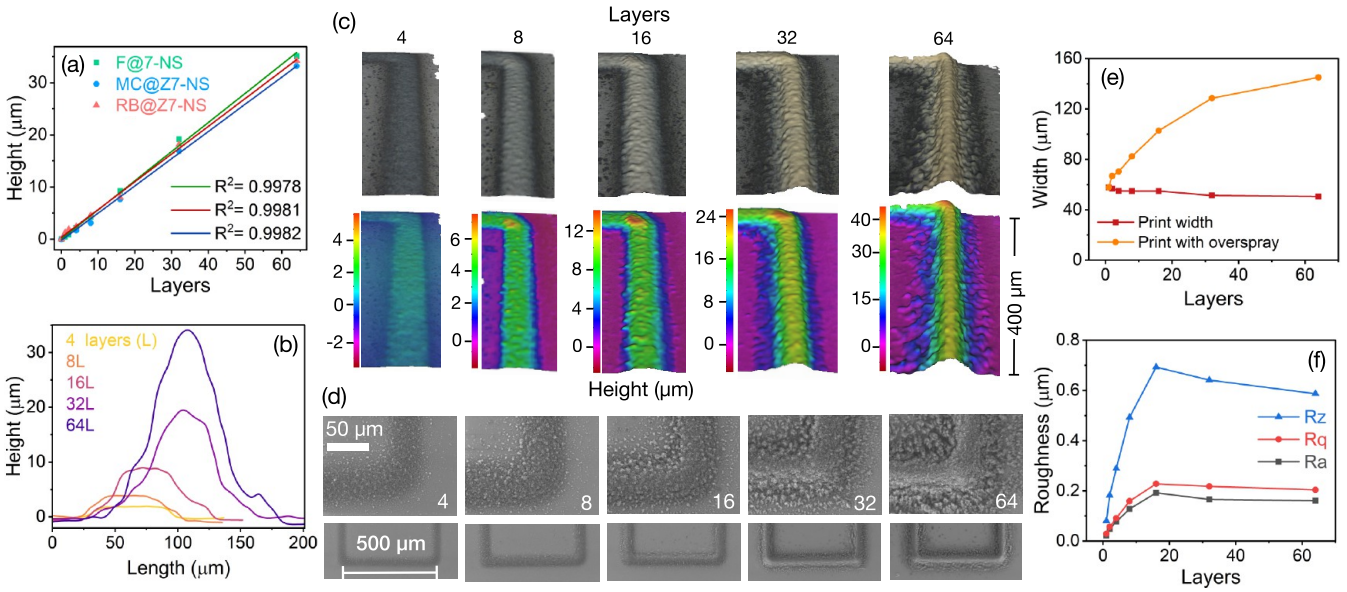

Figure 1. Characterization of aerosol-jet-printed luminescent metal−organic nanosheets (LMON). (a) Relative maximum heights of different LMON inks printed, showing linear relationships between the number of layers printed and printed pattern height. (b) Height profiles perpendicular to the printed line for F@Z7-NS prints of various layers. (c) Surface profiles of a single edge of F@Z7-NS square perimeter prints ($500 \times 500\ \mu m^2$) with various layers, presented as optical images (top) and height heat maps (bottom). (d) SEM of corresponding prints at various layers, showing print corners (top) and edge (bottom). (e) F@Z7-NS print widths (defined as width at 50% height, and complete width at base of height profile to include overspray), based on an average along one square edge of each print. (f) F@Z7-NS print surface roughness measured as R_z (mean distance between highest and lowest points on surface), R_a (mean), and R_q (root-mean-square) at varying layering.

connected to a computer running OceanView software for data logging and analysis. The diode was placed in a 3D-printed enclosed cylinder to prevent ambient light from interfering with measured signal.

Surface Roughness and Micropillar Dimensions. Surface roughness and micropillar dimensions were obtained using an InfiniteFocus Alicona optical profilometer. Images of the AJP prints were collected using a 20× objective lens at a vertical resolution of 50 nm and a lateral resolution of 3.5 μm. Data analysis, including height profiling and surface roughness, was computed using the Alicona IF Measure Suite. Surface roughness conformed with ISO 4287, using an area of width 30 μm and length 200 μm (26 profiles).

RESULTS AND DISCUSSION

Ink Development and Characterization. To create an LMON-based ink, the LMON particles were dissolved in a suitable solvent. Determining the solvent and optimal ink parameters is a sensitive process,[28] which required tuning of solvent and particle wt % before then modifying instrument parameters. While common solvents for AJP such as methanol, ethanol, and isopropanol were tested in various quantities and mixed ratios, toluene was found to be the ideal LMON ink solvent. One reason for this is its aprotic nonpolar character, limiting interaction with the Z7-NS dispersion, thereby discouraging aggregation. Lower volatility compared to that of methanol and isopropanol also meant that the ink remained more stable during printing, maintaining a good dispersion of LMON particles. To achieve proper deposition, the substrate platform was heated to 70 °C to assist in evaporation. Toluene viscosity at room temperature (0.68 cP at 20 °C) is below the optimal AJP viscosity window of 1−5 cP,[39] however cooling the ink to 14 °C achieved a viscosity appropriate for deposition. To determine the appropriate wt % of LMON in toluene, a range of values were tested for each dye (10, 20, 30, 40, and 50 mg/mL) across multiple layering (1, 2, 4, 8, 16, 32). Data showed beyond 40 mg/mL that the concentration of LMON particles was too high to effectively print. Below 40 mg/mL, the prints were undefined and inconsistent (see Figure S1). A concentration of 40 mg/mL was therefore selected for this study, with inks prepared in batches of 1.5 mL. PET film of 0.35 mm thickness was used as the substrate over glass slides, as the PET film was found to exhibit improved particle adhesion. Due to its thinness, flatness, and transparency, it is also ideal to place as a film over diodes or similar optical devices. The film was treated with EtOH as per previous studies to improve contact angle and increase particle adhesion further.[43]

Extensive trials were undertaken to optimize the focus ratio to produce prints with the highest resolution. Initial trials using low focus ratios resulted in diffuse and uneven printing (Figure S2). Ultimately a two-step focus ratio method was used to minimize deposition variability (see the Methods section), with precise parameters requiring minor adjustments given the inherent variability of the Optomec AJ200. This involved initiating the system with a low focus ratio (≈1) to initially create a flow of LMON particles. Before printing, the focus ratio was increased to 6−9, producing a consistent focused print with the least overspray possible. Depositions at high focus ratios that lasted over 1.5 h could be achieved without interference. For prints over 2 h (at a rate of 0.2 mm/s), incremental deposits of LMON formed on the walls of the ink vial and in the transfer tubing. This required redispersing the material in solvent from the walls and ensuring the set ink concentration remained.

To investigate the topography and printing quality of the optimized LMON prints, a series of printed square perimeters with edge length of 500 μm and varying layers (1, 2, 4, 8, 16, 32, 64) were prepared for three key LMON inks: the green emitter fluorescein@Z7-NS (F@Z7-NS), the blue emitter 7-methoxycoumarin@Z7-NS (MC@Z7-NS), and the red emitter rhodamine B@-7-NS (RB@Z7-NS). The prints were

https://doi.org/10.1021/acsami.4c10713
ACS Appl. Mater. Interfaces XXXX, XXX, XXX−XXX

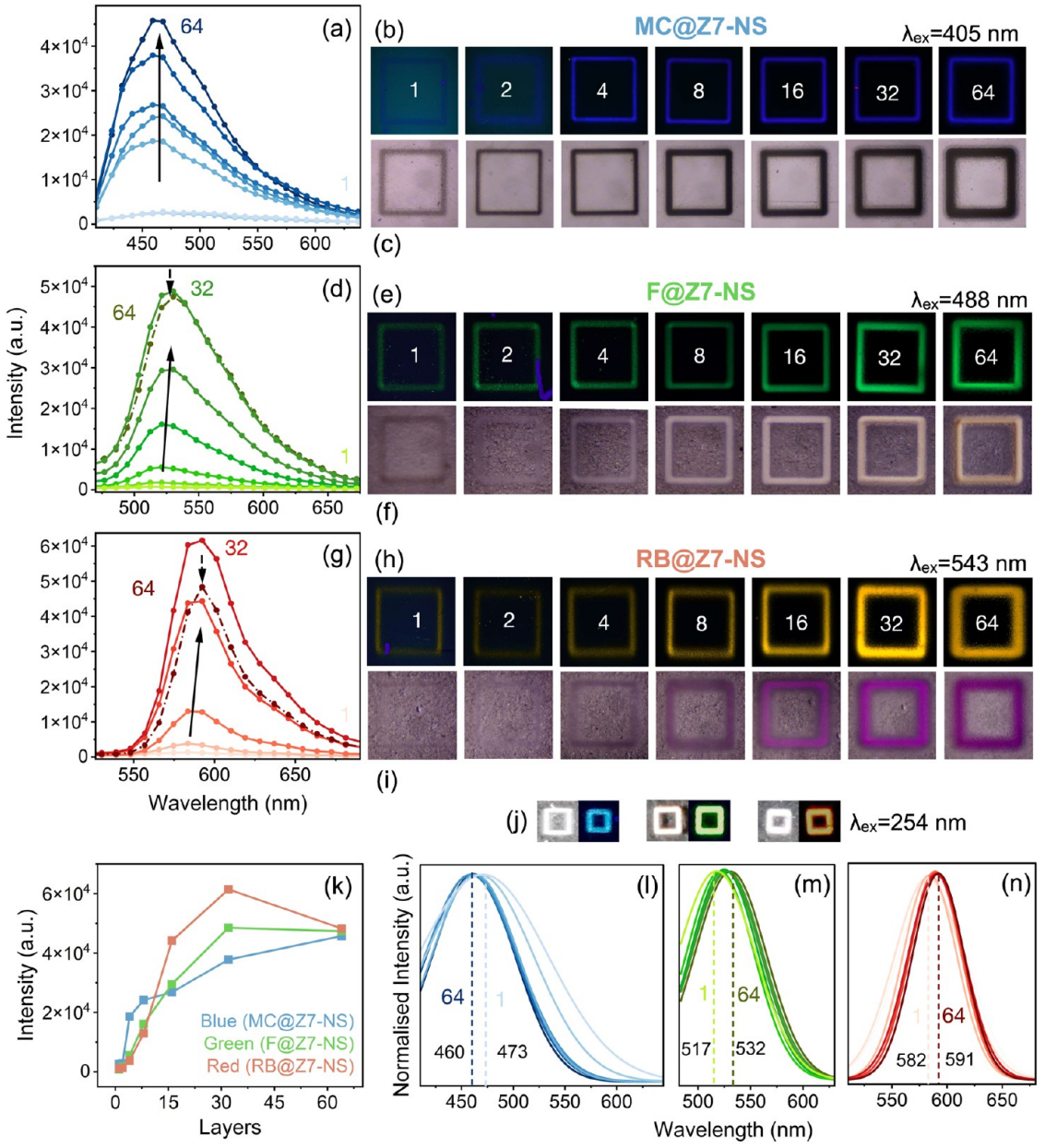

Figure 2. Fluorescence microscopy of AJP luminescent guest@Z7-NS square perimeter prints of side length 500 μm. Any dust or contamination on the substrate appears as bright purple marks. (a) Lambda scanning emission spectra from fluorescence microscopy for AJP MC@Z7-NS excited at 405 nm with increasing layering from 1 to 64 indicated by darkening of data points and lines. (b) Corresponding microscopy imaging of MC@Z7-NS prints excited at 405 nm, with numbers indicating layers in each image and color computed by Zeiss software, representing the intensity and chromaticity derived from the emission spectra. (c) Optical microscopy images of corresponding MC@Z7-NS prints. (d–f) Data as in (a)–(c) but for AJP of F@Z7-NS excited at 488 nm. (g–i) Data as in (a)–(c) but for AJP of RB@Z7-NS excited at 543 nm. (j) 32-Layer printed samples under ambient (left) and 254 nm UV light (right) for MC@Z7-NS, F@Z7-NS, and RB@Z7-NS (left to right). (k) Intensity of emission maximum for each print, relative to the 64-layering intensity. (l–n) Normalized and Gaussian fit spectral curves indicating any peak shift from 1- to 64-layer prints for MC@Z7-NS (left), F@Z7-NS (middle), and RB@Z7-NS (right).

characterized using optical surface profiling and scanning electron microscopy (SEM). The height of the prints (averaged along one square perimeter side of each print) was found to increase linearly with layers, with a maximum thickness of 32–34 μm (Figure 1a). This implies that each layer was of a similar consistency and height for all inks (0.53 ± 0.01 μm), suggestive of a reliable printing process; all layered prints of each LMON ink were printed in one session with no ink adjustment or intervention.

Investigating the height profiles of F@Z7-NS more closely, as an example, revealed a sequential transition from more rectangular surfaces with minimal overspray to a defined peak-shaped surface but with increased overspray (Figure 1b). Data show consistency along the line prints of each layer quantity (Figure 1c,d). These visual features were quantified by measuring printed line thickness at 50% of the maximum height to represent the line, compared to overspray at the lowest height profile width (Figure 1e). Data show that while the print width decreases from 57 to 50 μm with increasing layering, overspray significantly increases from effectively 0 to 95 μm (total overspray adding both edges of the print). Surface roughness of the samples revealed an increase in

https://doi.org/10.1021/acsami.4c10713
ACS Appl. Mater. Interfaces XXXX, XXX, XXX–XXX

roughness up to prints of 16 layers, followed by a slower decrease thereafter. This characterization suggests that depending on the resolution and shape of line desired, layering can be used to produce a flatter more even surface, or a more defined narrower surface, but with increased overspray. Of note, as these prints are intended for luminescent studies, the extent of overspray and print quality observed under ambient conditions is less significant than how these prints appear under UV and the effect any overspray and print shape will have on the observed luminescence. Indeed, increasing surface roughness exposes more surface area, which theoretically can increase the intensity of fluorescence emission. Notably, while not as precise as traditional AJP inks such as silver,[44] the consistency, control, and quality of these LMON AJP prints are comparable to more recently emerging sensitive organic/hybrid AJP inks in the literature (e.g., bioorganic inks and europium oxide phosphors).[45,46] They show significant improvement over the precision and repeatability obtained with inkjet printing LMON and LMOF materials.[42,43,47,48]

Controlling Luminescence through LMON AJP. What follows is a series of strategies that are systematically employed to examine how certain patterning and additive printing techniques can be used to tune the luminescence properties of the LMON ink. The work is compared to the previously established photophysical properties of the LMON materials in the literature.[41,42]

Strategy 1: Layering Homogeneous LMONs. We first examined the luminescent properties of the additive layering of the same LMON material using the square perimeter prints of side length 500 μm and the selection of 1, 2, 4, 8, 16, 32, and 64 layers. LMON inks included the green-emitting F@Z7-NS, red-emitting RB@Z7-NS, and blue-emitting MC@Z7-NS (Figure 2).

Fluorescence microscopy was employed to study the prints (Figure 2a–h), with lambda scans producing emission spectra for each print (Figure 2a,d,g), along with corresponding imaging of each print under laser excitation (Figure 2b,e,h) and ambient conditions (Figure 2c,f,i). Due to discrete laser wavelengths available, 405 nm was the highest energy excitation laser accessible to excite MC@Z7-NS while 488 nm was used for F@Z7-NS and 543 nm for RB@Z7-NS. These excitation wavelengths align well with the excitation ranges of each sample (Figure S3). The fluorescence imaging of each print was colored using Zeiss Zen software, calculated based on the emission profile of each print to simulate the color and intensity. To confirm these simulations against observed emission color, prints of 32 layers of each LMON were placed under a UV lamp (4 W, 254 nm) and photographed with zoom (Figure 2j).

Spectra (Figure 2a,d,g) confirm that all three LMONs emit consistent with the previously reported emission spectra of the LMON in powder form.[41] Line scans across the microscopy imaging confirm the homogeneity of the emission intensity along the patterning (Figure S4), with only minor intensity increases at the corners to be expected from the printing nozzle changing direction resulting in increased print thickness (seen also in Figure 2c). All prints (Figure 2b,e,h) show clear and defined luminescent patterns, with improved definition resulting from increased layering. While overspray was found to increase noticeably with layering, along with a shift from rectangular to peak-shaped topography, these adjustments appear to have minimal impact on the definition of the luminescence pattern observed in fluorescence imaging with little edge ghosting or shadow effects observed (see also photographs in Figure 2j). This is likely due to the relative minimal emission intensity contribution from overspray areas due to lower comparable thickness. Analysis of emission intensity perpendicular to F@Z7-NS line prints of varying layers (Figure S5) reveals single broad emission profiles (compared to profiles with multiple peaks and local maxima), supporting the observed defined visual appearance in imaging. These broad emission intensity profiles correspond to the overall line width of the prints, including overspray.

The PET substrate is emissive, with excitation λ_{max} = 340 nm and a corresponding broadband emission band from 300 to 600 nm with λ_{max} = 385 nm (Figure S6). In operating conditions, a 285 nm UV energy source was employed to avoid any noticeable contribution from the PET. The highest energy laser accessible for microscopy, however, was 405 nm and was used in this study to best represent operating conditions. Hence, the chromaticity of emission observed for each sample is blue-shifted by the emission contribution from the PET substrate, the intensity of which is dependent on the laser wavelength. For reference, images of each material with 32 layers under a 254 nm UV lamp (4 W, 5 cm from sample) taken with a digital camera and zoomed show each material's "true" operational color (Figure 1g).

Emission intensity from fluorescence imaging was normalized across different LMONs to the maximum layered sample of each LMON, achieved by adjusting the power of each excitation laser. This allowed for comparison not only between the layering of each LMON but also between different LMONs (Figure 2k). The maximum emission intensity for MC@Z7-NS increased mostly linearly with layer increase, apart from a sharp increase from 2 to 4 layers (Figure 2a). This is attributable to MC@Z7-NS being the weakest emitter, resulting in the patterns with the lowest material quantity exhibiting low intensity below the threshold of sensitivity of the detectors used. In contrast, the intensity of F@Z7-NS (Figure 2d) and RB@Z7-NS (Figure 2g), being stronger emitters, increases more linearly until 32 layers at which point intensity decreases for 64 layers. Given the linear increase in thickness with added layers (Figure 1a), this indicates there is a thickness threshold after which self-absorption by the bulk pattern dominates in competition with the intensity increase resulting from adding more LMON.

As a resolution of 9 nm was used to collect spectra, Gaussian peak fitting was employed to compare any peak maxima when analyzing potential energy shifts (Figure 2l–n). Fits reveal MC@Z7-NS emission bands narrow with increasing layering (a product of low detection), while F@Z7-NS and RB@Z7-NS present consistent peak shape and a red shift of 15 ± 9 and 9 ± 9 nm, respectively. Previous reports of these materials identified increasing aggregation to be the cause of red shift as guest loading increased.[41] As thickness increases with layering, there is increased particle content along the z axis, which may interfere with emission. This may create favorable conditions for increased interparticle guest interactions and further self-absorption, leading to enhanced aggregation effects seen in emission.

Strategy 2: Layering Mixed LMONs for Chromaticity Control. Second, we investigated the additive patterning of different LMONs to mix emission colors. Blue (32 layers, MC@Z7-NS)- and red (2 layers, RB@Z7-NS)-emitting LMONs were combined to produce a yellow emitter (Figure 3a). Emission spectra (Figure 3b, 3 nm resolution, λ_{ex} = 405

https://doi.org/10.1021/acsami.4c10713
ACS Appl. Mater. Interfaces XXXX, XXX, XXX−XXX

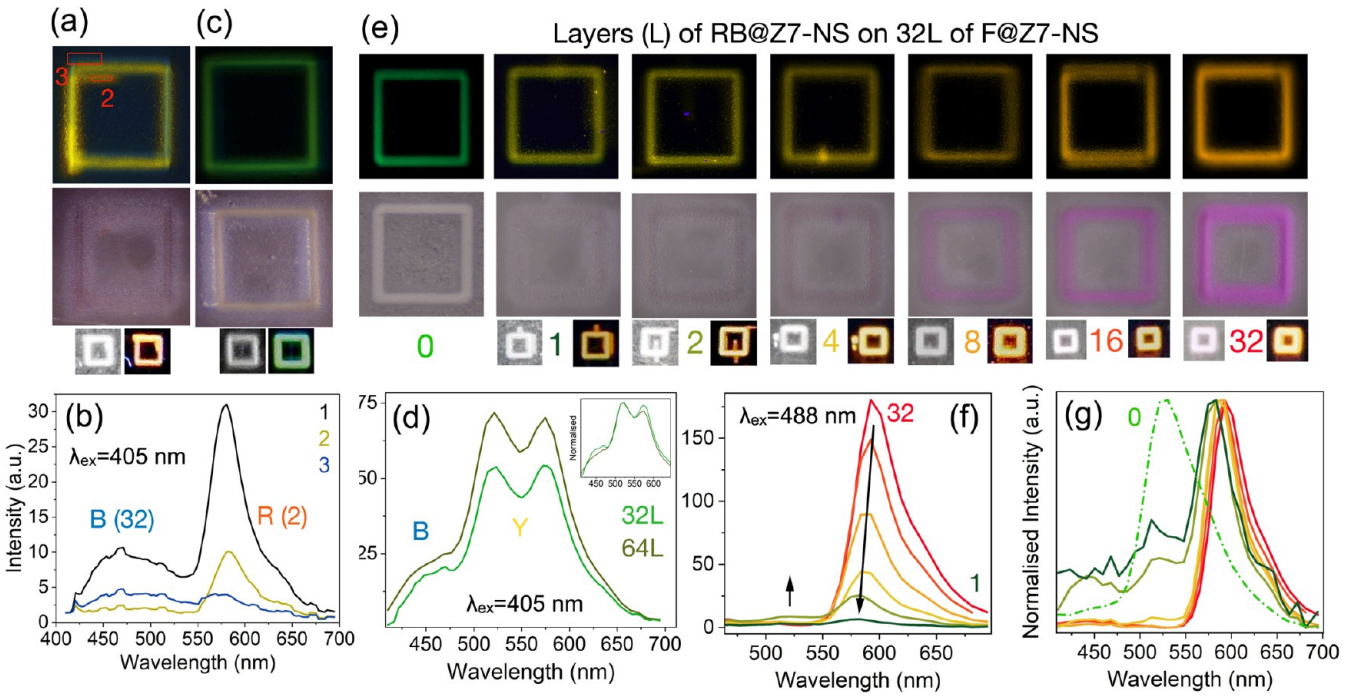

Figure 3. Square perimeter prints (500 × 500 μm^2 each) with layering of different MONs. (a) Microscopy of AJP of MC@Z7-NS (32 layers) + RB@Z7-NS (2 layers) excited at 405 nm (above) and under ambient conditions (middle), with the sample viewed using a digital camera in the same conditions (bottom); (b) emission spectra from pattern imaged in (a). (c) MC@Z7-NS with F + RB@Z7-NS print (in the same layout as (a)), with corresponding emission spectra and normalized emission spectra (inset) (d). (e) F@Z7-NS 32-layer prints with a series of increasing RB@Z7-NS layers (in the same layout as (a)). Numbers indicate the number of RB@Z7-NS layers. (f) Corresponding emission spectra and normalized spectra (g) of (e), including the initial 32-layer F@Z7-NS spectra as a broken green line. Colors indicate the number of RB@Z7-NS layers per the coloring of numbers in (e).

nm) reveal regions where printing did not overlap and either blue emission (λ_{max} = 475 nm) or orange-red emission dominates (λ_{max} = 590 nm). Spectra averaged across the entire print exhibit a blue/red emission band of 1:3, highlighting the intensity of RB@Z7-NS as an emitter compared with MC@Z7-NS. In contrast, combining MC@Z7-NS with RB + F@Z7-NS (yellow), 32 layers each, produced a bright-green-emitting pattern (Figure 3c,d). The same was achieved when the solution was scaled up to 64 layers each (Figures 3d and S7). The emission bands of each material MC@Z7-NS:RB + F@Z7-NS were measured in a 1:3.3 ratio to achieve emission mixing (Figure 3d, 3 nm resolution, λ_{ex} = 488 nm). Notably, we also inverted the samples and undertook lambda scanning of the samples (i.e., exciting the lower blue-emitting MC@Z7-NS printed layers first), to confirm that the spectral data collected matched the reported upright data and the sample appeared consistent.

A systematic study was further completed by layering RB@Z7-NS sequentially on 32 layers of green-emitting F@Z7-NS (Figure 3e–g). Spectra (Figure 3f,g, 9 nm resolution) show that from one layer, the RB@Z7-NS emission band dominates, and by four layers, is effectively the only contributor to the overall material emission. Indeed, as the F@Z7-NS emission band overlaps with the RB@Z7-NS excitation band (Figure S8), it is likely that the emission from F@Z7-NS printed MONs is, to some extent, being reabsorbed and emitted by RB@Z7-NS. Fluorescence imaging of the patterns shows a progressive shift from green to yellow, then to orange and dark orange/red. Chromaticity stabilizes at around eight layers, with the printing of further RB@Z7-NS layers only increasing emission intensity. SEM imaging of 1-layer vs 2-layer RB@Z7-NS on 32-layer F@Z7-NS (Figure S9) reveals the distinctive LMONs, with a well-dispersed coating of RB@Z7-NS over the base F@Z7-NS layers.

Strategy 3: Mixed LMON Multipatterning. Our third strategy involved the patterning of different materials at micrometer and larger centimeter scales. Blue- and yellow-emitting Z7-NS inks were printed as concentric square perimeters at two different scales. The smaller pattern (300 × 300 and 120 × 120 μm^2) (Figure 4a) appeared green when photographed under UV, with lambda scanning revealing the dominant yellow dye contribution to emission (Figure 4b). In contrast, when the squares were more distinct (500 × 500 and 120 × 120 μm^2) (Figure 4c,d), a blue square with yellow dot was visible when photographed and is differentiable by the eye (the average human eye resolution is 200 μm).[49] Emission spectra (Figure 4d) confirm an equal balance of emission from blue and yellow emitters across the entire print, with distinct emission profiles of blue or yellow light at each respective square print. A similar print was achieved by combining F@Z7-NS (32 layers, 120 × 120 μm^2) with RB@Z7-NS (1 or 2 layers 300 × 300 μm^2) to produce orange-red bordered green emission dot (Figure S10).

Toward developing LED systems, we explored the combination of red-green-blue-emitting dyes in concentric squares. A test with ordering from outer-inner squares of red-green-blue confirmed the intensity of the red dye overpowered any delineation in the separate prints (Figure S11). In contrast, printing with blue-green-red order (64-layer MC@Z7-NS, 32-layer F@Z7-NS, and 2-layer RB@Z7-NS) produced distinctive concentric square patterning of the key color components required for a white-light-emitting LED, when photographed

https://doi.org/10.1021/acsami.4c10713
ACS Appl. Mater. Interfaces XXXX, XXX, XXX−XXX

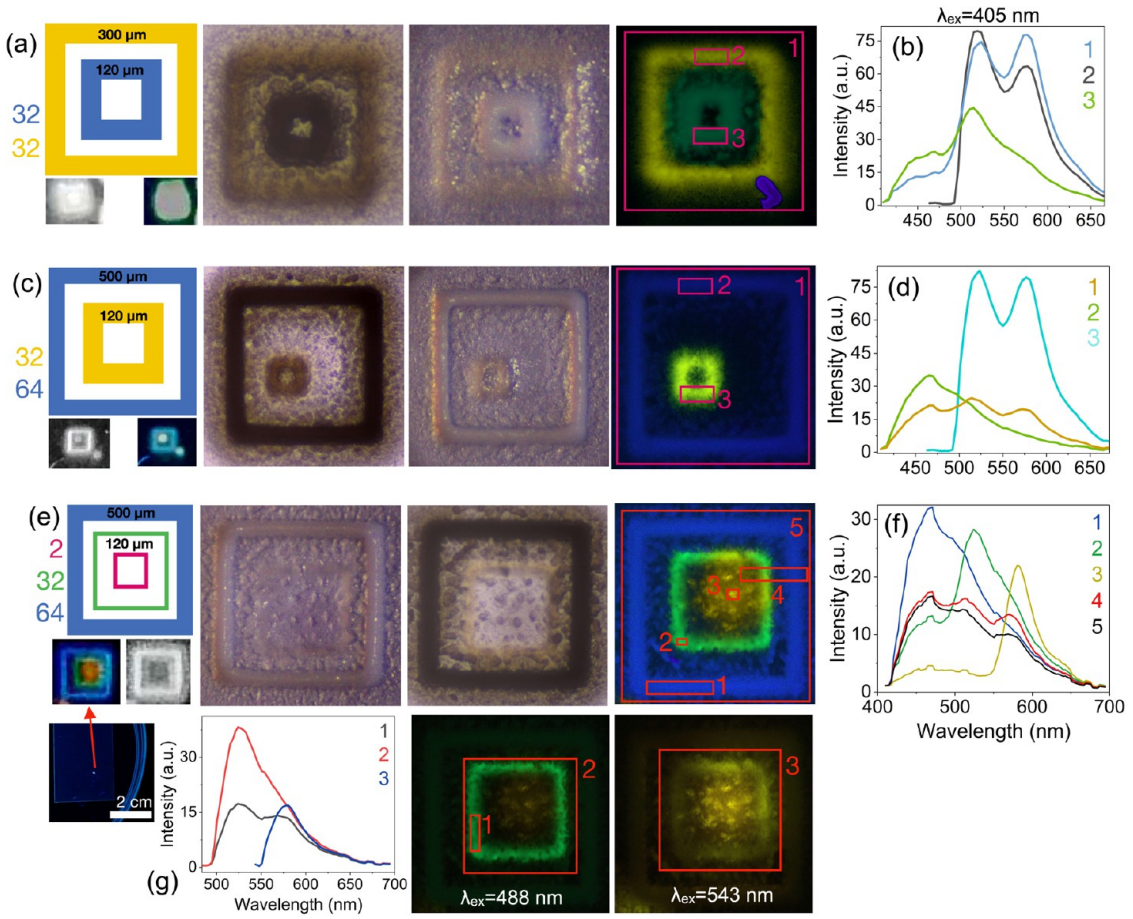

Figure 4. (a–d) MC@Z7-NS with F + RB@Z7-NS LMONs printed in various patterns of concentric squares (layers and dimensions indicated on the leftmost diagrams). Middle: optical microscopy images of prints under ambient conditions with uplighting (left) and downlighting (right). Right: microscopy images of prints excited at 405 nm. Bottom left images in (a) and (c) are taken with a digital camera to mimic observation by the eye under ambient (left) and UV light (right). (b, d) Emission spectra corresponding to highlighted squares in the rightmost image of (a) and (c), respectively. (e) MC@Z7-NS + F@Z7-NS + RB@Z7-NS multi-LMON print. Left: print conditions (leftmost diagram) with digital camera images below under UV (left) and ambient conditions (right) both zoomed and at eye level (lowest image). Middle: microscopy images of the print in (e) under optical ambient lighting (middle), and 405 nm excitation (right). (f) Emission spectra of print excited under 405 nm laser, with numbers corresponding to highlighted square sections of the print in (e). (g) Prints in (e) and (f) observed under 488 and 543 nm excitation showing microscopy images (right) and corresponding emission spectra (left). The spectral resolution is 3 nm.

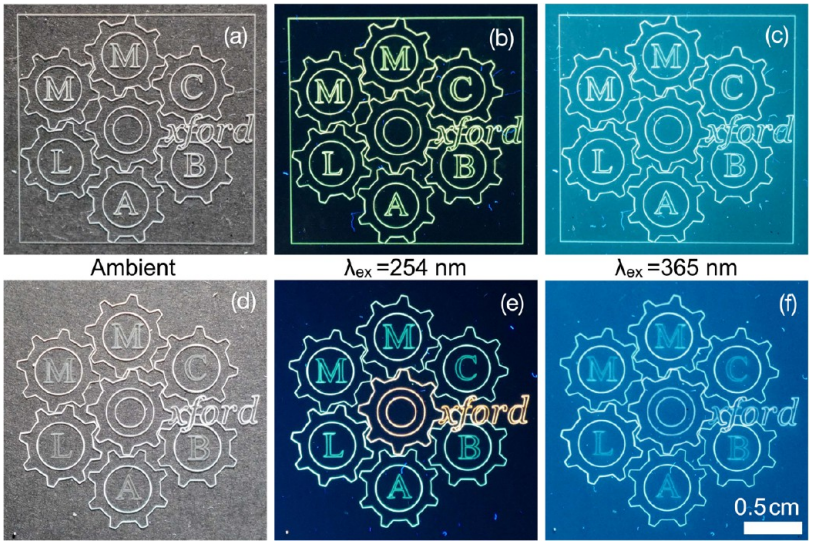

Figure 5. AJP print using yellow-emitting F + RB@Z7-NS LMON ink under ambient conditions (a), 254 nm UV light (b), and 365 nm light (c). AJP printed the logo using multiple LMONs of different emitters under ambient conditions (d), 254 nm UV light (e), and 365 nm light (f).

https://doi.org/10.1021/acsami.4c10713
ACS Appl. Mater. Interfaces XXXX, XXX, XXX–XXX

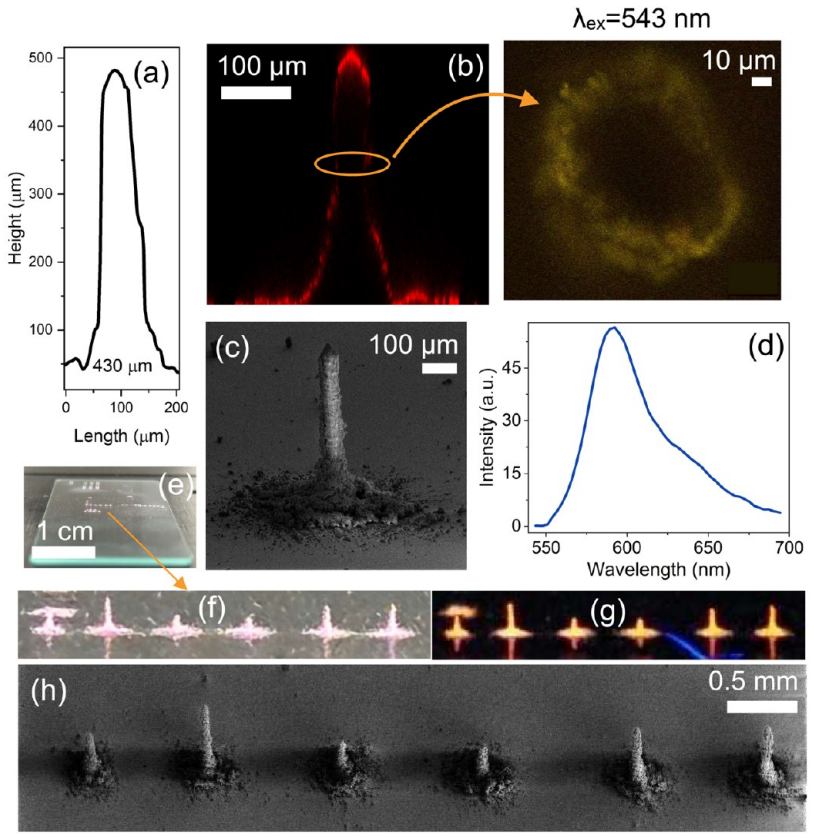

Figure 6. (a) Cross-sectional profile of the RB@Z7-NS printed micropillar. (b) Z-stack cross-sectional fluorescence microscopy image of the RB@Z7-NS micropillar excited with a 543 nm laser, including a horizontal slice through the pillar (right). (c) FE-SEM of RB@Z7-NS pillar. (d) Emission spectra from microscopy of RB@Z7-NS pillar. (e−g) RB@Z7-NS of various heights, under ambient (e, f) and UV (g) conditions. The second pillar from the left in (f)−(g) corresponds to the tallest RB@Z7-NS pillar in (a)−(d). (h) FE-SEM of images in (f)−(g).

and (Figure 4e). By eye, the print appeared a pale blue-white color (Figure 4e). Reducing the layering by 50% (from 64:32:2 to 32:16:1 for blue/green/red) produced even more defined pattern, apart from the single layer of red being too diffuse (Figure S12). Emission spectra from microscopy with 408, 488, and 543 nm laser excitations (Figure 4f) showed the distinctive emissions of each dye pattern. Their dynamic nature is also demonstrated, such that certain components can be turned on/off depending on the selected excitation wavelength range. These patterns are highly promising for enabling the future fabrication of miniaturized LEDs (100−200 μm). There is a potential to even print Micro LEDs (<100 μm),[50] if conditions and inks are optimized, given that a 40−50 μm line width was achieved.

In contrast, we also applied the inks on a larger scale, first to produce green filled red square emitting patterns (Figure S13). The prints show a clear separation between the green-emitting filler and red-emitting border. More usefully, we printed a logo pattern at 2 cm × 2 cm scale using a single yellow dye and then a multicolored dye (green, yellow, orange/red) (Figure 5). The printing exhibits high definition of all pattern components, including text lines and complex cog intersections, while the multidye process does not cause any smudging. On the contrary, the central cog is a precise overlap of yellow ink with one layer of red ink, producing a lighter orange emission than the remaining orange/red text. Usefully, if the logo is exposed to UV light within the absorption range of the PET substrate, the colors are muted to display a homogeneous white-light-emitting logo (Figure 5c,f). Hence, it is possible to discretely encode information (e.g., distinct dye coloring) only viewable under a targeted subset of desired wavelengths.

Strategy 4: Pillaring for 3D Directional Emission Control. Our fourth strategy was to expand printing in 3-dimensions using RB@Z7-NS. Initial static printing and increased layering of small circles or rectangles revealed frequent collapse of structures (Figure S14). By dynamically controlling the focus ratio, however, it was possible to prevent collapse and increase material addition to achieve cylindrical micropillars (Figure 6). For pillar creation, a low focus ratio was used to maximize material deposition while reducing the risk of pillar collapse due to high gas flow. After an initial 1 min deposit both sheath flow rate and atomizer flow rate were reduced to enable increased pillar height. Pillars achieved varying heights, depending on the parameters used, with a maximum height of 430 μm (Figure 6a−h). For the tallest pillars, the following settings were used; initial focus ratio 0.675 (sheath flow rate 27 sccm, atomizer flow rate 40 sccm), secondary focus ratio 0.5 (sheath flow rate 10 sccm, atomizer flow rate 20 sccm).

The pillars emitted in the orange-red region (Figure 6g) are seen in the average emission spectra (Figure 6d) and cross-section plane image (Figure 6b). A 3D-stack analysis of the pillar revealed that fluorescence was concentrated at the top of the structure (along with the aggregated base particles) (Figure 6b). This may be a waveguide effect, generating intensity at the edges of the structure as observed in luminescent coumarin microfibers.[51] Overspray is a common side-effect of pillar formation using AJP.[30,52] While only a proof of concept was demonstrated in this study, further optimization of parameters,

https://doi.org/10.1021/acsami.4c10713
ACS Appl. Mater. Interfaces XXXX, XXX, XXX−XXX

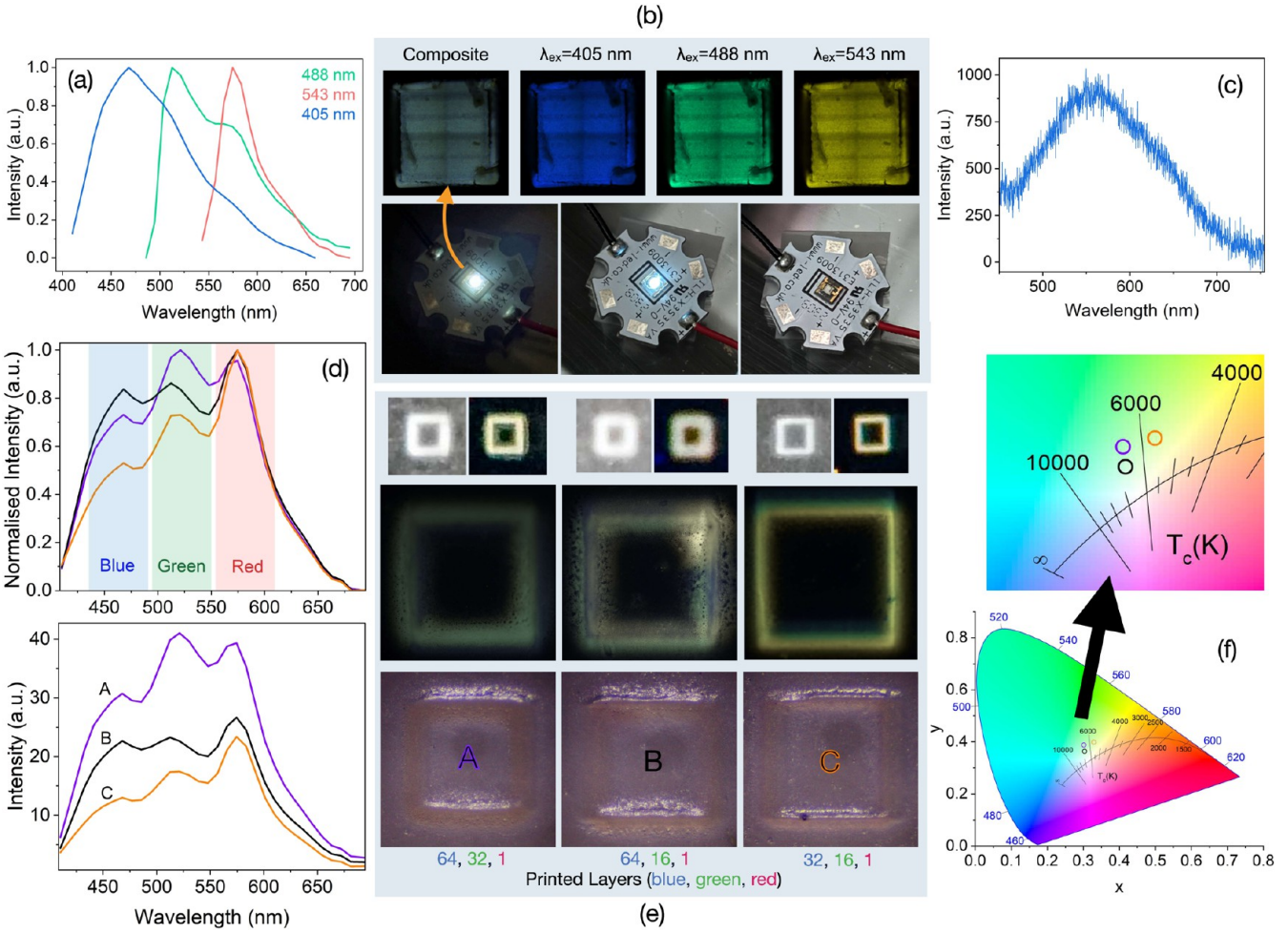

Figure 7. (a) Emission spectra of MC + F + RB@Z7-NS white-light-emitting ink on 365 nm emitting UV diode at various laser excitations (3 nm resolution). (b) Corresponding diode print (3.5 mm × 3.5 mm) microscopy images (top) with a combined average image (left). Images are a combination of four consecutive scans stitched together, causing the crosshair artifact. Bottom: Images of LMON-coated diode (3.4 V) off (right) and on (left). (c) Emission spectra of the diode when on. (d) Emission spectra of triple LMON layered WLE prints (3 nm resolution). (e) Images taken with a digital camera (top) and via microscopy (bottom) of corresponding prints (500 μm × 500 μm). (f) Chromatography of the layered prints.

along with the use of supporting sacrificial templates (e.g., hydrophilic polymer molds), may increase the control of structure growth.

Achieving White-Light Emission. Finally, two approaches were used to demonstrate white-light-emitting (WLE) LED (WLED) applicability of printing. For one, we coated a single thin layer of a white-light-emitting triple guest MC + RB + F@Z7-NS (previously reported) onto a flat square LED diode (3.5 mm × 3.5 mm, λ_{em} = 365 nm, 1 W at 3.4 V). Excitation with 405, 488, and 543 nm lasers confirms the presence of each guest emission band (MC at 460 nm, F at 515 nm, and RB at 580 nm) (Figure 7a,b). When operated at 3.4 V the LED glows white, most visible under darker conditions (Figure 7b). The emission spectra from the diode (Figure 7c) show a broadband of emission between 400 and 800 nm.

The synthesis of the triple guest WLE Z7-NS to achieve ideal white light is highly sensitive to guest concentration during synthesis; therefore, we also sought to develop a more robust WLE Z7-NS thin film methodology using additive manufacturing principles with our blue, green, and red MON emitter inks (MC, F, or RB@Z7-NS, respectively). Based on emission intensities from earlier strategy studies, a ratio of 64:32:1, 64:16:1, and 32:16:1 for blue/green/red Z7-NS emitter layers were selected. This produced prints of emission with CIE coordinates of (0.30, 0.38), (0.31, 0.36), and (0.32, 0.39) respectively (Figure 7d–f). Photographs of the prints under UV confirm their white appearance, and fluorescence microscopy confirms this emission color from lambda scanning, highlighting the change in the warmness of emission across samples (Figure 7e). The second print, achieving the closest to ideal white, exhibits three emission bands of near equivalent intensity, while the warmer third print shows a stronger RB emission contribution than MC (Figure 7d). As expected, the lighter white emission of the first sample has a stronger contribution by F.

CONCLUSIONS

Coupling the advanced techniques of aerosol-jet printing with nanosheets of metal–organic frameworks (MONs) as inks enabled a new strategy for effectively printing luminescent films with precise geometries and patterns at the micron scale. The morphology of the MONs overcame MOF printing limitations, allowing for atomization, effective continuous printing, and well-formed patterns of the particle aggregates.

https://doi.org/10.1021/acsami.4c10713
ACS Appl. Mater. Interfaces XXXX, XXX, XXX–XXX

Being digitally controlled, AJP was able to generate highly articulated images from logo patterns to intricate concentric squares. Functionalizing MONs with luminescent guests provided fluorescence emission-capable inks across a spectrum of colors. By variation of the layering and combination of inks, the emission chromaticity and intensity could be carefully tuned to a desirable output, including white-light emission. Meanwhile, printing with distinct inks enabled multiemission color prints at both the micron and centimeter scale. These prints are dynamically responsive to excitation wavelength, offering a platform for encoding environmentally sensitive information. Tuning the AJP parameters carefully further enabled the formation of 0.43 mm high-luminescence 3D pillars that exhibited a degree of directional emission.

These findings are critical for the advancement of luminescent MOF materials into devices from OLEDs to security tags and indicators. The potential of the established technique, however, goes far beyond. Altering the functionality of the MONs used as ink, such as enabling electroluminescence, sensing capabilities, or upconversion, could enable a wide gamut of luminescent-based devices for sensing (pressure, environments, temperature, etc.), optoelectronics, and energy storage. Beyond luminescence, conductive MONs could create carefully printed circuitry that could be immediately integrated into miniature devices. Collectively, the tunability of MONs coupled with the customizability of AJP offers a new platform for the patterning of integrated functional surfaces across scales from centimeters to microns.

■ ASSOCIATED CONTENT

Data Availability Statement

The data that support the findings of this study are available in the Supporting Information of this article. Any other data will be made available upon request.

Supporting Information

The Supporting Information is available free of charge at https://pubs.acs.org/doi/10.1021/acsami.4c10713.

Optical microscope images (Figure S1); SEM images (Figures S2 and S9); excitation spectra (Figure S3); emission intensity (Figures S4 and S5); PET substrate excitation (Figure S6); 64-layer F + RB@Z7-NS (Figure S7); solid-state powdered RB@Z7-NS absorption spectra (Figure S8); F@Z7-NS (32 layers) with RB@Z7-NS (Figure S10); RB@Z7-NS, F@Z7-NS, and MC@Z7-NS (Figures S11 and S12); large-scale RB@Z7-NS borders (Figure S13); and single position static printing of RB@Z7-NS (Figure S14) (PDF)

■ AUTHOR INFORMATION

Corresponding Author

Jin-Chong Tan − *Multifunctional Materials & Composites (MMC) Laboratory, Department of Engineering Science, University of Oxford, Oxford OX1 3PJ, U.K.;* orcid.org/0000-0002-5770-408X; Email: jin-chong.tan@eng.ox.ac.uk

Authors

Dylan A. Sherman − *Multifunctional Materials & Composites (MMC) Laboratory, Department of Engineering Science, University of Oxford, Oxford OX1 3PJ, U.K.;* orcid.org/0000-0003-1693-8661

Erik Landberg − *Department of Materials Science & Metallurgy, University of Cambridge, Cambridge CB3 0FS, U.K.*

Anjana Ramesh Peringath − *Department of Materials Science & Metallurgy, University of Cambridge, Cambridge CB3 0FS, U.K.*

Sohini Kar-Narayan − *Department of Materials Science & Metallurgy, University of Cambridge, Cambridge CB3 0FS, U.K.;* orcid.org/0000-0002-8151-1616

Complete contact information is available at: https://pubs.acs.org/10.1021/acsami.4c10713

Author Contributions

The manuscript was written through contributions of all authors. All authors have given approval to the final version of the manuscript. All images/artwork/photos that appear in this work, including supporting files and the table of contents graphic, were created by the authors of this manuscript.

Funding

D.A.S. acknowledges the scholarships from the General Sir John Monash Foundation and Clarendon Fund. J.-C.T. thanks the ERC Consolidator Grant (PROMOFS 771575) and EPSRC (EP/R511742/1) for funding the research. S.K.-N. acknowledges funding from UK Research and Innovation (UKRI) under the UK government's Horizon Europe funding guarantee (EP/Y032535/1). The authors acknowledge Dr Jana Koth, Facility Manager at the Wolfson Imaging Centre (MRC Weatherall Institute of Molecular Medicine), for the provision and operation of fluorescence microscopy equipment, Dr. Cyril Besnard and Professor Alexander Korsunsky for the acquisition of the FE-SEM images, and the Laboratory for In-Situ Microscopy and Analysis (LIMA).

Notes

The authors declare no competing financial interest.

■ REFERENCES

(1) Sun, Z.; Khurshid, A.; Sohail, M.; Qiu, W.; Cao, D.; Su, S. J. Encapsulation of dyes in luminescent metal-organic frameworks for white light emitting diodes. *Nanomaterials* **2021**, *11*, 2761.

(2) Lustig, W. P.; Mukherjee, S.; Rudd, N. D.; Desai, A. V.; Li, J.; Ghosh, S. K. Metal-organic frameworks: Functional luminescent and photonic materials for sensing applications. *Chem. Soc. Rev.* **2017**, *46*, 3242−3285.

(3) Tang, Y.; Wu, H. L.; Cao, W. Q.; Cui, Y. J.; Qian, G. D. Luminescent metal-organic frameworks for white leds. *Adv. Opt. Mater.* **2021**, *9*, No. 2001817.

(4) Karmakar, A.; Li, J. Luminescent mofs (lmofs): Recent advancement towards a greener wled technology. *Chem. Commun.* **2022**, *58*, 10768−10788.

(5) Gutiérrez, M.; Zhang, Y.; Tan, J. C. Confinement of luminescent guests in metal-organic frameworks: Understanding pathways from synthesis and multimodal characterization to potential applications of lg@mof systems. *Chem. Rev.* **2022**, *122*, 10438−10483.

(6) Xu, D. D.; Dong, W. W.; Li, M. K.; Han, H. M.; Zhao, J.; Li, D. S.; Zhang, Q. Encapsulating organic dyes in metal-organic frameworks for color-tunable and high-efficiency white-light-emitting properties. *Inorg. Chem.* **2022**, *61*, 21107−21114.

(7) Wang, J. X.; Yin, J.; Shekhah, O.; Bakr, O. M.; Eddaoudi, M.; Mohammed, O. F. Energy transfer in metal-organic frameworks for fluorescence sensing. *ACS Appl. Mater. Interfaces* **2022**, *14*, 9970−9986.

(8) Gutiérrez, M.; Martín, C.; Van der Auweraer, M.; Hofkens, J.; Tan, J. C. Electroluminescent guest@mof nanoparticles for thin film optoelectronics and solid-state lighting. *Adv. Opt. Mater.* **2020**, *8*, No. 2000670.

(9) Cui, Y.; Song, T.; Yu, J.; Yang, Y.; Wang, Z.; Qian, G. Dye encapsulated metal-organic framework for warm-white led with high color-rendering index. *Adv. Funct. Mater.* **2015**, *25*, 4796−4802.
(10) Yin, J. C.; Chang, Z.; Li, N.; He, J.; Fu, Z. X.; Bu, X. H. Efficient regulation of energy transfer in a multicomponent dye-loaded mof for white-light emission tuning. *ACS Appl. Mater. Interfaces* **2020**, *12*, 51589−51597.
(11) Wen, Y.; Sheng, T.; Zhu, X.; Zhuo, C.; Su, S.; Li, H.; Hu, S.; Zhu, Q. L.; Wu, X. Introduction of red-green-blue fluorescent dyes into a metal-organic framework for tunable white light emission. *Adv. Mater.* **2017**, *29*, No. 1700778.
(12) Li, Y.; Chen, Q.; Xie, L.-H.; Wang, K.; Zhao, M.; Li, J.-R. Single-phase white-light phosphors based on a bicarbazole-based metal−organic framework with encapsulated dyes. *ACS Mater. Lett.* **2022**, *4*, 2345−2351.
(13) Xia, Q. Q.; Wang, X. H.; Yu, J. L.; Xue, Z. Y.; Chai, J.; Wu, M. X.; Liu, X. Tunable fluorescence emission based on multi-layered mof-on-mof. *Dalton Trans.* **2022**, *51*, 9397−9403.
(14) Xiong, T.; Zhang, Y.; Donà, L.; Gutiérrez, M.; Möslein, A. F.; Babal, A. S.; Amin, N.; Civalleri, B.; Tan, J.-C. Tunable fluorescein-encapsulated zeolitic imidazolate framework-8 nanoparticles for solid-state lighting. *ACS. Appl. Nano Mater.* **2021**, *4*, 10321−10333.
(15) Gong, Q.; Hu, Z.; Deibert, B. J.; Emge, T. J.; Teat, S. J.; Banerjee, D.; Mussman, B.; Rudd, N. D.; Li, J. Solution processable mof yellow phosphor with exceptionally high quantum efficiency. *J. Am. Chem. Soc.* **2014**, *136*, 16724−16727.
(16) Chaudhari, A. K.; Tan, J. C. Dual-guest functionalized zeolitic imidazolate framework-8 for 3d printing white light-emitting composites. *Adv. Opt. Mater.* **2020**, *8*, No. 1901912.
(17) Zhang, Y.; Tan, J. C. Electrospun rhodamine@mof/polymer luminescent fibers with a quantum yield of over 90. *iScience* **2021**, *24*, No. 103035.
(18) Kachwal, V.; Tan, J. C. Stimuli-responsive electrospun fluorescent fibers augmented with aggregation-induced emission (aie) for smart applications. *Adv. Sci.* **2023**, *10*, No. 2204848.
(19) Lieu, W. Y.; Fang, D.; Tay, K. J.; Li, X. L.; Chu, W. C.; Ang, Y. S.; Li, D. S.; Ang, L. K.; Wang, Y.; Yang, H. Y. Progress on 3d-printed metal-organic frameworks with hierarchical structures. *Adv. Mater. Technol.* **2022**, *7*, No. 2200023.
(20) Yang, H.; Zhou, H.; Zhang, G.; Guo, X.; Pang, H. Recent progress of integrating mofs into printed devices and their applications. *Sci. China Mater.* **2023**, *66*, 441−469.
(21) Gregory, D. A.; Nicks, J.; Artigas-Arnaudas, J.; Harris, M. S.; Foster, J. A.; Smith, P. J. Controlling the composition and position of metal−organic frameworks via reactive inkjet printing. *Adv. Mater. Interfaces* **2023**, *10*, No. 2300027.
(22) Hazra, A.; Mondal, U.; Mandal, S.; Banerjee, P. Advancement in functionalized luminescent frameworks and their prospective applications as inkjet-printed sensors and anti-counterfeit materials. *Dalton Trans.* **2021**, *50*, 8657−8670.
(23) Alamán, J.; Lopez-Valdeolivas, M.; Alicante, R.; Pena, J. I.; Sanchez-Somolinos, C. Digital luminescence patterning via inkjet printing of a photoacid catalysed organic-inorganic hybrid formulation. *Polymers* **2019**, *11*, 430.
(24) Oh, J. W.; Lee, S.; Han, H.; Allam, O.; Choi, J. I.; Lee, H.; Jiang, W.; Jang, J.; Kim, G.; Mun, S.; Lee, K.; Kim, Y.; Park, J. W.; Lee, S.; Jang, S. S.; Park, C. Dual-light emitting 3d encryption with printable fluorescent-phosphorescent metal-organic frameworks. *Light: Sci. Appl.* **2023**, *12*, No. 226.
(25) Al-Ghazzawi, F.; Conte, L.; Wagner, K. K.; Richardson, C.; Wagner, P. Rapid spatially-resolved post-synthetic patterning of metal-organic framework films. *Chem. Commun.* **2021**, *57*, 4706−4709.
(26) Ruiz-Zambrana, C. L.; Malankowska, M.; Coronas, J. Metal organic framework top-down and bottom-up patterning techniques. *Dalton Trans.* **2020**, *49*, 15139−15148.
(27) Wilkinson, N. J.; Smith, M. A. A.; Kay, R. W.; Harris, R. A. A review of aerosol jet printing—a non-traditional hybrid process for micro-manufacturing. *Int. J. Adv. Des. Manuf. Technol.* **2019**, *105*, 4599−4619.
(28) Secor, E. B. Principles of aerosol jet printing. *Flexible Printed Electron.* **2018**, *3*, No. 035002.
(29) Smith, M.; Choi, Y. S.; Boughey, C.; Kar-Narayan, S. Controlling and assessing the quality of aerosol jet printed features for large area and flexible electronics. *Flexible Printed Electron.* **2017**, *2*, No. 015004.
(30) Chen, X.; Lawrence, J. M.; Wey, L. T.; Schertel, L.; Jing, Q.; Vignolini, S.; Howe, C. J.; Kar-Narayan, S.; Zhang, J. Z. 3d-printed hierarchical pillar array electrodes for high-performance semi-artificial photosynthesis. *Nat. Mater.* **2022**, *21*, 811−818.
(31) Fisher, C.; Skolrood, L. N.; Li, K.; Joshi, P. C.; Aytug, T. Aerosol-jet printed sensors for environmental, safety, and health monitoring: A review. *Adv. Mater. Technol.* **2023**, *8*, No. 2300030.
(32) Seiti, M.; Verma, A.; Degryse, O.; Vetrano, M. R.; Ferraris, E.Aerosol Jet-based Printing for Smart Multifunctional Nano-inks. In *Smart Multifunctional Nano-inks*; Elsevier, 2023; pp 75−90.
(33) Meruga, J. M.; Baride, A.; Cross, W.; Kellar, J. J.; May, P. S. Red-green-blue printing using luminescence-upconversion inks. *J. Mater. Chem. C* **2014**, *2*, 2221.
(34) Tait, J. G.; Witkowska, E.; Hirade, M.; Ke, T.-H.; Malinowski, P. E.; Steudel, S.; Adachi, C.; Heremans, P. Uniform aerosol jet printed polymer lines with 30μm width for 140ppi resolution rgb organic light emitting diodes. *Org. Electron.* **2015**, *22*, 40−43.
(35) Lin, A.; Zhang, Y.; Zhao, D.; Wu, Y.; Wang, S.; Li, J.; Fan, L.; Xiong, S.; Cao, L.; Gu, F. Flexible droplet printing of prominently luminescent patterns of europium-doped yttrium oxide nanospheres. *Addit. Manuf.* **2023**, *63*, No. 103412.
(36) Rudorfer, A.; Tscherner, M.; Palfinger, C.; Reil, F.; Hartmann, P.; Seferis, I. E.; Zych, E.; Wenzl, F. P. In *A Study on Aerosol Jet Printing Technology in LED Module Manufacturing*, Fifteenth International Conference on Solid State Lighting and LED-based Illumination Systems, 2016; Vol. 9954, p 99540E.
(37) Lin, H.-Y.; Sher, C.-W.; Hsieh, D.-H.; Chen, X.-Y.; Chen, H.-M. P.; Chen, T.-M.; Lau, K.-M.; Chen, C.-H.; Lin, C.-C.; Kuo, H.-C. Optical cross-talk reduction in a quantum-dot-based full-color micro-light-emitting-diode display by a lithographic-fabricated photoresist mold. *Photonics Res.* **2017**, *5*, 411.
(38) Han, H. V.; Lin, H. Y.; Lin, C. C.; Chong, W. C.; Li, J. R.; Chen, K. J.; Yu, P.; Chen, T. M.; Chen, H. M.; Lau, K. M.; Kuo, H. C. Resonant-enhanced full-color emission of quantum-dot-based micro led display technology. *Opt. Express* **2015**, *23*, 32504−32515.
(39) *Optomec. Aerosol Jet Deposition System Manual*, 2015.
(40) Kravchenko, D. E.; Matavž, A.; Rubio-Giménez, V.; Vanduffel, H.; Verstreken, M.; Ameloot, R. Aerosol jet printing of the ultramicroporous calcium squarate metal−organic framework. *Chem. Mater.* **2022**, *34*, 6809−6814.
(41) Sherman, D. A.; Gutiérrez, M.; Griffiths, I.; Mollick, S.; Amin, N.; Douhal, A.; Tan, J. C. Guest entrapment in metal-organic nanosheets for quantifiably tuneable luminescence. *Adv. Funct. Mater.* **2023**, *33*, No. 2214307.
(42) Sherman, D. A.; Kamal, W.; Elston, S. J.; et al. Stable photoinduced metal-organic nanosheet blue phosphor for white light emission. *Mater. Today Chem.* **2024**, *38*, No. 102089.
(43) da Luz, L. L.; Milani, R.; Felix, J. F.; Ribeiro, I. R.; Talhavini, M.; Neto, B. A.; Chojnacki, J.; Rodrigues, M. O.; Junior, S. A. Inkjet printing of lanthanide-organic frameworks for anti-counterfeiting applications. *ACS Appl. Mater. Interfaces* **2015**, *7*, 27115−27123.
(44) Li, M.; Yin, S.; Liu, Z.; Zhang, H. Machine learning enables electrical resistivity modeling of printed lines in aerosol jet 3d printing. *Sci. Rep.* **2024**, *14*, No. 14614.
(45) Xu, X. Eu_2O_3 microsphere luminescent material based on aerosol jet printing. *E3S Web Conf.* **2023**, *385*, No. 01014.
(46) Williams, N. X.; Watson, N.; Joh, D. Y.; Chilkoti, A.; Franklin, A. D. Aerosol jet printing of biological inks by ultrasonic delivery. *Biofabrication* **2020**, *12*, No. 025004.
(47) Mollick, S.; Zhang, Y.; Kamal, W.; Tricarico, M.; Möslein, A. F.; Kachwal, V.; Amin, N.; Castrejón-Pita, A. A.; Morris, S. M.; Tan, J.-C.

https://doi.org/10.1021/acsami.4c10713
ACS Appl. Mater. Interfaces XXXX, XXX, XXX−XXX

Resilient photoswitchable metal−organic frameworks for sunlight-induced on-demand photochromism in the solid state. *Chem. Eng. J.* **2023**, *476*, No. 146727.
(48) Zhang, H. B.; Liu, M.; Lei, X.; Wen, T.; Zhang, J. Digital controlled luminescent emission via patterned deposition of lanthanide coordination compounds. *ACS Appl. Mater. Interfaces* **2014**, *6*, 12594−12599.
(49) Ul-Hamid, A.*A Beginners' Guide to Scanning Electron Microscopy*; Springer Cham, 2018; pp 1−5.
(50) Liu, Z.; Lin, C. H.; Hyun, B. R.; Sher, C. W.; Lv, Z.; Luo, B.; Jiang, F.; Wu, T.; Ho, C. H.; Kuo, H. C.; He, J. H. Micro-light-emitting diodes with quantum dots in display technology. *Light: Sci. Appl.* **2020**, *9*, No. 83.
(51) Min, S.; Dhamsaniya, A.; Zhang, L.; Hou, G.; Huang, Z.; Pambhar, K.; Shah, A. K.; Mehta, V. P.; Liu, Z.; Song, B. Scale effect of a fluorescent waveguide in organic micromaterials: A case study based on coumarin microfibers. *J. Phys. Chem. Lett.* **2019**, *10*, 5997−6002.
(52) Vlnieska, V.; Gilshtein, E.; Kunka, D.; Heier, J.; Romanyuk, Y. E. Aerosol jet printing of 3d pillar arrays from photopolymer ink. *Polymers* **2022**, *14*, 3411.

https://doi.org/10.1021/acsami.4c10713
ACS Appl. Mater. Interfaces XXXX, XXX, XXX−XXX

Statement of Authorship for joint/multi-authored papers for PGR thesis

To appear at the end of each thesis chapter submitted as an article/paper

The statement shall describe the candidate's and co-authors' independent research contributions in the thesis publications. For each publication there should exist a complete statement that is to be filled out and signed by the candidate and supervisor **(only required where there isn't already a statement of contribution within the paper itself).**

Title of Paper	Fine-scale Aerosol-Jet Printing of Luminescent Metal-Organic Framework Nanosheets
Publication Status	☑ **Published** ☐ Accepted for Publication ☐ Submitted for Publication ☐ Unpublished and unsubmitted work written in a manuscript style
Publication Details	**D. A. Sherman,** E. Landberg, A. R. Peringath, S. Kar-Narayan, J.-C. Tan, "Fine-scale Aerosol-Jet Printing of Luminescent Metal-Organic Framework Nanosheets", *ACS Applied Materials & Interfaces*, Article in Press, (2024).

Student Confirmation

Student Name:	Dylan A. Sherman		
Contribution to the Paper	D.A.S: conceptualization, methodology, synthesis, data collection (unless stated otherwise below), all data analysis, first draft manuscript, review and editing. D.A.S and Jana Koth.: fluorescence microscopy data collection by collaboration (equipment operated initially by J.K. in presence of D.A.S, then D.A.S. and J.K.). D.A.S, E.L., A.R.P.: aerosol-jet printing by collaboration (equipment operated by E.L. and A.R.P.). E.L., A.R.P., S.K.-N, and J.-C.T.: manuscript review and editing. J.-C.T.: supervision. Note: 'by collaboration' indicates D.A.S was present and participating in data collection.		
Signature		Date	1/10/2024

Supervisor Confirmation

By signing the Statement of Authorship, you are certifying that the candidate made a substantial contribution to the publication, and that the description described above is accurate.

Supervisor name and title:	Prof J. C. Tan		
Supervisor comments	I support this applicatin		
Signature		Date	1 Oct 2024

This completed form should be included in the thesis, at the end of the relevant chapter.

5

From nanosheets to ‘nano’ leaves: luminescent guests@ZIF-L

5.1 Premise

This chapter acts as a counterpoint to the previous thesis chapters. Thus far, reported studies in this thesis have aimed to minimise the thickness of MOF materials to access improved functional properties. This final study removed this major constraint by exploring luminescent guest engineering in a thicker (100-300 nm) 2D MOF material, ZIF-L. Increased atomic density in the *z* direction increases the control achievable as a material engineer: 3D pore cavities can now be defined, crystallinity is more regular, and structure can be more precisely probed with diffraction and microscopy. This allowed for improved predictability of material structural properties, which can be leveraged through rational design to successfully tune a material. In essence, this offers a balance between 2D MON and 3D MOF properties more weighted towards MOF characteristics, but still with the benefits of 2D MOF materials. This work establishes guest@ZIF-L systems as viable alternatives to guest@MONs for creating enhanced luminescent functional materials.

5.2 2D Zeolitic Imidazolate Framework L

First reported in 2013, ZIF-L is synthesised from zinc nitride hexahydrate and 2-methylimidazole (Hmim) at room temperature using only deionised water (DI). The structure ($(Zn(mim)_2 \cdot (Hmim)_{1/2} \cdot (H_2O)_{3/2}$ or $C_{10}H_{16}N_5O_{3/2}Zn$) is comprised of 2D layers, alternating between an A- and B- type, with Zn centres that are coordinated by four N atoms.[160] The framework contains two large pore cavities: one cushion shaped cavity of 9.4 × 7 × 5.3 $Å^3$ (Figure 5.1) and a smaller cavity of 3.6 × 2.8 × 2.3 $Å^3$.[13]

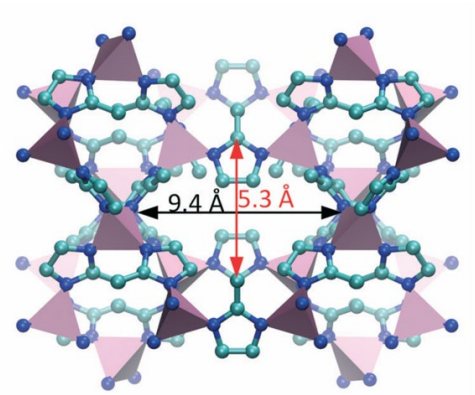

Figure 5.1. Structure of cushion pore cavity in ZIF-L based on reported crystal structure. Cyan = carbon, blue = nitrogen, pink polyhedral = Zn centres. Reproduced with permission from Ref. [161]. Copyright Royal Society of Chemistry, 2017.

Using a higher linker to Zn ratio (8:1 vs 1:1) and DI for synthesis leads to the formation of ZIF-L over ZIF-8. Water can hydrolyse by protonation of the unsaturated N of Hmim, slowing the rate of deprotonation needed to create coordination N^- sites on Hmim. The conditions also ensure the retention of free Hmim in the pores of ZIF-L, thereby reinforcing the 2D layered structure.

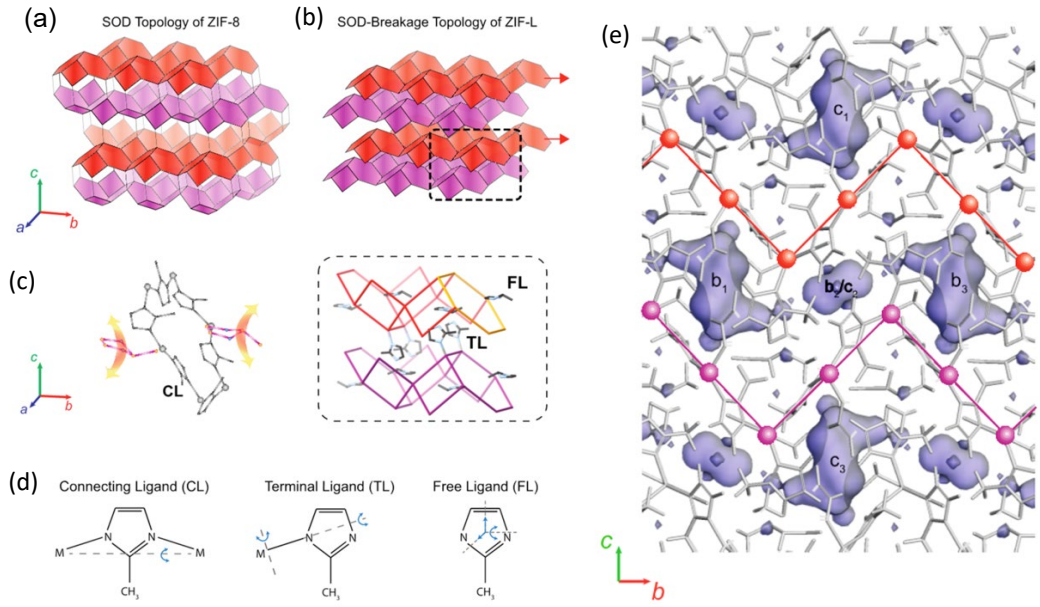

Figure 5.2. (a-b) Comparison of ZIF-8 and ZIF-L topologies. (c) Location of free and terminal ligands in ZIF-L. (d) Degrees of freedom for each Hmim type in ZIF-L. (e) Estimated pore cavities (purple) in ZIF-L. Adapted with permission from Ref. [162]. Copyright American Chemical Society, 2015.

The ZIF-L structure is derivable from segments of ZIF-8, the 3D sodalite framework synthesised from the same metal and ligand building blocks.[13] Specifically, ZIF-8 can be viewed as the composition of two alternating 2D layers (A- and B-) stacked along the *c*-axis (Figure 5.2). While in ZIF-8 these layers are connected through Zn centres by Hmim ligands, in ZIF-L there are no inter-layer connecting ligands. Rather, there are Hmim terminal ligands (monodentate *vs* bidentate bridging) and "free" Hmim ligands that are hydrogen bonded to the free end of the terminal ligands and weakly bonded *via* Van der Waals interactions with fully connected Hmim ligands (Figure 5.2). The free and terminal ligands are highly influential in the structure of ZIF-L:

- They are critical for preventing layers from linking to form ZIF-8 during synthesis and also provide strong interlayer bonding.[13]
- They segment the channels of ZIF-L into porous cavities and provide separation of the two different sized spaces (Figure 5.2).[162]
- They create additional degrees of freedom, increasing the flexibility of ZIF-L. Indeed, while there is no continuous channel network in ZIF-L, there is evidence of reformable channel systems given significant CO_2 adsorption and longer molecules such as CO_2 have been found to cause significant reformable channel widening compared to N_2 (6.48 Å vs 6.13 Å).[162]

ZIF-L exhibits a number of beneficial properties arising from blending a 2D morphology with the building blocks of ZIF-8, including high density (1.4 g/cm^3 vs 0.94 g/cm^3 for ZIF-8), regular porosity, interlayer space and flexibility, high thermal and chemical stability, negligible cytotoxicity, and high external surface area with exposed active sites.[13] Initial reports of ZIF-L focussed on the high CO_2 adsorption properties (0.94 mmol/g vs 0.78 mmol/g for ZIF-8) and enhanced CO_2/CH_4 selectivity (7.2 vs 2.8 for ZIF-8), due to more flexible inter-layer cavities compared to the cage-type sodalite ZIF-8 structure,[13,163-164] leading to uses as membranes to separate gas molecules.[160] More recently, ZIF-L has been used as an effective filter to remove toxic waste from water, including metal ions (e.g. Cd(II)), phosphate, and molecules such as the pharmaceutical tetracycline hydrochloride.[161,165-169] One report has also employed a ZIF-L based material as a catalyst for polymerisation.[170]

5.2.1 Leaf-shaped morphology

ZIF-L forms in a unique leaf-shaped morphology (Figure 5.3). In 2017, Motevalli *et al*. undertook *ab initio* studies on ZIF-L to rationalise the morphology by generating surface slab models and calculating surface energies.[160] The work found the (001) surface to be significantly lower in energy as cutting the surface only breaks intermolecular forces between layers. Coordination bonds are required to be broken for other surfaces, greatly increasing surface energies, hence explaining the predominance of the (001) crystal face. Specifically, the (100) and (110) facets have similar energies as each requires one single bond per Zn to be broken (Figure 5.3). The (010) surface requires two bonds to be broken, the second of which requires more energy than the first, greatly increasing the energy of a cut surface along the (010) plane (Figure 5.3). To minimise energy, and stabilise the structure, self-assembly favours (100) and (110) edges, while eliminating (010), leading to the pointy ends and curved edges of ZIF-L (Figure 5.3).[160]

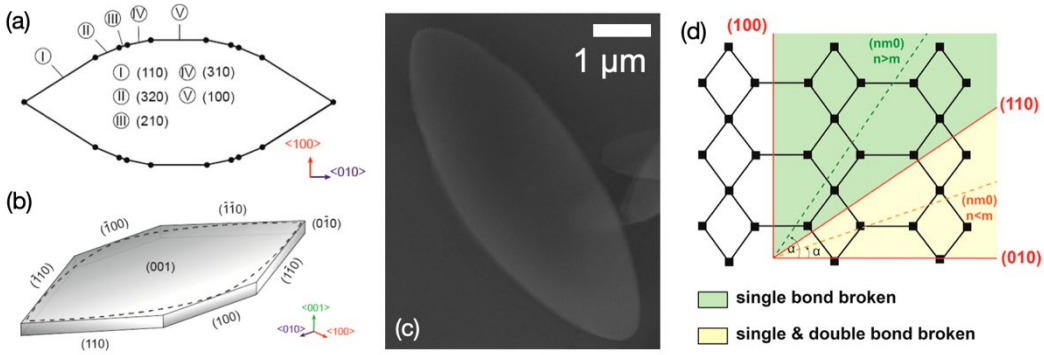

Figure 5.3. (a-b) Predicted crystal morphology of ZIF-L by Motevalli *et al.* using a DFT method. (c) FE-SEM of ZIF-L. (d) Range of crystal planes in *xy*-plane of ZIF-L. Adapted with permission from Ref. [160]. Copyright American Chemical Society, 2017.

5.2.2 ZIF-L for as a host framework and composite

The cushion cavity in ZIF-L, coupled with interlayer and ligand flexibility, makes the framework a promising candidate for guest@host engineering. To date, there have been reports of phosphate doped ZIF-L and carbon dot@ZIF-L composites, both for luminescent applications. ZIF-L has inherent low-intensity fluorescence in the violet to deep-blue visible region, attributable to the π*–π transition of the Hmim ligand. The addition of phosphate was found to enhance this fluorescence sufficiently to enable Fe^{3+} detection.[171] The four reported carbon dot@ZIF-L composites were used to create fluorescent probes for detecting cyclines (e.g., doxycycline)[172] and metal ions,[173-174] and as components of antimicrobial hydrogels to identify and adsorb Cu^{2+} ions.[175]

The findings clearly demonstrate the effectiveness of ZIF-L composites as functional luminescent materials, namely sensors. Less clear is whether the reported materials can be defined as guest@host systems by encapsulating guests within the ZIF-L cavities, or if they are a mixed hybrid of two materials *via* surface interactions. Interestingly, the reports do show mixed evidence of some form of encapsulation, including the widening of ZIF-L leaf shaped particles, but state that "the mechanism underlying the change is not supported by literature and requires further investigation".[172] Defining this is important, as effective guest encapsulation can produce more stable and resilient materials, with minimal guest leaching, along with regular host-guest interactions that can be more rationally tuned.

5.3 Guest@ZIF-L

5.3.1 Experimental Design

Paper IV presents a study that demonstrated common luminescent organic dyes can be effectively encapsulated in ZIF-L to produce functionally luminescent guest@ZIF-L materials. Only guests compatible with the pore size of ZIF-L were examined to minimise the potential of surface aggregation or composites of guest and ZIF-L (Figure 5.4). F was selected for a comprehensive study due to:

1) the need to 'turn on' fluorescence by preventing aggregation caused quenching (ACQ),[176]
2) a degree of flexibility in F molecules *via* rotation of the phenyl substituent, and
3) well understood luminescent behaviour and comparison available to F@ZIF-8.[83]

Perylene and 7-hydroxycoumarin (HC) were also successful in producing guest@ZIF-L materials. HC is an often-employed effective blue emitter for white light systems and acts as an example of a small molecule well within the limits of the ZIF-L pore.[177] Perylene, contrastingly, is an example of a planar aromatic compound with precise dimensions for the ZIF-L pore, with potential for stacking arrangements within a single pore.[178] The molecule is primarily used also as a blue emitter dopant for WLE systems but has been reported in the solid state to stack in dimer arrangements that produces green or yellow emission.[133,178-179]

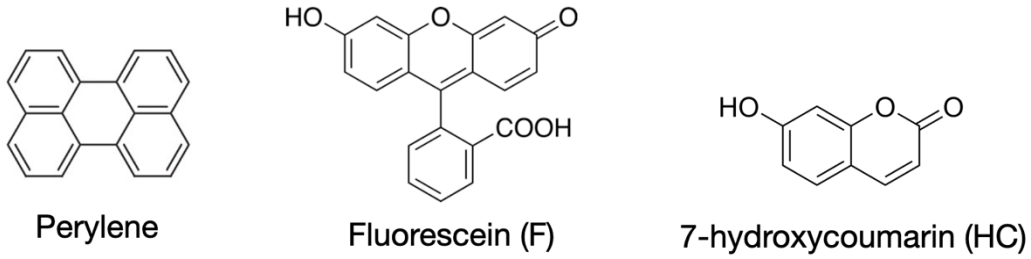

Figure 5.4. Guests used in Paper IV for encapsulation in ZIF-L.

The work comprised three parts:

(1) Providing insight into the mechanisms behind guest incorporation in ZIF-L.

(2) Using these insights to tune guest loading and arrangement for optimising luminescent properties.

(3) Demonstrating the growth of self-oriented luminescent thin films.

5.3.2 Structural mechanisms of ZIF-L guest engineering

Guests were introduced into ZIF-L using an *in situ* encapsulation strategy by adding guest molecules into the reaction mixture.[109] PXRD and High-angle annular dark-field scanning transmission electron microscopy (HAADF-STEM) confirmed the product (Guest@ZIF-L) retained the ZIF-L crystal structure at the bulk and local scale (Paper IV, Figures 1-2), while ATR-FTIR, nano-FTIR and Raman spectroscopy confirmed the chemical bonding of ZIF-L was retained also at the bulk and local scale (Paper IV, Figures 1 and 4).

NMR analysis of the digested samples confirmed the presence of guests by comparing the ratio of characteristic peaks of the guest with Hmim (Figure 5.5). Data reveal a logarithmic relationship between F mass used in synthesis and the % loading into ZIF-L. Increasing the quantity of MeOH used during synthesis at a particular F mass increased the loading % linearly.

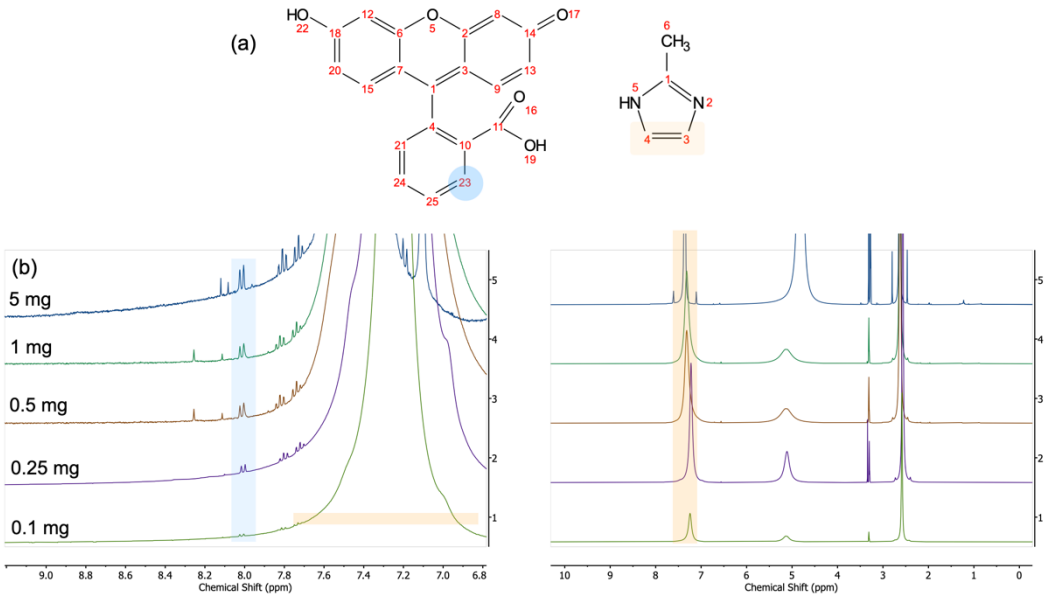

Figure 5.5. (a) F (left) and Hmim (right) indicating proton signals analysed with ^{1}H NMR. (b) Sample F@ZIF-L NMR spectra (full – right, zoomed – left) varied by guest loading, indicating peaks and associated molecular protons (blue for F and orange for Hmim).

Further, these data confirm the absence of guest surface species or aggregates, consistent with the approach in previous studies of this thesis. Firstly, no additional vibrational bands were observed in far-field spectroscopy of bulk samples. To provide a counterfactual, the quantity of F was increased to the point (≥10 mg) that

surface aggregates did result (observable in SEM and confirmed to be F with nanoFTIR), and new bands were observable in bulk ATR-FTIR attributable to F (Paper IV, SI S7). Secondly, nanoFTIR single point, line scans, and 2D maps, did not reveal any signals from F (Paper IV, Figure 4). Additionally, this study employed a further technique: pseudo-heterodyne (PsHet) imaging by scattering-type scanning near-field optical microscopy (s-SNOM) collected in collaboration by Lars Mester. This involved illuminating the sample with a monochromatic quantum cascade laser (QCL) that can be tuned to an absorption band of interest, thereby assessing the intensity of signal from the sample at specific wavelengths (Figure 5.6). To ensure consistency between data, a widefield fluorescence microscope was incorporated into the instrument so that particles measured with s-SNOM could also be tested for fluorescence behaviour. For this work, the source was tuned to 1146 cm^{-1} (characteristic C-H bending of ZIF-L), 1580 cm^{-1} (strongest band from F), and 1072 cm^{-1} (reference band with minimal intensity from both ZIF-L and F). Data showed strong consistent signal intensity at 1146 cm^{-1} across the particle, confirming the presence of ZIF-L, but only a very minimal consistent signal from F, indicating a degree of homogenous incorporation throughout the F@ZIF-L particle. Previous work demonstrated similar results after washing a RB@ZIF-8 sample with effective guest incorporation, compared to a stronger intensity indicating surface species before washing.[87]

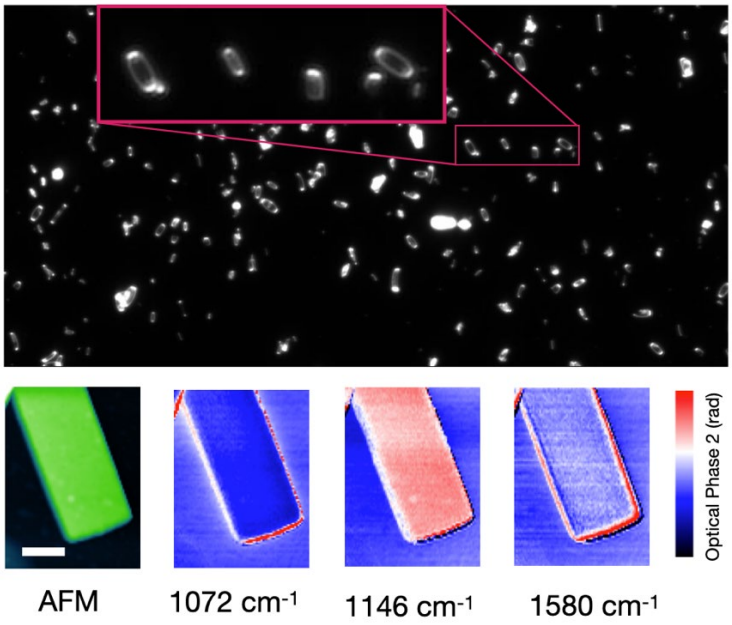

Figure 5.6. Example of s-SNOM data on F@ZIF-L particle, indicating irradiation wavelength of QCL for PsHet imaging. Above: example image of widefield fluorescence module attached to s-SNOM instrument. Scale bar represents 1 μm.

Additional indicators suggested positively that a degree of incorporation of F into the ZIF-L host had occurred. NanoFTIR spectra for F@ZIF-L exhibited a reduction in the intensity of the band at 780 cm^{-1} compared to 997 cm^{-1} and 1148 cm^{-1} as guest loading increased (Paper IV, Figure 4). This corresponded to a reduction in out-of-plane ring bending mode relative to the in-plane ring bending, a behaviour that could result from a guest within porous space that sterically hinders Hmim movement. Secondly, N_2 adsorption at 77.3 K reduced in maximum volume from 26.34 cm^3/g for ZIF-L to 12.24 cm^3/g for F@ZIF-L, with a 30 % reduction in Brunauer–Emmett–Teller (BET) surface area and 65 % reduction in microporous volume (Paper IV, Figure 1). These data suggest the presence of guests within porous cavities of ZIF-L. Finally, TGA showed that a percentage mass loss

attributable to the free Hmim in ZIF-L reduced exponentially from 15 % to 12.5 % with increasing guest loading (Paper IV, Figure 1).[13] This implies less uncoordinated Hmim. As these reside in the porous cavities of ZIF-L, being less present in F@ZIF-L as more F is loaded further suggests the incorporation of F into the porous cavities of F@ZIF-L. While attempted, beam sensitivity (previously reported for ZIF-L)[180] precluded further crystallographic positioning of guests using electron diffraction or high resolution TEM (HR-TEM).

5.3.2.1 Changing morphologies

The most prominent evidence of guest incorporation was a morphological transition as guest incorporation changed. Paper IV outlines a systematic study with F@ZIF-L used to isolate the changes attributable to guest incorporation as distinct from solvent conditions for synthesis (Paper IV, Figures 2-3). PXRD, FE-SEM, and AFM data revealed that as guest loading increased, particle morphology morphed on a continuum from the ZIF-L pointed leaf, to a wider leaf, rounded rectangle, then precisely rectangular (Figure 5.7). From the theory in §5.2.1 a rationalisation and hypothesis was formed. The shift towards a rectangle eliminates the (110) surface edge, while increasing the presence of (010), which for ZIF-L alone is energetically unfavourable. The (110) plane intersects the cushion pore cavity of ZIF-L, suggesting that if a guest was incorporated into this position the bonds required to be broken would now be unfavoured, hence the edge is eliminated in preference to (010).

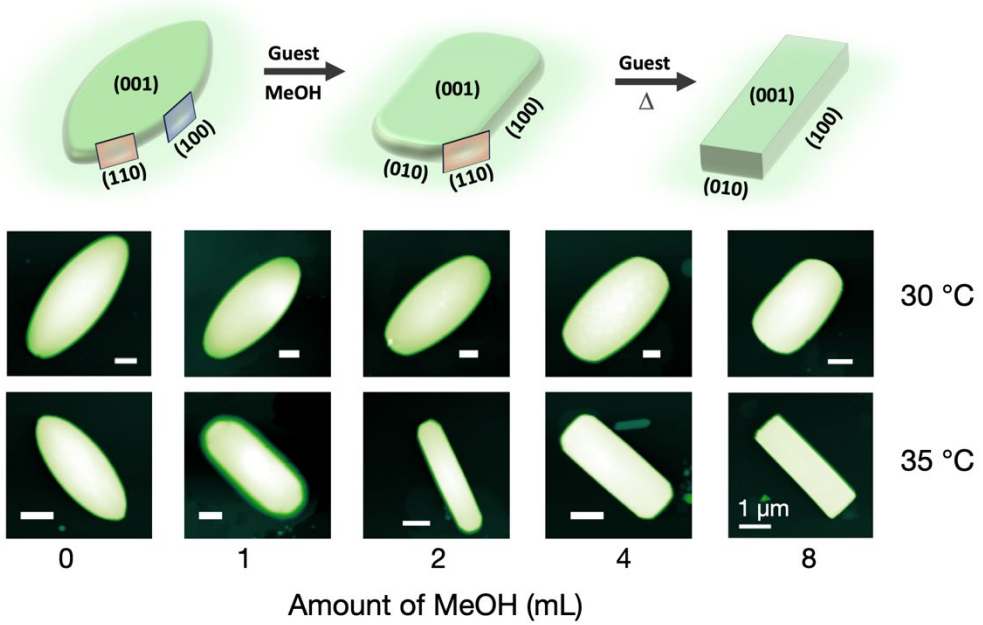

Figure 5.7. Above: sketch of F@ZIF-L morphological changes with guest loading, temperature, and increased MeOH during synthesis. Below: AFM images of F@ZIF-L synthesised with varying conditions. Scale bars indicate 1 µm. See Paper IV, Figure 2, for comprehensive analysis.

Density Functional Theory (DFT) calculations (undertaken by collaboration with Lorenzo Dona and Bartolomeo Civalleri) were employed to confirm the veracity of these hypotheses. Slab models were built with a thickness between 9-12 Å for the (100), (010), and (110) faces. Adsorption of F and perylene was modelled on each surface (Figure 5.8 and see Paper IV Figure 3). F was studied in its dianionic form, using Zn^{2+} as a counterion, based on basic pH conditions that preference the dianion during synthesis, along with NMR signals that align with the F dianion. Modelling revealed that both guests exhibit the lowest binding energy, hence their preference to absorb on the (110) surface. This surface also resulted in the strongest dipole moment, i.e., instability. Hence, once the guest absorbs to the surface during self-

assembly, reconstruction to eliminate the dipole can occur to achieve stability, thereby reducing the (110) surface edge. Two further observations are notable. The (110) surface had two possible binding sites, with the more accessible site closer to the centre of the cavity modelled to have the lowest binding energy. Secondly, the binding energy of perylene at the (110) exposed site was 27 % lower than F, suggesting perylene is a preferred guest.

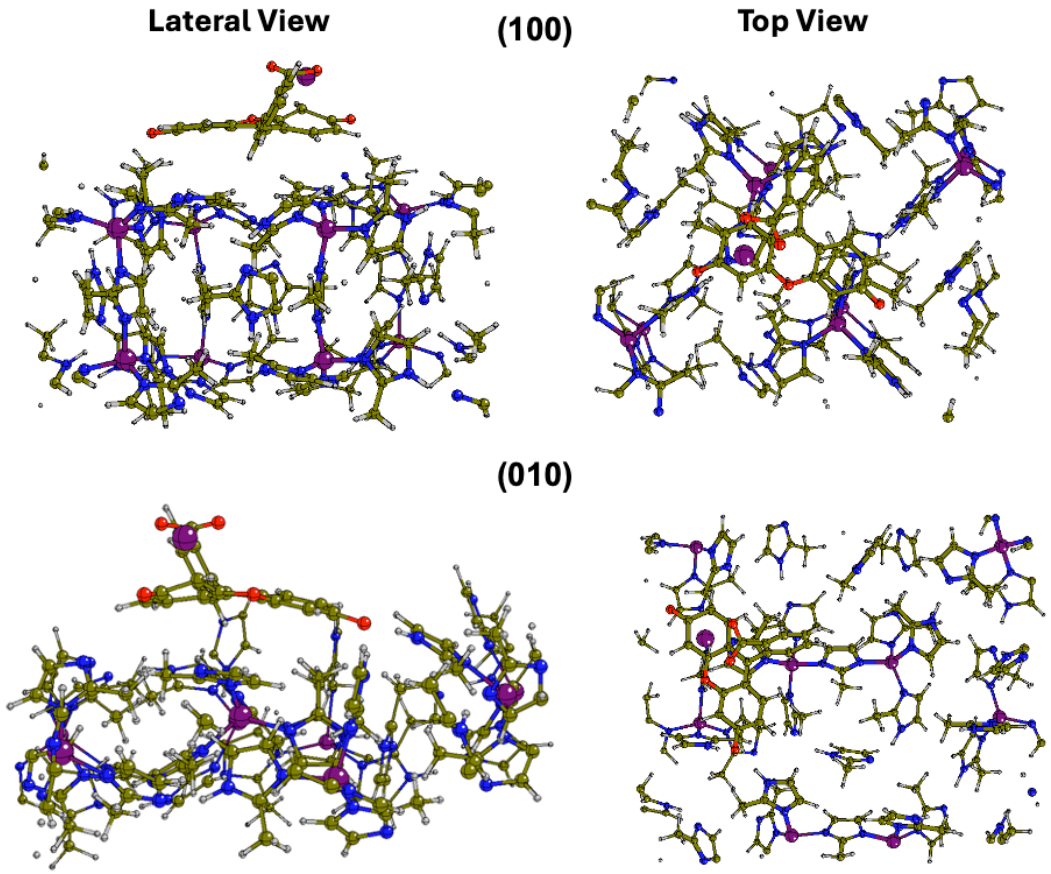

Figure 5.8. Modelling F adsorption on F@ZIF-L (100) (above) and (010) (below) surfaces using DFT (Zn = purple, N = blue, C = yellow, O = red, O = white).

Significantly, the observed morphology continuum was only fully accessed when synthesising F@ZIF-L at higher temperatures (35-45 vs 30 °C). This is likely due to a combination of factors including increased dissolution of F, more volatile MeOH that is less likely to compete with F for pore space in ZIF-L, and the increased energy available for guest-host binding.

5.3.3 Luminescent properties

F@ZIF-L exhibited strong luminescence expected of F when not quenched by aggregation (Figure 5.9). A detailed analysis with the effect of guest loading is provided in Paper IV and aligns with the behaviour of F in Z7-NS and ZIF-8 (Paper IV, Figure 5). That is, strong green emission is observed at low guest loadings, due to dominant monomer and J-aggregate species. Increasing guest loading (from 0.2 mg for F@ZIF-L) led to H-aggregation beginning to dominate, suppressing emission and red shifting chromaticity to orange/yellow. When synthesised at higher temperatures, i.e., more effective guest loading in the pores of ZIF-L, an increase in monomeric species was observed, contributing to an increase in fluorescence lifetimes (indicative of better confinement). This corresponded to an increase in emission intensity at the same guest loading. Remarkably, PLQY of 99.95 % was achieved by F@ZIF-L and reasonable photostability was reported (35.5-39.3 % loss over 24-hours when exposed to concentrated irradiation under a 150 W UV lamp). Moreover, 13 months of suspending F@ZIF-L in MeOH did not

cause any guest leaching (only a trace quantity of 0.014 ppm was observed in MeOH) and the F@ZIF-L particles remained strongly luminescent.

A comparison to F@ZIF-8 offered a useful assessment of the effectiveness of 2D encapsulation. Based on published data from our lab,[83] using consistent equipment and techniques, F@ZIF-8 with a comparable guest loading (0.03 %) achieved 98 % PLQY, while emission intensity was 20 % of that achieved with ZIF-L. Additionally, emission and excitation were more blue shifted in F@ZIF-8 (515-535 nm vs 535-555 nm for F@ZIF-L and 499 vs 510 nm for F@ZIF-L). Lifetimes of each component contributing to emission were also longer than F@ZIF-L (6.5 vs 5.5 ns, 3.9 vs 3 ns and 0.4 vs 1.1 ns). These data indicate a more stable system is achieved by F@ZIF-L but with less confined F. This results in a more efficient and effective luminescent system.

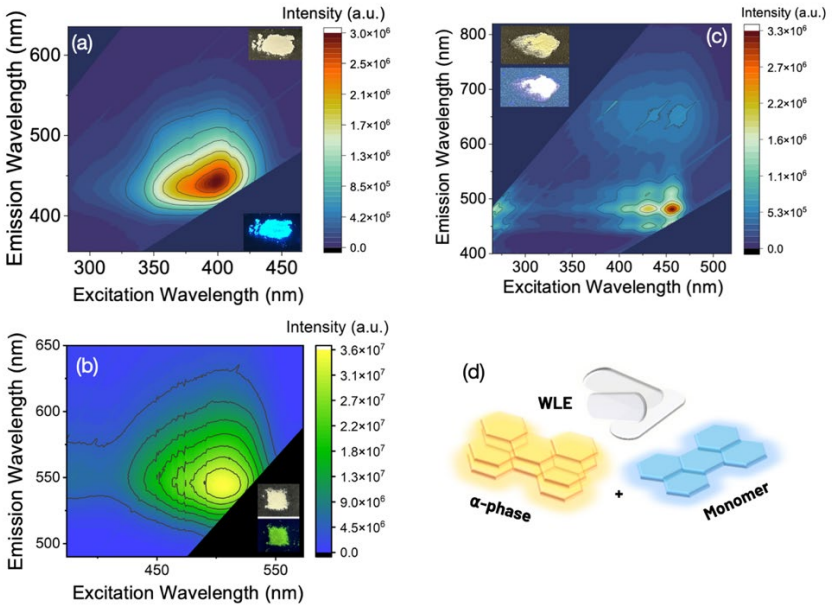

Figure 5.9. Excitation-emission maps for (a) HC@ZIF-L, (b) F@ZIF-L and (c) perylene@ZIF-L (inset: samples under ambient (above) and 365 nm UV (below)). (d) sketch outlining guest arrangements for perylene@ZIF-L to produce WLE.

Perylene@ZIF-L was found to emit blue at low guest loadings (0.03 % mol) but an ideal WLE (CIE = 0.33, 0.34) at higher loadings (0.1 %) (Figure 5.9 and see Paper IV Figure 7). This is the first report of perylene alone emitting white light, with perylene@ZIF-8 either showing blue, green, or yellow emission depending on the pressure applied to the system and another report requiring mixed RB@ZIF-8 and perylene@ZIF-8 to achieve WLE. [133,181] The cause of this emission is due to a balance of monomeric emission from perylene in the blue region, and α-phase dimers emitting in the yellow-orange region. Dimers in α-phase stack parallel due to strong π-π interactions in the delocalised electron cloud of perylene and are reported to emit as E-excimers. These dimer species form after excitation and stabilise the lowest excited state, thereby reducing the emission energy and red-shifting emission chromaticity. The requirement for higher guest loading suggests that perylene is preferentially arranged as single species in ZIF-L cavities, but higher loading may force stacked species within single cavities to produce α-phase dimers.

HC@ZIF-L emitted the blue as expected from HC (Figure 5.9 and Paper IV, Figure 7). No further analysis was conducted on this sample, as it was a proof of the generalisability of the guest@ZIF-L technique. A broader study of coumarins in ZIF-L may be a useful extension of the coumarin@ZIF7-NS study, to assess the protection afforded by ZIF-L from photodimerization.

5.3.4 Fabricating thin films

Oriented films are critical for high performance thin-film optoelectronics and sensors. ZIF-L can be grown directly along the *b*-axis to create oriented heteroepitaxial growth for thin film coatings, attributed to the Van der Drift growth model where to obtain sufficient growth space the crystals preferentially grow upwards, preferring orientation along the longest axis.[166,182-186] For this study, we briefly demonstrated that this process could be applied to guest@ZIF-L systems by forming an oriented fluorescent film of F@ZIF-L on a Zn substrate with strong and fairly homogenous emission (Paper IV, Figure 8). Notably, growth has been studied for ZIF-L over 120 minutes on a polyacrylonitrile membrane and shown to incrementally thicken, with larger particle layers forming over oriented films.[185] Similar behaviours were observed for ZIF-L and F@ZIF-L on Zn film, although further investigation is needed to systematically determine the optimal reaction length to maximise film orientation, along with the effect film orientation has on improving optical properties. Of note, one work has intentionally exploited the growth variation by growing smaller ZIF-L particles as branches on larger ZIF-L particle 'trunks' that form oriented films. It would be interesting to determine if two different luminescent materials could be grown in a similar manner to fabricate a multi-emitter system.[185]

5.4 Implications and Further Studies

ZIF-L has been demonstrated as a versatile and robust host system for luminescent organic guest molecules. Controlling guest quantity and reaction temperature offered tuneability of guest loading and arrangement. This was tracked visually by observing distinct morphological changes. By optimising guest loading and arrangement, the luminescent properties of guests were finely tuned. This produced high PLQY and intense emission, in the case of F@ZIF-L, and WLE in the case of perylene@ZIF-L. Significantly, these materials exhibited desirable photo and chemical stability to be applied in lighting and optoelectronic devices, while also having the convenience of being fabricated in oriented thin films direct from synthesis.

The work is only an initial illustration of the broad potential of this strategy, and selecting further luminescent guests could lead to developing fast acting sensors, or pressure indicators that take advantage of the oriented 2D nature of ZIF-L. Employing a diverse range of guests could unlock myriad new properties for ZIF-L including conductivity or more general chromatic applications such as electrochromic systems. As a proof of concept for this direction, we successfully encapsulated naphthalene tetracarboxylic acid@ZIF-L (NTC@ZIF-L) and pyromellitic diimide@ZIF-L (PD@ZIF-L) in ZIF-L (Figure 5.10). Both NTC and PD are known to be electrochromic and used as ligands in redox active MOF materials, creating the possibility of charge transfer systems in ZIF-L for catalysis or energy storage and capacitance.[187-188] Of note, both systems also exhibited a

uniform windmill morphology, rather than single particles. Given NTC and PD molecules have well oriented sets of carbonyl functional groups at each end, it is possible these act as directing groups to increase hydrogen-bonding and other intermolecular interactions. These could promote particle splicing, as seen with other molecules that contain directing groups added to ZIF-L synthesis.[175,189] To further probe this phenomenon, a suite of guest molecules are proposed that could examine the effect of terminal functional groups on directing ZIF-L morphology, which could further be used to tune the electron transport behaviour of the material (Figure 5.10). The increasing scale, with the third tier of molecules incorporating the perylene core, could also present opportunities for ligand substitution to form a modified ZIF-L structure directly with additional functionality.

Two other tangential directions are of interest from this study. Guan *et al.* in 2017 reported a process of mixing ZIF-L with the organic dye 1,4-diethoxybenzene in ethanol to produce a dye@ZIF-8 by structural transformation. The ZIF-L to ZIF-8 transformation is well studied and involves solvent molecules interacting with inter-layer Hmim followed by a sliding of layers to align sodalite cages.[190] It has been shown to occur at the kilogram scale.[191] It could be interesting to examine whether guest@ZIF-L materials would transform under solvent and heat to ZIF-8, potentially acting as a 'switch' to turn on or off properties distinct to the 2D and 3D phases of the host. Finally, ZIF-L nanosheets have been reported in one study, albeit by ball-milling exfoliation assisted by viscous polyethyleneimine liquid to develop monolayer 0.6 nm sheets of around 1 μm lateral dimensions.[192] To link the work

undertaken on MONs in this thesis, an exploration of ZIF-L MONs could offer an even more ideal combination of 2D and 3D material properties to target more superior functional materials.

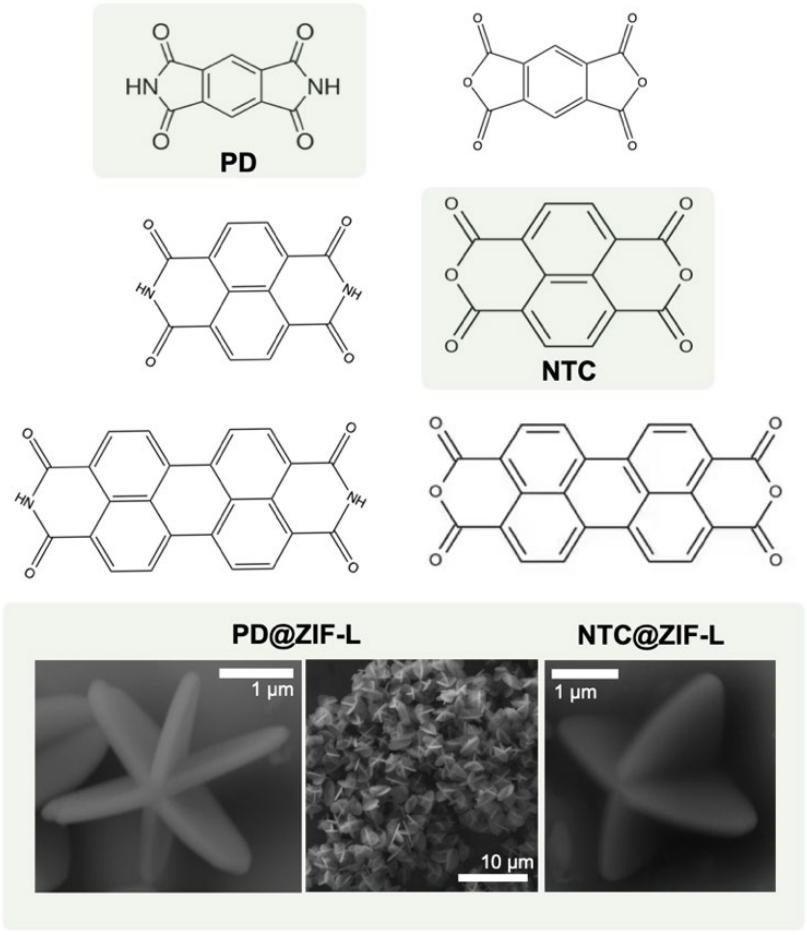

Figure 5.10. Suite of candidate molecules for future guest@ZIF-L studies, with FE-SEM of PD@ZIF-L and NTDC@ZIF-L illustrating windmill morphology.

5.5 Paper IV

Elucidating guest-host mechanisms in ZIF-L for tuneable highly luminescent functional materials

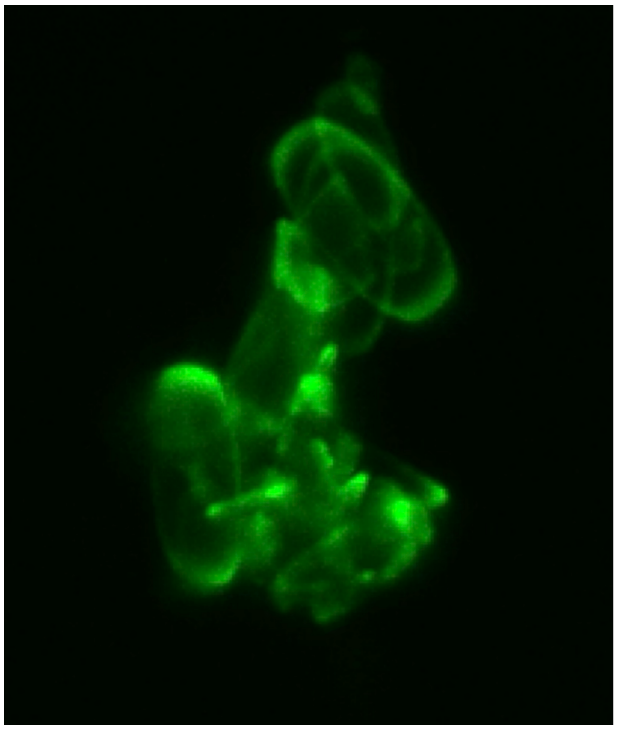

Figure 5.11. Illustration of F@ZIF-L, based on artificial coloured composite fluorescence microscopy images.

Supporting information for this manuscript can be found here.

Elucidating Guest-Host Mechanisms in ZIF-L for Tuneable Highly Luminescent Functional Materials

Dylan A. Sherman,[a] Lorenzo Donà,[b] Cyril Besnard,[a] Lars Mester,[c] Ben Slater,[a] Judit Farrando-Pérez,[d] Christopher Allen,[e] Joaquín Silvestre-Albero,[d] Bartolomeo Civalleri,[b] and Jin-Chong Tan[a]*

[a] *Multifunctional Materials & Composites (MMC) Laboratory, Department of Engineering Science, University of Oxford, Parks Road, Oxford OX1 3PJ, United Kingdom.*

[b] *Department of Chemistry, NIS and INSTM Reference Centre, University of Turin, via Pietro Giuria 7, Torino 10125, Italy.*

[c] *Attocube Systems AG, Eglfinger Weg 2, DE-85540 Haar, Germany.*

[d] *Laboratorio de Materiales Avanzados, Departamento de Química Inorgánica-Instituto Universitario de Materiales, Universidad de Alicante, Ap. 99, E-03080 Alicante, Spain*

[e] *Electron Physical Science Imaging Centre (EPSIC), Diamond Light Source Ltd., OX11 0DE, United Kingdom.*

** Corresponding author's e-mail: jin-chong.tan@eng.ox.ac.uk*

Keywords

ZIF-L, morphology control, guest-host engineering, metal-organic framework, luminescence

Abstract

3D metal-organic frameworks (MOFs) are well known effective hosts for luminescent guests that improve tuneability, photostability and material fabricability. 2D guest@MOF systems, while less explored, offer competitive advantages over 3D guest@MOF systems due to their optical transparency, inter-layer spacing, and often thinness. This work examines luminescent organic dyes@ZIF-L to establish the underlying mechanisms of guest incorporation in ZIF-L and demonstrate the advantages of the 2D ZIF-L architecture for the material's functional luminescence. Analysing a case study system, fluorescein@ZIF-L (F@ZIF-L), using nanoscale FTIR, diffraction, and topology mapping, confirmed that F resided in the ZIF-L framework cavities. Supported by surface energy simulations, the extent of guest incorporation was confirmed to be indicated by a morphological continuum, from the characteristic leaf shaped ZIF-L to rectangular F@ZIF-L. By modifying synthesis temperature and solvent ratios, the luminescent properties of F@ZIF-L could be rationally tuned in terms of guest loading and arrangement (i.e. the ratio of monomers to aggregates). When optimised, F@ZIF-L exhibited tuneable emission chromaticity, 99.7 % photoluminescent quantum yield, minimal guest leaching in solution over 12 months, and high photostability. Perylene@ZIF-L exhibited unique white light emitting properties, with CIE coordinates (0.33, 0.34) arising from a combination of yellow α-phase excimer and blue monomeric perylene emission. Finally, oriented luminescent thin films of guest@ZIF-L materials were grown on Zn film, demonstrating an *in situ* fabrication technique. Together, the work highlights the potential for guest@ZIF-L systems in developing tuneable and resilient luminescent components of next generation optoelectronics, sensors, and lighting systems.

Introduction

Functional luminescent materials that can be carefully tuned are critical for new generation nanoscale sensors and indicators, lighting systems, and optoelectronics.[1] White light emission (WLE), for example, requires precise attainment of Commission Internationale de l'éclairage (CIE) coordinates (0.33, 0.33).[2,3] While many organic dyes, such as fluorescein (F), perylene, and coumarins, can exhibit strong functional fluorescence for these purposes, as free molecules these properties are challenging to control. F, for example, is non-emissive in the solid state due to aggregation caused quenching (ACQ).[4,5]

Metal-organic frameworks (MOFs) have been employed as effective 3D structures to host organic luminescent dyes, providing a system of control through host-guest interactions.[6] Due to the high porosity and customisability afforded by MOF materials, myriad dye@MOF systems have been developed that are tailored to optimise the properties of the luminescent dye, leading to stronger emission and improved photoluminescent quantum yield (PLQY).[7] Zeolitic imidazolate frameworks (ZIFs) in particular offer large cages to encapsulate organic dyes, while also exhibiting high thermal and chemical stability, attributable in part to their zeolite-type structure.[8]

3D frameworks do have limitations, however, including limited optical transparency, challenging fabricability, dye leaching, self-quenching through reabsorption, and delayed sensing due to limited target molecular diffusion through the MOF superstructure.[9,10] 2D guest@MOF materials have been proven to overcome some of these issues by offering additional properties including increased external surface area, number of active sites, interlayer spacing for diffusion and molecular transport, orientability, and in some cases, thinness.[11] One particularly promising candidate is

ZIF-L ($Zn(mim)_2 \cdot (Hmim)_{1/2} \cdot (H_2O)_{3/2}$ or $C_{10}H_{16}N_5O_{3/2}Zn$, Hmim = 2-methylimidazole), which is formed by the alteration of 2 layers that are part of the ZIF-8 sodalite topology.[12] In each asymmetric unit, there are two crystallographically unique Zn(II) ions, each coordinated by four N atoms, four Hmim ligands and one free Hmim molecule.[13] The free Hmim, and additional terminal ligands interact in interlayer spacing *via* hydrogen bonds and *van der Waals* interactions, critical to preventing layers from linking to form ZIF-8 during synthesis but also creating strong interlayer bonding.[12] The framework contains two large pore cavities: one cushion type cavity of 9.4 x 7 x 5.3 Å and a smaller cavity of 3.6 x 2.8 x 2.3 Å.[12] Notably, the terminal and free Hmim ligands create flexibility of the framework, with longer molecules such as CO_2 causing significant channel widening compared to N_2 (6.48 Å vs 6.13 Å).[14]

ZIF-L combines the stability and large cavities of typical of ZIF materials with the 2D morphology, creating a denser framework than ZIF-8 (1.4 g/cm^3 vs 0.94 g/cm^3)[15] that is reported to have high thermal and chemical stability, negligible cytotoxicity and high surface area with exposed active sites.[12] The material was initially explored for its high CO_2 adsorption capacity (higher than ZIF-8 at room temperature).[11,12,16] It has also been proven to be effective as a filter for wastewater treatment,[17,18,19,20,21,22] catalyst for polymerisation,[23] and as a membrane to separate gas molecules,[13] with the interlayer space facilitating mass diffusion. Usefully, ZIF-L can be grown along the *b*-axis to create oriented heteroepitaxial growth for thin film coatings, attributed to the *Van der Drift* growth model where to obtain sufficient growth space the crystals preferentially grow upwards. Preferring orientation along the longest axis.[18,24,25,26,27] Oriented films are critical for high performance thin-film optoelectronics and sensors.

Despite ZIF-L being an appealing structure for guest@host engineering, due to the large cavities, interlayer channels, and framework flexibility, very few reports of guest@ZIF-L solid-state systems exist, and luminescent ZIF-L materials are limited. While ZIF-L exhibits emission under 365 nm in the violet-deep blue region due to the π–π* transition of the Hmim ligand, it is typically not intense or sensitive enough to provide useful functionality alone.[28,29] Phosphate has been doped in ZIF-L to enhance the framework's natural fluorescence to enable Fe^{3+} detection.[30] There are also four reports of carbon dot@ZIF-L composites to create fluorescent probes for detecting cyclines,[31] metal ions,[29,32] or be used as components of antimicrobial hydrogels to identify and adsorb Cu^{2+} ions.[33] While these developments show the effectiveness of ZIF-L composites for luminescent sensors, works have not attempted to understand the extent of guest encapsulation into ZIF-L or the underlying mechanisms of guest incorporation. Indeed, a number of works identify ZIF-L particles widening on guest encapsulation, but note further investigation is required to interpret these observations.[31]

Herein, we report a collection of highly luminescent dye@ZIF-L materials. F was selected as the candidate guest given its character as a strong green emitter and the need to be 'turned on' in the solid state by preventing ACQ with host interactions. The dimensions of F's molecular aromatic core (8.5 x 6.9 x 5.0 Å) are theoretically compatible with the flexible ZIF-L pore, and F itself has a degree of flexibility via rotation of the phenyl substituent. Other guests included perylene, which showed unique WLE upon encapsulation. The luminescence of F@ZIF-L and perylene@ZIF-L was found to be highly tuneable based on guest loading and synthesis conditions that varied the arrangement of guests in the host framework. Employing *ab initio* density functional theory (DFT) simulations and nanoscale analysis techniques, the

mechanisms behind guest encapsulation in ZIF-L were elucidated, revealing that the degree of guest incorporation into ZIF-L pores is indicated by a morphological progression from the pointed leaf shaped particles to wider ovals, then rectangles. Finally, due to the orientable growth of ZIF-L, luminescent thin films were grown on Zn foil to produce functional fluorescent lighting surfaces.

Synthesis

In situ guest encapsulation was used to synthesis F@ZIF-L. The typical ZIF-L synthesis,[12,34] was modified by dissolving guest molecules into the reagent mixture before stirring (see Methods in Supporting Information). Typically, ZIF-L synthesis is H_2O based, as water can hydrolyze and postpone growth into a third dimension to form ZIF-8.[35] After the N amine of the Hmim ligand forms hydrogen bonds with water, it induces the formation of further H bonded Hmim ligands, linking sodalite layers to form ZIF-L. However, the solubility of F in water is very low: at the 80 mL scale used for synthesis, only 0.10 mg of F fully dissolved. F is more soluble in organic solvents such as MeOH and EtOH. Solvent, however, causes the amine H to dissociate and coordinate with Zn^{2+} ions, to then form 4-coordinated Zn^{2+} via the dehydrogenated Hmim and assemble ZIF-8.[11] We therefore tested the addition of very dilute quantities of common organic solvents to the H_2O (80 mL). Powder X-ray diffraction (PXRD) confirmed that toluene, isopropyl alcohol, acetone, acetonitrile and tetrahydrofuran all formed ZIF-8 at any concentration tested, while dimethylformamide and EtOH formed ZIF-L but only up to 2 mL and 5 mL respectively, after which ZIF-8 formed (Figure S1). Finer testing was undertaken with MeOH (F solubility of ≈ 10 mg/mL), confirming up to 10 mL can be added and still form pure phase ZIF-L, while pure phase ZIF-8 forms from 20 mL of MeOH (Figure S2).

A range of F@ZIF-L samples were synthesised: 5 using H_2O only (up to 0.5 mg F content during synthesis), 16 using a constant MeOH content of 4 mL but varying F content during synthesis (from 0.01 mg to 80 mg), 3 sets of samples (0.1, 0.3, 0.5 mg) each with varying MeOH content (1, 2, 4, 8 mL), and various samples with 0.3 mg F synthesis content with varied temperature (from the standard 30 °C to 35, 40, 45, and 50 °C). The guest synthesis content was based on the range of guest quantities reported for ZIF-L carbon dot composites (from 1.5 mg to 25 mg).[29,31,33] All samples, after drying, formed an average of 500 mg F@ZIF-L (85 % yield based on Zn content), which aligns with expected yields from previous reports.[11]

F@ZIF-L Bulk Structure and Composition

PXRD patterns of F@ZIF-L up to and including 10 mg of F during synthesis exhibit sharp peaks and align with the experimental and simulated patterns of ZIF-L, confirming the retention of the ZIF-L crystalline framework (Figures 1a, S3). From 20 mg of F, a mixed ZIF-L/ZIF-8 phase results, with only ZIF-8 forming at 80 mg of F (Figure S4). Vibrational spectroscopy of F@ZIF-L with up to 5 mg of F further confirmed the retention of the ZIF-L framework, with attenuated total reflectance-Fourier transform infrared (ATR-FTIR) and Raman spectra aligning with the vibrational bands of ZIF-L without any additional bands present (Figures 1b, S5-S6).

From ≥ 10mg of F, a series of additional vibrational bands were observable (Figure S7). These increased in intensity with increased guest loading and align well with the FTIR spectra of solid state F, and reported simulation FTIR spectra of the dianion of F.[36] For example, at 918 cm^{-1} a peak forms attributable to the out-of-plane bending of

the CH group on the benzenecarboxylate unit of F. This indicates the presence of aggregated F species either on the surface of F particles, or as a mixture with F particles. Field emission scanning electron (FE-SEM) micrographs of 10 mg, 20 mg and 40 mg F@ZIF-L confirm the latter, with large growths of F forming between ZIF-L particles (Figure S8). Nearfield infrared nanospectroscopy (nanoFTIR) was used to probe one of these clumps, revealing the nanoFTIR spectra aligned well with the nanoFTIR spectra of a F as a solid powder (Figure S9-S10). Meanwhile, the FE-SEM of the 80 mg F sample exhibits a unique morphology comparable to ZIF-8 (Figure S11). For these reasons, we excluded all samples of F@ZIF-L synthesised from 10 mg or more F from further studies, preferencing instead materials that exhibit behaviours typical of well incorporated guest@host systems.

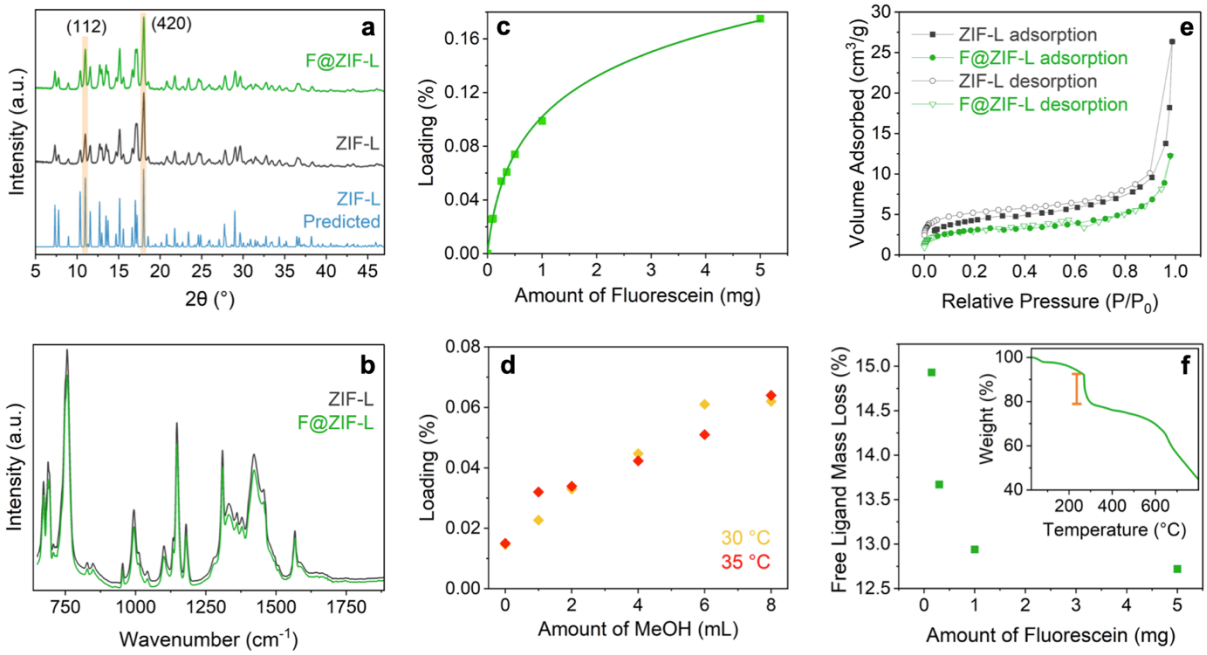

Figure 1. a) PXRD patterns of F@ZIF-L (0.3 mg, F) and ZIF-L, compared to simulated data.[12] b) ATR-FTIR of F@ZIF-L (0.3 mg, F) and ZIF-L. c) Loading of F in ZIF-L compared to synthesis quantities of F determined by NMR digest. d) Loading of F in ZIF-L from 0.3 mg synthesis quantity when MeOH synthesis content varied. e) N_2 sorption isotherms (77.3 K) of F@ZIF-L (0.3 mg, F) compared to ZIF-L. f) TGA of F@ZIF-L (0.3 mg, F) (inset) with TGA determined free ligand mass loss (orange bar) from F@ZIF-L samples various F content during synthesis.

The loading of F in F@ZIF-L was determined using NMR digest and the signal ratio from the 2-methylimidazolate ligand (singlet at 7.3 ppm corresponding to the two methine protons of the imidazole ring) and F (doublet at 8.3 ppm corresponding to a single proton in the ortho position relative to the carboxy group) (Figure S12). A logarithmic relationship between guest content during synthesis and loading % mol was determined, with a maximum loading of 0.16 % mol (Figure 1c). A F@ZIF-8 material also reported a logarithmic guest loading.[36] Introducing dilute MeOH content (up to 8 mL) into the synthesis further increased guest loading linearly compared to H_2O only synthesis (Figure 1d). When synthesised at 35 °C, loading remained similar in quantity to that observed at 30 °C, also exhibiting a strong correlation with increased MeOH during synthesis (Figure 1d).

N_2 adsorption and desorption at 77 K was investigated to examine porosity. Isotherms revealed a reduction in maximum volume of N_2 adsorbed from 26.34 cm^3/g for ZIF-L to 12.24 cm^3/g for F@ZIF-L (0.3 mg, F) (Figure 1e). Similar reduction in adsorption capacity of N_2 is well reported for guest@ZIF systems, including phosphate@ZIF-L, and is indicative of effective guest incorporation into the host framework.[30] Furthermore, BET surface was measured to be 15.44 m^2/g for ZIF-L, aligned with reported values,[21] while a 30% reduction to 10.81 m^2/g was observed for F@ZIF-L (Table S1). The materials exhibited some microporosity, as expected for ZIF-L, with a sharp increase in adsorption at low pressure ($P/P_0 < 0.1$).[29] A 65 % reduction of microporous volume was observed for F@ZIF-L. These differences in surface area and micropores are comparable to those reported for the phosphate and carbon dot@ZIF-L composite materials (Table S1). [29,30,31,32]

Thermogravimetric analysis (TGA) appears consistent with ZIF-L reported data:[12] an initial loss at 100 °C from solvent (H_2O), then at 250 - 300 °C a second mass loss due to removal of the weakly linked Hmim molecules between the layers of ZIF-L, followed by framework decomposition at 550 °C to form ZnO (Figure 1f, S15). F is reported to exhibit thermal instability from 330 °C, after the second thermal loss step for ZIF-L.[36] While typical reported loss due to trapped solvent is around 4.3 %,[15] F@ZIF-L materials only exhibit a 2% weight loss. Moreover, the loss due to weakly bound Hmim molecules reduces exponentially from an expected 15% loss for ZIF-L as guest loading increases to 12.72 % (Figure 1f).[29,36] Close observation of ATR-FTIR spectra revealed that the broad band around 3250 cm^{-1}, assignable to the free Hmim, [37] gradually decreased with increased guest loading (Figures S5, S7). These data indicate that with increased F used during ZIF-L synthesis, there is (1) less solvent within the F@ZIF-L framework and (2) a progressive reduction of free Hmim (that protrude into open framework space), both indicia that instead F guest molecules are being incorporated into the porous space of the ZIF-L framework. In the absence of Hmim, F could act as a similar directing unit to control framework growth, forming similar intermolecular bonds, including H-bonds, that supress growth between sodalite layers to form ZIF-8.

Morphology

Atomic force microscopy (AFM) and FE-SEM data were correlated to observe morphological changes for F@ZIF-L (Figure 2a-q). ZIF-L appears in the well-known ‘leaf’ morphology with dimensions of 7.33 x 2.76 μm (Figure 2a-b). Synthesis of F@ZIF-L with low guest loadings (H_2O only) produced the expected ZIF-L morphology

but with smaller particle sizes (Figure S14, 2o). Increasing MeOH content during synthesis incrementally widened the particle at all guest loading concentrations, so that an oval then curved rectangular particle shape formed, along with decreasing the overall particle size (Figure 2c-h, 2o). Similar particle widening was reported for carbon dot@ZIF-L materials.[31,33] Synthesising ZIF-L with the same increased MeOH content, but no guest content, resulted in the same particle widening, clarifying the change is primarily a result of the MeOH content (Figure S15). Surfaces of all particles are consistent with the arc topology of ZIF-L (Figure 2p), with no indication of guest surface aggregation.

Adjusting synthesis temperature, however, resulted in unique changes attributable to guest content. Between 35-45 °C, smaller rectangular particles were synthesised when both F (0.1 mg to 0.5 mg) and MeOH (6 mL) were used in synthesis (Figure 2m-o, S16). As guest loading increased, the rectangle became longer but narrower (Figure S17-18). From ≥ 50 °C and/or F content > 0.5 mg, an elongated hexagon formed (Figure S16-17). From 35 °C, when MeOH was included during synthesis without F, only the elongated hexagonal particle was observed (Figure S17), while increasing temperature with F but without MeOH resulted in the typical leaf shaped morphology (Figure S19). At 35 °C when F content remained constant (0.3 mg), but MeOH content was adjusted from 0-8 mL, the particle morphed from a leaf shape to pill, then towards a rectangle by 6 mL (Figure S19). These data highlight that while MeOH is required to attain the ideal rectangular morphology, it is not sufficient alone, rather a combination of MeOH and F is necessary. The rectangular particles also exhibited uniformly flat surfaces, in contrast to the gradually curved topology of ZIF-L and leaf-shaped F@ZIF-L (Figure 2p, S20 for AFM mechanical phase), indicating more complete crystal growth and a structure with more effective guest encapsulation.

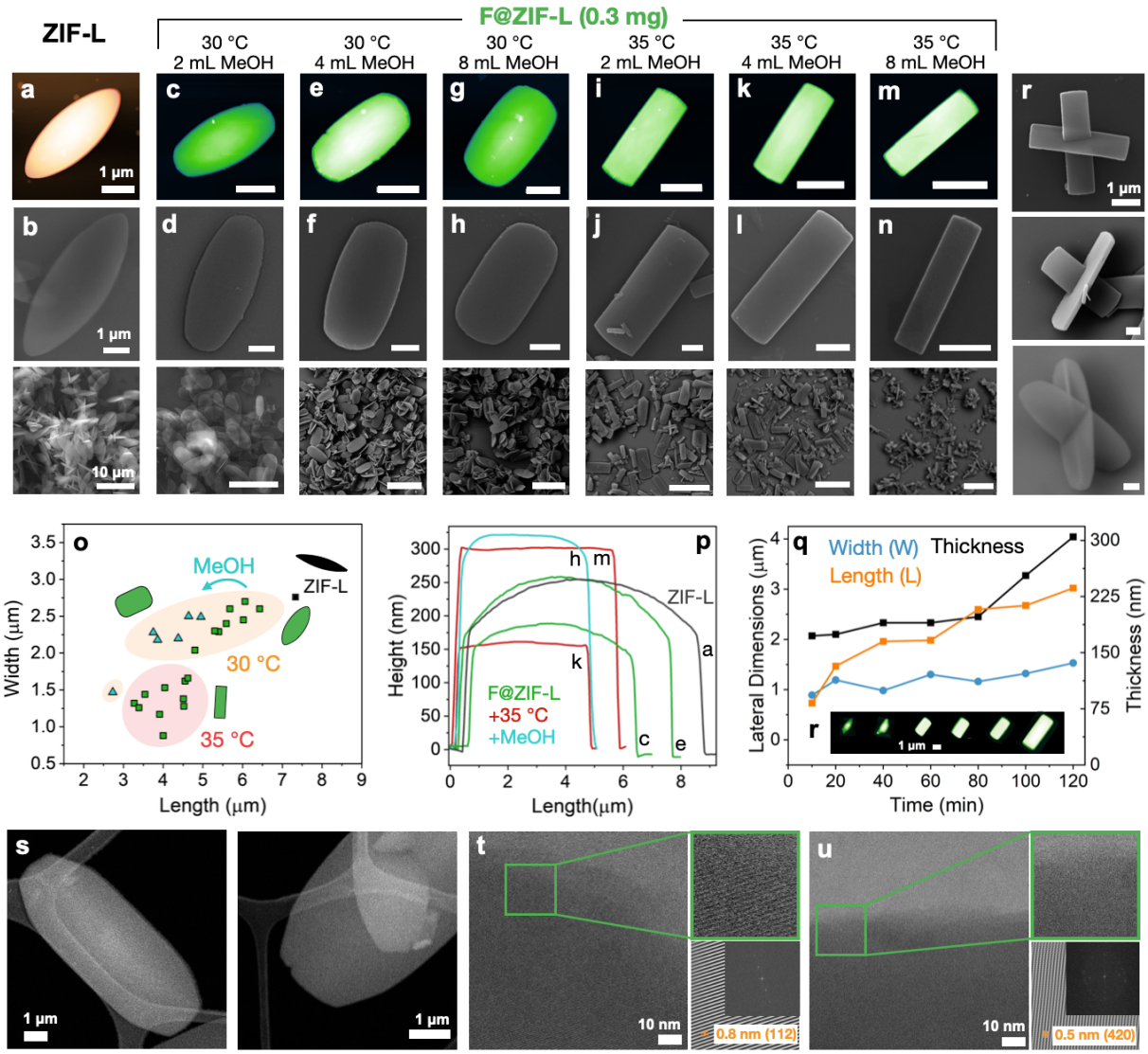

Figure 2. AFM and FE-SEM images, both of a single particle (above) and wider field of view (below), of ZIF-L (a-b), and F@ZIF-L (c-m). o) lateral dimension of F@ZIF-L samples (green) and ZIF-L (black) compared, highlighting clusters of data from reactions at 35 °C (red), 30 °C (orange) and 30 °C with added MeOH (blue, triangles). p) height profiles of F@ZIF-L and ZIF-L from select AFM images. q) lateral dimensions and thickness of F@ZIF-L during 120-minute synthesis (inset: images of particle growth during synthesis at each 20-minute interval). s) HAADF-STEM images of @ZIF-L (0.3 mg, F). t-u) BF-STEM images of F@ZIF-L particle edges, showing uniform domains of crystallinity. Right, above: sample zoomed in section of domain. Right, below: Fourier transform showing *d*-spacing and corresponding (hkl) lattice plane of ZIF-L.

Morphology of the rectangular F@ZIF-L tracked during the 120-minute synthesis (35 °C, 0.3 mg F, 6 mL MeOH) (Figure 2q). Data reveals initial growth along the *b*-axis, consistent with previously reported ZIF-L growth data.[27,37] The particle formed in the first 60 minutes, after which an approximately linear increase in all dimensions resulted progressively.

Of note, all particle morphologies appear to exist in a windmill-type particle form, involving the amalgamation of 2-3 particles (Figure 2r). FE-SEM revealed the central intersection of the two particles was often perpendicular, and that 'slits' formed in some single F@ZIF-L particles that appear to be suitable growth sites for the perpendicular windmill particles (Figure S21). These windmill morphologies were observed to be a minimal percentage of F@ZIF-L samples, at most 1 in every 100 particles, observed.

Local structure and energetics influencing morphology

To rationalise morphology based on structural energetics, we first needed to establish that individual F@ZIF-L particles exhibited crystallinity. High-angle annular dark-field imaging scanning transmission electron microscopy (HAADF-STEM) was employed to probe the local structure of F@ZIF-L particles (Figure 2s). Studies report ZIF-L is highly sensitive to electron dose, and exhibits a loss of crystallinity at >25 e/Å^2, followed by linker decomposition at >100 e/Å^2.[15,38] Maintaining a low beam strength (10-20 e/A^2) HAADF micrographs were collected of ZIF-L (Figure 2t) and F@ZIF-L (Figure S22). HAADF images of F@ZIF-L confirm the more rectangular morphology. Bright field (BF) STEM micrographs of F@ZIF-L particle edges displayed uniform crystallinity across the entire particle view (Figure 2t-u). Fourier transform was used to

measure *d* spacing equal to 0.5 nm in one image, and 0.8 nm in another (Figure 2t-u, S23). These correspond to the (420) and (112) crystal lattice planes using the (hkl) Miller indices, the two most intense reflections observed in PXRD diffraction patterns. These data confirm the local crystalline structure of F@ZIF-L, and that this is well represented by the bulk.

Previous studies have rationalised the unique leaf morphology of ZIF-L based on surface energies (Figure 3a).[13] In brief, energies are influenced by the dangling bonds, arising from terminal and free Hmim ligands in the structure. The surface energies of (100) and (110) are similar, each requiring one single bond per Zn to be broken, while the energy doubled for (010) due to both a single and double coordination bond required to be broken per Zn centre. The more energetically favourable assembly, therefore, minimises the presence of (010), leading to the pointed ZIF-L ends. The ZIF-L curve was previously determined to be comprised of (100) edges along the b-axis and (110) comprising most of the particle curvature, towards the pointed end, connected by small surfaces of the (320), (310), and (210) facets.[13]

The most extreme F@ZIF-L morphology change, a rectangular particle, contrastingly exhibits only the (100) and (010) edges along the *b*- and *a*-axis respectively, with (001) on the top and bottom surfaces along the *c*-axis (Figure 3a). The rounded rectangular and oval shaped F@ZIF-L particles show the incremental increase in (010) along the *a*-axis, reducing the presence of the (110) curvature contribution linking (010) to (100). This suggests the inclusion of guest molecules has varied surface energetics extensively, along with evidence that guests are well incorporated into the crystalline framework itself, rather than mere surface adhesion. Indeed, Figure 3b shows that the (110) surface intersects diagonally through the ZIF-L pore, breaking the pore, so the

sequential removal of (110) surfaces observed in F@ZIF-L particles indicates an energetic preference to maintain enclosed full pore structures upon guest incorporation, instead favouring the typically higher energy (010) surface.

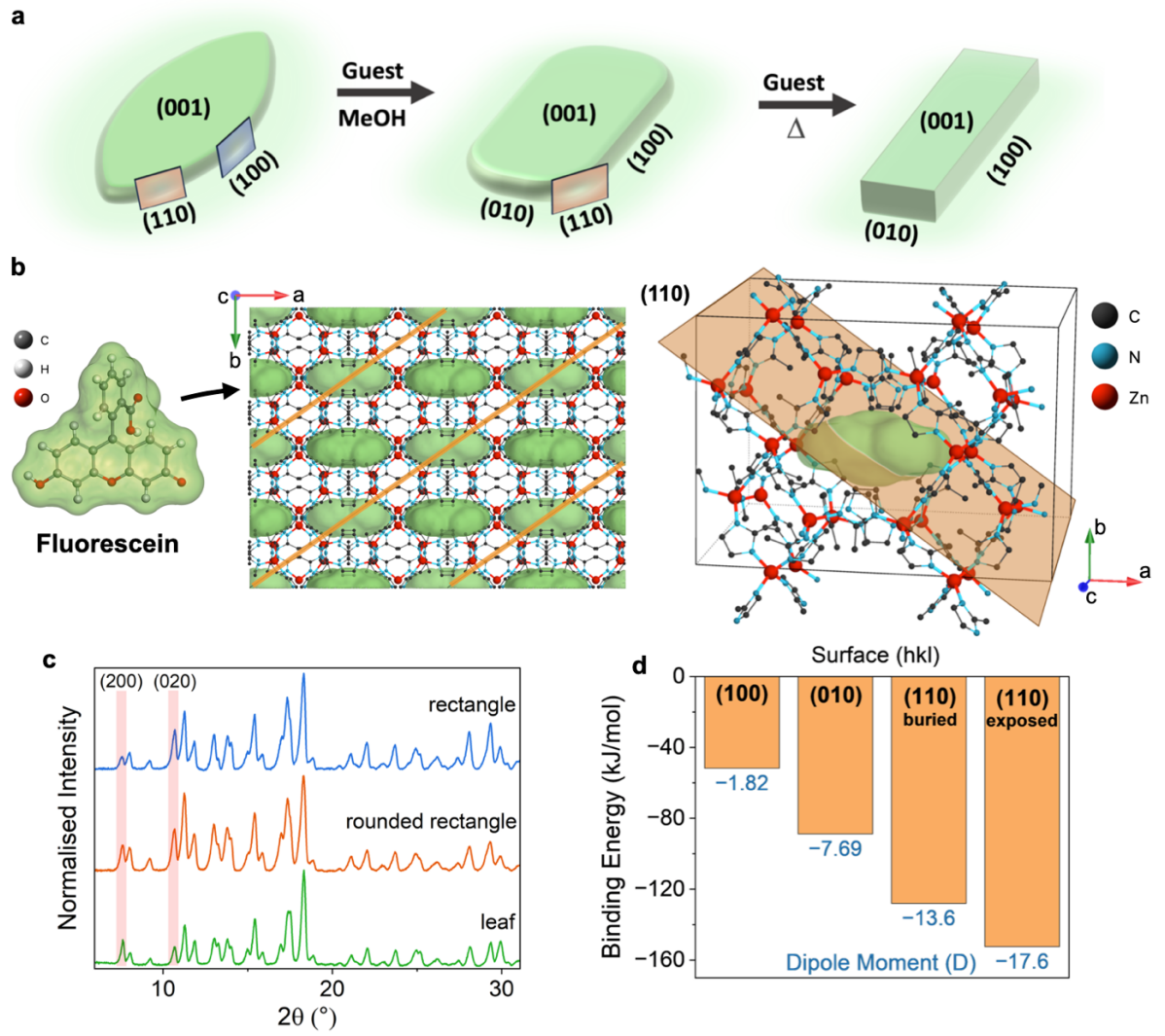

Figure 3. a) Sketch of the primary F@ZIF-L morphologies, indicating exposed surfaces with (hkl) lattice planes (orange plane show for (110) and blue plane shown for (100) where particles have no straight edge). b) Left: sketch of fluorescein. Centre: (001) cross section of ZIF-L indicating pore cavity in green, showing staggered pores in/out of the *c*-axis along the *a*-axis. Orange lines indicate (110) planes. Right: component of ZIF-L unit cell, representing pore cavity in green and the (110) plane in orange. c) PXRD patterns of F@ZIF-L with varying morphologies. d) Binding energy and dipole moments (blue) of F (dianion) on various surfaces of ZIF-L, calculated from periodic density functional theory (PBEsol0-3c) using slab models of 9-12 Å in thickness.

PXRD of F@ZIF-L samples synthesised at 35 °C with varying morphology reflects these changes at a bulk scale (Figure 3c). Specifically, the (020) reflection increases in intensity, while the (200) peak is reduced, indicating increased growth of the {010} family of planes in the rectangular morphologies. Generally, after normalisation to the most intense reflection (420), all reflections also appeared more intense and sharper in samples with rectangular particles, indicating increased crystallinity. These changes were also observed in the diffraction patterns of the 30 °C F@ZIF-L (0.3 mg, F) series when 8 mL of MeOH was used (creating the widest more rectangular particle) (Figure S24), while synthesis with only H_2O that exhibited no variation from the leaf morphology did not exhibit any changes in diffraction (Figure S24).

To test this hypothesis, employing *ab initio* DFT we modelled the adsorption of fluorescein on three difference surfaces of ZIF-L, (110), (010), and (110) using slab models of 9-12 Å thickness. Based on reported pH effects on fluorescein and a measured pH of 8.5-9 during F@ZIF-L synthesis,[36] along with observed NMR peaks from F@ZIF-L digest, it was assumed that fluorescein is incorporated into F@ZIF-L in its dianion form, so Zn^{2+} was used as a counterion (feasible to arise from minor defects in the framework). Importantly, two binding sites were possible for F on the (110) surface: a 'buried' site within the pore and an exposed site at the centre of the pore if fully enclosed (i.e. along the surface diagonal) (Figure S25). As expected, the binding energy of F was most favourable on the (110) surface (-152.4 kJ/mol), being in contrast significantly higher for (010) and (100) (-88.8 kJ/mol and -51.8 kJ/mol respectively) (Figure 3d). These data suggest that F has a strong energetic preference to bind to the pore opening site of ZIF-L at the (110) surface over other exposed surfaces during ZIF-L self-assembly. The dipole moment resulting for adsorption at the (110) surface, however, is significantly higher than for (010) and (100) (Figure 3d). This creates

instability, which would engage reconstruction or further self-assembly during F@ZIF-L growth to remove exposure of the surface. Hence, a particle morphology results that contains minimal (110) in favour instead of (010), contrasted to guest free ZIF-L.

This leads to a critical finding: exposed ZIF-L pores during synthesis are energetically favourable sites of guest adsorption, and a more rectangular ZIF-L crystal after synthesis indicates more complete incorporation of guest particles into the framework pores. This allows for further deduction as to why temperature and solvent varied the morphology of F@ZIF-L. Temperature is known to be an influential factor in MOF morphology.[35,39] MeOH molecules can be trapped in the ZIF-L framework, and likely result in the particle broadening seen for MeOH/H_2O synthesised ZIF-L. F is therefore in competition with MeOH for encapsulation. At a higher temperature, MeOH is more volatile, and confinement is less energetically favourable. Additionally, F solubility increases with temperature and heat increases the amount of energy available to the reaction system.[40] Collectively, these factors likely favour the energetics of adsorbing F onto surfaces constructing pore space, leading to more effective incorporation and the observed rectangular morphology.

Near Field Vibrational Spectroscopy

NanoFTIR has been established as an effective technique to detect guest vibrational bands if guest molecules are located on the surface of MOF materials.[41] NanoFTIR spectra of F@ZIF-L were therefore measured for various guest loadings then compared to the nanoFTIR spectra of ZIF-L and fluorescein (Figure 4a-f). Observing the F@ZIF-L (0.3 mg, F) spectra (Figure 4a), all vibrational bands can be seen to align well with those of ZIF-L including the out-of-plane Hmim ring bending at 750 cm^{-1}, the

in-plane bending mode of C-H at 1146 cm^{-1}, and the entire imidazole ring stretching bands from 1300-1500 cm^{-1}.[23,29,30] No additional peaks were observable that could be attributed to the expected vibrations from F, indicating effective encapsulation of F in ZIF-L. The spectra is also consistent with bulk material ATR-FTIR spectra.

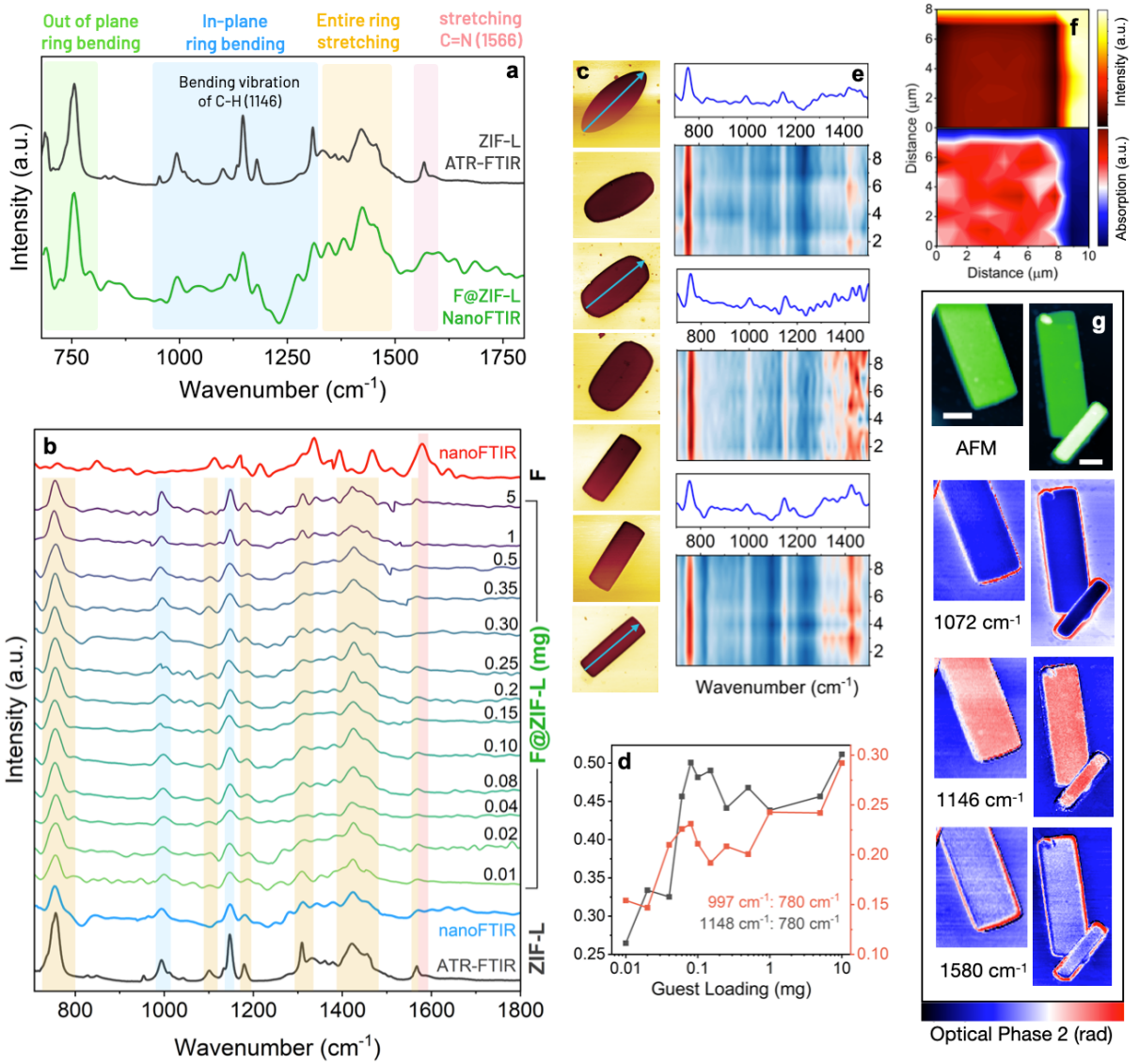

Figure 4. a) NanoFTIR of F@ZIF-L (0.3 mg, F), compared with ZIF-L ATR-FTIR. b) nanoFTIR of F@ZIF-L samples with varying guest loading (indicating in mg). c) Optical amplitude images of F@ZIF-L particles measured by nanoFTIR, confirming consistent intensity of signal across particles. d) ratio of vibrational bands in-plane:out-of-plane relative to guest loading, derived from spectra in b. e) 9-point line scans of three F@ZIF-L particles (blue lines in c indicate position of scans), with colour indicating intensity of signal across each spectra. f) 10x10 nanoFTIR spectral map of F@ZIF-L rectangular particle (0.3 mg, F) showing intensity of 780 cm^{-1} peak from each spectra. g) AFM (top, scale bar indicating 1 μm) and SNOM of three F@ZIF-L (0.5 mg, F) rectangular particles across three different wavelengths, colour indicating 2nd optical phase signal.

Comparing spectra across all guest loadings up to 5 mg (10 mg and above were excluded due to the presence of mixed F aggregate particles and ZIF-L), also reveal no observable bands arising from F (Figure 4b). While the spectra exhibited consistent bands, the 997 and 1141 cm^{-1} bands exhibited a significant increase in intensity compared to the 750 cm^{-1} band as guest loading increased (Figure 4d), indicating the reduction in signal from out-of-plane ring bending relative to in-plane. This is evidence of guest presence in pores and framework cavities, given guests would sterically hinder the extent of out-of-plane bending modes throughout the framework.

Across all morphologies, uniform optical amplitude signal was observed (Figure 2c). For the three distinct morphologies (leaf, rounded rectangle, rectangle) line scans comprised of 9 spectra were collected across the [010] axis of the particles (Figure 2e, S26). All characteristic peaks, particularly 750 cm^{-1}, of the ZIF-L framework remained consistent along the axis. To further probe the ends of the rectangular and rounded rectangular particles, 2D maps of 10 x 10 scans were also measured to show uniformity of the 750 cm^{-1} signal across the entire region (Figure 2f, S27).

Finally, scattering-type scanning near-field optical microscopy (s-SNOM) was used to assess the intensity of signal observable at specific wavelengths (Figure 2g). By using a monochromatic irradiation source compared with the broadband laser employed for nano-FTIR, illumination wavelength of the sample with SNOM can be tuned to an absorption band of interest.[41] A widefield fluorescence microscope was attached to the s-SNOM instrument also so that particles examined could first be confirmed as exhibiting the expected fluorescence of F@ZIF-L (see photophysical properties below). Imaging by tuning the irradiation source to 1146 cm^{-1}, the characteristic C-H bending vibration of ZIF-L, showed homogeneity of strong absorption and reflectance

across the entire F@ZIF-L particle observed (0.5 mg, 35 °C, 6 mL MeOH). Minimal contrast was obtained when the particle was illuminated at 1580 cm^{-1}, where the strongest F band occurs (the closest ZIF-L band being C=N at 1566 cm^{-1}). At most, a comparatively very weak but homogenous signal was observable across the entire particle (0.13-0.2 rad). Absorbance at the edge of the crystals is disregarded as shadowing and noise, typical edge effects seen in SNOM imaging, and a phenomenon also observed at a reference wavelength of 1072 cm^{-1}. This supports homogenous incorporation of F into the ZIF-L framework, and no apparent regions of concentrated guest aggregation.

Luminescent Behaviour of F@ZIF-L

The photophysical properties of 15 F@ZIF-L samples with varying guest loading but consistent MeOH reaction quantity (6 mL) were first examined (Figure 5a-h). All samples exhibited strong solid-state fluorescence with emission properties typical of F: a single emission band from 500-650 nm with a corresponding 450-550 nm excitation band (Figure 5a-e).[4,42,43] Importantly, this excitation and emission range does not overlap with emission from ZIF-L itself, avoiding issues of band mixing (Figure S28). The emission behaviour of F@ZIF-L is distinct from simply mixing ZIF-L with F in the ratios from the F@ZIF-L synthesis, which produced negligible emission due to aggregation-caused quenching (ACQ) (Figure S29).[5] It required a mass ratio of 1:1 of ZIF-L:F to observe low intensity F emission. This confirms that in F@ZIF-L the F molecules have been incorporated into the framework to an extent that overcomes ACQ to exhibit intense fluorescence.

MeOH was found to be an important variable in syntheses to ensure proper dissolution of F to then enable framework encapsulation. Indeed, synthesis using only H_2O yielded five samples with comparably low emission intensity (Figure S30). Emission increased from 0.01 to 0.1mg F synthesis content, after which intensity stabilised despite further increasing F content, indicating maximum solubility was reached in H_2O (Figure S30). Emission intensity at 0.01 mg was twice as strong when MeOH was used compared with H_2O only.

Examining the 15 F@ZIF-L samples (6 mL MeOH) when excited at 470 nm, emission λ_{max} red shifted with 0.01 to 20 mg F content from 534 to 555 nm (Figure 5a-b, S31), resulting in emission chromaticity adjusting from pale green to bright green, then yellow (Figure 5g-h, S32). Emission intensity increased 336% from the lowest loading (0.01 mg) to 0.2 mg (Figure 5a). Further guest loading caused a decrease in intensity, until comparatively negligible emission was observed (Figure 5b) for ≥10mg. Photoluminescent quantum yield (PLQY) followed emission trends, initially increasing from 0.01 to 0.08 mg F content to reach a maximum 99.95% from 84.76% (Figure 5f). PLQY then decreased exponentially with guest loading to less than 2% for ≥10mg. Excitation spectra observed at 600 nm for up to 5 mg F content, showed a primary excitation band at 510 nm, which followed the intensity variations seen emission spectra (Figure 5d, S33). Notably, these values are red shifted compared to reported F@ZIF-8 emission with λ_{max}=515-535 nm and excitation with λ_{max}=499 nm,[36] suggesting 2D ZIF-L more favourably stabilises F emission pathways compared to the analogous 3D ZIF-8. From ≥10mg a distinct excitation spectral profile was observed, with a sharp excitation band at 533 nm and less intense shoulder bands from 450-525 nm (Figure 5e). These distinct changes, along with minimal emission, at higher guest content arise from the oversaturation of guest relative to host and aggregated F

particles forming, as observed in SEM and ATR-FTIR. In contrast, the ideal guest loading for the best photophysical properties appears to occur between 0.1-0.2 mg of F during synthesis (0.02-0.04 % mol loading).

F is known to aggregate,[44] including in ZIF-8,[36] so such behaviour was more precisely probed by examining fluorescence lifetime using time-correlated single-photon counting (TCSPC). Data was collected for each sample at emission λ_{max} (540 nm) along with 520 and 560 nm (Figure 5i-j, S34). Data indicated multiexponential decay behaviour, modelled with three-time components: $\tau_1 \approx$ 0.4-0.8 ns, $\tau_2 \approx$ 1.1-3.4 ns, and τ_3 = 3.1 – 6.0 ns (Table S2). It is well agreed in literature that τ_3 is attributable to the F monomer, τ_2 to the J-aggregated F (head-to-tail), and τ_1 to the H-aggregated F (head-to-head) (Figure 5i).[36,45] At lower guest loadings (0.01-0.2 mg), monomer and J-aggregate components dominate (Figure 2i), leading to strong emission and a red shift attributable to the longer wavelength emission from J-aggregates (Figure 5a-b).[46] This corresponds to the broadening of excitation bands at longer wavelengths (Figure 5d), which is also indicative of J-aggregate formation.[45] These data indicate effective encapsulation of F in ZIF-L, creating a combination of isolated species likely residing in ZIF-L pores, along with interactions between species in adjacent pores (end to end) or due to a staggered overlap. As guest loading increases from the 0.2 mg sample, monomer content decreases while h-aggregates increase, which quench emission as seen in spectra (Figure 5b). A higher energy shoulder is also seen forming in excitation spectra, a further indicator of H-aggregate formation (Figure 5d-e).[45] This suggests 0.2 mg is near the host interior saturation limit for F, after which excess guest more easily aggregates as head-to-head stacked particles, potentially on particle surfaces or defective regions of the ZIF-L crystalline framework. H-aggregation is so significant for ≥10mg (32% contribution) that emission is effectively quenched.

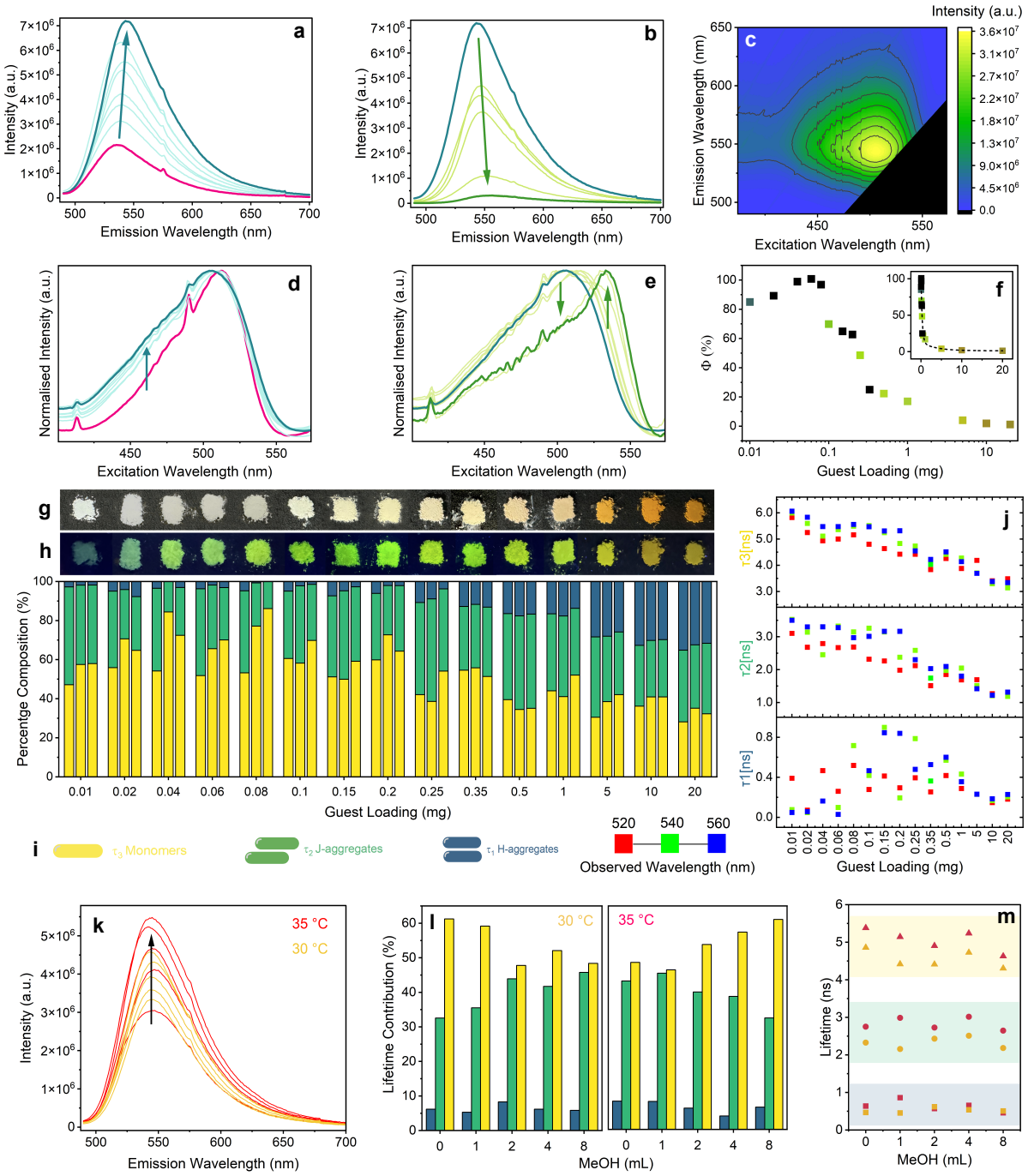

Figure 5. a-b) Emission spectra of F@ZIF-L (30 °C, 4 mL MeOH) excited at 470 nm with guest loadings from 0.01 (pink), to 0.2 mg (blue), then to 20 mg (green). Arrows indicate spectral progression with increasing guest loading. c) emission map of F@ZIF-L (0.3 mg, F). d-e) excitation spectra observe at 600 nm of F@ZIF-L samples as in (a-b). Arrows indicate spectral progressions with increasing guest loading. f) photoluminescent quantum yield of F@ZIF-L samples. g-h) F@ZIF-L samples shown under ambient (g) and 365 nm UV light (h). i) lifetime decay parameters observed at 520, 540 and 560 nm (left to right for each sample) with a sketch of corresponding F arrangements below (yellow = monomers, green = J-aggregates, blue = H-aggregates). j) component lifetime values for all F@ZIF-L samples, with observed wavelength indicated by data point colour (red = 520 nm, green = 540 nm, blue = 560 nm). k) emission spectra of F@ZIF-L (0.3 mg) synthesised at 30 °C (yellow) and 35 °C (red) with increasing MeOH content (0, 1, 2, 4, 8 mL). Arrow indicates increase in intensity resulting from increasing MeOH content. l) lifetime decay parameters observed at 540 nm for F@ZIF-L (0.3 mg) with varying temperature and MeOH content during synthesis. m) corresponding lifetime parameter values.

Lifetime values also provide insight into guest incorporation. F@ZIF-L exhibits a longer monomeric lifetime decay component (5-6 ns for lower guest loadings) compared to the typical F lifetime of 4.08 ns (Figure 5j). This is caused by the confinement effect, often seen for dye@MOF materials, where non-radiative processes are supressed due to encapsulation, resulting in increased lifetime and quantum yield.[6] The lifetime of the monomer and J-aggregate components decrease as guest loading increases. This behaviour has been reported in dye@MOF systems previously and was attributed to increased probability of interactions between F species across adjacent pores and through framework channels or structural defects.[45,47]

Optimising F@ZIF-L Luminescence by tuning reaction conditions

The effect of guest loading and emission behaviour observed above remained consistent at different MeOH content (1, 2, 4, and 8 mL) (Figure S35). Increasing MeOH content at a constant guest loading, interestingly, increased emission intensity (and corresponding excitation spectra intensity) (Figure S35). At 0.1 mg, from 1 mL to 8 mL of MeOH, a 2.3x increase resulted, while for 0.3 and 0.5 mg a 1.5x intensity increase occurred. Emission profiles remained consistent when the data was normalised, indicating no additional emission bands resulting from MeOH content (Figure S35). TSPC lifetime data showed that at 0.1 mg (S36, Table S3), increasing methanol resulted in a reduction in monomers and increase in J-aggregates, while H-aggregates remained consistent. As NMR indicated guest loading increased with MeOH content, this may simply be the result of increased F, imitating the data observed at higher F synthesis content examined earlier. Introducing more bulky MeOH solvent molecules may also disrupt the self-assembly of the framework,

introduce more defects and open pore sites, increasing the overlap of adjacent guests to interact as J-aggregates. The same effect is observable, but with a lesser reduction in monomers at 0.3 mg. For 0.5 mg, the composition remains consistent across MeOH loading. This supports the premise that loading is already oversaturated at this guest concentration, so any benefits MeOH provides to guest incorporation are less relevant. Hence, while guest loading is a dominant force influencing emission guest properties, at lower guest content the variability of MeOH can have significant effects also.

Noting the morphology variance achieved with temperature adjustment, the resultant fluorescent variations were also examined at a set guest loading of 0.3 mg. With increasing MeOH content, the samples synthesised at 35 °C exhibited more intense emission and stronger excitation spectra relative to the same MeOH used at 30 °C (Figure 5k, Figure S37). Given guest loadings were similar at each temperature as MeOH content varies, this improved emission efficiency must instead be attributable to the pathways of emission and guest arrangement. Indeed, lifetime data indicates clear opposing trends (Figure 5l, Table S4): while at 30 °C monomer content decreases and J-aggregates increase with increasing MeOH content, at 35 °C monomer content increases but J-aggregates decrease with MeOH content. H-aggregates remain consistent; expected given they arise from surface-species guest loading oversaturation. The lifetime of monomer and J-aggregate components are observed to increase by nearly 1 ns at 35 °C, compared to 30 °C (Figure 5m). This suggests improved confinement, increasing emission intensity due to increased suppression of non-radiative decay pathways. This could arise from the improved framework structural completeness, providing more complete pore space for the confinement of guests, hence increased monomeric species.

Fluorescence Microscopy

Single F@ZIF-L particles were examined under fluorescence confocal microscopy. Using lambda scanning (3 nm resolution), all particles excited with a 488 nm laser showed consistent emission spectra to bulk F@ZIF-L, confirming the luminescent behaviour observed in bulk resulted from F@ZIF-L crystals (Figure 6a). The increasing band broadness across the sample spectra also aligns with the increasing proportion of aggregates present in each sample based on bulk analysis. Particles are reported both with colouring simulated from lambda scanning to reflect emission seen by eye, along with artificial colouring from averaging z-stack scanning (14 slices across 7 μm) (Figure 6b). While the simulated emission colour appears homogenous across the particles, the z-stack scan revealed more nuanced behaviour: both as single particles and windmill-type particles exhibited stronger emission at particle ends ((010) surfaces with curves of predominantly (110)), with weaker emission (30% of ends) throughout the particle (Figure 6c).

A similar emission distribution across MOF crystals has been attributed to incomplete diffusion of guests during post-synthesis modification.[48] Here, however, we employed *in situ* encapsulation of F as the framework self assembles. SNOM and nanoFTIR data also clearly demonstrate a consistent and strong signal from the ZIF-L framework across the entire particle, eliminating the possibility of fragmented edges that may expose more guest material. One justification for the variability in emission intensity across particles is guest arrangement: at the crystal edges, it is more feasible for the more J-aggregates to form where framework features are incomplete or contain defects, intensifying emission. Through the particle, monomeric guest positioning is more expected. We do not discount the possibility of edge effects and light scattering

also, given the 100-150 nm thinness of particles, leading to the appearance of intense emission at the particle edges. Similar effects were observed in luminescent microrods of lanthanide MOFs, where active optical waveguides resulted in brighter emission spots at the tip of each particle by propagating emission waves through the particle.[49]

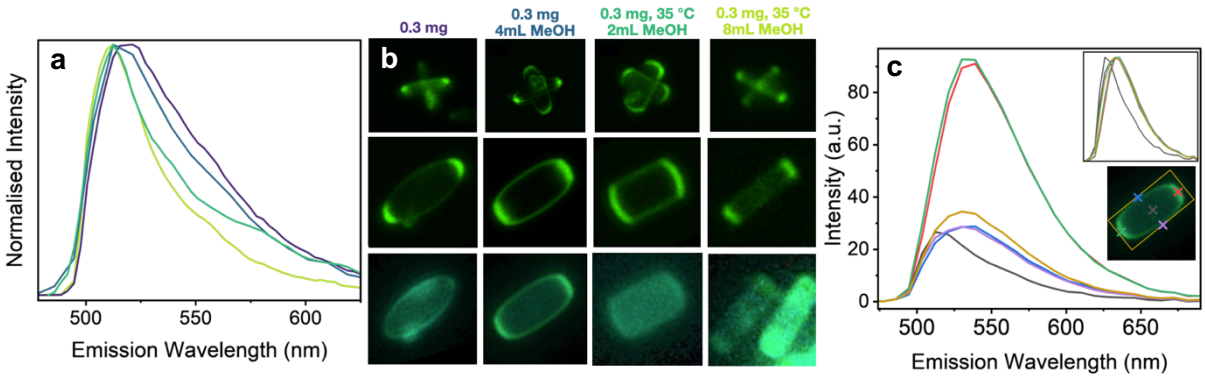

Figure 6. a) Emission spectra from individual F@ZIF-L particles excited at 488 nm, the colour of each spectra matching the sample description in (b). b) Fluorescence microscopy of F@ZIF-L particles with artificial colouring to represent signal intensity (above, middle), and predicted emission colour based on emission profile (bottom). c) Emission intensity variation across a single 0.3 mg F@ZIF-L (4 mL MeOH) particle, with normalised spectra inset. Colours of spectra match the positions on the particle.

Stability

Photostability was examined using three guest loadings, 0.04, 0.30, and 1 mg (Figure S38). Data shows similar decomposition, (35.5 - 39.3%) over 24-hour exposure to exposed to 150 W concentrated UV irradiation from a Xenon lamp at the absorption maximum of each F@ZIF-L sample. Compared with a typical 4 W LED cell, these results reflect a simulation of long-term working-time use. Importantly, the decay did not exhibit significant exponential loss in the initial minutes of exposure, a typical feature of surface attached dye species on MOF materials, and chromaticity did not alter after exposure (Figure S38).

F@ZIF-L was dispersed in MeOH and after 13 months remained luminescent (Figure S39). The MeOH did not exhibit fluorescence, and only negligible trace quantities of F were detected in the MeOH (0.071 % of the intensity of F@ZIF-L, calculated to be 0.014 ppm), indicating robust entrapment of F in the ZIF-L framework (Figure S39).

Other luminescent guest@ZIF-L systems

With an understanding of optimal guest loading and synthesis strategies, the wide applicability of the guest@ZIF-L design to create luminescent functional materials was demonstrated by attempting to incorporate 4 different organic dyes molecules into ZIF-L that theoretically have suitable dimensions for the largest ZIF-L pore. Of these, perylene@ZIF-L and 7-hydroxycoumarin@ZIF-L (HC@ZIF-L) were successfully synthesised. Pyrene and coronene were not successfully incorporated, primarily due to incompatible solvents for dissolution. PXRD confirmed the retention of the ZIF-L crystalline framework (Figure S40), while FTIR spectra indicated no vibrational bands from guest molecules (Figure S41). FE-SEM showed all particles exhibited widening, as for F@ZIF-L (Figure 7a-e), and a shift from pointed ends to rounded rectangular corners, indicia for effective incorporation of guest@ZIF-L.

Perylene and HC are luminescent, emitting green/yellow and blue respectively in the solid state.[50] When encapsulated in ZIF-L, HC@ZIF-L retained the emission behaviour of HC but with an enhancement in emission intensity, partially resulting from the additional contribution of ZIF-L Hmim emission overlapping in the same region (Figure 7c, S42). Remarkably, perylene@ZIF-L emits a near ideal white light with CIE coordinates (0.33, 0.34) when synthesised in H_2O/DMF (2 mL) solvent mix and with higher guest loadings (0.1 % mol measured by NMR digest) (Figure 7f-j, S43)). In

contrast, lower loadings (0.03 %) using the same solvent mix resulted in a light blue emission and using H_2O (very low solubility of perylene) a darker blue emitter resulted with 0.009 % guest loading. Notably the H_2O synthesised perylene@ZIF-L retained the leaf ZIF-L morphology, indicating minimal guest loading compared with DMF syntheses (Figure S43).

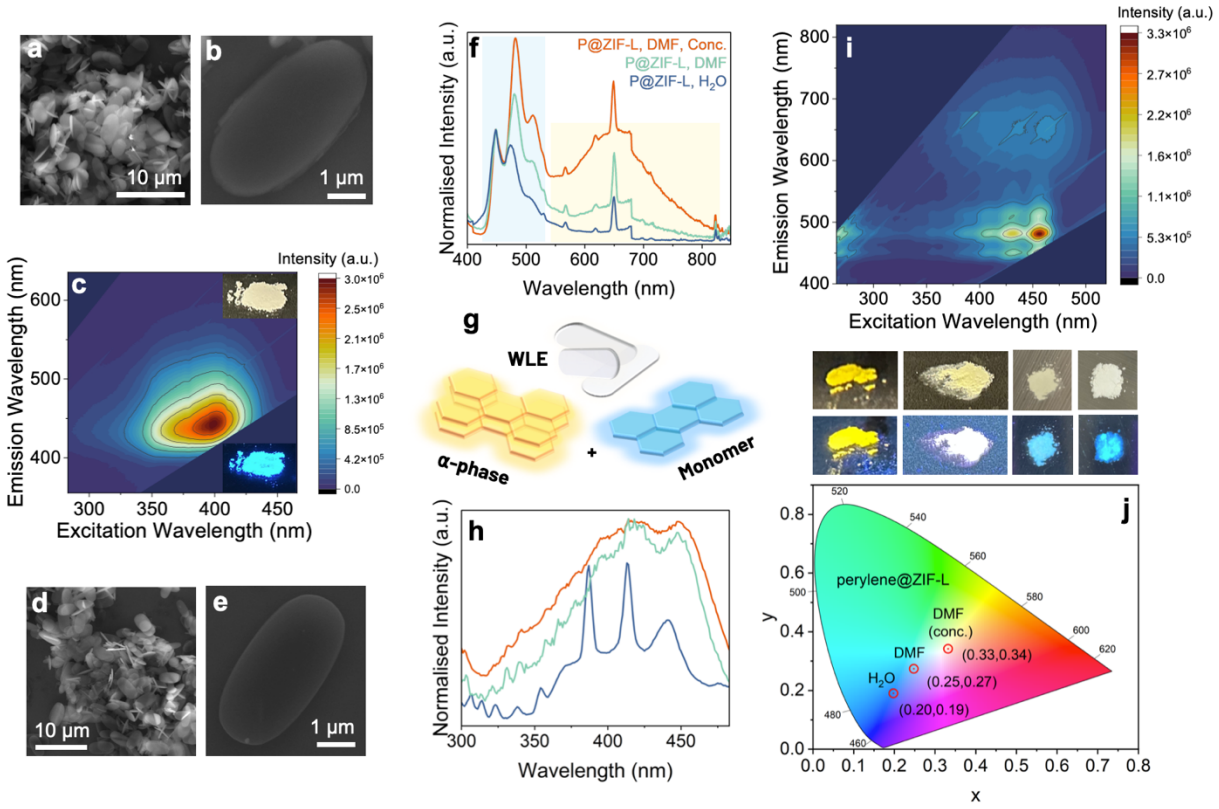

Figure 7. a-b) FE-SEM of HC@ZIF-L showing rounded rectangular particles. c) emission map of HC@ZIF-L. d-e) FE-SEM of perylene@ZIF-L showing rounded rectangular particles. f) emission spectra of perylene@ZIF-L (excited at 380 nm) highlighting the monomer (blue) and excimer (yellow) regions. g) sketch illustrating WLE perylene@ZIF-L particles, formed from arrangements of single perylene monomers emitting in the blue region and α-phase dimers emitting in the yellow-orange region. h) excitation spectra of perylene@ZIF-L samples, according to colour key of (f), observed at 500 nm. i) emission map of perylene@ZIF-L (DMF, with concentrated guest), j) emission chromaticity of perylene@ZIF-L, showing near ideal WLE coordinates, with corresponding photographs (above) of the samples under ambient and a 365-nm UV light (below).

While white light emitting (WLE) perylene has not been reported, other perylene@MOF systems such as ZIF-8 provide theoretical explanations for the observed WLE phenomenon in ZIF-L.[47,51,52] The emission spectra of the perylene@ZIF-L samples (excited across 350-475 nm) contain two components: sharp peaks around 450-500 nm, followed by a broad intense band from 600-700 nm (Figure 7i). The first band is assignable to emission of single monomeric perylene molecules, and is rare to observe in the solid state due to needing to isolate molecules. The second arises due to STE emission, with α-phase perylene units (dimeric stacked molecules) emitting as an E-state excimer (Figure 7g).[50,53] This state was observed when entrapping perylene in MIL-68 due to confinement inducing the dimeric structure. Uniquely, perylene@ZIF-L is formed of both dimeric α-phase units and monomers, a similar arrangement seen for F. This combination creates broad-band emission distributed appropriately to form WLE. For lower guest loaded perylene@ZIF-L samples, the α-phase contribution reduces until non-existent, indicating the preference for perylene to remain as monomers (Figure 7f). Excitation spectra observed at 700 nm support this, with the lowest guest loading perylene@ZIF-L exhibiting discrete sharp bands corresponding to monomer emission, in contrast to a broad structureless band observed at higher guest loading, indicative of α-phase dimeric emission.

This aligns with a crystallographic and steric understanding: dimensions of perylene align closely with the pore size of ZIF-L (9.3 x 6.7 vs 9.4 v 7 Å) and with 5.3 Å of height per pore. It is therefore possible for dimeric perylene to form, especially considering the flexibility of ZIF-L, and the pore space would encourage the precise stacked placement required for the α-phase. However, less strain and a more energetically

favourable, and stable, material would be produced by isolating a single perylene species in each pore. Interestingly, perylene adsorption was modelled on the (100), (010), and (110) surfaces of ZIF-L using the same method as for F (Figure S45). The data showed consistent trends, indicating an even stronger preference than F for binding at (110) over (010) or (100), along with a 27 % lower binding energy at (110) over F@ZIF-L. Given the calculated energy of perylene molecules to aggregate is -129.7 kJ/mol, the adsorption at (110) in ZIF-L is a highly favourable energetic process, either as a monomer or dimeric unit.

Heteroepitaxial Growth of F@ZIF-L films

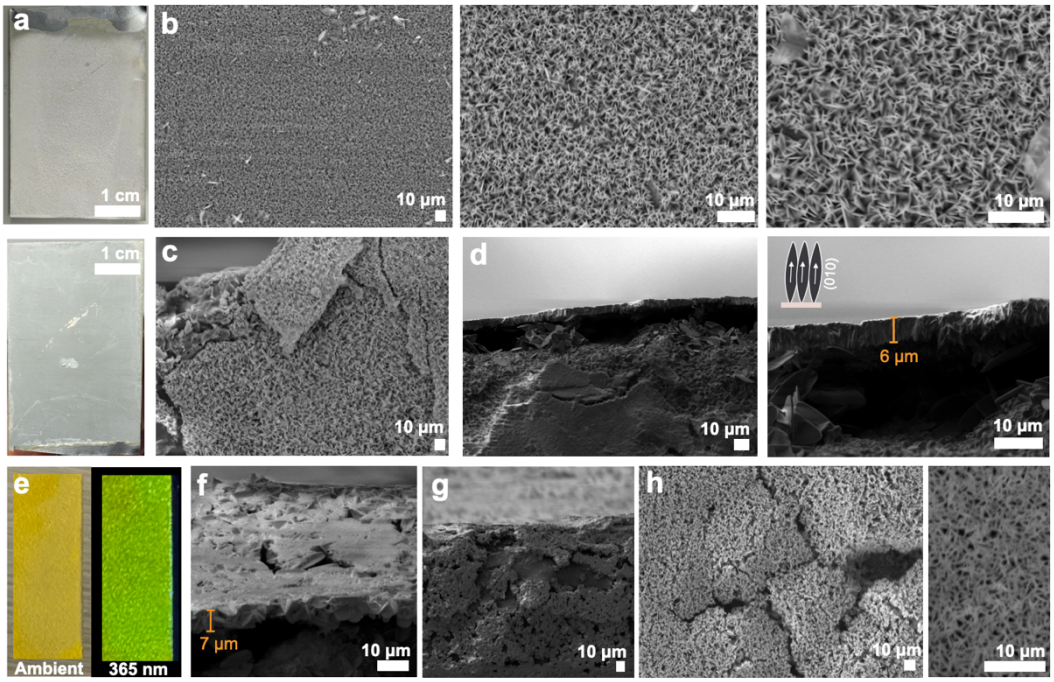

Figure 8. a) Images of ZIF-L coated Zn foil. b) FE-SEM of ZIF-L film at various levels of magnification. c) FE-SEM at the edge of the ZIF-L film. d) FE-SEM of ZIF-L film highlighting orientation and thickness. e) F@ZIF-L layer on Zn foil under ambient and UV (365 nm) light. (f-h) FE-SEM of F@ZIF-L film showing uniformity of orientation and thickness near a film edge.

We finally briefly demonstrate a secondary benefit to the ZIF-L morphology: creating oriented films. Immersing Zn film in the reagent mixture for ZIF-L produced well oriented thin-films of ZIF-L around 5 μm thick,[25] comparable to the *b*-axis length of a single ZIF-L particle (Figure 8a-d). By including F in the synthesis, an oriented thin-film of F@ZIF-L was formed of 6-8 μm thickness (Figure 8e-h). The incorporation of F into the ZIF-L framework, rather than merely coating a ZIF-L film was confirmed by FE-SEM images, which showed the rounder F@ZIF-L particles forming the film itself and no regions of F particle aggregation (Figure 8f-h). The film exhibited strong fluorescence of F@ZIF-L character, further confirming guest-host interactions (Figure 8e).

Conclusions

This study has established fundamental principles directing the formation of solid-state guest@ZIF-L materials. Employing fluorescein as a case study molecule, systematic studies revealed a morphological continuum that was indicative of guest incorporation: as guest loading increased, particles adjusted from the characteristic leaf shape of ZIF-L to rounded rectangles then rectangular particles. From crystallographic data and DFT theory it was concluded that these variations arise due to limiting the presence of the (110) plane, which intersects the pore cavities of ZIF-L and is the preferential binding site of guests in ZIF-L out of the possible exposed surfaces, preferring instead to expose (010). This meant greater retention of pore space in the particle, and higher crystallinity. Indeed, nanoFTIR confirmed the lack of surface guest species on ZIF-L particles, along with supporting structural and chemical data.

Encapsulating F in ZIF-L prevent ACQ, turning on the molecule to form highly luminescent F@ZIF-L particles. Particles with a rectangular morphology were found to be more luminescent and proportionally composed of F arranged as monomers, indicative of effective guest incorporation. HC@ZIF-L exhibited blue emission, while encapsulating perylene@ZIF-L produced either blue emitting materials or an ideal white-light emitter with CIE (0.33, 0.34) depending on the guest loading. This result derived (as for F) from guest arrangement, being a combination of blue emitting monomer perylene units and yellow emitting dimer α-phase excimers. The materials showed high photostability and guest retention over long-term testing, attributable to the dense 2D layers of ZIF-L that are tightly interconnected by hydrogen bonding. A final advantage of the 2D morphology was unlocked by growing uniformly oriented luminescent thin films of F@ZIF-L directly on a Zn foil substrate.

Together, the findings demonstrate the advantageous functionality accessible by incorporating luminescent guests into ZIF-L to produce stable and highly effective lighting materials. The now elucidated nanosheet growth mechanisms may be employable for many more organic guests, however, and myriad opportunities exist to encapsulate organic molecules with sensing, electroluminescent, electrochromic potential, or more, to create and customise a new generation of chromatic-based functional 2D ZIF-L materials.

Data Statement

The data that support the findings of this study are available in the supplementary material of this article. Any other data will be made available on request.

Acknowledgments

D.A.S. acknowledges the scholarships from the General Sir John Monash Foundation and Clarendon Fund. J.C.T. thank the ERC Consolidator Grant (PROMOFS 771575) and EPSRC (EP/R511742/1) for funding the research. The authors would like to acknowledge Dr Jana Koth, Facility Manager at the Wolfson Imaging Centre (MRC Weatherall Institute of Molecular Medicine) for the provision and operation of fluorescence microscopy equipment. We acknowledge the ePSIC beamtimes MG31944-1 to -6 at the Diamond Light Source.

Author Contributions

The manuscript was written through contributions of all authors.

References

1. Lustig W. P., Mukherjee S., Rudd N. D., Desai A. V., Li J., Ghosh S. K. Metal-organic frameworks: functional luminescent and photonic materials for sensing applications. *Chem. Soc. Rev.* **46**, 3242-3285 (2017).

2. Pan M., Liao W. M., Yin S. Y., Sun S. S., Su C. Y. Single-Phase White-Light-Emitting and Photoluminescent Color Tuning Coordination Assemblies. *Chem. Rev.* **118**, 8889-8935 (2018).

3. Tang Y., Wu H. L., Cao W. Q., Cui Y. J., Qian G. D. Luminescent Metal-Organic Frameworks for White LEDs. *Adv. Opt. Mater.* **9**, 2001817 (2020).

4. Sjöback R. N., J.; Kunista, M. . Absorption and fluorescene properties of fluorescein. *Spectrochim. Acta* **51**, 7-21 (1995).

5. Ma X.*, et al.* Fluorescence Aggregation-Caused Quenching versus Aggregation-Induced Emission: A Visual Teaching Technology for Undergraduate Chemistry Students. *J. Chem. Educ.* **93**, 345-350 (2015).

6. Gutierrez M., Zhang Y., Tan J. C. Confinement of Luminescent Guests in Metal-Organic Frameworks: Understanding Pathways from Synthesis and Multimodal Characterization to Potential Applications of LG@MOF Systems. *Chem. Rev.* **122**, 10438-10483 (2022).

7. Li P., Zhou Z., Zhao Y. S., Yan Y. Recent advances in luminescent metal-organic frameworks and their photonic applications. *Chem. Commun.* **57**, 13678-13691 (2021).

8. Kaneti Y. V.*, et al.* Strategies for Improving the Functionality of Zeolitic Imidazolate Frameworks: Tailoring Nanoarchitectures for Functional Applications. *Adv. Mater.* **29**, 1700213 (2017).

9. Nicks J., Sasitharan K., Prasad R. R. R., Ashworth D. J., Foster J. A. Metal‐Organic Framework Nanosheets: Programmable 2D Materials for Catalysis, Sensing, Electronics, and Separation Applications. *Adv. Funct. Mater.* **31**, 2103723 (2021).

10. Chakraborty G., Park I.-H., Medishetty R., Vittal J. J. Two-Dimensional Metal-Organic Framework Materials: Synthesis, Structures, Properties and Applications. *Chem. Rev.* **121**, 3751-3891 (2021).

11. Feng Y., Wang H., Yao J. Synthesis of 2D nanoporous zeolitic imidazolate framework nanosheets for diverse applications. *Coord. Chem. Rev.* **431**, 213677 (2021).

12. Chen R., *et al*. A two-dimensional zeolitic imidazolate framework with a cushion-shaped cavity for CO2 adsorption. *Chem. Commun*. **49**, 9500-9502 (2013).

13. Motevalli B., Taherifar N., Wang H., Liu J. Z. Ab Initio Simulations To Understand the Leaf-Shape Crystal Morphology of ZIF-L with Two-Dimensional Layered Network. *J. Phys. Chem. C* **121**, 2221-2227 (2017).

14. Motevalli B., Wang H., Liu J. Z. Cooperative Reformable Channel System with Unique Recognition of Gas Molecules in a Zeolitic Imidazolate Framework with Multilevel Flexible Ligands. *J. Phys. Chem. C* **119**, 16762-16768 (2015).

15. Deacon A., *et al*. Understanding the ZIF-L to ZIF-8 transformation from fundamentals to fully costed kilogram-scale production. *Commun. Chem*. **5**, 18 (2022).

16. Valencia L., Abdelhamid H. N. Nanocellulose leaf-like zeolitic imidazolate framework (ZIF-L) foams for selective capture of carbon dioxide. *Carbohydr. Polym*. **213**, 338-345 (2019).

17. Zou X., Zhang H., Xiang L., Huang C., Li J. Designing a dual-functional ultrathin ZIF-L@GO adsorbent for simultaneous removal of phosphate and tetracycline hydrochloride: Adsorption capacity and mechanism. *Colloids Surf. A* **683**, 132851 (2024).

18. Gu Q., *et al*. Heterogeneous ZIF-L membranes with improved hydrophilicity and anti-bacterial adhesion for potential application in water treatment. *RSC Adv.* **9**, 1591-1601 (2019).

19. Ting H., Chi H.-Y., Lam C. H., Chan K.-Y., Kang D.-Y. High-permeance metal–organic framework-based membrane adsorber for the removal of dye molecules in aqueous phase. *Env. Sci.: Nano* **4**, 2205-2214 (2017).

20. Low Z.-X., Razmjou A., Wang K., Gray S., Duke M., Wang H. Effect of addition of two-dimensional ZIF-L nanoflakes on the properties of polyethersulfone ultrafiltration membrane. *J. Membr. Sci*. **460**, 9-17 (2014).

21. Chen M.-J., *et al*. Influence of crystal topology and interior surface functionality of metal-organic frameworks on PFOA sorption performance. *Microporous and Mesoporous Mater.* **236**, 202-210 (2016).

22. Ahmad S. Z. N., Salleh W. N. W., Ismail N. H., Razali N. A. M., Hamdan R., Ismail A. F. Effects of operating parameters on cadmium removal for wastewater treatment using zeolitic imidazolate framework-L/graphene oxide composite. *J. Environ. Chem. Eng*. **9**, 106139 (2021).

23. Rahaman M. A., Mousavi B., Naz F., Verpoort F. Two-Dimensional Zeolitic Imidazolate Framework ZIF-L: A Promising Catalyst for Polymerization. *Catalysts* **12**, 521 (2022).

24. Zhong Z.*, et al*. Oriented two-dimensional zeolitic imidazolate framework-L membranes and their gas permeation properties. *J. Mater. Chem. A* **3**, 15715-15722 (2015).

25. Xiang Q.*, et al*. Heterostructure of ZnO Nanosheets/Zn with a Highly Enhanced Edge Surface for Efficient CO2 Electrochemical Reduction to CO. *ACS Appl. Mater. Interfaces* **13**, 10837-10844 (2021).

26. Chen T.*, et al*. Smart ZIF-L mesh films with switchable superwettability synthesized via a rapid energy-saving process. *Sep. Purif. Technol.* **240**, 116647 (2020).

27. Yuan S.*, et al*. Structure architecture of micro/nanoscale ZIF-L on a 3D printed membrane for a superhydrophobic and underwater superoleophobic surface. *J. Mater. Chem. A* **7**, 2723-2729 (2019).

28. Wang S., Zang B., Chang Y., Chen H. Synthesis and carbon dioxide capture properties of flower-shaped zeolitic imidazolate framework-L. *CrystEngComm* **21**, 6536-6544 (2019).

29. Gao M.*, et al*. A novel fluorescent probe for Fe3+ detection based on two-dimensional leaf-like structure CDs@ZIF-L. *Microchem. J.* **182**, 107868 (2022).

30. Liu X., Wang X., Sun C., Hu X., Song W. Brine available two-dimensional nano-architectonics of fluorescent probe based on phosphate doped ZIF-L for detection of Fe^{3+}. *Heliyon* **9**, e17884 (2023).

31. Zhang S., Mao Y., Wei L., Song Z., Zhao X., Wang W. Full-value preparation of biochar and 2D N-doped CDs@ZIF-L from fermentation residues for sensitive sensing tetracyclines in food samples. *Colloids Surf. A* **676**, 132073 (2023).

32. Liu X., Sun C., Chai M., Song W. Highly dispersive PEI-modified CDs@ZIF-L dual-emitting fluorescent sensor for detecting metal ions. *RSC Adv.* **13**, 31353-31364 (2023).

33. Li H.-J.*, et al*. Tailoring Morphology and Fluorescence Properties of Zeolitic Imidazolate Frameworks via Carbon Dots. *ACS Appl. Nano Mater.* **7**, 15535-15546 (2024).

34. Wijaya C. J., Ismadji S., Aparamarta H. W., Gunawan S. Facile and Green Synthesis of Starfruit-Like ZIF-L, and Its Optimization Study. *Molecules* **26**, 4416 (2021).

35. Bustamante E. L., Fernandez J. L., Zamaro J. M. Influence of the solvent in the synthesis of zeolitic imidazolate framework-8 (ZIF-8) nanocrystals at room temperature. *J. Colloid Interface Sci.* **424**, 37-43 (2014).

36. Xiong T., *et al*. Tunable Fluorescein-Encapsulated Zeolitic Imidazolate Framework-8 Nanoparticles for Solid-State Lighting. *ACS. Appl. Nano Mater.* **4**, 10321-10333 (2021).

37. Mor J., Utpalla P., Kumar R., Bahadur J., Sharma S. K. Evolution of Local Structure and Pore Architecture during Zeolitic Imidazolate Framework-L to Zeolitic Imidazolate Framework-8 Phase Transformation Investigated Using Raman, Extended X-ray Absorption, and Positron Annihilation Lifetime Spectroscopy. *Chem. Mater.* **35**, 6625-6636 (2023).

38. Ghosh S., Yun H., Kumar P., Conrad S., Tsapatsis M., Mkhoyan K. A. Two Distinct Stages of Structural Modification of ZIF-L MOF under Electron-Beam Irradiation. *Chem. Mater.* **33**, 5681-5689 (2021).

39. Sun Y.-X., Sun W.-Y. Influence of temperature on metal-organic frameworks. *Chinese Chem. Lett.* **25**, 823-828 (2014).

40. Łuczak J., Kroczewska M., Baluk M., Sowik J., Mazierski P., Zaleska-Medynska A. Morphology control through the synthesis of metal-organic frameworks. *Adv. Colloid Interface Sci.* **314**, 102864 (2023).

41. Möslein, A. F., Gutierrez M., Cohen B., Tan J. C. Near-field infrared nanospectroscopy reveals guest confinement in metal-organic framework single crystals. *Nano Lett.* **20**, 7446-7454 (2020).

42. Feng S., Gong S., Feng G. Aggregation-induced emission and solid fluorescence of fluorescein derivatives. *Chem. Commun.* **56**, 2511-2513 (2020).

43. Martin M. M. L., L. The pH Dependence of Fluorescein Fluorescence. *J. Lumin.* **10**, 381-390 (1975).

44. Casalini T., Salvalaglio M., Perale G., Masi M., Cavallotti C. Diffusion and aggregation of sodium fluorescein in aqueous solutions. *J. Phys. Chem. B* **115**, 12896-12904 (2011).

45. Zhang Y., Gutierrez M., Chaudhari A. K., Tan J. C. Dye-Encapsulated Zeolitic Imidazolate Framework (ZIF-71) for Fluorochromic Sensing of Pressure, Temperature, and Volatile Solvents. *ACS Appl. Mater. Interfaces* **12**, 37477-37488 (2020).

46. Hestand N. J., Spano F. C. Expanded Theory of H- and J-Molecular Aggregates: The Effects of Vibronic Coupling and Intermolecular Charge Transfer. *Chem. Rev.* **118**, 7069-7163 (2018).

47. Chaudhari A. K., Tan J. C. Mechanochromic MOF nanoplates: spatial molecular isolation of light-emitting guests in a sodalite framework structure. *Nanoscale* **10**, 3953-3960 (2018).

48. Yu J.*, et al.* Confinement of pyridinium hemicyanine dye within an anionic metal-organic framework for two-photon-pumped lasing. *Nat. Comm.* **4**, 2719 (2013).

49. Yang X., Lin X., Zhao Y., Zhao Y. S., Yan D. Lanthanide Metal–Organic Framework Microrods: Colored Optical Waveguides and Chiral Polarized Emission. *Angew. Chem.* **56**, 7853-7857 (2017).

50. Ito F., Kogasaka Y., Yamamoto K. Fluorescence Spectral Changes of Perylene in Polymer Matrices during the Solvent Evaporation Process. *J. Phys. Chem. B* **117**, 3675-3681 (2013).

51. Zhang Y., Mollick S., Tricarico M., Ye J., Sherman D. A., Tan J. C. Turn-On Fluorescence Chemical Sensing through Transformation of Self-Trapped Exciton States at Room Temperature. *ACS Sens.* **7**, 2338-2344 (2022).

52. Hamasaki A., Kubo K., Harashima M., Katsuki A., Ozeki S. Reversible Change between Excimer and Monomer Forms of Perylene Induced by Water Absorption and Dehydration of Poly-N-isopropylacrylamide Gel. *J. Phys. Chem. B* **125**, 2987-2993 (2021).

53. Von Freydorf E., Kinder J., Michel-Beyerle M. E. On low temperature fluorescence of perylene crystals. *Chem. Phys.* **27**, 199-209 (1978).

Statement of Authorship for joint/multi-authored papers for PGR thesis

To appear at the end of each thesis chapter submitted as an article/paper

The statement shall describe the candidate's and co-authors' independent research contributions in the thesis publications. For each publication there should exist a complete statement that is to be filled out and signed by the candidate and supervisor **(only required where there isn't already a statement of contribution within the paper itself).**

Title of Paper	Elucidating Guest-Host Mechanisms in ZIF-L for Tuneable Highly Luminescent Functional Materials
Publication Status	☐Published ☐ Accepted for Publication ☐Submitted for Publication written in a manuscript style ☑ **Unpublished and unsubmitted work**
Publication Details	**D. A. Sherman**, L. Doná, C. Besnard, L. Mester, B. Slater, C. Allen, B. Civalleri, J.-C. Tan, "Elucidating Guest-Host Mechanisms in ZIF-L for Tuneable Highly Luminescent Functional Materials".

Student Confirmation

Student Name:	Dylan A. Sherman		
Contribution to the Paper	D.A.S: conceptualization, methodology, synthesis, data collection (unless stated otherwise below), all data analysis, first draft manuscript, review and editing. Chemistry NMR Facility: NMR digest data collection. D.A.S and C.B: FE-SEM data collection by collaboration (equipment operated by C.B.). L.M.: s-SNOM data collection and partial analysis. L.D.: computational surface calculations and results. Analysis by D.A.S. and L.D. C.A. and D.A.S.: TEM data collection (equipment operated by C.A.). L.D., B.S., and J.-C.T.: manuscript review and editing. J.F.P.: gas sorption data collection and partial analysis. B.S. and D.A.S.: perylene@ZIF-L in water and low guest loading DMF (2 sample) syntheses, PXRD, SEM, and FTIR by collaboration. J.-C.T.: supervision. Note: 'by collaboration' indicates D.A.S was present and participating in data collection.		
Signature		Date	1/10/2024

Supervisor Confirmation

By signing the Statement of Authorship, you are certifying that the candidate made a substantial contribution to the publication, and that the description described above is accurate.

Supervisor name and title:	Prof. J.-C. Tan.		
Supervisor comments	I support this application.		
Signature	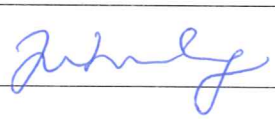	Date	1 Oct 2024

This completed form should be included in the thesis, at the end of the relevant chapter.

6

Conclusions and outlook

6.1 Concluding Remarks

This thesis coalesces two disparate fields of precedent, luminescent guest@MOF materials and guest intercalation in thin (up to 200 nm) 2D layered materials, from metal oxides to clays and MXenes. The result was the development of a blueprint for a new field of luminescent guest@2D-MOF materials, demonstrated in particular with ZIFs. These materials exhibited enhanced photophysical properties, in terms of functionality and tuneability, beyond those achievable in analogous guest@3D-ZIF systems. These improved properties derived from the combination of a 2D structure with metal-organic framework constitution. When synthesised as nanosheets (2-5 nm), to form LMONs, these materials exhibited further optical property enhancement, and critically, the ability to more precisely and effectively fabricate luminescent thin films by printing. This brings closer the possibility of incorporating ZIF materials into key applications including next-generation OLED lighting, selective and sensitive sensing, covert security tagging, and UV exposure indicators.

6.2 Chapter 3

This chapter comprised Paper I and Paper II. In Paper I, *Advanced Functional Materials*, 33, 2214307 (2023):

- A facile low-energy bottom-up salt-template strategy was established for synthesising guest@MON materials using ZIF-7-III. The synthesised few-layer nanosheets exhibited heights of 2-5 nm and widths of 3x6 μm.

- Using structural, chemical, and photophysical analysis at both the bulk and nanoscale (e.g., nanoFTIR), it was concluded that the guests are likely to reside within the inter-layer spacing of the nanosheet particles.

- The fluorescence of RB and F was turned on by entrapment in Z7-NS. The resultant materials (F@Z7-NS and RB@Z7-NS) exhibited high photostability and emission that was tuneable in terms of colour and intensity by guest concentration.

- A mixed-guest system was also synthesised, resulting in a dual-guest yellow, fluorescent material (F+RB@Z7-NS = DG@Z7-NS). Due to the close proximity of F and RB in the interlayer Z7-NS spacing, RB and F in DG@Z7-NS exhibited Förster Resonance Energy Transfer (FRET).

- A 20-sample systematic analysis of the dual guest system allowed a formula to be derived that quantifiably predicted the precise chromaticity of emission by the dual-guest NS dependent on the synthesis ratio of fluorophore guests. This enabled quantifiable tuneability of luminescence chromaticity. By varying

guest concentration, emission chromaticity can be quantitatively tuned to attain precisely desired wavelengths. This also allowed a definition of a unique "spectral fingerprint" subset of the visible spectrum unique to DG@Z7-NS; a critical finding for advanced luminescent tagging and sensing.

In Paper II, *Materials Today Chemistry*, 38, 102089 (2024):

- A blue Z7-NS phosphor was developed by introduction of the guest MC. This system exhibited two key properties:
  (1) Prevention of photodimerization. Typically, MC undergoes photodimerization when exposed to UV-A light. The resultant dimer is non-emissive and readily decomposes due to chemical instability. The entrapment of MC in Z7-NS created physical constraints that prevented the geometries needed to form the photodimer. Z7-NS also absorbs in the region of UV-A, so could act as a UV shield.

  (2) Advantageous photo behaviour. Upon UV-exposure (365 nm for 2 hours) the material exhibited higher quantum yield and brighter blue (red-shifted) emission (Figure 2e). Photophysical studies suggested this may be derived from intra- or inter-molecular interactions between the methyl electron donor and carboxyl electron acceptor in the MC guest molecules.

- A white-light emitting Z7-NS sample series was synthesised by simultaneously entrapping F, RB and MC in Z7-NS, forming the triple guest@Z7-NS materials (TG@Z7-NS). Varying guest concentrations

allowed emission chromaticity to be controlled, to tune emission from cold to warm white light, and achieve near ideal (0.33, 0.34) CIE coordinates.

6.3 Chapter 4

This chapter comprised findings from Paper II and Paper III. In Paper II,

- Films of MC@Z7-NS were deposited on glass and PET film using an inkjet printer. The films were demonstrated to be more homogenous and evenly printed compared to MC@ZIF-7 (3D analogue). The technique was limited in customisation, however, particularly due to ink particles frequently blocking the printing nozzle as they were too large.

In Paper III, *ACS Applied Materials & Interfaces* (2024):

- Aerosol jet printing was used for the first time with a MOF-based ink to create fine-scale complex thin-film patterning on surfaces. This was achieved by using MONs, overcoming the particle size limitations of MOFs. The inks were observed to be stable and reliable in printing, with a linear relationship observed between the number of layers printing and film thickness. Surface roughness and line width was adjustable dependent on the extent of layers added.

- As the MONs were luminescent (LMONs), prints were shown to be highly luminescent, with patterning achieved at micron and cm scales without any shadowing effects (e.g. from drift or extensive overspray) or defects.

- The luminescent properties of the LMONs were found to be altered as a function of printing properties. Specifically, (1) the amount of layering altered emission intensity to a point of self-quenching after which emission decreased, and (2) combining different colour emitting LMONs led to emission colour being tuneable.
- By printing WLE LMONs onto a UV diode, it was possible to fabricate a functioning WLE diode, critical for lighting applications.
- Initial proof of concept prints of 0.44 mm 3D luminescent pillars were reported that exhibited a degree of directional emission, with more complex 3D structures accessible with ink and printing parameter tuning.

6.4 Chapter 5

This chapter comprised Paper IV, to be published, which included:

- The first encapsulation of fluorophores in the cushion-shaped cavities of ZIF-L to create luminescent guest@ZIF-L materials. These included perylene, 7-hydroxycoumarin, and fluorescein.
- Correlating crystal morphology with guest encapsulation, showing a continuum from the characteristic leaf shape of ZIF-L to a rectangular crystal shape that forms dependent on the degree of effective encapsulation of F in the cavities of ZIF-L.

- For F@ZIF-L, achieving 99 % PLQY. Emission intensity was also increased by tuning guest arrangement to optimise the ratio of monomer and J-aggregate emission.

- The first report of WLE from solid-state perylene by optimising guest arrangement in perylene@ZIF-L with an ideal balance of blue monomeric emission along with yellow excimer emission.

- Heteroepitaxy of fluorescent thin films by growing F@ZIF-L on Zn film, demonstrating an effective *in situ* method of luminescent thin film fabrication.

6.5 Outlook

Collectively, this thesis established guest@MON design along with demonstrating that LMONs are promising materials for nanophotonic applications due to the combination of MOF tuneable structures and programmability with an atomically thin morphology of large planar dimension.

In each chapter, direct further studies were noted where relevant. A number of broader divergent investigative directions could also be taken.

The first is expanding the strategy to other MONs beyond Z7-NS. This may include other ZIFs, such as the cobalt analogue of ZIF-7, ZIF-9, or ZIF-67 (shown to form nanosheets).[61] Beyond 2D materials, nanosheets of 3D MOFs could provide interesting comparisons. Preliminary studies indicated that ZIF-8 nanosheets could

be successfully synthesised using the salt templating strategy established for Z7-NS in this work. A systematic study of interest could be examining the effect of thickness on material properties. If thickness could be controlled by optimising nanosheet synthesis strategies, certain properties of LMON materials such as sensing sensitivity, or PLQY could be compared to layer thickness, as an intermediary to the 2D/3D bulk comparisons undertaken in this thesis.

A second direction is selecting luminescent guests that go beyond static lighting properties to achieve dynamic function. This would typically be for applications of sensing, and in the case of the MON morphology, sensitivity and speed of sensing should increase along with favourable conditions for more effective directionally dependent measures, such as pressure. Guests based on tetraphenylethylene have already shown sensing behaviours for pressure, albeit typically irreversible, in MOF materials.[193] The use of MONs may improve reversibility, as compared to 3D frameworks, the layers may offer a degree of compressibility without framework degradation. Electrochromic guests may also be well suited to the MON structure, with electron transport theoretically constrained to inter-layer routes in MON structures, which may offer enhanced conductive substrates. Certain electrochromic guests such as viologen-based molecules could be studied in MONs,[194-196] or MON-conductive polymer composites could be synthesised using polymers such as polyaniline or polypyrolle or methylviologen.[197] Taking advantage of the nanoscale control in MONs, quantum dots could also be intriguing candidates as guests to create LMON materials. This would enable the use of quantum effects in controlling light properties within a tuneable framework. A range of quantum

dot@MOF materials have been reported,[198] and the additional benefits of LMONs now established indicate the enhanced properties that could be obtained with quantum dot LMONs.

This thesis concludes, perhaps unorthodoxly, with a demonstration of the realistic prospects in the ideas above by presenting preliminary results obtained for a sensing device by entrapping coronene in Z7-NS (Figure 6.1). In preparation for future publication, this work demonstrated that the entrapment of coronene within the layers of Z7-NS resulted in selective sensing to the extent that the material only luminesced green when in H_2O and blue in all other common organic solvents that were tested (Figure 6.1). The source of this fluorescent behaviour can be attributed to aggregation enhanced excimer emission (AEEE).[199] Coronene emits blue as a single molecule. Polar solvents such as MeOH and H_2O form intermolecular interactions with coronene molecules to form dimer pairs. These dimers absorb energy individually but emit energy as one more stable dimer (AEEE). By entrapping coronene within the narrow inter-layer spaces of Z7-NS, only the smallest molecule H_2O is able to be adsorbed by coronene@Z7-NS, thereby limiting the AEEE effect to the presence of water only. This was confirmed in vapour sorption studies, indicating at least a 50x preference for the adsorption of H_2O over MeOH or ethyl acetate. Further aspects of this study involve sensitivity of detection analysis, along with comparison to a 3D analogue, ZIF-8-NS (as coronene is too large to be encapsulated in ZIF-7). Additional work involved attempting to form mixed-matrix polymer films to generate a strip (Figure 6.1) that can be used to test for water contaminated with organic solvent impurities. With

over 25 % of drinking water globally being contaminated, and up to 829,000 deaths per year due to unclean water, a reusable cost-effective local source water purity indicator could be significant for remote and developing communities who don't have access to large scale industrial water quality monitoring.[200-201] This preliminary work, ultimately, is just one example of enhanced functional luminescent materials that can be achieved using guest@MON systems.

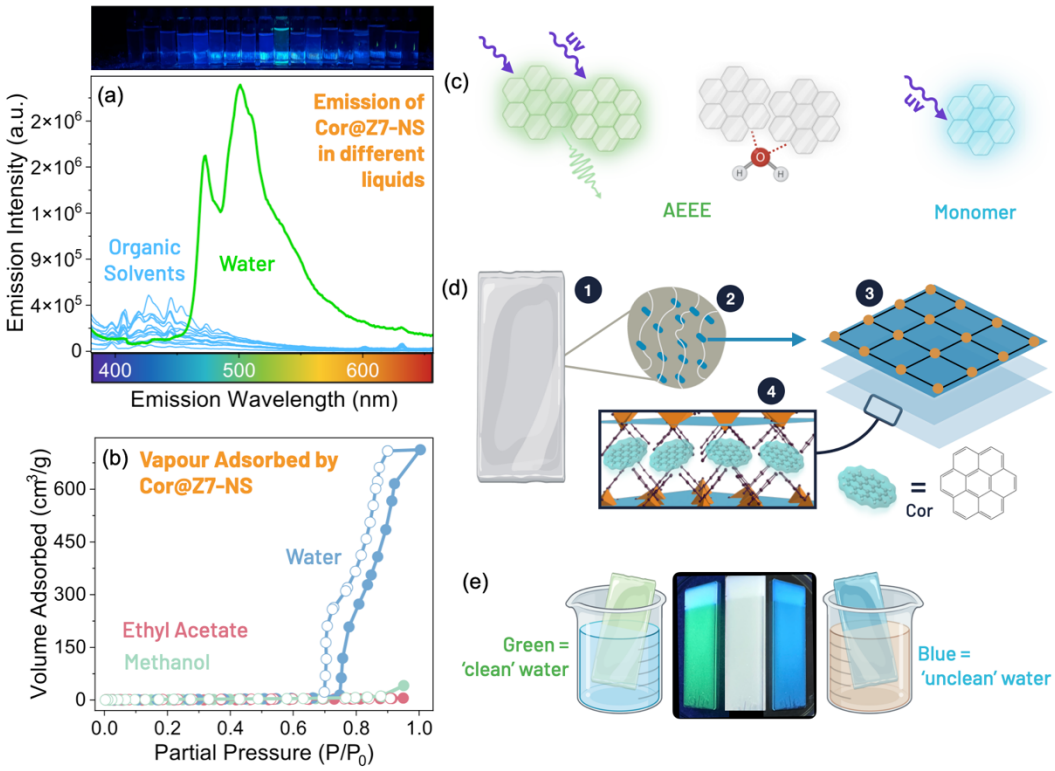

Figure 6.1. (a) Emission spectra of coronene@Z7-NS in various organic solvents (blue) and water (green). Above: corresponding vials of coronene@Z7-NS in solvents and water (centre). (b) vapour sorption at 25 °C of water (blue), ethyl acetate (red) and methanol (green) by coronene@Z7-NS (collected by Judit Parrando Pérez and Joaquin Silvestre-Albero). (c) sketches of coronene emitting as a dimer (left) and monomer (right). (d) design of a potential mixed-matrix membrane water sensor (1), comprising coronene@Z7-NS (3-4) loaded into a polymer (2) such as polydimethylsiloxane (PDMS). (e) Concept of a functioning water sensor, showing PDMS film on glass substrate prototype in the centre.

References

[1] M. D. Forbes, What We Talk About When We Talk About Light, *ACS Cent. Sci.* **2015**, *1*, 354-363.

[2] A Year to Remember, *Nat. Photon.* **2014**, *9*, 1.

[3] A. Karmakar, J. Li, Luminescent MOFs (LMOFs): recent advancement towards a greener WLED technology, *Chem. Commun.* **2022**, *58*, 10768-10788.

[4] D. M. Jameson, *Introduction to fluorescence*, Taylor & Francis, **2014**.

[5] T. C. Lovell, B. P. Branchaud, R. Jasti, An Organic Chemist's Guide to Fluorophores - Understanding Common and Newer Non-Planar Fluorescent Molecules for Biological Applications, *Eur. J. Org. Chem.* **2024**, *27*, e202301196.

[6] M. Gutierrez, Y. Zhang, J. C. Tan, Confinement of Luminescent Guests in Metal-Organic Frameworks: Understanding Pathways from Synthesis and Multimodal Characterization to Potential Applications of LG@MOF Systems, *Chem. Rev.* **2022**, *122*, 10438-10483.

[7] L. Su, X. Fan, T. Yin, et al., Inorganic 2D Luminescent Materials: Structure, Luminescence Modulation, and Applications, *Adv. Opt. Mater.* **2019**, *8*, 1900978.

[8] J. Nicks, K. Sasitharan, R. R. R. Prasad, et al., Metal-Organic Framework Nanosheets: Programmable 2D Materials for Catalysis, Sensing, Electronics, and Separation Applications, *Adv. Funct. Mater.* **2021**, *31*, 2103723.

[9] Y. S. Zheng, F. Z. Sun, X. Han, et al., Recent Progress in 2D Metal-Organic Frameworks for Optical Applications, *Adv. Opt. Mater.* **2020**, *8*, 2000110.

[10] M. Zhao, Y. Huang, Y. Peng, et al., Two-dimensional metal–organic framework nanosheets: synthesis and applications, *Chem. Soc. Rev.* **2018**, *47*, 6267-6295.

[11] Q. Jiang, C. Zhou, H. Meng, et al., Two-dimensional metal–organic framework nanosheets: synthetic methodologies and electrocatalytic applications, *J. Mater. Chem. A* **2020**, *8*, 15271-15301.

[12] S. Li, C. Wang, Y. Yin, et al., Novel layered 2D materials for ultrafast photonics, *Nanophotonics* **2020**, *9*, 1743-1786.

[13] R. Chen, J. Yao, Q. Gu, et al., A two-dimensional zeolitic imidazolate framework with a cushion-shaped cavity for CO2 adsorption, *Chem. Commun.* **2013**, *49*, 9500-9502.

[14] M. Eddaoudi, J. Kim, N. Rosi, et al., Systematic design of pore size and functionality in isoreticular MOFs and their application in methane storage, *Science* **2002**, *295*, 469-472.

[15] R. Robson, Design and its limitations in the construction of bi- and poly-nuclear coordination complexes and coordination polymers (aka MOFs): a personal view, *Dalton Trans.* **2008**, 5113-5131.

[16] S. R. Batten, N. R. Champness, X.-M. Chen, et al., Coordination polymers, metal–organic frameworks and the need for terminology guidelines, *CrystEngComm* **2012**, *14*, 3001-3004.

[17] D. J. Tranchemontagne, J. L. Mendoza-Cortes, M. O'Keeffe, et al., Secondary building units, nets and bonding in the chemistry of metal-organic frameworks, *Chem. Soc. Rev.* **2009**, *38*, 1257-1283.

[18] P. Z. Moghadam, Y. G. Chung, R. Q. Snurr, Progress toward the computational discovery of new metal–organic framework adsorbents for energy applications, *Nat. Energy* **2024**, *9*, 121-133.

[19] S. Majumdar, S. M. Moosavi, K. M. Jablonka, et al., Diversifying Databases of Metal Organic Frameworks for High-Throughput Computational Screening, *ACS Appl. Mater. Interfaces* **2021**, *13*, 61004-61014.

[20] C. Wang, D. Liu, W. Lin, Metal-organic frameworks as a tunable platform for designing functional molecular materials, *J. Am. Chem. Soc.* **2013**, *135*, 13222-13234.

[21] O. Yaghi, Li, G., Li, H., Selective binding and removal of guests in a microporous metal–organic framework, *Nature* **1995**, *378*, 703-706.

[22] P. Horcajada, C. Serre, M. Vallet-Regi, et al., Metal-organic frameworks as efficient materials for drug delivery, *Angew. Chem.* **2006**, *45*, 5974-5978.

[23] H. Furukawa, K. E. Cordova, M. O'Keeffe, et al., The chemistry and applications of metal-organic frameworks, *Science* **2013**, *341*, 1230444.

[24] P. Silva, S. M. Vilela, J. P. Tome, et al., Multifunctional metal-organic frameworks: from academia to industrial applications, *Chem. Soc. Rev.* **2015**, *44*, 6774-6803.

[25] R. Haldar, S. Bhattacharyya, T. K. Maji, Luminescent metal-organic frameworks and their potential applications, *J. Chem. Sci.* **2020**, *132*, 1-25.

[26] H. Xu, R. Chen, Q. Sun, et al., Recent progress in metal-organic complexes for optoelectronic applications, *Chem. Soc. Rev.* **2014**, *43*, 3259-3302.

[27] W. P. Lustig, S. Mukherjee, N. D. Rudd, et al., Metal-organic frameworks: functional luminescent and photonic materials for sensing applications, *Chem. Soc. Rev.* **2017**, *46*, 3242-3285.

[28] J. Mei, Y. N. Hong, J. W. Y. Lam, et al., Aggregation-Induced Emission: The Whole Is More Brilliant than the Parts, *Adv. Mater.* **2014**, *26*, 5429-5479.

[29] B. Heyne, Self-assembly of organic dyes in supramolecular aggregates, *Photochem. Photobiol. Sci.* **2016**, *15*, 1103-1114.

[30] M. Kasha, in *Spectroscopy of the Excited State* (Eds.: B. Di Bartolo, D. Pacheco, V. Goldberg), Springer US, Boston, MA, **1976**, pp. 337-363.

[31] J. H. Kim, T. Schembri, D. Bialas, et al., Slip-Stacked J-Aggregate Materials for Organic Solar Cells and Photodetectors, *Adv. Mater.* **2022**, *34*, e2104678.

[32] N. J. Hestand, F. C. Spano, Expanded Theory of H- and J-Molecular Aggregates: The Effects of Vibronic Coupling and Intermolecular Charge Transfer, *Chem. Rev.* **2018**, *118*, 7069-7163.

[33] Y. Hong, J. W. Lam, B. Z. Tang, Aggregation-induced emission, *Chem. Soc. Rev.* **2011**, *40*, 5361-5388.

[34] G. R. Suman, M. Pandey, A. S. J. Chakravarthy, Review on new horizons of aggregation induced emission: from design to development, *Mater. Chem. Front.* **2021**, *5*, 1541-1584.

[35] G. L. Yang, X. L. Jiang, H. Xu, et al., Applications of MOFs as Luminescent Sensors for Environmental Pollutants, *Small* **2021**, *17*, 2005327.

[36] I. Roy, S. Goswami, R. M. Young, et al., Photon Upconversion in a Glowing Metal-Organic Framework, *J. Am. Chem. Soc.* **2021**, *143*, 5053-5059.

[37] T. N. Nguyen, F. M. Ebrahim, K. C. Stylianou, Photoluminescent, upconversion luminescent and nonlinear optical metal-organic frameworks: From fundamental photophysics to potential applications, *Coord. Chem. Rev.* **2018**, *377*, 259-306.

[38] Z. Y. Zhuang, D. X. Liu, Conductive MOFs with Photophysical Properties: Applications and Thin-Film Fabrication, *Nanomicro Lett.* **2020**, *12*, 1-32.

[39] Y. Tang, H. L. Wu, W. Q. Cao, et al., Luminescent Metal-Organic Frameworks for White LEDs, *Adv. Opt. Mater.* **2020**, *9*, 2001817.

[40] M. D. Allendorf, C. A. Bauer, R. K. Bhakta, et al., Luminescent Metal–Organic Frameworks, *Chem. Soc. Rev.* **2009**, *38*, 1330-1352.

[41] Y. J. Cui, Y. F. Yue, G. D. Qian, et al., Luminescent Functional Metal-Organic Frameworks, *Chem. Rev.* **2012**, *112*, 1126-1162.

[42] A. K. Chaudhari, H. J. Kim, I. Han, et al., Optochemically Responsive 2D Nanosheets of a 3D Metal-Organic Framework Material, *Adv. Mater.* **2017**, *29*, 1701463.

[43] S.-R. Zhang, G.-J. Xu, W. Xie, et al., A luminescent metal–organic framework with mixed-linker strategy for white-light-emitting by iridium-complex encapsulation, *Inorg. Chem. Commun.* **2021**, *123*, 108359.

[44] H. Xu, J. Gao, X. Qian, et al., Metal–organic framework nanosheets for fast-response and highly sensitive luminescent sensing of Fe3+, *J. Mater. Chem. A* **2016**, *4*, 10900-10905.

[45] B. B. Guo, J. C. Yin, N. Li, et al., Recent Progress in Luminous Particle-Encapsulated Host–Guest Metal-Organic Frameworks for Optical Applications, *Adv. Opt. Mater.* **2021**, *9*, 2100283.

[46] C. Tan, X. Cao, X. J. Wu, et al., Recent Advances in Ultrathin Two-Dimensional Nanomaterials, *Chem. Rev.* **2017**, *117*, 6225-6331.

[47] B. Li, C. Lai, G. Zeng, et al., Black Phosphorus, a Rising Star 2D Nanomaterial in the Post-Graphene Era: Synthesis, Properties, Modifications, and Photocatalysis Applications, *Small* **2019**, *15*, 1804565.

[48] N. K. Chaudhari, H. Jin, B. Kim, et al., MXene: an emerging two-dimensional material for future energy conversion and storage applications, *J. Mater. Chem. A* **2017**, *5*, 24564-24579.

[49] H. Yin, Z. Tang, Ultrathin two-dimensional layered metal hydroxides: an emerging platform for advanced catalysis, energy conversion and storage, *Chem. Soc. Rev.* **2016**, *45*, 4873-4891.

[50] L. H. Li, Y. Chen, Atomically Thin Boron Nitride: Unique Properties and Applications, *Adv. Funct. Mater.* **2016**, *26*, 2594-2608.

[51] W.-J. Ong, L.-L. Tan, Y. H. Ng, et al., Graphitic Carbon Nitride (g-C3N4)-Based Photocatalysts for Artificial Photosynthesis and Environmental Remediation: Are We a Step Closer To Achieving Sustainability?, *Chem. Rev.* **2016**, *116*, 7159-7329.

[52] D. J. Ashworth, J. A. Foster, Metal–organic framework nanosheets (MONs): a new dimension in materials chemistry, *J. Mater. Chem. A* **2018**, *6*, 16292-16307.

[53] Y. Fan, J. Zhang, Y. Shen, et al., Emerging porous nanosheets: From fundamental synthesis to promising applications, *Nano Res.* **2020**, *14*, 1-28.

[54] C. Tan, G. Liu, H. Li, et al., Ultrathin two-dimensional metal-organic framework nanosheets-an emerging class of catalytic nanomaterials, *Dalton Trans.* **2020**, *49*, 11073-11084.

[55] Y. Cheng, Y. Pu, D. Zhao, Two-Dimensional Membranes: New Paradigms for High-Performance Separation Membranes, *Chem. Asian J.* **2020**, *15*, 2241-2270.

[56] D. Zhu, M. Qiao, J. Liu, et al., Engineering pristine 2D metal–organic framework nanosheets for electrocatalysis, *J. Mater. Chem. A* **2020**, *8*, 8143-8170.

[57] W. M. Liao, J. H. Zhang, S. Y. Yin, et al., Tailoring exciton and excimer emission in an exfoliated ultrathin 2D metal-organic framework, *Nat. Commun.* **2018**, *9*, 2401.

[58] T. Rodenas, I. Luz, G. Prieto, et al., Metal-organic framework nanosheets in polymer composite materials for gas separation, *Nat. Mater.* **2015**, *14*, 48-55.

[59] S. C. Junggeburth, L. Diehl, S. Werner, et al., Ultrathin 2D coordination polymer nanosheets by surfactant-mediated synthesis, *J. Am. Chem. Soc.* **2013**, *135*, 6157-6164.

[60] M. Zhao, Y. Wang, Q. Ma, et al., Ultrathin 2D Metal-Organic Framework Nanosheets, *Adv. Mater.* **2015**, *27*, 7372-7378.

[61] L. Huang, X. Zhang, Y. Han, et al., In situ synthesis of ultrathin metal–organic framework nanosheets: a new method for 2D metal-based nanoporous carbon electrocatalysts, *J. Mater. Chem. A* **2017**, *5*, 18610-18617.

[62] K. Zhao, S. Liu, G. Ye, et al., Ultrasmall 2 D Cox Zn2-x (Benzimidazole)4 Metal-Organic Framework Nanosheets and their Derived Co Nanodots@Co,N-Codoped Graphene for Efficient Oxygen Reduction Reaction, *ChemSusChem* **2020**, *13*, 1556-1567.

[63] Y. Peng, W. Yang, 2D Metal-Organic Framework Materials for Membrane-Based Separation, *Adv. Mater. Interfaces* **2019**, *7*.

[64] X. Chen, S. Song, L. Wang, et al., Ultrathin Metal-organic Framework Membranes Used for Industrial Separation, *IOP Conf. Ser.: Earth Environ. Sci.* **2018**, *170*, 052040.

[65] J. Liu, X. Song, T. Zhang, et al., 2D Conductive Metal-Organic Frameworks: An Emerging Platform for Electrochemical Energy Storage, *Angew. Chem.* **2020**, *60*, 5612-5624.

[66] H. L. Zhu, D. X. Liu, The synthetic strategies of metal-organic framework membranes, films and 2D MOFs and their applications in devices, *J. mater. Chem. A* **2019**, *7*, 21004-21035.

[67] Y. Peng, W. Yang, Metal-organic framework nanosheets: a class of glamorous low-dimensional materials with distinct structural and chemical natures, *Sci. China Chem.* **2019**, *62*, 1561-1575.

[68] Z. Hu, E. M. Mahdi, Y. Peng, et al., Kinetically controlled synthesis of two-dimensional Zr/Hf metal–organic framework nanosheets via a modulated hydrothermal approach, *J. Mater. Chem. A* **2017**, *5*, 8954-8963.

[69] J. Wang, J. Zhang, S. B. Peh, et al., Dimensional Impact of Metal–Organic Frameworks in Catalyzing Photoinduced Hydrogen Evolution and Cyanosilylation Reactions, *ACS Appl. Energy Mater.* **2018**, *2*, 298-304.

[70] C. Wang, C. He, Y.-H. Luo, et al., Efficient mercury chloride capture by ultrathin 2D metal-organic framework nanosheets, *Chem. Eng. J.* **2020**, *379*, 122337.

[71] R. Xu, M. Jian, Q. Ji, et al., 2D water-stable zinc-benzimidazole framework nanosheets for ultrafast and selective removal of heavy metals, *Chem. Eng. J.* **2020**, *382*, 122658.

[72] Y. Peng, R. Yao, W. Yang, A poly(amidoamine) nanoparticle cross-linked two-dimensional metal-organic framework nanosheet membrane for water purification, *Chem. Commun.* **2019**, *55*, 3935-3938.

[73] Y. Ning, X. Lou, C. Li, et al., Ultrathin Cobalt-Based Metal-Organic Framework Nanosheets with Both Metal and Ligand Redox Activities for Superior Lithium Storage, *Chem.* **2017**, *23*, 15984-15990.

[74] C. Li, X. Hu, W. Tong, et al., Ultrathin Manganese-Based Metal-Organic Framework Nanosheets: Low-Cost and Energy-Dense Lithium Storage Anodes with the Coexistence of Metal and Ligand Redox Activities, *ACS Appl. Mater. Interfaces* **2017**, *9*, 29829-29838.

[75] S. Liu, Y. C. Wang, C. M. Chang, et al., Solution-processed organometallic quasi-two-dimensional nanosheets as a hole buffer layer for organic light-emitting devices, *Nanoscale* **2020**, *12*, 6983-6990.

[76] K. Sasitharan, R. C. Kilbride, E. L. K. Spooner, et al., Metal-Organic Framework Nanosheets as Templates to Enhance Performance in Semi-Crystalline Organic Photovoltaic Cells, *Adv. Sci.* **2022**, *9*, e2200366.

[77] K. Sasitharan, D. G. Bossanyi, N. Vaenas, et al., Metal–organic framework nanosheets for enhanced performance of organic photovoltaic cells, *J. Mater. Chem. A* **2020**, *8*, 6067-6075.

[78] X.-Y. Ren, L.-H. Lu, Luminescent nanoscale metal–organic frameworks for chemical sensing, *Chin. Chem. Lett.* **2015**, *26*, 1439-1445.

[79] R. A. Natour, Z. K. Ali, A. Assoud, et al., Two-Dimensional Metal-Organic Framework Nanosheets as a Dual Ratiometric and Turn-off Luminescent Probe, *Inorg. Chem.* **2019**, *58*, 10912-10919.

[80] W. W. Zhao, J. L. Peng, W. K. Wang, et al., Ultrathin two-dimensional metal-organic framework nanosheets for functional electronic devices, *Coord. Chem. Rev.* **2018**, *377*, 44-63.

[81] Y. Zhu, X. Sun, Y. Tang, et al., Two-dimensional materials for light emitting applications: Achievement, challenge and future perspectives, *Nano Res.* **2020**, *14*, 1912-1936.

[82] J. Tang, Z. Liang, M. Huang, et al., A combined bottom-up and top-down strategy to fabricate lanthanide hydrate@2D MOF composite nanosheets for direct white light emission, *J. Mater. Chem. C* **2021**, *9*, 14628-14636.

[83] T. Xiong, Y. Zhang, L. Donà, et al., Tunable Fluorescein-Encapsulated Zeolitic Imidazolate Framework-8 Nanoparticles for Solid-State Lighting, *ACS. Appl. Nano Mater.* **2021**, *4*, 10321-10333.

[84] P. J. Larkin, Basic Principles in *Infrared and Raman Spectroscopy*, **2018**, pp. 7-28.

[85] K. I. Hadjiivanov, D. A. Panayotov, M. Y. Mihaylov, et al., Power of Infrared and Raman Spectroscopies to Characterize Metal-Organic Frameworks and Investigate Their Interaction with Guest Molecules, *Chem. Rev.* **2021**, *121*, 1286-1424.

[86] F. Huth, A. Govyadinov, S. Amarie, et al., Nano-FTIR absorption spectroscopy of molecular fingerprints at 20 nm spatial resolution, *Nano Lett.* **2012**, *12*, 3973-3978.

[87] A. F. Moslein, M. Gutierrez, B. Cohen, et al., Near-field infrared nanospectroscopy reveals guest confinement in metal-organic framework single crystals, *Nano Lett.* **2020**, *20*, 7446-7454.

[88] F. Keilmann, Scattering-type near-field optical microscopy, *Microscopy* **2004**, *53*, 187-192.

[89] G. G. Stokes, On the Change of Refrangibility of Light, *Phil. Trans. R. Soc.* **1852**, *142*, 463-562.

[90] G. N. Lewis, M. Kasha, Phosphorescence and the Triplet State, *J. Am. Chem. Soc.* **1944**, *66*, 2100-2116.

[91] J. C. Del Valle, J. Catalan, Kasha's rule: a reappraisal, *Phys. Chem. Chem. Phys.* **2019**, *21*, 10061-10069.

[92] K.-L. Wong, J.-C. G. Bünzli, P. A. Tanner, Quantum yield and brightness, *J. Lumin.* **2020**, *224*, 117256.

[93] C. Wurth, M. Grabolle, J. Pauli, et al., Comparison of methods and achievable uncertainties for the relative and absolute measurement of photoluminescence quantum yields, *Anal. Chem.* **2011**, *83*, 3431-3439.

[94] J. R. Lakowicz, *Principles of Fluorescence Spectroscopy*, Springer, **2006**.

[95] K. S. Park, Z. Ni, A. P. Cote, et al., Exceptional chemical and thermal stability of zeolitic imidazolate frameworks, *PNAS* **2006**, *103*, 10186-10191.

[96] A. U. Ortiz, A. P. Freitas, A. Boutin, et al., What makes zeolitic imidazolate frameworks hydrophobic or hydrophilic? The impact of geometry and functionalization on water adsorption, *Phys. Chem. Chem. Phys.* **2014**, *16*, 9940-9949.

[97] Y. Sun, Y. Li, J.-C. Tan, Liquid Intrusion into Zeolitic Imidazolate Framework-7 Nanocrystals: Exposing the Roles of Phase Transition and Gate Opening to Enable Energy Absorption Applications, *ACS Appl. Mater. Interfaces* **2018**, *10*, 41831-41838.

[98] H. L. Liu, Y. J. Chang, T. Fan, et al., Two-dimensional metal-organic framework nanosheets as a matrix for laser desorption/ionization of small molecules and monitoring enzymatic reactions at high salt concentrations, *Chem. Commun.* **2016**, *52*, 12984-12987.

[99] Y. Peng, Y. Li, Y. Ban, et al., Two-Dimensional Metal-Organic Framework Nanosheets for Membrane-Based Gas Separation, *Angew. Chem.* **2017**, *56*, 9757-9761.

[100] Y. Peng, Y. S. Li, Y. J. Ban, et al., Metal-organic framework nanosheets as building blocks for molecular sieving membranes, *Science* **2014**, *346*, 1356-1359.

[101] W. Wu, J. Xu, X. Tang, et al., Two-Dimensional Nanosheets by Rapid and Efficient Microwave Exfoliation of Layered Materials, *Chem. Mater.* **2018**, *30*, 5932-5940.

[102] L. Huang, Z. Hu, H. Jin, et al., Salt-Assisted Synthesis of 2D Materials, *Adv. Funct. Mater.* **2020**, *30*, 1908486.

[103] B. Yan, W. Zhang, X. Qin, et al., Salt powder assisted synthesis of nanostructured materials and their electrochemical applications in energy storage devices, *Chem. Eng. J.* **2020**, *400*, 125895.

[104] X. Xiao, H. Song, S. Lin, et al., Scalable salt-templated synthesis of two-dimensional transition metal oxides, *Nat. Commun.* **2016**, *7*, 11296.

[105] Y. Zhang, Z. Teng, Q. Ni, et al., Orderly Curled Silica Nanosheets with a Small Size and Macromolecular Loading Pores: Synthesis and Delivery of Macromolecules To Eradicate Drug-Resistant Cancer, *ACS Appl. Mater. Interfaces* **2020**, *12*, 57810-57820.

[106] Y. Zhang, M. Gutierrez, A. K. Chaudhari, et al., Dye-Encapsulated Zeolitic Imidazolate Framework (ZIF-71) for Fluorochromic Sensing of Pressure, Temperature, and Volatile Solvents, *ACS Appl. Mater. Interfaces* **2020**, *12*, 37477-37488.

[107] I. Cazin, E. Rossegger, G. Guedes de la Cruz, et al., Recent Advances in Functional Polymers Containing Coumarin Chromophores, *Polymers* **2020**, *13*.

[108] S. Fery-Forgues, M. Cantuel, C. Fournier-Noel, Searching for fluorescent nanocrystals in aqueous solutions of 7-methoxycoumarin, *Dyes and Pigments* **2010**, *87*, 241-248.

[109] A. K. Chaudhari, J. C. Tan, Dual-Guest Functionalized Zeolitic Imidazolate Framework-8 for 3D Printing White Light-Emitting Composites, *Adv. Opt. Mater.* **2020**, *8*, 1901912.

[110] T. Xiong, Y. Zhang, N. Amin, et al., A Luminescent Guest@MOF Nanoconfined Composite System for Solid-State Lighting, *Molecules* **2021**, *26*, 7583.

[111] K. Yano, R. Nishimura, Y. Hattori, et al., Photoinduced topographical surface changes and photoresponse of the crystals of 7-methoxycoumarin, *Cryst. Eng. Comm.* **2021**, *23*, 5780-5787.

[112] M. D. Cohen, G. M. J. Schmidt, F. I. Sonntag, 384. Topochemistry. Part II. The photochemistry of trans-cinnamic acids, *J. Chem. Soc.* **1964**, 2000-2013.

[113] G. M. J. Schmidt, Photodimerization in the solid state, *Pure Appl. Chem.* **1971**, *27*, 647-678.

[114] K. Gnanaguru, N. Ramasubbu, K. Venkatesan, et al., A Study on the Photochemical Dimerization of Coumarins in the Solid-State, *J. Org. Chem.* **1985**, *50*, 2337-2346.

[115] B. C. M. A. Ashwin, A. Herculin Arun Baby, M. Prakash, et al., A combined experimental and theoretical study on p-sulfonatocalix[4]arene encapsulated 7-methoxycoumarin, *J. Phys. Org. Chem.* **2018**, *31*, e3788.

[116] B. D. Wagner, S. J. Fitzpatrick, G. J. McManus, Fluorescence suppression of 7-methoxycoumarin upon inclusion into cyclodextrins, *J. Incl. Phenom. Macrocycl. Chem.* **2003**, *47*, 187-192.

[117] W. Thongyod, C. Buranachai, T. Pengpan, et al., Fluorescence quenching by photoinduced electron transfer between 7-methoxycoumarin and guanine base facilitated by hydrogen bonds: an in silico study, *Phys. Chem. Chem. Phys.* **2019**, *21*, 16258-16269.

[118] J. Orbulescu, P. Kele, A. Kotschy, et al., Synthesis and spectroscopy of coumarin derivatives for saxitoxin detection, *J. Mater. Chem.* **2005**, *15*, 3084-3088.

[119] C. Y. Hsu, Y. L. Liu, UV-induced rhodamine B aggregation into nanoparticles exhibiting reversible changes of yellow- and white-light photoluminescent emissions, *Chem.* **2011**, *17*, 5522-5525.

[120] Q. Liu, X. Chen, J. Wu, et al., Enhanced Luminescence of Dye-Decorated ZIF-8 Composite Films via Controllable D-A Interactions for White Light Emission, *Langmuir* **2023**, *39*, 3656-3667.

[121] S. Pal, S. Bayan, D. K. Goswami, et al., Boron Carbonitride Nanosheet/ZnO Nanorod Heterojunctions for White-Light Emission, *ACS Appl. Nano Mater.* **2021**, *4*, 8572-8585.

[122] S. Vempati, J. Mitra, P. Dawson, One-step synthesis of ZnO nanosheets: a blue-white fluorophore, *Nanoscale Res. Lett.* **2012**, *7*, 470.

[123] S. Turkdogan, F. Fan, C.-Z. Ning, Color-Temperature Tuning and Control of Trichromatic White Light Emission from a Multisegment ZnCdSSe Heterostructure Nanosheet, *Adv. Funct. Mater.* **2016**, *26*, 8521-8526.

[124] N. Sharma, C.-H. Chi, N. Swaminathan, et al., Introducing Stanene oxyboride nanosheets as white light emitting probe for selectively identifying <5 μm microplastic pollutants, *Sens. Actuator B-Chem.* **2021**, *348*, 130617.

[125] J. Xie, S. Li, R. Wang, et al., Grain boundary engineering in atomically-thin nanosheets achieving bright white light emission, *Chem. Sci.* **2014**, *5*, 1328-1335.

[126] X. Hu, Z. Wang, B. Lin, et al., Two-Dimensional Metal-Organic Layers as a Bright and Processable Phosphor for Fast White-Light Communication, *Chem.* **2017**, *23*, 8390-8394.

[127] S. Wuttke, D. D. Medina, J. M. Rotter, et al., Bringing Porous Organic and Carbon-Based Materials toward Thin-Film Applications, *Adv. Funct. Mater.* **2018**, *28*, 1801545.

[128] D. D. Xu, W. W. Dong, M. K. Li, et al., Encapsulating Organic Dyes in Metal-Organic Frameworks for Color-Tunable and High-Efficiency White-Light-Emitting Properties, *Inorg. Chem.* **2022**, *61*, 21107-21114.

[129] Y. Cui, T. Song, J. Yu, et al., Dye Encapsulated Metal-Organic Framework for Warm-White LED with High Color-Rendering Index, *Adv. Funct. Mater.* **2015**, *25*, 4796-4802.

[130] J. C. Yin, Z. Chang, N. Li, et al., Efficient Regulation of Energy Transfer in a Multicomponent Dye-Loaded MOF for White-Light Emission Tuning, *ACS Appl. Mater. Interfaces* **2020**, *12*, 51589-51597.

[131] Y. Wen, T. Sheng, X. Zhu, et al., Introduction of Red-Green-Blue Fluorescent Dyes into a Metal-Organic Framework for Tunable White Light Emission, *Adv. Mater.* **2017**, *29*, 1700778.

[132] Y. Li, Q. Chen, L.-H. Xie, et al., Single-Phase White-Light Phosphors Based on a Bicarbazole-Based Metal–Organic Framework with Encapsulated Dyes, *ACS Mater. Lett.* **2022**, *4*, 2345-2351.

[133] Q. Q. Xia, X. H. Wang, J. L. Yu, et al., Tunable fluorescence emission based on multi-layered MOF-on-MOF, *Dalton Trans.* **2022**, *51*, 9397-9403.

[134] J. X. Wang, J. Yin, O. Shekhah, et al., Energy Transfer in Metal-Organic Frameworks for Fluorescence Sensing, *ACS Appl. Mater. Interfaces* **2022**, *14*, 9970-9986.

[135] A. Betard, R. A. Fischer, Metal-organic framework thin films: from fundamentals to applications, *Chem. Rev.* **2012**, *112*, 1055-1083.

[136] C. L. Ruiz-Zambrana, M. Malankowska, J. Coronas, Metal organic framework top-down and bottom-up patterning techniques, *Dalton Trans.* **2020**, *49*, 15139-15148.

[137] J. Liu, C. Woll, Surface-supported metal-organic framework thin films: fabrication methods, applications, and challenges, *Chem. Soc. Rev.* **2017**, *46*, 5730-5770.

[138] E. R. Kearns, R. Gillespie, D. M. D'Alessandro, 3D printing of metal–organic framework composite materials for clean energy and environmental applications, *J. Mater. Chem. A* **2021**, *9*, 27252-27270.

[139] W. Y. Lieu, D. Fang, K. J. Tay, et al., Progress on 3D-Printed Metal-Organic Frameworks with Hierarchical Structures, *Adv. Mater. Technol.* **2022**, *7*, 2200023.

[140] H. Yang, H. Zhou, G. Zhang, et al., Recent progress of integrating MOFs into printed devices and their applications, *Sci. China Mater.* **2022**, *66*, 441-469.

[141] D. A. Gregory, J. Nicks, J. Artigas-Arnaudas, et al., Controlling the Composition and Position of Metal–Organic Frameworks via Reactive Inkjet Printing, *Adv. Mater. Interfaces* **2023**, *10*, 2300027.

[142] A. Hazra, U. Mondal, S. Mandal, et al., Advancement in functionalized luminescent frameworks and their prospective applications as inkjet-printed sensors and anti-counterfeit materials, *Dalton Trans.* **2021**, *50*, 8657-8670.

[143] H. B. Zhang, M. Liu, X. Lei, et al., Digital controlled luminescent emission via patterned deposition of lanthanide coordination compounds, *ACS Appl. Mater. Interfaces* **2014**, *6*, 12594-12599.

[144] J. Alaman, M. Lopez-Valdeolivas, R. Alicante, et al., Digital Luminescence Patterning via Inkjet Printing of a Photoacid Catalysed Organic-Inorganic Hybrid Formulation, *Polymers* **2019**, *11*, 430.

[145] J. W. Oh, S. Lee, H. Han, et al., Dual-light emitting 3D encryption with printable fluorescent-phosphorescent metal-organic frameworks, *Light. Sci. Appl.* **2023**, *12*, 226.

[146] F. Al-Ghazzawi, L. Conte, K. K. Wagner, et al., Rapid spatially-resolved post-synthetic patterning of metal-organic framework films, *Chem. Commun.* **2021**, *57*, 4706-4709.

[147] E. B. Secor, Principles of aerosol jet printing, *Flex. Print. Electron.* **2018**, *3*, 035002.

[148] C. Fisher, L. N. Skolrood, K. Li, et al., Aerosol-Jet Printed Sensors for Environmental, Safety, and Health Monitoring: A Review, *Adv. Mater. Technol.* **2023**, *8*, 2300030.

[149] N. J. Wilkinson, M. A. A. Smith, R. W. Kay, et al., A review of aerosol jet printing—a non-traditional hybrid process for micro-manufacturing, *J. Adv. Manuf. Technol.* **2019**, *105*, 4599-4619.

[150] M. Smith, Y. S. Choi, C. Boughey, et al., Controlling and assessing the quality of aerosol jet printed features for large area and flexible electronics, *Flex. Print. Electron.* **2017**, *2*, 015004.

[151] X. Chen, J. M. Lawrence, L. T. Wey, et al., 3D-printed hierarchical pillar array electrodes for high-performance semi-artificial photosynthesis, *Nat. Mater.* **2022**, *21*, 811-818.

[152] M. Seiti, A. Verma, O. Degryse, et al., Aerosol jet-based printing for smart multifunctional nano-inks in *Smart Multifunctional Nano-inks*, **2023**, pp. 75-90.

[153] H.-Y. Lin, C.-W. Sher, D.-H. Hsieh, et al., Optical cross-talk reduction in a quantum-dot-based full-color micro-light-emitting-diode display by a lithographic-fabricated photoresist mold, *Photonics Res.* **2017**, *5*, 411-416.

[154] H. V. Han, H. Y. Lin, C. C. Lin, et al., Resonant-enhanced full-color emission of quantum-dot-based micro LED display technology, *Opt. Express.* **2015**, *23*, 32504-32515.

[155] A. Lin, Y. Zhang, D. Zhao, et al., Flexible droplet printing of prominently luminescent patterns of europium-doped yttrium oxide nanospheres, *Addit. Manuf.* **2023**, *63*, 103412.

[156] D. E. Kravchenko, A. Matavž, V. Rubio-Giménez, et al., Aerosol Jet Printing of the Ultramicroporous Calcium Squarate Metal–Organic Framework, *Chem. Mater.* **2022**, *34*, 6809-6814.

[157] E. Jabari, F. Ahmed, F. Liravi, et al., 2D printing of graphene: a review, *Mater.* **2019**, *6*, 042004.

[158] A. Ul-Hamid, *A Beginners' Guide to Scanning Electron Microscopy*, Springer, **2018**.

[159] S. Min, A. Dhamsaniya, L. Zhang, et al., Scale Effect of a Fluorescent Waveguide in Organic Micromaterials: A Case Study Based on Coumarin Microfibers, *J. Phys. Chem. Lett.* **2019**, *10*, 5997-6002.

[160] B. Motevalli, N. Taherifar, H. Wang, et al., Ab Initio Simulations To Understand the Leaf-Shape Crystal Morphology of ZIF-L with Two-Dimensional Layered Network, *J. Phys. Chem. C* **2017**, *121*, 2221-2227.

[161] H. Ting, H.-Y. Chi, C. H. Lam, et al., High-permeance metal–organic framework-based membrane adsorber for the removal of dye molecules in aqueous phase, *Environ. Sci. Nano* **2017**, *4*, 2205-2214.

[162] B. Motevalli, H. Wang, J. Z. Liu, Cooperative Reformable Channel System with Unique Recognition of Gas Molecules in a Zeolitic Imidazolate Framework with Multilevel Flexible Ligands, *J. Phys. Chem. C* **2015**, *119*, 16762-16768.

[163] Y. Feng, H. Wang, J. Yao, Synthesis of 2D nanoporous zeolitic imidazolate framework nanosheets for diverse applications, *Coord. Chem. Rev.* **2021**, *431*, 213677.

[164] L. Valencia, H. N. Abdelhamid, Nanocellulose leaf-like zeolitic imidazolate framework (ZIF-L) foams for selective capture of carbon dioxide, *Carbohydr. Polym.* **2019**, *213*, 338-345.

[165] X. Zou, H. Zhang, L. Xiang, et al., Designing a dual-functional ultrathin ZIF-L@GO adsorbent for simultaneous removal of phosphate and tetracycline hydrochloride: Adsorption capacity and mechanism, *Coll. Surf. A* **2024**, *683*, 132851.

[166] Q. Gu, T. C. Albert Ng, Q. Sun, et al., Heterogeneous ZIF-L membranes with improved hydrophilicity and anti-bacterial adhesion for potential application in water treatment, *RSC Adv.* **2019**, *9*, 1591-1601.

[167] Z.-X. Low, A. Razmjou, K. Wang, et al., Effect of addition of two-dimensional ZIF-L nanoflakes on the properties of polyethersulfone ultrafiltration membrane, *J. Membr. Sci.* **2014**, *460*, 9-17.

[168] M.-J. Chen, A.-C. Yang, N.-H. Wang, et al., Influence of crystal topology and interior surface functionality of metal-organic frameworks on PFOA sorption performance, *Micropor. Mesopor. Mat.* **2016**, *236*, 202-210.

[169] S. Z. N. Ahmad, W. N. W. Salleh, N. H. Ismail, et al., Effects of operating parameters on cadmium removal for wastewater treatment using zeolitic imidazolate framework-L/graphene oxide composite, *J. Environ. Chem. Eng.* **2021**, *9*, 106139.

[170] M. A. Rahaman, B. Mousavi, F. Naz, et al., Two-Dimensional Zeolitic Imidazolate Framework ZIF-L: A Promising Catalyst for Polymerization, *Catalysts* **2022**, *12*, 521.

[171] X. Liu, X. Wang, C. Sun, et al., Brine available two-dimensional nano-architectonics of fluorescent probe based on phosphate doped ZIF-L for detection of Fe3+, *Heliyon* **2023**, *9*, e17884.

[172] S. Zhang, Y. Mao, L. Wei, et al., Full-value preparation of biochar and 2D N-doped CDs@ZIF-L from fermentation residues for sensitive sensing tetracyclines in food samples, *Coll. Surf. A* **2023**, *676*, 132073.

[173] X. Liu, C. Sun, M. Chai, et al., Highly dispersive PEI-modified CDs@ZIF-L dual-emitting fluorescent sensor for detecting metal ions, *RSC Adv.* **2023**, *13*, 31353-31364.

[174] M. Gao, G. Liu, Q. Tan, et al., A novel fluorescent probe for Fe3+ detection based on two-dimensional leaf-like structure CDs@ZIF-L, *Microchem. J.* **2022**, *182*, 107868.

[175] H.-J. Li, H. Wang, T. Si, et al., Tailoring Morphology and Fluorescence Properties of Zeolitic Imidazolate Frameworks via Carbon Dots, *ACS Appl. Nano Mater.* **2024**, *7*, 15535-15546.

[176] R. N. Sjöback, J.; Kunista, M. , Absorption and fluorescene properties of fluorescein, *Spectrochim. Acta* **1995**, *51*, L7-L21.

[177] Y. Chen, B. Yu, Y. Cui, et al., Core–Shell Structured Cyclodextrin Metal–Organic Frameworks with Hierarchical Dye Encapsulation for Tunable Light Emission, *Chem. Mater.* **2019**, *31*, 1289-1295.

[178] E. Von Freydorf, J. Kinder, M. E. Michel-Beyerle, On low temperature fluorescence of perylene crystals, *Chem. Phys.* **1978**, *27*, 199-209.

[179] A. Hamasaki, K. Kubo, M. Harashima, et al., Reversible Change between Excimer and Monomer Forms of Perylene Induced by Water Absorption and Dehydration of Poly-N-isopropylacrylamide Gel, *J. Phys. Chem. B* **2021**, *125*, 2987-2993.

[180] S. Ghosh, H. Yun, P. Kumar, et al., Two Distinct Stages of Structural Modification of ZIF-L MOF under Electron-Beam Irradiation, *Chem. Mater.* **2021**, *33*, 5681-5689.

[181] A. K. Chaudhari, J. C. Tan, Mechanochromic MOF nanoplates: spatial molecular isolation of light-emitting guests in a sodalite framework structure, *Nanoscale* **2018**, *10*, 3953-3960.

[182] Z. Zhong, J. Yao, R. Chen, et al., Oriented two-dimensional zeolitic imidazolate framework-L membranes and their gas permeation properties, *J. Mater. Chem. A* **2015**, *3*, 15715-15722.

[183] Q. Xiang, F. Li, J. Wang, et al., Heterostructure of ZnO Nanosheets/Zn with a Highly Enhanced Edge Surface for Efficient CO2 Electrochemical Reduction to CO, *ACS Appl. Mater. Interfaces* **2021**, *13*, 10837-10844.

[184] T. Chen, A. Lewis, Z. Chen, et al., Smart ZIF-L mesh films with switchable superwettability synthesized via a rapid energy-saving process, *Sep. Purif. Technol.* **2020**, *240*, 116647.

[185] S. Yuan, J. Zhu, Y. Li, et al., Structure architecture of micro/nanoscale ZIF-L on a 3D printed membrane for a superhydrophobic and underwater superoleophobic surface, *J. Mater. Chem. A* **2019**, *7*, 2723-2729.

[186] J. Zhu, H. Li, J. Hou, et al., Heteroepitaxial growth of vertically orientated zeolitic imidazolate framework-L (Co/Zn-ZIF-L) molecular sieve membranes, *AIChE J.* **2020**, *66*, e16935.

[187] A. Kumar, J. Li, A. K. Inge, et al., Electrochromism in Isoreticular Metal–Organic Framework Thin Films with Record High Coloration Efficiency, *ACS Nano* **2023**, *17*, 21595-21603.

[188] C. F. Leong, T. B. Faust, P. Turner, et al., Enhancing selective CO2 adsorption via chemical reduction of a redox-active metal-organic framework, *Dalton Trans.* **2013**, *42*, 9831-9839.

[189] S. Wang, B. Zang, Y. Chang, et al., Synthesis and carbon dioxide capture properties of flower-shaped zeolitic imidazolate framework-L, *CrystEngComm* **2019**, *21*, 6536-6544.

[190] Z.-X. Low, J. Yao, Q. Liu, et al., Crystal Transformation in Zeolitic-Imidazolate Framework, *Cryst. Growth Des.* **2014**, *14*, 6589-6598.

[191] A. Deacon, L. Briquet, M. Malankowska, et al., Understanding the ZIF-L to ZIF-8 transformation from fundamentals to fully costed kilogram-scale production, *Commun. Chem.* **2022**, *5*, 18.

[192] Z. Wang, X. Yan, Q. Hou, et al., Scalable high yield exfoliation for monolayer nanosheets, *Nat. Commun.* **2023**, *14*, 236.

[193] Y. Zhang, T. Xiong, A. F. Möslein, et al., Nanoconfinement of tetraphenylethylene in zeolitic metal-organic framework for turn-on mechanofluorochromic stress sensing, *Appl. Mater. Today* **2022**, *27*, 101434.

[194] K. Madasamy, D. Velayutham, V. Suryanarayanan, et al., Viologen-based electrochromic materials and devices, *J. Mater. Chem. C* **2019**, *7*, 4622-4637.

[195] C.-a. Tao, Y. Li, J. Wang, The progress of electrochromic materials based on metal–organic frameworks, *Coord. Chem. Rev.* **2023**, *475*, 214891.

[196] A. K. Chaudhari, B. E. Souza, J.-C. Tan, Electrochromic thin films of Zn-based MOF-74 nanocrystals facilely grown on flexible conducting substrates at room temperature, *APL Mater.* **2019**, *7*.

[197] H. Yao, F. Zhang, G. Zhang, et al., A novel two-dimensional coordination polymer-polypyrrole hybrid material as a high-performance electrode for flexible supercapacitor, *Chem. Eng. J.* **2018**, *334*, 2547-2557.

[198] T. Balakrishnan, W. L. Ang, E. Mahmoudi, et al., Recent development of quantum dots@metal-organic framework composites as potential chemical and biological luminescence nanosensors, *Physica B* **2024**, *673*, 415485.

[199] E. Hussain, N. Niu, H. Zhou, et al., Aggregation enhanced excimer emission (AEEE) of benzo[ghi]perylene and coronene: multimode probes for facile monitoring and direct visualization of micelle transition, *Analyst* **2018**, *143*, 4283-4289.

[200] P. Kruse, Review on water quality sensors, *J. Phys. D-Appl. Phys.* **2018**, *51*, 203002.

[201] World Health Organisation, Progress on Drinking Water, Sanitation and Hygiene, **2023**.